UiO : University of Oslo

Kevin G. Both

Plasmonically Enhanced Photocatalysis

Synthesis, Physical Properties, and Applications

Thesis submitted for the degree of Philosophiae Doctor

Department of Chemistry
Faculty of Mathematics and Natural Sciences

Centre for Materials Science and Nanotechnology (SMN)

2022

Series of dissertations submitted to the
Faculty of Mathematics and Natural Sciences, University of Oslo
No. 2586

ISSN 1501-7710

Print production: Graphics Center, University of Oslo.

"The greatest accomplishment is not in never falling, but in rising again after you fall."

Vince Lombardi

Preface

This thesis is submitted in partial fulfillment of the requirements for the degree of *Philosophiae Doctor* at the University of Oslo. The research presented here was conducted at the University of Oslo under the supervision of professor Truls E. Norby; professor Oystein Prytz, Dr. Athanasios Chatzitakis, Dr. Kristin Bergum, and Dr. Per-Anders Stensby Hansen as co-supervisors. This work was enabled by funding from the Department of Chemistry at the University of Oslo and received support from the Research Council of Norway (PH2ON, 288320). Support of the Norwegian Center for Transmission Electron Microscopy is also acknowledged (NORTEM 197405/F50).

Acknowledgments

I want to thank the scientific community I was allowed to be part of during these years here at the University of Oslo, specifically SMN. This work would not have been possible without a divers group of people near and far from Oslo. I would like to thank my supervisor, professor Truls E. Norby, co-supervisors professor Oystein Prytz, Dr. Athanasios "Sakis" Chatzitakis, Dr. Kristin Bergum, and Dr. Per-Anders Stensby Hansen for their guidance and discussions, forcing me to look at the bigger picture and leave my scientific comfort zone. Trusting me with co-supervising two M.Sc. students and giving me the freedom to pursue any scientific direction within the topic of this work enabled me to grow and learn even more than just through this work. Particularly I am grateful to Sakis for including me in many different aspects of his work, including some variations of the work presented in this thesis, for the frequent discussions, suggestions, the enjoyable conference in Italy, and all the feedback provided.

Naturally, I also want to thank Vilde for the close collaboration and the company in the office. Your computational insights and astute comments, and suggestions aided my understanding and improved the resulting work. I appreciate Thomas Aarholt for the collaboration and the discussion about TEM and related data analysis. The collaboration with Xiaolan was very fruitful, and I appreciated having someone in the lab running exsolution experiments with the same equipment and sharing notes on parameters. I am grateful to Dragos Neagu for his insights into exsolution and the debates surrounding different aspects encountered in this work. I thank everyone at Electrochemistry and Structure Physics for creating an enjoyable working environment and always providing help if needed. Specifically, I want to thank Phuong Dan Nguyen for her excellent support and expertise on the TEM and Ole Bjorn Karlsen for his help and suggestions during sample prep and XRD analysis. Also, Jonathan Polfus for reading parts of the thesis and providing feedback. Finally, Håkon

and Stine, you have been not only great co-workers but also good friends, always ready to play some ping pong or take a break during stressful times.

I cannot thank my friends in Oslo enough for their support and great company during these challenging years. I don't take it for granted that you invited me to participate in activities, partake in cabin trips, or celebrate special events with you. I appreciate my friends scattered around the globe, creating an environment where I was able to reach out to a friend at any hour of the day if I needed or wanted to. To my friends in Switzerland, thank you for taking the time whenever I visit Switzerland, called or texted. Despite my infrequent visits, I always felt like we just saw each other, and you made me feel part of your life despite the distance.

Finally, I want to thank my family; this work would not have been possible without you. You supported me unconditionally, visited whenever possible, sent care packages with my favorite Swiss goods, and provided feedback and suggestions whenever I needed of such. There is no doubt that I forgot to thank numerous people, and I have certainly named only a fraction of the people I am thankful for by name. I am truly grateful for all your support, and thank you from the bottom of my heart.

Kevin G. Both
Oslo, October 2022

Summary

In this work, plasmonic metal nanoparticles (MNPs) are utilized to improve the photoelectrochemical (PEC) response of strontium titanate (STO). These MNPs were introduced by either direct exsolution, i.e., nickel (Ni), copper (Cu), iron (Fe), ruthenium (Ru), and silver (Ag), or by galvanically replacing exsolved less noble MNPs, i.e., Ni by Gold (Au), or Cu for Ag. Au, Ag, and Cu were the materials chosen with significant plasmonic activity; Fe, Ru, Pt, and Ni were used to make MNPs with minimal plasmonic response.

Two different stoichiometries of STO were synthesized. One, La-doped A-site deficient STO ($La_{0.6}Sr_{0.2}Ti_{0.9}Ni_{0.1}O_{3-x}$), was exclusively doped with Ni and utilized as powder samples. The other stoichiometry was A-site excess STO ($Sr_{1.07}Ti_{0.93}M_{0.07}O_{3\pm\delta}$, where M is the dopant) was doped with various metals. These excess perovskites were studied in thin film and powder forms.

A-site excess STO thin films were deposited by pulsed laser deposition on silicon substrates. The as-deposited thin films appeared nanocrystalline or amorphous until the exsolution process was engaged. The exsolution step was studied explicitly for these A-site excess STO thin films where the formation of MNPs occurred not only at or near the thin film surface but also on grain interfaces and in bulk. Moreover, the dopant diffused significantly during the process.

While the size of the template particles depended on the exsolution conditions, the galvanic replacement reaction determined the shapes and sizes of the newly formed MNPs. The replacement time and the form (thin film/powder) of STO

influenced the results, both completely replaced particles and partially replaced particles with complex structures were obtained. Additionally, more prolonged galvanic replacement reactions lead to larger particles. In turn, the specific shape of the plasmonic MNPs determined the localized surface plasmon resonance band shape and peak position.

Overall, exsolution leads to well-socketed MNPs, a property seemingly inherited by the MNPs created by galvanic replacement. Well-socketed MNPs are extremely difficult to obtain by any other technique and have a favorable localized surface plasmon resonance peak shift. The PEC response revealed that reducing STO first decreases the material's response. Reducing it further, however, increases the PEC response significantly. Au MNPs increase the PEC performance until the MNPs reach a specific size and subsequently decrease the PEC performance when growing more prominent. This work highlights the ease by which well-socketed plasmonic MNPs can be created, some impossible to synthesize by another technique, and how different reaction conditions can change the shape and size of the MNPs, ultimately tuning the localized surface plasmon resonance band shape and peak position. The method of exsolution and galvanic replacement reaction was generalized by utilizing different elements, implying that the tuning of catalytic activity depends on the choice of elements and reaction conditions.

List of Papers

Paper I

X. Kang, V.M. Reinertsen, K. G. Both, A. Galeckas, T. Aarholt, Ø. Prytz, T. Norby, D. Neagu and A.s Chatzitakis "Galvanic Restructuring of Exsolved Nanoparticles for Plasmonic and Electrocatalytic Energy Conversion". Small, 2022, 18(29), 2201106, DOI: https://doi.org/10.1002/smll.202201106.

Paper II

K. G. Both, V. M. Reinertsen, T. M. Aarholt, I. J. T. Jensen, D. Neagu, Ø. Prytz, T. Norby, and A. Chatzitakis "Ni-doped A-site excess SrTiO3 thin films modified with Au nanoparticles by a thermodynamically-driven restructuring for plasmonic activity". Submitted, *Catalysis Today* Special Issue: SPEA11, Under Review

Paper III

K. G. Both "Exsolution of Ni Nanoparticles in A-site Excess STO Thin Films I: Thin Film Properties". Manuscript

Contents

Chapter 1

Introduction

The Holocene, the name given to the last 11'700 years, marks the era when planet earth moved from a nature-governed environment to a human-dominated one [1–3]. With most of the cultural and technological development occurring within the Holocene, it is arguably the most crucial period in the history of humanity [1, 2]. Over the same period, the global population and productivity can be closely correlated to global energy consumption [2]. It is not surprising that the industrial revolution of the 19^{th} century and the utilization of atomic energy accelerated the growth of population, productivity, and energy consumption noticeably [2]. Simultaneously, humanity learned to utilize new forms of energy, enabling these and other revolutions [1]. Renewable energies have attracted enormous interest both in research and in everyday life. The unique advantage of renewable energy sources is, as the name suggests, the ability to sustainably utilize them without running into supply issues or contributing to climate change [4].

Despite their advantage, renewable energy sources also have drawbacks. An example of such a drawback is the day-night cycle for solar-powered devices, limiting their usage to hours with sunlight. Moreover, clouds can significantly decrease the efficiency of devices [5]. Similar drawbacks can be found for other renewable energy sources [6]. While adjusting the energy consumption to the hours when energy can be produced is a, theoretically, potential solution; practically, renewable energy sources should be coupled to effective energy storage to produce energy whenever possible and have it readily available at

times convenient to the consumers [6, 7]. Photocatalytic devices offer the solution to store energy in chemical bonds and are a valid alternative to conventional batteries [8, 9].

A photocatalyst is a semiconducting material with a band gap where an electron-hole pair can be excited by light. Driving a chemical reaction via photocatalyst results in particular requirements for the photocatalyst and the incoming photon [8]. The reaction's activation energy is the minimum energy necessary to perform it. However, in a real system, energy losses often lead to significantly higher energy demands than just the activation energy [8, 9]. To facilitate the demand, the band gap energy of a viable photocatalyst needs to be as large as the sum of activation energy and energy losses. This, in turn, poses a prerequisite for any photon interacting with the photocatalyst. The photon energy must be at least as large as the band gap energy [8–10].

An additional demand for a potential photocatalyst is its stability in reaction conditions. The water-splitting reaction exemplifies how the different requirements significantly raise the energy of the incoming photon. Splitting water, the reaction shown in equation (1.1) requires $237.2\,\mathrm{kJ\,mol^{-1}}$, resulting, via the Nernst equation, in a requirement of $\Delta E^\circ = 1.23\,\mathrm{V}$ per electron transferred (or a band gap of at least $1.23\,\mathrm{eV}$) [9].

$$\mathrm{H_2O} \longrightarrow \mathrm{H_2} + \frac{1}{2}\,\mathrm{O_2} \tag{1.1}$$

However, due to these losses, a realistic device requires 1.6 - $2.4\,\mathrm{eV}$ [8, 9]. Unfortunately, narrow band gap materials are usually unstable during the photocatalytic reaction [9]. Wide band gap materials such as strontium titanate ($\mathrm{SrTiO_3}$, STO), with a band gap of $3.2\,\mathrm{eV}$, would be stable but require a higher energetic photon, diminishing their efficiency [11, 12]. The efficiency can be increased by either decreasing the band gap energy or introducing new particles

enabling the energy absorption from photons with lower energy than the band gap energy. The latter will be further discussed in this thesis.

1.1 The Solar Spectrum

The sun, or rather, its surface temperature, determines the energy distribution of photons released into space. Some of these make their way to the earth's surface. The initial energy distribution approximately obeys the black body radiation distribution described by Planck's radiation law, given in equation (1.2) in wavelength form, and is displayed as a graph in figure 1.1 [13, 14]. While the actual spectrum just outside the earth's atmosphere deviates slightly from this ideal distribution [15], one can observe that the majority of photons have an energy of less than 3.2 eV.

$$S_\lambda = \frac{8\pi hc}{\lambda^5} \frac{1}{\exp\left(\frac{hc}{\lambda kT}\right) - 1} \tag{1.2}$$

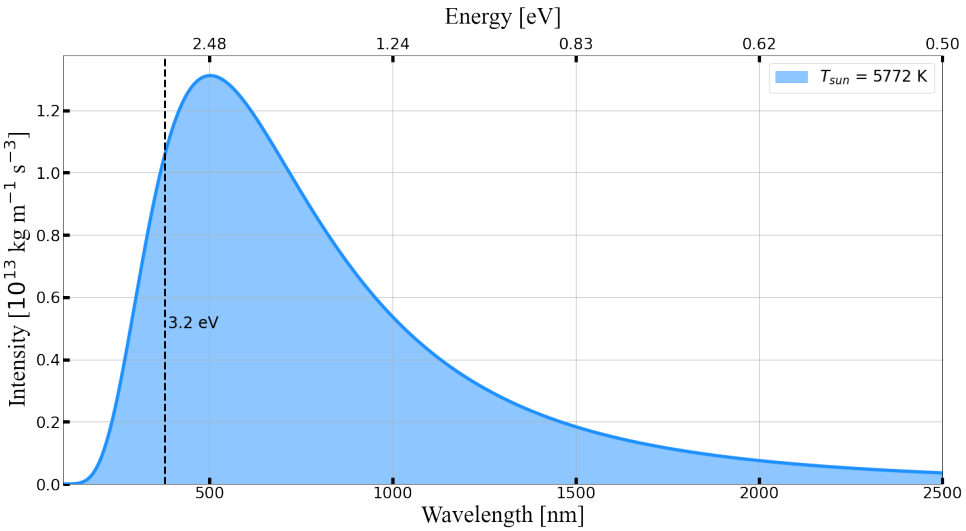

Figure 1.1: The black body radiation of a system with $T = 5772\,\mathrm{K}$, like the sun's photosphere (also referred to as the surface) [16].

Unfortunately, by far, not all photons emitted by the sun reach the earth's surface. Specifically, while the sun's radiation without any atmospheric interaction can be described as black body radiation, the interaction with the atmosphere near earth absorbs a significant part of the spectrum, resulting in daily changes at the same location [17]. The interaction of light with atoms and chemical species can be utilized in a plethora of different scientific areas and techniques, i.e., spectroscopy techniques [18, 19], sensors [20], or creating gauge potentials [21]; however, the loss due to atmospheric interaction is detrimental for photocatalysis because many high energy photons are not reaching the photocatalytic devices [17].

1.2 Photocatalysts

The sun can be regarded as a photon emitter, and, as discussed in section 1.1, both the sun and the requirement for photons to travel through the atmosphere to reach a photocatalyst on the surface of the earth lead to a particular energy distribution of the incoming photons [17]. Similarly, the photocatalyst can be viewed as a photon receiver because every photon reaching the material interacts with it. These interactions can be useful by exciting an electron-hole pair able to perform in a chemical reaction, or the photon can heat the device, resulting in no catalytic activity [22].

The inspiration for photocatalysis is nature itself. Photosynthesis, used by nature for millions of years, is a two-step process leading to the oxidation of H_2O to O_2 and the reduction of $NADP^+$ to NADPH. NADPH and the proton gradient, created during the reaction, fuel the Calvin cycle essential to fixate carbon in nature [22].

In contrast to nature, humanity has been driving chemical reactions by sunlight next to no time. The first to discover the photoelectric effect was

Edmond Becquerel in 1839 [23]. The field of modern photoelectrochemistry eventually developed from this discovery, evolving into a multidisciplinary field [24]. As part of photoelectrochemistry, photocatalysis benefited from pioneering works by Boddy, Honda, and Fujishima, among others, advancing the field substantially [25, 26]. Moreover, the recent public interest in renewable energy technology boosted the field further [10, 22].

Strictly speaking, a system that drives a chemical reaction thermodynamically uphill (change in Gibbs free energy, $\Delta G > 0$) performs photosynthesis [9, 27–29]. On the other hand, a system that drives a thermodynamically downhill reaction ($\Delta G < 0$) by enabling kinetically faster reaction pathways is performing photocatalysis [27, 30, 31]. However, due to the similarity in materials properties and mechanisms, such as light absorption, charge separation, and charge transfer of photosynthesis and photocatalysis, the definition of the International Union of Pure and Applied Chemistry (IUPAC) will be used in this thesis [32].

IUPAC Definition: Photocatalyst [32]

"Catalyst able to produce, upon absorption of light, chemical transformations of the reaction partners. The excited state of the photocatalyst repeatedly interacts with the reaction partners forming reaction intermediates and regenerates itself after each cycle of such interactions."

Most photocatalysts stable under reaction conditions have large band gaps, as introduced at the beginning of this chapter and elaborated in section 2.4, significantly limiting the number of photons with enough energy to excite an electron-hole pair. Efforts are being made to stabilize narrow band gap photocatalysts during operation conditions to increase the number of photons able to participate in an electron-hole generation [33, 34]. Another way to increase the number of photons participating is by introducing metal nanoparticles (MNPs) with plasmonic activity [8].

1.3 Plasmonics

Introducing MNPs to a photocatalytic system creates heterojunctions between the MNPs and the semiconductor photocatalyst [8]. These heterojunctions between plasmonically active MNPs and the semiconductor can enhance the activity of the photocatalyst by transferring and consequently utilizing the plasmonic energy from the metal to the semiconductor [35]. By illuminating metals like gold (Au), silver (Ag), copper (Cu), and aluminum (Al), localized surface plasmon resonance (LSPR) modes are excited [8, 36]. In theory, light absorption can be tuned across the visible light spectrum [37, 38]. Consequently, the MNPs can act as tunable light antennas for the photocatalyst. Several mechanisms allow plasmonically active MNPs to transfer energy to the semiconductor [8, 35, 39]. Among them are light scattering/trapping, plasmon-induced resonance energy transfer (PIRET), and hot charge carrier injection [8].

Definition: Plasmonics (as found in [40])

"Plasmonics may be defined as the study of the interaction between electromagnetic radiation and free electrons in a metal and all the accompanying collective phenomena [41]."

Humanity has utilized plasmonics for more than two millennia. In ancient Rome, gold and silver MNPs were used to color objects [42]. While the mechanism behind the color was not clear at the time, it did not prevent the manufacturing of astonishing objects, such as the Lycurgus cup in 400 AD. The Lycurgus cup is covered in Au and Ag MNPs and changes color when exposed to different lighting conditions, as seen in figure 1.2 [43]. One and a half millennia later, in 1908, Gustav Mie published his famous paper "Beiträge zur Optik trüber Medien, speziell kolloidaler Metallösungen" (Engl. "Contributions to the optics of turbid media, particularly of colloidal metal solutions" [44]) describing the interaction of electromagnetic waves with MNPs and explicitly solving Maxwell's

equations for perfectly spherical particles [45]. Since then, Endriz and Spicer reported photoemission peaks at energies near the surface plasma frequency of a roughed surface aluminum film, with the intensity dependent on the surface roughness [46]. Kostecki and Augustynski presented plasmon-induced photoelectrochemical activity by a rough Ag film electrode in the early 1990s [47, 48]. Many publications have focused on describing the absorption or energy transfer mechanisms in plasmonic photocatalytic systems [8].

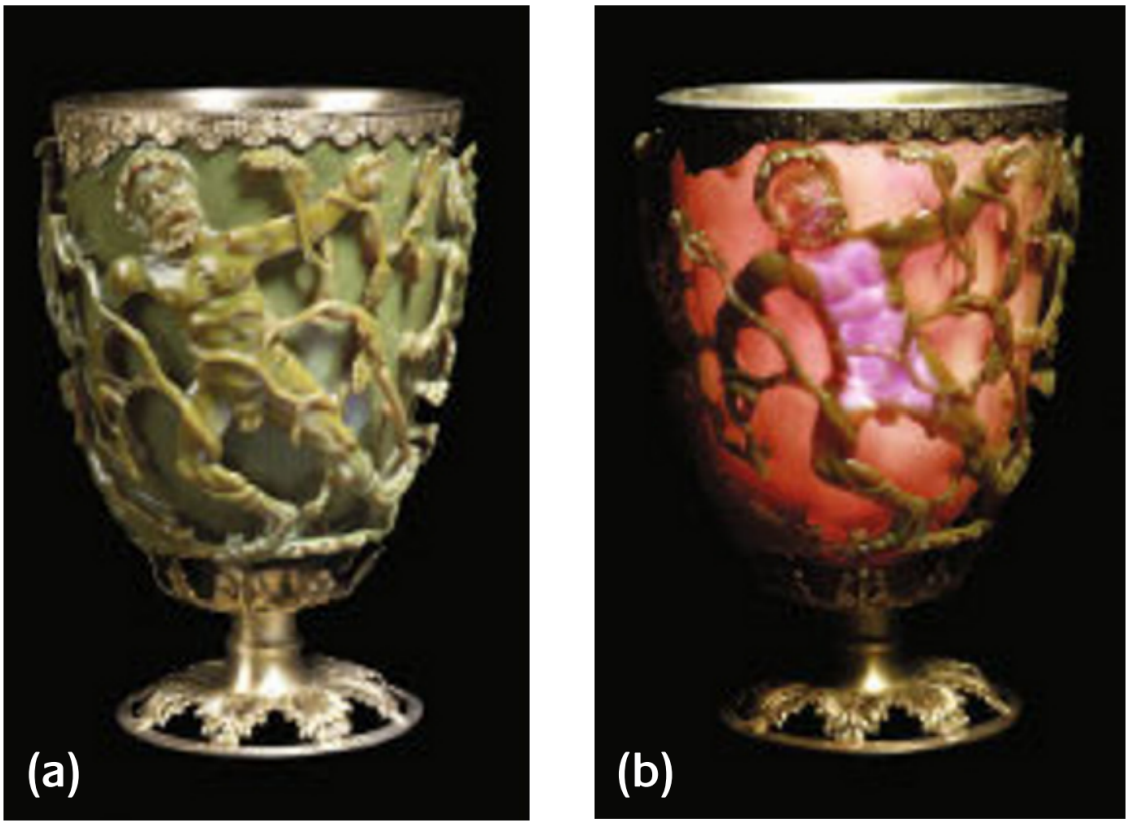

Figure 1.2: The Lycurgus Cup under different lighting conditions. (a) The cup is lit from the front (reflective light), appearing jade green. In (b), the cup is illuminated from the back (transmitted light), changing the color to ruby. The figure was reproduced from [43] under the Creative Commons Attribution Noncommercial License.

Plasmonic MNPs, together with photocatalysts or photoelectrodes, can exhibit different effects, namely (i) strong light absorption, (ii) intensive far-field light scattering, (iii) abundant hot carrier generation, and (iv) plasmonic heating

effects [8]. Each decay mechanism exhibits a system-dependent occurrence probability, expressed by dividing the number of charge carriers generated by a particular process by the total number of charge carriers generated [49]. Moreover, the enhancement mechanisms depend on the balance of near-field dipole-dipole interactions, light scattering, and hot carrier responses to incident light. Consequently, the plasmon's dephasing time, determined by the radiative and non-radiative damping mechanisms, directly influences which step of the plasmon evolution is dominant [8].

1.4 Aim and Content

This work aims to introduce and study a way to create well-socketed plasmonically active MNPs. Particularly, the synthesis method requires minimal engineering and low amounts of precious metal. The synthesis route also aims at going beyond the state of the art, synthesizing nanomaterials difficult or tedious to obtain. It is hypothesized that these nanomaterials and their unique placement in the surface and subsurface of the supporting materials improve their photocatalytic properties. Furthermore, the exsolution behavior within a thin film is examined to deepen the understanding of the formation process. Here we suggest that exsolution occurs not only at the surface but also at internal surfaces, i.e., grain boundaries, etc., and in bulk, which can be of interest when designing and realizing tunable functional materials utilizing exsolution.

This work will discuss various aspects of photocatalysis and plasmonics to create a foundation for the papers presented in chapter 4. First, the perovskite structure, with STO as a representative, is introduced in section 2.1. Exsolution, an elegant process to introduce MNPs into a perovskite structure, is covered in section 2.2. Not every plasmonically active metal can be exsolved, but the galvanic replacement reaction offers the ability to introduce the plasmonically

active element into the appropriate host material (see section 2.3). In section 2.4, a closer look at photocatalysis is taken, followed by a discussion of plasmonics (section 2.5).

The methodology used in the experiments conducted is described in chapter 3. A selection of publications concerned with the main topic of this thesis is introduced and reprinted in chapter 4. Additional publications are found in the appendices. In chapter 5, more results of experiments relevant to the thesis but not published in the publications presented can be found, and a summarizing discussion is given. The conclusion of all results presented in the main part of this thesis can be found in chapter 6 before an outlook is given in chapter 7.

References

[1] Roberts, N. *The Holocene: An Environmental History*. Wiley, 2013.

[2] Syvitski, J. et al. "Extraordinary human energy consumption and resultant geological impacts beginning around 1950 CE initiated the proposed Anthropocene Epoch". In: *Communications Earth & Environment* vol. 1, no. 1 (2020). Publisher: Nature Publishing Group, pp. 1–13.

[3] Walker, M. et al. "Formal definition and dating of the GSSP (Global Stratotype Section and Point) for the base of the Holocene using the Greenland NGRIP ice core, and selected auxiliary records". In: *Journal of Quaternary Science: Published for the Quaternary Research Association* vol. 24, no. 1 (2009). Publisher: Wiley Online Library, pp. 3–17.

[4] Alrikabi, N. "Renewable energy types". In: *Journal of Clean Energy Technologies* vol. 2, no. 1 (2014), pp. 61–64.

[5] Femia, N. et al. "Distributed maximum power point tracking of photovoltaic arrays: Novel approach and system analysis". In: *IEEE Transactions on Industrial Electronics* vol. 55, no. 7 (2008). Publisher: IEEE, pp. 2610–2621.

[6] Turner, J. A. "A realizable renewable energy future". In: *Science* vol. 285, no. 5428 (1999), pp. 687–689.

[7] Wang, T., Kamath, H., and Willard, S. "Control and optimization of grid-tied photovoltaic storage systems using model predictive control". In: *IEEE Transactions on Smart Grid* vol. 5, no. 2 (2014). Publisher: IEEE, pp. 1010–1017.

[8] Wu, N. "Plasmonic metal–semiconductor photocatalysts and photoelectrochemical cells: a review". En. In: *Nanoscale* vol. 10, no. 6 (Feb. 2018). Publisher: The Royal Society of Chemistry, pp. 2679–2696.

[9] Walter, M. G. et al. “Solar Water Splitting Cells”. In: *Chemical Reviews* vol. 110, no. 11 (Nov. 2010). Publisher: American Chemical Society, pp. 6446–6473.

[10] Wenderich, K. and Mul, G. “Methods, mechanism, and applications of photodeposition in photocatalysis: a review”. In: *Chemical reviews* vol. 116, no. 23 (2016). Publisher: ACS Publications, pp. 14587–14619.

[11] Reihl, B. et al. “Electronic structure of strontium titanate”. In: *Physical Review B* vol. 30, no. 2 (1984). Publisher: APS, p. 803.

[12] Phoon, B. L. et al. “Recent developments of strontium titanate for photocatalytic water splitting application”. In: *A Special Issue on Advanced Hydrogen Production Technologies* vol. 44, no. 28 (May 2019), pp. 14316–14340.

[13] Sheridan, K. and McLean, D. “The quiet sun at metre wavelengths”. In: *Solar radiophysics*. 1985.

[14] Ranganath, G. “Black-body radiation”. In: *Resonance* vol. 13, no. 2 (2008). Publisher: Springer, pp. 115–133.

[15] Granqvist, C. G. “Solar energy materials”. In: *Advanced Materials* vol. 15, no. 21 (2003), pp. 1789–1803.

[16] Williams, D. *Sun Fact Sheet. NASA Goddard Space Flight Center*. https://nssdc.gsfc.nasa.gov/planetary/factsheet/sunfact.html. 2013.

[17] King, D., Kratochvil, J., and Boyson, W. “Measuring solar spectral and angle-of-incidence effects on photovoltaic modules and solar irradiance sensors”. In: *Conference Record of the Twenty Sixth IEEE Photovoltaic Specialists Conference - 1997*. 1997, pp. 1113–1116.

[18] Van Den Broeke, J., Langergraber, G., and Weingartner, A. “On-line and in-situ UV/vis spectroscopy for multi-parameter measurements: a brief review”. In: *Spectroscopy europe* vol. 18, no. 4 (2006), pp. 15–18.

[19] Kalashnikov, D. A. et al. “Infrared spectroscopy with visible light”. In: *Nature Photonics* vol. 10, no. 2 (2016), pp. 98–101.

[20] Cao, C. and Sim, S. J. “Resonant Rayleigh light scattering response of individual Au nanoparticles to antigen–antibody interaction”. In: *Lab on a Chip* vol. 9, no. 13 (2009), pp. 1836–1839.

[21] Goldman, N. et al. “Light-induced gauge fields for ultracold atoms”. In: *Reports on Progress in Physics* vol. 77, no. 12 (2014), p. 126401.

[22] Yang, X. and Wang, D. “Photocatalysis: from fundamental principles to materials and applications”. In: *ACS Applied Energy Materials* vol. 1, no. 12 (2018). Publisher: ACS Publications, pp. 6657–6693.

[23] Becquerel, A.-E. “Recherches sur les effets de la radiation chimique de la lumiere solaire au moyen des courants electriques”. In: *CR Acad. Sci* vol. 9, no. 145 (1839), p. 1.

[24] Zhao, W.-W. et al. “Photoelectrochemical bioanalysis: A mini review”. In: *Electrochemistry Communications* vol. 38 (2014), pp. 40–43.

[25] Boddy, P. “Oxygen evolution on semiconducting TiO_2”. In: *Journal of The Electrochemical Society* vol. 115, no. 2 (1968), p. 199.

[26] Fujishima, A. and Honda, K. “Electrochemical Photolysis of Water at a Semiconductor Electrode”. In: *Nature* vol. 238, no. 5358 (July 1972), pp. 37–38.

[27] Osterloh, F. E. “Photocatalysis versus photosynthesis: A sensitivity analysis of devices for solar energy conversion and chemical transformations”. In: *ACS Energy Letters* vol. 2, no. 2 (2017), pp. 445–453.

[28] Chen, S., Takata, T., and Domen, K. “Particulate photocatalysts for overall water splitting”. In: *Nature Reviews Materials* vol. 2, no. 10 (2017), pp. 1–17.

[29] Chang, X., Wang, T., and Gong, J. “CO_2 photo-reduction: insights into CO_2 activation and reaction on surfaces of photocatalysts”. In: *Energy & Environmental Science* vol. 9, no. 7 (2016), pp. 2177–2196.

[30] Lange, N. A. and Dean, J. *Lange’s handbook of chemistry / Ed. John A. Deam; Formely compiled and edited by Norbert Adolph Lange.* Tech. rep.

[31] Lide, D. R. *CRC handbook of chemistry and physics*. Vol. 85. CRC press, 2004.

[32] McNaught, A. and Wilkinson, A. “Compendium of Chemical Terminology. Volume 1669 Blackwell Science Oxford”. In: (1997). Publisher: Oxford, UK.

[33] Jiang, H.-Y. et al. “Synthesis and photocatalytic properties of metastable β-Bi_2O_3 stabilized by surface-coordination effects”. In: *Journal of Materials Chemistry A* vol. 3, no. 9 (2015), pp. 5119–5125.

[34] Santato, C. et al. “Crystallographically Oriented Mesoporous WO_3 Films: Synthesis, Characterization, and Applications”. In: *Journal of the American Chemical Society* vol. 123, no. 43 (2001). PMID: 11673995, pp. 10639–10649. eprint: https://doi.org/10.1021/ja011315x.

[35] Abouelela, M. M., Kawamura, G., and Matsuda, A. “A review on plasmonic nanoparticle-semiconductor photocatalysts for water splitting”. In: *Journal of Cleaner Production* vol. 294 (2021), p. 126200.

[36] Kreibig, U. and Vollmer, M. *Optical Properties of Metal Clusters*. Springer Berlin Heidelberg, 2013.

[37] Rodríguez-Lorenzo, L. et al. “Reshaping and LSPR tuning of Au nanostars in the presence of CTAB”. In: *Journal of Materials Chemistry* vol. 21, no. 31 (2011), pp. 11544–11549.

[38] Kriegel, I., Scotognella, F., and Manna, L. "Plasmonic doped semiconductor nanocrystals: Properties, fabrication, applications and perspectives". In: *Physics Reports* vol. 674 (2017). Plasmonic Doped Semiconductor Nanocrystals: Properties, Fabrication, Applications and Perspectives, pp. 1–52.

[39] Gellé, A. and Moores, A. "Plasmonic nanoparticles: Photocatalysts with a bright future". In: *Current Opinion in Green and Sustainable Chemistry* vol. 15 (2019). Nanocatalysis Special Issue on the Green and Sustainable Chemistry Conference, Berlin, May 2018, pp. 60–66.

[40] Manfredi, G. *Preface to special topic: Plasmonics and solid state plasmas*. 2018.

[41] Stockman, M. I. "Nanoplasmonics: past, present, and glimpse into future". In: *Optics express* vol. 19, no. 22 (2011), pp. 22029–22106.

[42] Savage, G. *Glass and Glassware*. Octopus Books, 1973.

[43] Freestone, I. et al. "The Lycurgus cup—a roman nanotechnology". In: *Gold bulletin* vol. 40, no. 4 (2007), pp. 270–277.

[44] Mie, G. *Contributions to the optics of turbid media, particularly of colloidal metal solutions*. Contributions to the optics of turbid media, particularly of colloidal metal solutions Transl. into English from Ann. Phys. (Leipzig), v. 25, no. 3, 1908 p 377-445. Feb. 1976.

[45] Mie, G. "Beiträge zur Optik trüber Medien, speziell kolloidaler Metallösungen". In: *Annalen der Physik* vol. 330, no. 3 (Jan. 1908). Publisher: John Wiley & Sons, Ltd, pp. 377–445.

[46] Endriz, J. G. and Spicer, W. E. "Study of Aluminum Films. II. Photoemission Studies of Surface-Plasmon Oscillations on Controlled-Roughness Films". In: *Phys. Rev. B* vol. 4 (12 Dec. 1971), pp. 4159–4184.

[47] Kostecki, R. and Augustynski, J. "Unusually strong cathodic photoeffect at silver in contact with aqueous solutions containing carbon dioxide". In: *Chemical Physics Letters* vol. 194, no. 4 (1992), pp. 386–390.

[48] Kostecki, R. and Augustynski, J. "Effect of the surface roughness on the spectral distribution of photoemission current at the silver/solution contact". In: *Journal of Applied Physics* vol. 77, no. 9 (1995), pp. 4701–4705. eprint: https://doi.org/10.1063/1.359438.

[49] Kumar, P. V. et al. "Plasmon-Induced Direct Hot-Carrier Transfer at Metal–Acceptor Interfaces". In: *ACS Nano* vol. 13, no. 3 (2019). PMID: 30768238, pp. 3188–3195. eprint: https://doi.org/10.1021/acsnano.8b08703.

Chapter 2

Theory and Literature Review

The work presented in the subsequent chapters builds on various subfields of both physics and chemistry. Here, the theory and literature of this thesis's most important topics are reviewed. First, the perovskite structure (section 2.1), serving as substrate for the metal nanoparticles (MNPs), is introduced, followed by exsolution and galvanic replacement (section 2.2 and section 2.3), describing the state of the art of processes used to create MNPs. Photocatalysis (section 2.4) and plasmonics (section 2.5) summarize the energy transfer mechanisms utilized during the experiments.

2.1 Perovskites: Structure, Substitution, and Properties

Many perovskite structures have been studied since the name first appeared in 1839, describing the mineral $CaTiO_3$ [1]. Since then, perovskite evolved from describing a specific mineral in 1839 to the general name given to compounds with the formula ABX_3 today [1, 2]. In this work, perovskite generally refers to perovskite oxides ABO_3. Strontium titanate ($SrTiO_3$, STO) is an example of a perovskite often studied in its A-site deficient or reduced form. The properties of interest cover a wide range, from superconductivity, ferroelectric and piezoelectric properties to phase transitions, i.e., from cubic to tetragonal phase [2, 3]. At least since the 1970s, STO, a wide band gap semiconductor (band gap: 3.2 eV [4]), has also been considered a photocatalyst [5]. In this work, STO was not only used as the photocatalyst but also as a substrate for different metal nanoparticles

(MNPs) and will serve as a prototype of the perovskite structure in this section.

Like any ideal perovskite oxide with the stoichiometry ABO_3, STO consists of a large cation (Sr on the A-site), a smaller cation (Ti on the B-site), and three oxygen ions [1]. STO has a cubic perovskite structure (space group $Pm\bar{3}m$) with lattice parameter $a = 0.3905\,\text{nm}$ [6, 7]. It has a melting point of 2080 °C and consists of abundant elements [8]. The B-site cation is in 6-fold coordination, occupying the corners of the cube, and the A-site cation is located in the center of the cube with 12-fold coordination. The oxygen ions are positioned in the middle of the edges [2]. The two structures in figure 2.1 represent two different ways to display the perovskite structure, focusing on slightly different properties. It is evident from (b) that the BO_6 simultaneously has an important structural role and is more connected than the A-site cations. The octahedral network can be distorted or disconnected to accommodate defects and dopants, resulting in different properties [9, 10].

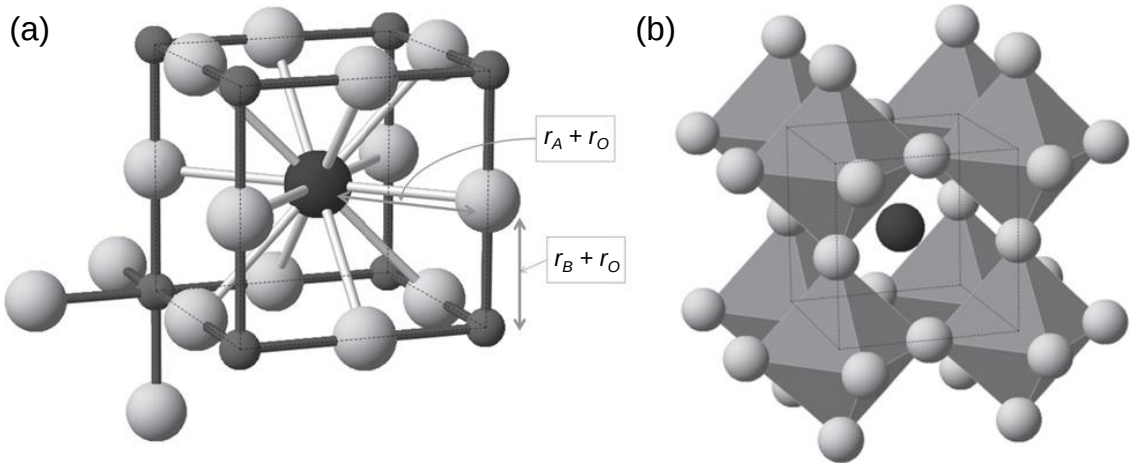

Figure 2.1: Two different ways of presenting the perovskite structure. In both, the A-site is the central site. In (a), the focus is on the unit cell and the coordination of the cations. The B-site is at the corners, and the large oxygen ions are located in the middle of the cube's edges. In (b), the corner-sharing network of TiO_2 is emphasized. The B-site is not visible; only the octahedra with the oxygen corners can be seen. The figure is reproduced from [2] with permission.

STO has a rich and diverse defect chemistry, originating from various factors such as the variety and number of defects that the perovskite structure can accommodate, the corresponding formation and migration energies, the resulting equilibrium, and the response of this equilibrium to external stimuli [2, 11–14]. This results in a manifold of different possible structures based on the elemental constituents of the perovskite and environmental conditions surrounding the perovskite structure [2, 15–24]. Moreover, introducing dopants, such as Lanthanum (La) for Sr, results in further defect formations due to the electro-neutrality condition [2, 13]. As a result, STO is well suited to host a variety of dopants but may also be used to expel these dopants from the original structure [25].

2.1.1 Excess and Deficiency

Typically, two different excess and deficiencies are considered: the A-site, or Sr, excess and deficiency, and the oxygen excess and deficiency [13]. Alternatively, super-stoichiometric or substoichiometric can describe excess and deficiency, respectively. While theoretically, any non-stoichiometry of the three sites can occur [15], B-site non-stoichiometry will not be considered directly. Rather, they will be considered by discussing the Ruddlesden-Popper (RP) phases (AO + ABO_3) [15]. Figure 2.4 shows examples of potential structures obtained with non-stoichiometric STO. An excess of oxygen and Sr results in the RP phase, i.e., intergrowths of SrO [16, 17], which has a rock-salt structure [26]. The number of perovskite, or $SrTiO_3$, layers per SrO layer is typically given by the number of layers n. Three different structures for $n = 1$, 2, and 3, are shown in figure 2.3, resulting in Sr_2TiO_4, $Sr_3Ti_2O_7$, and $Sr_4Ti_3O_{10}$, respectively, with the general formula of $Sr_{n+1}Ti_nO_{3n+1}$ [26]. It should be noted that while super-stoichiometry is used in literature and this work, perovskites cannot

accommodate any interstitial ions but rather either contain intergrown layers, such as the Ruddlesden-Popper structure or have substoichiometry of the other sites ($ABO_{3+\delta}$ is, in fact, $A_{1-\gamma}B_{1-\gamma}O_3$) [15].

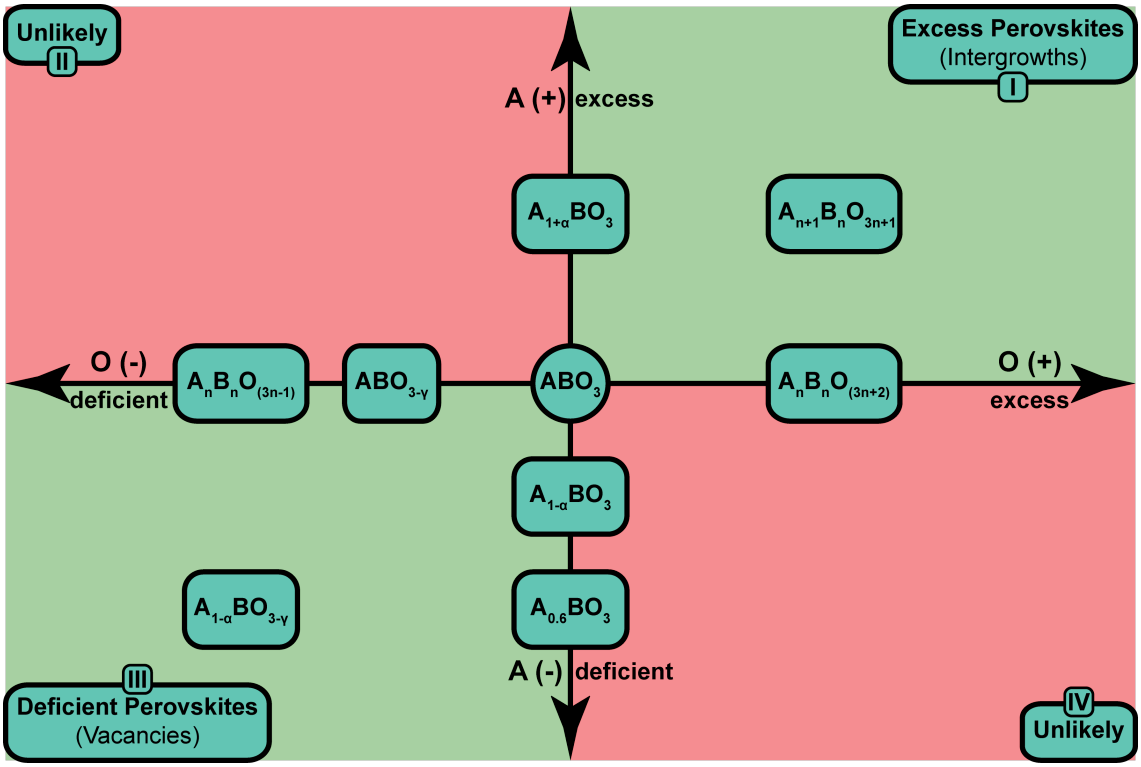

Figure 2.2: Examples of potential stoichiometries observed by a perovskite are shown here. The x-axis describes the O-stoichiometry, and the y-axis represents the A-site stoichiometry, with the origin being the ideal structure. The red zones symbolize stoichiometries that are unlikely. $A_{0.6}BO_3$, an example of A-site substoichiometry, is a tungsten bronze structure. The figure was adopted from [27].

Similarly, A-site and oxygen deficiencies can prevail simultaneously in the material, leading to $A_{1-x}BO_{3-x}$. Moreover, A-site excess or deficiency with a stoichiometric amount of oxygen, or oxygen deficiency and excess with a stoichiometric amount of A can also be observed. A deficiency of either A-site or oxygen ions and simultaneous excess of the other is unlikely without cation substitution [27].

The excess or deficiency of A-site cations or oxygen anions can be controlled

by subjecting the material to different conditions (i.e., T or p_{O_2} changes) or mixing the material with a non-stoichiometric amount of A-site cations. In addition, partially substituting either the A-site cation or B-site cation can also lead to excess or deficiencies. Briefly, substituting the A-site cation, such as Sr^{2+}, with a cation with a higher charge cation, i.e., La^{3+}, can be compensated by oxygen excess, for example, by $La_xSr_{1-x}TiO_{3+x/2}$ [2]. Conversely, substituting the B-site cations, such as Ti^{4+}, with a cation M^{m+} of lower or higher charge leads to non-stoichiometric oxygen given by $SrTi_{1-x}M_xO_{3-(4-m)x/2}$ or a combination of both $La_xSr_{1-3x/2}Ti_{1-y}M_yO_{3-(4-m)y/2}$ [2].

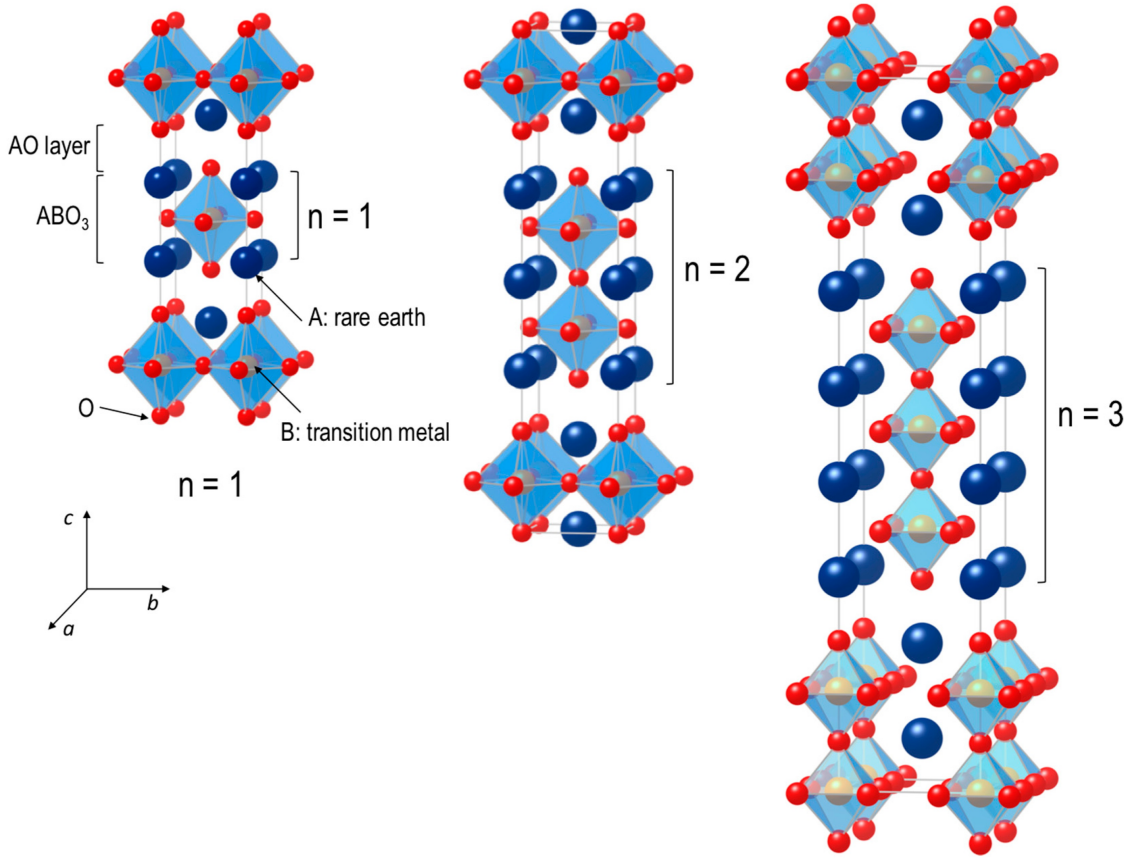

Figure 2.3: A representation of the Ruddlesden-Popper type perovskite $A_{n+1}B_nO_{3n+1}$ with $n = 1$, 2, and 3, respectively. It can be observed that n represents the number of perovskite layers between the rock salt AO interlayer. The figure was reproduced from [26] under open access Creative Common CC BY license.

As mentioned above, the oxygen partial pressure of the surrounding significantly impacts the sample's stoichiometry. For example, reducing conditions (low p_{O_2}, i.e., achieved by H_2 atmosphere) at high temperature led to oxygen vacancy formation in the material [2, 25, 28]. An example of this effect is given in equation (2.1).

$$2\,\mathrm{Ti}_{\mathrm{Ti}}^{\times} + \mathrm{O}_{\mathrm{O}}^{\times} \rightleftharpoons 2\,\mathrm{Ti}_{\mathrm{Ti}}^{\prime} + \mathrm{V}_{\mathrm{O}}^{\bullet\bullet} + \frac{1}{2}\,\mathrm{O}_2 \tag{2.1}$$

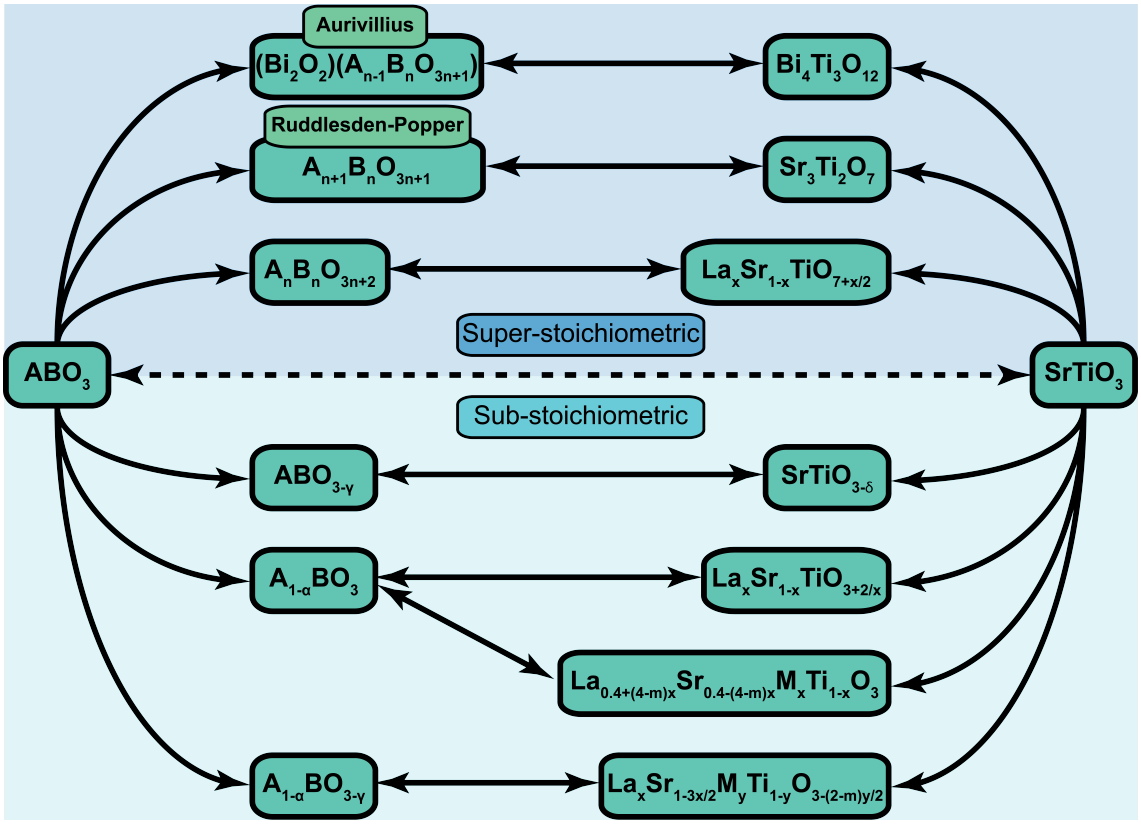

Figure 2.4: Sub- and superstoichiometries of general perovskites with examples. The figure was inspired by [2].

It should be noted that most B-site cations in the perovskite can support at least two oxidation states [2, 29]. This allows the control of the oxygen content in the perovskite and hence the ability to move along the x-axis in figure 2.2, as shown in equation (2.2). In fact, as seen in figure 2.4, including substitutions, excess and deficiencies, perovskites, and, as an example, STO, show a wide range

of possible obtainable stoichiometries [2, 12–16].

$$\mathrm{ABO}_{3+\gamma} \xrightarrow{\text{Red.}} \underbrace{\mathrm{ABO}_{3+\gamma-\delta}}_{\substack{\delta<\gamma \\ \text{(excess)}}} \xrightarrow{\text{Red.}} \underbrace{\mathrm{ABO}_{3+\gamma-\delta}}_{\substack{\delta=\gamma \\ \text{(stoichiometric)}}} \xrightarrow{\text{Red.}} \underbrace{\mathrm{ABO}_{3+\gamma-\delta}}_{\substack{\delta>\gamma \\ \text{(deficient)}}} \tag{2.2}$$

2.1.2 Cation Substitution

Above, the effect of cation substitution on excess and deficiency of oxygen has already been discussed. Here, the accommodation of the substituents is examined more closely. Generally, the size and charge of the substituent (M^{m+}) relative to the cation being replaced determines the manner of incorporation [2, 30, 31]. The size determines which site (A or B) the cation M^{m+} can replace. Substituents for A-site cations are typically large, with a high coordination number, usually between 8 and 12 [32].

On the other hand, the substituents for the B-site are smaller and require a coordination number of 6, in some cases even 5 or 4 [32]. Figure 2.5 shows the ionic radii-coordination number requirements for both sites, A (red) and B (green). The potential cations to substitute the A-site and the B-site do not overlap. The lack of overlap also allows for predicting which cation occupies which site in the perovskite system. This is in contrast to other systems like the spinel system, where inversion between sites can occur easily due to the similar sizes [33].

At this point, the Goldschmidt tolerance factor τ has to be introduced. The tolerance factor describes the mismatch between the $A-O$ and $B-O$ bond lengths, measuring how close the perovskite structure is to the perfect cubic cell, and is given in equation (2.3) [34]. The Goldschmidt factor can be derived from the geometry of the unit cell of perovskites. The empirical ionic radii (r_A, r_B, and r_O), obtained from X-ray diffraction at room temperature and atmospheric

pressure, are utilized to calculate the tolerance factor.

$$\tau = \frac{r_A + r_O}{\sqrt{2}(r_B + r_O)} \tag{2.3}$$

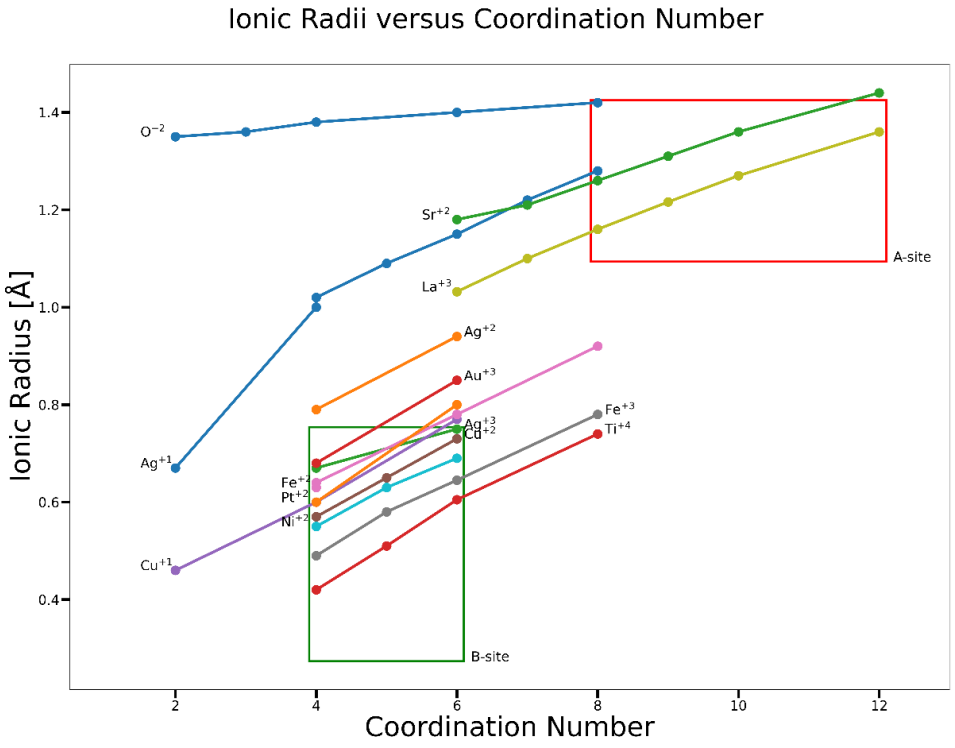

Figure 2.5: The ionic radii in Ångstrom versus the coordination number of commonly used ions. The two boxes mark regions where A-site (red) and B-site (green) cations would fulfill a Goldschmidt tolerance factor of $0.78 < \tau < 1$, for $La_{0.6}Sr_{0.1}TiO_3$. Ni^{2+}, Fe^{3+}, and Cu^{2+} fit easily into the B-site, while Au has to be in oxidation state +3 and fourfold coordinated. The figure is inspired by [2], and the atomic radii and coordination numbers used are from Shannon [29].

The average ionic radius of cations occupying the same site is used upon introducing additional cations. For STO, the radii of Sr^{2+} and Ti^{4+} have just the proper ratio to create the cubic lattice with $\tau \approx 1$ [29]. In contrast, if the perovskite observes a $\tau > 1$, the A-site cation is too large, forcing the TiO_6 octahedra to stretch slightly to accommodate the A-site ion. If the size mismatch is significant, the hexagonal polytype is observed [2, 35]. Moreover,

the elongation of the TiO_6 octahedra can lead to the Ti ion being located slightly off the symmetry center of the octahedral, resulting in a potential rise of ferroelectricity, as in the case of $BaTiO_6$ [36].

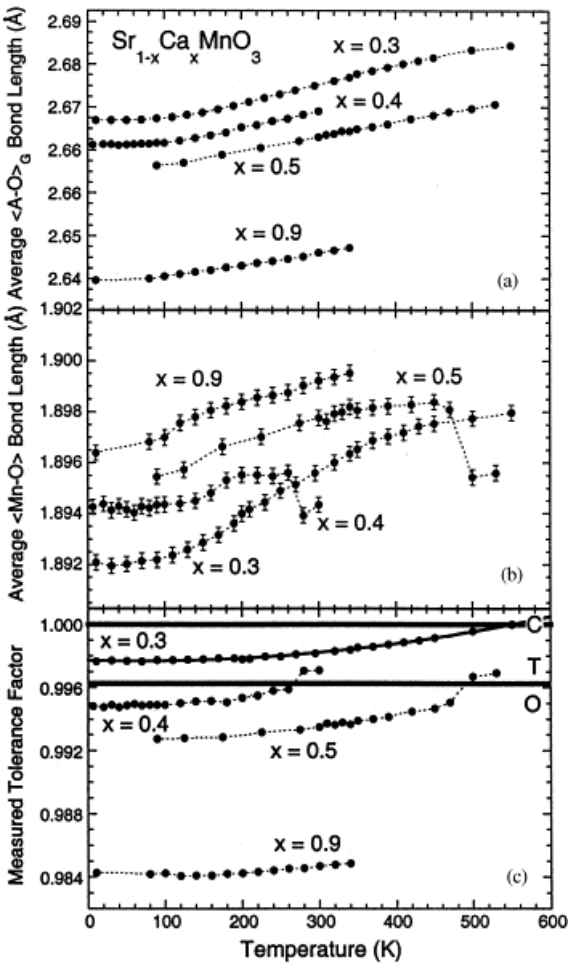

Figure 2.6: Three plots depicting the average bond length of $A-O$ (a), $B-O$ (b), and the measured tolerance factor (c) as a function of temperature, respectively, for the $Sr_{1-x}Ca_xMnO_3$ perovskite. The x-values represent the amount of Ca in the structure. Comparing (a) and (b) shows that the $A-O$ bond length expands more than the $B-O$ bond length. Furthermore, in (c), solid horizontal lines divide between the stability ranges of cubic (c), tetragonal (T), and orthorhombic structure (O) for the system. The figure was taken from [37] with permission.

In the case where $\tau < 1$, such as when the A-site is substituted by a smaller cation (La^{3+} or $Ce^{4+/3+}$ for Sr^{2+}) or the B-site is substituted by a larger cation (Fe^{3+} for Ti^{4+}), the A-site cation is undersized. The cuboctahedral cavity

is too large, preventing the A-site ion from contacting all 12 oxide ions. To accommodate this, the octahedra cooperatively rotate while retaining their regularity and corner-sharing. This process allows some of the oxide ions to be in touch with the A-site cations and is called octahedral tilting [38–42]. Two different kinds are observed. First, they can tilt in the same direction, known as in-phase tilting, and second, they can tilt in the opposite direction, known as out-of-phase tilting, with respect to all three crystallographic directions.

The tilting of the octahedra has two further consequences. The first is that the angle between the $Ti - O - Ti$ bond decreases from the ideal 180° by a small angle Φ. Typically, this small angle is never larger than 15°, but the change of bond angle leads to a change in the $Ti - O$ interaction (i.e., orbital overlap, inter-atomic distances, etc.), impacting the properties of the material, such as the width of the conduction band, band gap, or even $Ti - O$ bond strength directly [43, 44]. The second consequence is that, as mentioned before, the A-site cation is undercoordinated, typically with a coordination number of 8 - 10 instead of 12 [39]. This may result in changes in the diffusion pathways or cause further splitting of the degeneracy [45]. Elevated temperatures (500 - 1500 °C) can minimize or even reverse these trends, as reported in [19, 20, 46–51], possibly because the $A - O$ bond length expands more than the $B - O$ bond length [37] (see figure 2.6). While the cause for the tilting is probably due to the desire to increase the covalent interactions between cations and anions rather than steric causes, the tilting allows the perovskite to host a variety of substituents, regardless of the actual mechanism. The tilting can allow the system to host cations that change the tolerance factor such that $0.78 < \tau < 1$ holds true. A lower tolerance factor typically describes a system where the ilmenite structure becomes more stable [52–55]. Doping levels of the perovskite can also affect the ordering of the structure. Typically, a small number of dopants will be randomly

distributed, and ordering is unfavorable. However, by increasing the doping level, the formation of ordered structures can become more favorable over random distribution, leading to a plethora of A or B-site ordered perovskites [39, 56].

Deficiency Accommodation

A lack or deficiency of an ion is commonly described as a vacancy of the corresponding ion, i.e., V_A, if the A-site is deficient. The octahedral BO_6 retains its corner-sharing connectivity despite A- and/or O-site vacancies. Frequently, vacancies lead to tilting of the octahedra, likely due to the vacancies acting as dopants of different sizes [27]. A-site vacancies can be illustrated using a La-doped STO, $La_xSr_{1-3x/2}TiO_3$. Until a doping level of roughly $x \sim 0.4$, corresponding to an A-site deficiency of 0.2, the vacancies are randomly distributed, sometimes appearing in pairs but only slightly distorting the overall perovskite structure [19, 21, 22]. Upon raising the doping level to $x \sim 0.6$, the perovskite rearranges to a repetitive arrangement with tilted TiO_6 octahedra. The A-site vacancies are ordered such that full planes alternate with planes that are only $\sim \frac{1}{3}$ occupied [27]. The octahedral tilting occurs only around the x-axis, which is perpendicular to the direction of the cation-vacancy. Using the La-doped STO with a doping level of $x = 0.4$, Ti can be substituted by Ni on the B-site, with accompanying oxygen vacancies, resulting in $La_xSr_{1-3x/2}Ti_{1-y}Ni_yO_{3-y}$, which does not lead to significant changes in the perovskite lattice, or show any order, but the tilting of the BO_6 octahedra with respect to all three axes persists [27, 57]. An overview of ten different tilting orientations with corresponding Glazer notation can be found in figure 2.7 [58, 59].

Oxygen vacancies alone can alter the structure of the perovskite significantly. Considering an $A_nB_nO_{3n-1}$ perovskite for ($n \geq 2$) with oxygen vacancies, it follows that not all BO_6 octahedra are complete [60, 61]. Different cations on the B-site favor different coordination geometries, leading to different BO_z (4

$\leq$ z $\leq$ 6) geometries depending on the B cation. For example, B = Mn, Fe, and Ni can be used. For Mn ions, oxygen vacancies can be accommodated until 0.5 oxygen vacancies per unit cell by removing one oxygen from each MnO_6 octahedra, effectively forming a network of corner-sharing square pyramids [62]. The oxygen deficiency in Fe-containing structures is accommodated by combining FeO_6 octahedra and FeO_4 tetrahedral units, known as brownmillerite [63–65]. Ni, on the other hand, utilizes NiO_6 octahedra alternating with NiO_4 square planar units [66].

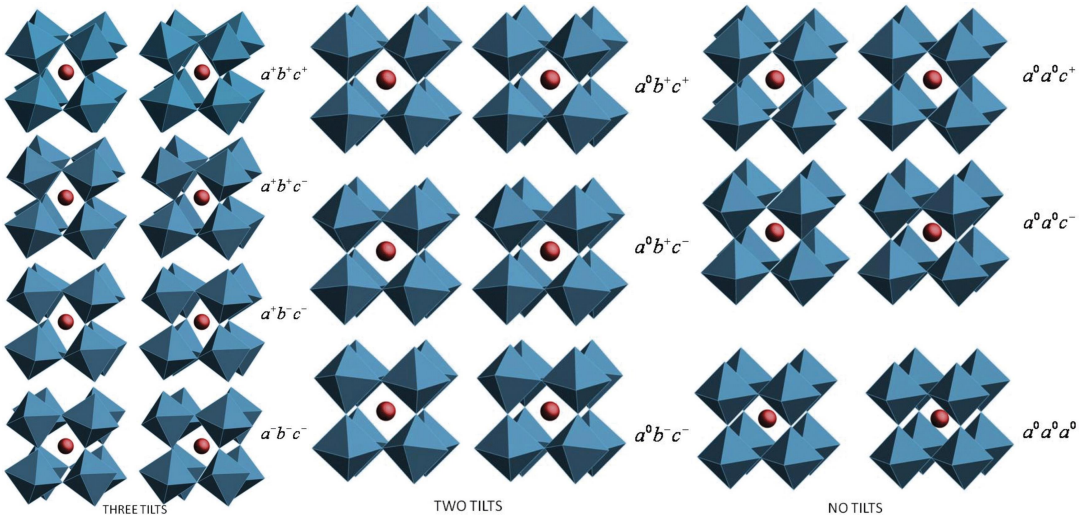

Figure 2.7: Ten different tilting of the octahedra, with the corresponding Glazer notation [58] on the right side of each rotation. The four leftmost rotations consist of three tilts, the middle three rotations consist of two simultaneous tilts, the top two on the right side are comprised of one tilt, and finally, the bottom rotation on the right shows no tilt. The figure was reproduced from [59] with permission.

Excess Accommodation

The incorporation of excess oxygen into the perovskite structure is heavily discussed in the literature [15, 16, 67]. Accommodating oxygen interstitially into a cubic close-packed arrangement is hard to imagine [15]. Furthermore, compensation through cation vacancies has also been eliminated as a potential

mechanism to accommodate oxygen excess [67]. However, intergrowths of oxygen can alternate with the ordinary crystal structure, essentially breaking the corner-sharing between octahedra of adjacent slabs [16].

Ruddlesden-Popper phases, as previously mentioned, can accommodate A-site excess by rock-salt intergrowths between n-layer thick perovskite blocks [16, 17]. Furthermore, similarly Aurivillius phases (i.e., $[Bi_2O_2]^+$ alternating with $(A_{n-1}B_nO_{3n-1})^-$ blocks) [68, 69], or Dion-Jacobson structures, perovskite blocks intergrown with halides, also achieve the accommodation of A-site excess [69].

Another well-studied group of perovskites is the $A_nB_nO_{3n+2}$ ($n \geq 4$) structures, suggesting that the slabs of {110} perovskite are joined by crystallographic shearing along the cubic [001] direction [18, 67, 70]. As an example, $La_4Ti_4O_{14}$ consists of four-layer thick perovskite blocks, offset towards each other by a crystallographic shear. At the crystallographic shear, the octahedra edges are no longer connected. It is also the location of the excess oxygen. Moreover, the octahedra are more distorted the closer to the shear they are. Finally, the A-site cations are displaced significantly the closer to the shear they are [70, 71].

2.1.3 Electronic Structure of Perovskites

The discussion above viewed the ions as spheres with rigid ionic radii, simplifying the geometric discussion, but not accurately describing the electronic state of the ions. The resulting interactions between the ions are incomplete, where, i.e., the structural differences in perovskite with B = Mn, Fe, and Ni cannot be explained entirely by the geometric picture alone [57, 65]. A more complete picture follows if the electronic structure and the change of the electronic structure on an ion occupying a particular site are also considered. This includes the combination of the influence of the electrostatic field exerted by the neighboring ions and the geometrical arrangement of the ions around the site. In addition, with the

octahedral coordination, B-site ions have their five-fold degenerated d states split into two subgroups [72].

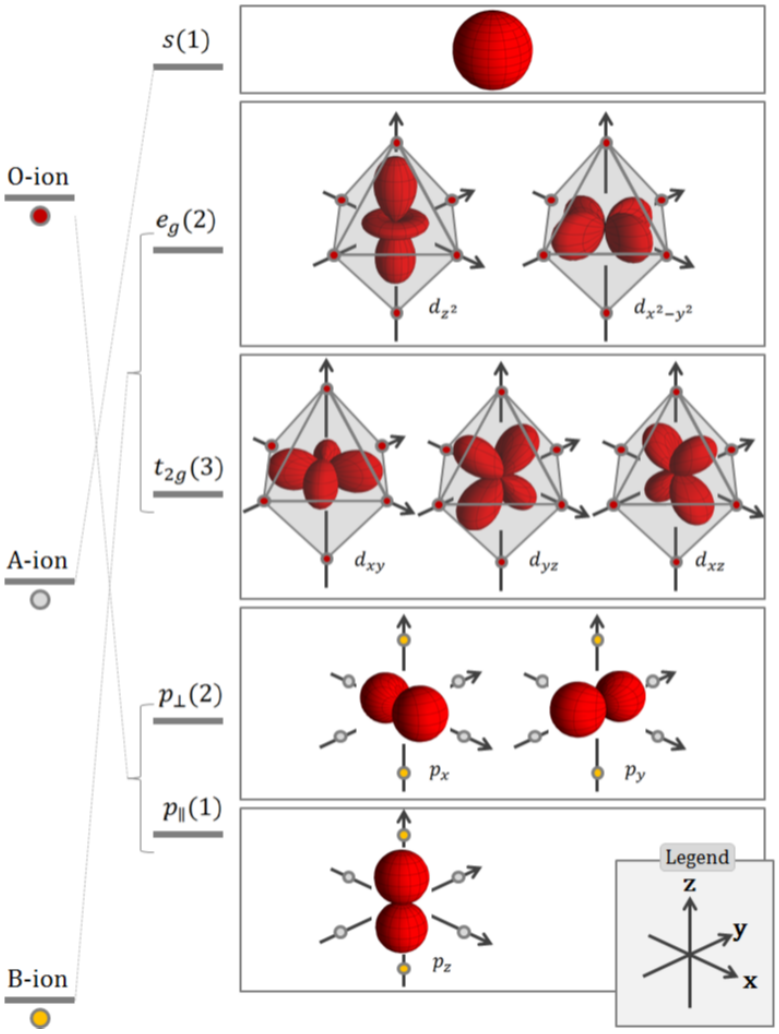

Figure 2.8: The orbitals of a general ABO_3 perovskite, including electrostatic potential effects, are shown. The bracket indicates the degeneracy, while the colored dots represent the corresponding nuclei. The figure was taken from [27].

Looking at the orbitals of a general ABO_3 perovskite, including the effect of electrostatic potentials on the ion states, reveals that the lowest unoccupied state of the A ions, an s state, experiences no splitting due to the non-degenerate spherical charge distribution of the A-site in the cubic symmetry [45, 73]. The d orbitals of the B-site ions have orbitals in a doubly degenerated level, and one

three-fold degenerated level, namely the e_g and t_{2g}, respectively. The e_g groups consist of orbitals with $d_{x^2-y^2}$ and d_{z^2} symmetry, while the t_{2g} group entails the d_{xy}, d_{yz}, and d_{xz} symmetries. Finally, the $2p$ orbitals of the oxygen ions are split into a doubly degenerated level $p_\perp$ and a non-degenerated level $p_\parallel$. The $p_\perp$ consists of p_x and p_y symmetries oriented perpendicular to a B − O axis and the $p_\parallel$ consists of the p_x symmetry, oriented parallel to a B − O axis [45, 73]. Figure 2.8 graphically represents the effect of the electrostatic potentials.

Ordinarily, the p states are filled completely, while the electronic configuration of the B-site ions determines the occupation level of the d states. For most perovskites, the s states remain empty due to the high energy level of these states compared to other states [73, 74]. Consequently, the s states play a minor role in describing the electronic properties and are usually omitted from calculations and interpretations of such properties [73]. It, in terms, leads to the situation where the electronic properties of the perovskite can be described by only considering the BO_3 part of ABO_3, specifically, the BO_6 octahedra mentioned previously [73, 74]. The A-site cation still affects the electronic properties, but it is expressed mainly through the electrostatic potential exerted on the other energy states and through the tilting of the BO_6 octahedra previously described [38, 39, 44, 45].

Further complicating the determination of the electronic properties is the non-negligible influence of covalent bonds between the transition metal ions and the oxygen ions. The overlap of orbitals leading to p − d hybridizations affects various properties. Here, σ bonding occurs between the e_g and $p_\parallel$ states, while π bonding occurs between t_{2g} and $p_\perp$ states [73, 75, 76]. Consequently, the d orbitals still split into the e_g and t_{2g} levels; for simplicity, they are now labeled $3e_g$ and $2t_{2g}$, but the energy separation between them is much more significant. In addition, $3e_g$ and $2t_{2g}$ are now a mixture of p and d orbitals, consisting of wavefunctions where the d orbitals combine out of phase with the p orbitals [73,

75, 76]. Hence, they are a representation of antibonding states. Bonding states are present, called e_g and $1t_{2g}$, consisting of roughly 30% d character and 70% p character [76]. Finally, states not contributing to the B − O bonding, so-called non-bonding states, are combinations of p orbitals located on the oxygen ion [73, 75, 76]. The energy splitting of the BO_6 octahedra with covalent interactions is given in figure 2.9.

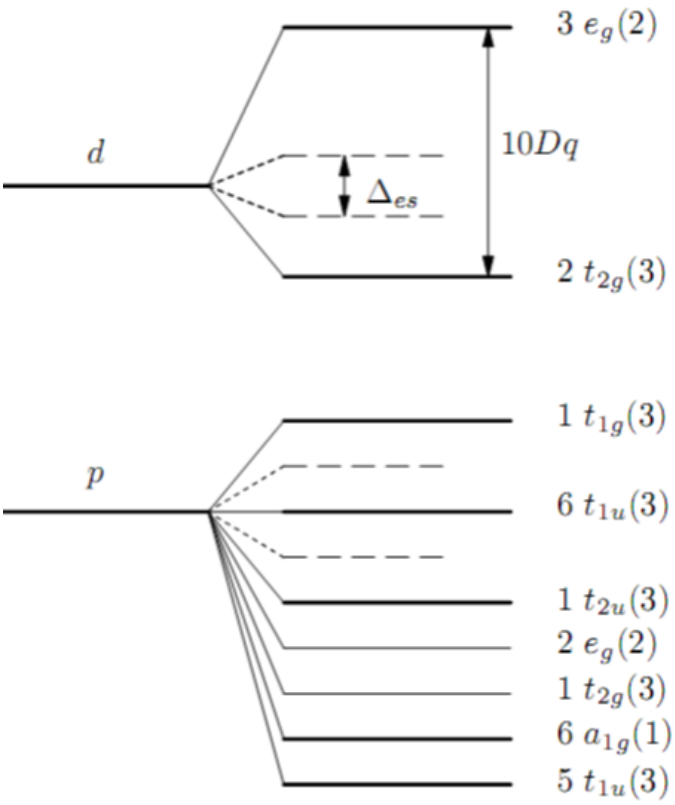

Figure 2.9: The energy levels of the BO_6 octahedra due to covalent interactions, where the dashed lines symbolize the energy levels due to the electrostatic splitting model. The figure was taken from [27].

2.1.4 Conductivity in Perovskites

Electronic conductivity in perovskites originates from the underlying electronic structure described above. As such BO_6 octahedra are again at the center of attention, and the partial covalent behavior of the B − O bonds allows the

electrons to be transferred back and forth between the ions and between B-site cations of adjacent octahedra via the shared oxygen anions [73, 74]. The electron delocalization leads to the formation of energy bands.

Metallic perovskites have partially filled d states and commonly only a single electron in the t_{2g} state. More electrons in the t_{2g} state may lead to a preference for localized electrons [77]. Perovskites with a small band gap also tend to have a partially filled d state, while wide band gap semiconductors, such as STO, have filled p states but empty d states [77]. Reducing STO leads to a narrowing of the band gap because oxygen ions are removed while they leave behind their electrons. The additional electrons can be expressed by reducing the Ti^{4+} to Ti^{3+}, as stated in equation (2.1). The electrons on Ti^{3+} preferentially delocalize to the neighboring Ti^{+4}, enabling the visualization of electronic conductivity as electron hopping between Ti^{3+} and Ti^{4+} ions. At very low temperatures (0.3 K), STO doped with electrons in such a manner can become superconductive [78].

Macroscopically speaking, the concentration of (free) charge carriers (n), their charge Z, and their mobility μ_e define the conductivity, as seen in equation (2.4) [79]. In STO, the concentration of free charge carriers depends on the concentration of Ti^{3+}. If the electrons are delocalized, hence free charge carriers, then $[e'] = [Ti^{3+}]$. This is usually true in a system with only Ti^{3+}/Ti^{4+} on the B-site. The mobility of electrons depends mainly on the crystal composition, nature, and geometry of the $Ti - O - Ti$ bond (i.e., the orbital overlap) and the microstructure (i.e., polycrystallinity, etc.) [27]. As outlined above, the tilting, cell size, and nature of A-site cation influence the nature of the $Ti - O - Ti$ bond by, i.e., changing the degree of overlap between the orbitals.

$$\sigma_e = n \cdot Z \cdot e \cdot \mu_e \tag{2.4}$$

Oxygen vacancies are a prerequisite for ionic conduction in perovskites.

Oxygen ions can hop to an adjacent vacancy, resulting in diffusion and bulk ionic conductivity at elevated temperatures [80–83]. Oxide ion diffusion is studied extensively in $La_{1-x}Sr_xGa_{1-y}Mg_yO_{3-(x+y)/2}$ (LSGM) [47, 80, 84, 85]. Mathematically, the diffusion of oxide ions can be expressed by equation (2.5) [27, 86–88]. The expression describes a thermally activated process proportional to the concentration of mobile vacancies $[V_O^{\bullet\bullet}]$ and the cell parameter a squared [88]. In addition, three main processes and their associated thermal effects or energies, formation ΔH_f, migration ΔH_m, and association ΔH_a factor into the diffusion expression. R and T are the Boltzmann constant and temperature in Kelvin, respectively.

$$D_{O_2} \propto [V_O^{\bullet\bullet}] \cdot a^2 \cdot \exp\left(\frac{\Delta H_f + \Delta H_m + \Delta H_a}{RT}\right) \tag{2.5}$$

For a given oxygen ion to diffuse, it has to break its bonds. The $A-O$ bond is significantly longer than the $B-O$ bond, as seen in figure 2.10, and thus the former is weaker. Consequently, the $A-O$ bonds only play a limited role in determining the diffusion rate, as shown in figure 2.10 (b) [88]. Breaking the $B-O$ bond leads to undercoordinated B-sites, i.e., lowering of coordination number from 6 to 5. Again, the nature of the B-site ions is crucial. Most B-site ions tend to favor 6-fold coordination, forming very strong bonds between $B-O$, ultimately resulting in a high energy for the formation of vacancies ΔH_f [88]. Titanium is exemplary for this, where the $Ti-O$ bond is strong, leading to reduced promotion of oxide ion diffusion but remarkable stability of $SrTiO_3$ [27]. Conversely, cations stable with different coordination numbers can be used to design materials that promote oxide ion mobility. Examples of cations promoting oxygen diffusion are $Mn^{2+/3+}$, $Co^{2+/3+}$, $Fe^{2+/3+}$, and Ga^{3+}, among others [13, 30, 88, 89]. Upon breaking one of the $B-O$ bonds, the oxide ion moves between two A-site cations, with a constant distance to the B-site ion still bonded to the

oxygen, leading to a curved path. Previous studies identified this step as the most energy-intensive and consequently limiting step [37, 90–92]. The nature of the A-site cation and the distortion of the lattice are other important factors determining the diffusion rate. Overall, the energy required to form a vacancy remains higher than the migration energy [88, 91].

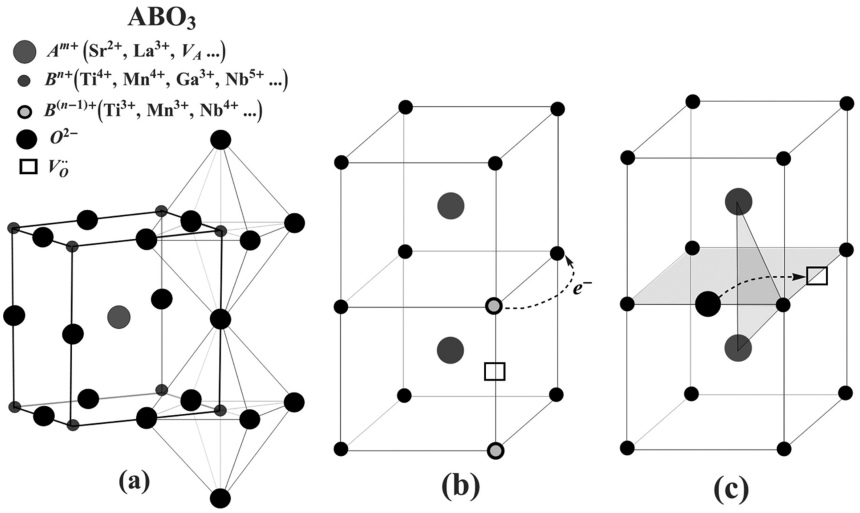

Figure 2.10: (a) Shows the unit cell of the perovskite with A-, B-, and O-site. (b) Represents the schematic view of the electronic conduction in perovskites, where the oxygen lattice is omitted for clarity. (c) The oxygen ion diffusion is illustrated. It is evident that the B − O bond length is $\frac{a}{2}$, and the A − O bond length is $\frac{a}{\sqrt{2}}$, where a is the unit cell side length. The figure was taken from [88] with permission.

Additionally, the number of defects has to be considered. With low concentrations of defects, the interaction between them is negligible. However, if many defects are present, defect-defect interactions occur, and their energy can become the dominant factor in the requirement for ion diffusion [93]. These defect associations can occur locally or over extended distances, potentially leading to an increase in association energy ΔH_a, or a significant decrease in mobile vacancies. A random distribution of oxygen vacancies has been shown to maximize the ionic conductivity [93]. The considerations of oxygen ion diffusion, and the connected vacancy diffusion, are also of concern when reducing

a perovskite. While the ionic conductivity during the process is unimportant, the associated changes in structure and electronic structure are.

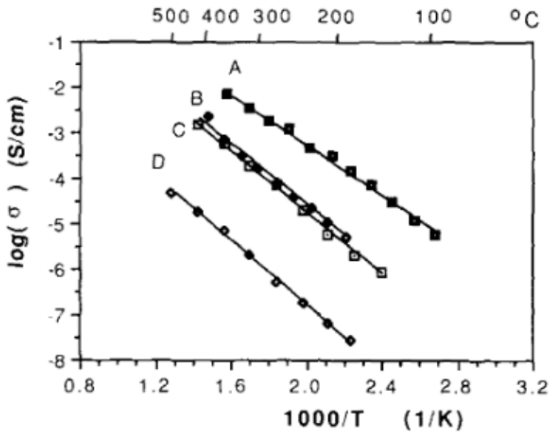

Figure 2.11: The Arrhenius plots of lattice conductivity for (A) $Ba_3In_2ZrO_8$, (B) $Ba_3In_2CeO_8$, (C) $Ba_3In_2HfO_8$, and (D) $Ba_2In_2O_8$, where the random distribution of the B-site dopant was found to introduce random distribution of the oxygen vacancy distribution [93]. The figure was taken from [93] with permission.

2.1.5 Reduction of Perovskite Titanate

Reduction of a perovskite is generally achieved by exposing the material to reducing conditions (i.e., low p_{O_2}) at elevated temperatures (500 - 1400 °Cor use different means of reduction, i.e., applied potentials [94]. However, the latter will not be considered further in this work. A range of low p_{O_2} can be achieved by utilizing a variety of different gases, ranging from inert gases (e.g., Ar, N_2), reducing gases (e.g., HArmix (5% H_2 + 95%Ar), H_2), to mixtures of both. As equation (2.1) describes, a reaction occurs upon exposing the material to these conditions. Formally, a perovskite, ABO_3, is reduced to $ABO_{3-\delta}$, where δ represents the oxygen lost during the reduction process. From equation (2.1), it follows that $\delta \propto [V_O^{\bullet\bullet}]$ and $2\delta \propto [Ti'_{Ti}]$. As shown in the discussion above, δ plays an essential role in describing the structure-property relationship in perovskites because it correlates with a range of properties,

including electronic conductivity, catalytic activity, the transition temperature of oxide superconductors, or magnetic ordering [78, 95–99].

In literature, reducing polycrystalline titanates is considered slow and a thermally activated process [100–103]. The same B-site cations that allow fast oxide ion mobility can enhance the kinetics and extent of exsolution, similar to A-site vacancies and unordered defects [13, 30, 89, 100, 104].

2.2 Exsolution of Metallic Nanoparticles

The utilization of MNPs has soared to new heights in recent years, with various applications stretching across the fields of catalysis, electrochemical energy devices, electronics, optics, and photocatalysis [105–111]. MNPs are extensively researched, and have industrial applications, for example, in automotive exhaust catalysts [105, 112–115]. Keeping MNPs secure and stable is challenging, especially under reaction conditions; however, heterogeneous composites can be employed, utilizing a support material to immobilize MNPs. Creating MNPs on a supporting material is achievable by a top-down approach, with techniques like impregnations, electro(less) deposition, or chemical vapor deposition (CVD). The disadvantage of these top-down approaches is that the particles tend to agglomerate and coarsen during experimental conditions, resulting in degrading performance [105, 116, 117]. Alternatively, exsolution has been used to create MNPs on solid oxide supports [25, 28]. MNPs created by exsolution are more stable than their top-down counterparts [105, 118]. Exsolved particles also tend to have better interaction with the support, are known to influence the activity, selectivity, and stability of MNPs, and are more resistant to coking (the accumulation of carbon on the metal in a hydrocarbon environment) [119]. Exsolution can be viewed as decomposition with phase separation, where the process is controlled such that MNPs in bulk and well anchored on the surface

result [120].

Perovskites are commonly used to exsolve MNPs because of their flexibility to exhibit different stoichiometries [118]. As discussed in section 2.1, perovskites have the remarkable ability to host several dopants and can accommodate oxygen deficiency, too. In addition to perovskites, exsolution can be achieved using spinel- and fluorite-type oxides such as Y-doped ZrO_2 and CeO_2 [121–124]. However, these structures are beyond the scope of this thesis. Independent of which structure provides the framework of exsolution, macroscopically, the origin of the thermodynamic driving force of exsolution is the reducibility of exsolved cations dissolved in the lattice [125].

In perovskites, after substituting part of the cations, usually the B-site, with the ions of the desired MNPs, the structure can exsolve MNPs [25, 28, 105]. Redox exsolution can be triggered by thermal or electrical reduction, creating MNPs on the surface and bulk of the perovskite [125]. Particles emerge epitaxially and are at least partially socketed [28, 126].

2.2.1 Cation Selection

Selecting a suitable substitute metal for one of the perovskite cation sites is crucial. A primary requirement is the size of a potential substituent, being evaluated within the frame of the tolerance factor (see equation (2.3)), introduced in section 2.1. Typically, a tolerance factor below 0.78 leads to the ilmenite structure, while for $\tau > 1$, the unit cell takes a hexagonal form [2, 35, 52, 127]. Furthermore, the coordination number of the cations is an additional requirement, as also outlined in section 2.1. Here potential substituents are evaluated based on these two criteria. Table 2.1 shows the tolerance factor of a given perovskite, while figure 2.5, shown above, gives the ionic radii versus the coordination number. Two boxes mark configurations of ions that would be

suitable for A-site (red, figure 2.5) and B-site (green, figure 2.5) substitution while fulfilling a Goldschmidt tolerance factor of $0.78 < \tau < 1$. A-site and B-site cations form distinct regions, allowing the specific doping of one of the sites. The τ of less than one indicates that all the presented perovskites can host ions with a smaller radius than Ti^{+4} on the B-site while simultaneously still having some freedom to accommodate smaller ions on the A-site, too. Smaller radii on the B-site increase τ, while smaller radii on the A-site decrease it. Examples of different tolerance factors are given in table 2.1.

Table 2.1: The Goldschmidt tolerance factor for different stoichiometries is given, combined with some details.

Stoichiometry	τ	Details
$Ba_4Ti_3O_{10}$	1.062	RP phase (n = 3)
$Sr_3Ti_2O_7$	1.002	RP phase (n = 2)
$SrTiO_3$	1.002	Perovskite
$La_{0.4}Sr_{0.6}TiO_3$	0.990	La-doped
$La_{0.4}Sr_{0.4}TiO_3$	0.889	La-doped, A-site deficient
$La_{0.4}Sr_{0.4}Ti_{0.9}Ni_{0.1}O_3$	0.885	La-doped, A-site deficient, Ni-doped

Naturally, the size requirements change based on the structural size distribution. As stated above, to calculate the tolerance factor for a La-doped strontium titanate, the A-site ionic radius is defined by the ionic radius of La and Sr, multiplied by their respective stoichiometry (without the RP phase), and added together. Typically, the resulting radius is slightly smaller than the Sr^{2+} radius because La^{+3} has a smaller ionic radius [29]. Similarly, the resulting radius for the B-site is the combination of the radius of the Ti^{+4} multiplied by its stoichiometry and the substituent multiplied by its stoichiometry.

Determining the correct stoichiometry is crucial for for calculating of the correct Goldschmidt tolerance factor and creating stable charge-neutral perovskites. Generally, charge neutrality needs to be kept [105, 128]. It is essential to realize that, to exsolve the B-site substituent, the initial substitution

should always occur in oxidizing conditions. This thesis considers two base stoichiometries: A-site excess and La-doped A-site deficiency. In the former case, equation (2.6) describes the system without any B-site doping, resulting in the formation of Ruddlesden-Popper interlayers, as discussed above. In the latter situation, shown in equation (2.7), the correct initial stoichiometry of La and Sr results in no need for B-site or oxygen ion changes. The perovskite is stable, without additional phases, despite the A-site deficiency.

$$Sr_{1+x}TiO_{3+x} \rightleftharpoons x{\cdot}SrO + SrTiO_3 \tag{2.6}$$

$$\frac{x}{2}La_2O_3 + (1 - \frac{3x}{2})SrO + TiO_2 \longrightarrow La_xSr_{1-\frac{3x}{2}}TiO_3 \tag{2.7}$$

However, introducing the B-site substituent into the materials given in equation (2.6) and equation (2.7) leads to charge compensation requirements. Selecting, without limiting the generality of this example, 7% substitution of the B-site by Ni in the A-site excess structure and substituting 10% of the B-site by Ni in the A-site deficient sample, leads to two different behaviors. In the case of the A-site excess sample a hypothetical charge compensating mechanism is shown in equation (2.8). The stoichiometry of the A-site excess sample will experience a slight change, namely from its original $Sr_{1+x}TiO_{3+x}$ to $Sr_{1+x}Ti_{1-x}Ni_xO_3$ if the Sr excess is chosen to be equal to the amount of Ni and x is small. Most notably, there would be no need for oxygen excess, and Ruddlesden-Popper phases would not be present. However, as discussed above, perovskites cannot accommodate interstitial ions. In fact, by incorporating both Ni'_{Ti} and $V^{\bullet\bullet}_{O}$ defects in combination with a Ruddlesden-Popper phase, the perovskite can take the structure given in equation (2.9), mainly an oxygen-deficient perovskite phase with some Ruddlesden-Popper interlayers. For the A-site deficient case, the Ni'_{Ti} can be compensated by adding an equal amount of Sr and Ni to the initial structure, changing its stoichiometry to equation (2.10).

Again, no oxygen excess is required to maintain charge neutrality.

$$\mathrm{Sr_i^{\bullet\bullet}} + \mathrm{Ni_{Ti}^{//}} = {}_0 \tag{2.8}$$

$$\mathrm{Sr_{1.07}Ti_{0.93}Ni_{0.07}O_{3\pm\gamma}} \rightleftharpoons \mathrm{SrTi_{0.93}Ni_{0.07}O_{3-\delta}} + 0.07\,\mathrm{SrO} \tag{2.9}$$

$$\frac{x}{2}\,\mathrm{La_2O_3} + (1 - \frac{3x}{2} + \mathrm{y})\mathrm{SrO} + (1 - \mathrm{y})\mathrm{TiO_2} + \mathrm{yNiO} \longrightarrow \mathrm{La_xSr_{1-\frac{3x}{2}+y}Ti_{1-y}Ni_yO_3} \tag{2.10}$$

2.2.2 Mechanism and Defect Chemistry

The precise mechanism of exsolution is still a heavily debated topic in literature. Nonetheless, there is consensus that four steps are involved. These steps are: (i) cation diffusion, (ii) cation reduction, (iii) nucleation, and (iv) particle growth [129]. Exposing the material to a reductive environment leads to an oxygen gradient within the structure. The oxygen ions can move towards the lower oxygen content, creating more oxygen vacancies throughout the structure. Equation (2.11) shows the defect chemistry equation for oxygen vacancy formation, where oxygen ions diffuse to the surface, are released from the lattice as oxygen gas, and leave behind effectively positively charged vacancies with compensating electrons [28, 125].

$$\mathrm{O^{-2}} \rightleftharpoons \mathrm{V_O^{\bullet\bullet}} + 2\,\mathrm{e^-} + \frac{1}{2}\,\mathrm{O_2(g)} \tag{2.11}$$

It destabilizes the perovskite structure, and the average oxidation state of reducible ions declines gradually. This continues until these ions reach a metallic state. In other words, a sufficiently high oxygen vacancy concentration leads to metallic species within the structure. Subsequently, these metal atoms can nucleate and form particles, growing in size as the reduction of the materials continues [125]. The reducibility of each species can be determined to a first approximation by considering the Gibbs free energy of the reduction reaction,

where simple oxides with alkaline earth metals have a positive ΔG when reducing. In contrast, simple oxides of transition metals tend to have a negative ΔG at temperatures above 600 °C [125, 130]. The reduction of a simple oxide is given in equation (2.12), while the reduction of a perovskite is stated in equation (2.13). Comparing equation (2.12) and equation (2.13) shows that only one metallic species is reduced in both cases. In the first case, there is only one metallic species. However, in this case, the change in Gibbs free energy for the B-site in equation (2.13) is more favorable than the change in Gibbs free energy for the A-site, leading to reduction and ultimately exsolution of the B-site. Considering the Gibbs free energy of simple oxides and drawing conclusions for the reduction in perovskite is helpful, but it should be regarded as a coarse model guiding an initial screening of potential candidates. Iron (Fe) can be a prime example of an exception. Fe can be exsolved, despite the positive ΔG of its simple oxide under reducing conditions indicating it should not be [125]. Nonetheless, for the most part, transition metals and precious metals with negative ΔG are primarily shown to exsolve [125].

$$\frac{1}{x}\,\mathrm{M_xO_y} + \frac{y}{x}\,\mathrm{H_2(g)} \rightleftharpoons \mathrm{M} + \frac{y}{x}\,\mathrm{H_2O(g)} \tag{2.12}$$

$$\mathrm{ABO_3} + \mathrm{xH_2(g)} \rightleftharpoons \mathrm{AB_{1-y}O_{3-\frac{x}{2}}} + \mathrm{yB} + \mathrm{xH_2O(g)} \tag{2.13}$$

Another factor in the ability to exsolve an element is the lattice mismatch between the ion to be exsolved and the native cation occupying the site in the perovskite. This can be exemplified by taking Ni^{2+} ($r_{\mathrm{ion}} = 0.69\,\text{Å}$) and Fe^{3+} ($r_{\mathrm{ion}} = 0.645\,\text{Å}$) and trying to exsolve them from $La_{0.4}Sr_{0.4}M_{0.06}Ti_{0.94}O_{3-\gamma-\delta}$, where the oxygen non-stoichiometry is dependent on the oxidation state of the metal M (indicated by γ) and the A-site substitution and deficiency (indicated by δ). As described by Tsekouras et al., Ni exsolves easier because it has a bigger size mismatch than Fe compared to Ti^{4+} ($r_{\mathrm{ion}} = 0.609\,\text{Å}$) [131].

Advancements in surface imaging techniques have allowed the study of the surface while exsolution was occurring. Oh et al. in [132] applied temporal resolved atomic force microscopy (AFM) to study the surface morphology evolution during exsolution. They reported the appearance of a pit or hole on the surface before the formation of the MNP, and the MNP subsequently nucleated below the surface. Finally, the MNP then gradually emerged from the pit. TEM observations of exsolution revealed the emergence of the MNP through the pit ending up well socketed [132]. The facet of the perovskite influences the degree of exsolution, and MNPs generally grow epitaxially to the perovskite substrate [133]. The variety and sometimes contradictory observations of the exsolution behavior lead to the conclusion that the mechanism is highly system-dependent [125].

The observation of emerging particles close to the surface can be explained using strain field modeling, as shown in [132]. A spherical metal nucleus, formed within the bulk, can reduce its elastic energy by emerging to the surface because the surrounding oxide matrix no longer constrains the surface of the particle. Simultaneously, the surface energy of the particle increases. The total energy is still lowered if the MNP is sufficiently large because the elastic energy scales with the volume, while the surface energy only scales with the surface. The pit formation is driven by a free energy decrease, as stated by the same study. However, it is only the case if the depth d of the particle and the radius of the particle R have a ratio smaller than 3, i.e., $\frac{d}{R} < 3$ [132]. The socketing of the surface particles has been confirmed by HNO_3 etching, leaving behind pits with the same density number and size as the previous particles, as shown by AFM in [25]. The same publications showed that samples with conventionally grown MNPs on the surface treated similarly to the exsolved samples, including HNO_3, showed little to no embedding of the particles when observed by AFM. This

morphological difference is changing the catalytic properties of the MNPs, and in the case of plasmonically active MNPs, the plasmonic response may change severely [134].

Socketing stabilizes the particles during catalysis and prevents the coalescence of particles during exsolution. Again, [25] showed that during an aging test, roughly 90% of the initial particles remained on the surface during the test. While the test was conducted, the particles grew in size, suggesting continued exsolution fed the growth. Furthermore, the interaction between the substrate and the MNPs also prevents the uplifting of the Ni particles by carbon fibers, typically grown by small Ni MNPs in a hydrocarbon environment, called coking. If the carbon-fiber growth occurs in exsolved samples, the length of the fibers is shorter than the length of fibers grown in conventional samples. These stability improvements generally do not come at the trade-off of reduced activity [25, 125].

The formation of MNPs can also be explained by classical nucleation theory. It accounts for particles near the surface that have an additional drive to form and emerge due to different energies, as above, and also for potential particles formed in bulk far from the surface. Utilizing the classical nucleation theory of particles in solution as a starting point, the critical size, describing a size where further growth no longer requires energy but releases energy, can be introduced. To state it clearly, particles below the critical size require energy to increase their size, while growth for particles of larger size releases energy [135]. The radius at which the change occurs is called the critical radius, r^* [135]. The nucleation rate per unit volume of such particles, $N(T(t))$ in the classical theory of nucleation is given by equation (2.14), where c_{nuc} is the density of suitable nucleation sites, and ω is the characteristic frequency factor [136].

$$N(T(t)) = c_{\mathrm{nuc}}\omega \exp\left[- \frac{\Delta G^*(T(t)) + Q_{\mathrm{N}}}{RT(t)} \right] \tag{2.14}$$

$$\Delta G_{\mathrm{r}} = 4\pi r^2\gamma + \frac{4}{3}\pi r^3 \Delta G_{\mathrm{V}} = 4\pi r^2\gamma - \frac{4}{3}\pi r^3 \frac{RT \ln S}{V_{\mathrm{m}}} \tag{2.15}$$

$$S = \frac{[A]_{\mathrm{s}}}{[A]_{\mathrm{eq}}} \tag{2.16}$$

The exponent of equation (2.14) contains the Boltzmann constant R, and the time-dependent temperature $T(t)$, the critical free energy of nucleus formation ΔG^*, and finally, the activation energy required for an atom to jump through the matrix-particle interface, Q_{N} [135, 136]. The critical free energy of nucleus formation ΔG^* is associated with the critical radius r^*. The Gibbs free energy associated with the nucleation process is often used in classical nucleation theory [135], and the excess free energy ΔG_r, given in equation (2.15), reaches its maximum when the particle reaches the critical radius. The excess free energy consists of two terms, the first describing changes in surface free energies and the second describing bulk free energies [135]. Equation (2.15) consists of the radius r of the particle, the surface free energy per unit area γ, and the change in free energy between solute atoms in solution and bulk crystal per unit volume ΔG_{V}. As shown, the second term can be expressed with the ideal gas constant R, and as a function of the temperature T, the molar volume of bulk crystal V_{m}, and the ratio S given by equation (2.16), where $[A]_s$ is the solute concentration under saturation conditions and $[A]_{\mathrm{eq}}$ the solute concentration under equilibrium conditions [135]. It should be noted that changes in enthalpy ΔH_V are not considered in the relation between ΔG_V and S.

While equation (2.14) yields an impression of the nucleation rate, it does not give a measure of the number of clusters per size. This, in turn, can be obtained by utilizing equation (2.15) and the Boltzmann distribution, resulting in equation (2.17). In equation (2.17), N_0 is the total number of free solute

atoms per unit volume in the system, and N_A is the Avogadro constant, in addition to the previously introduced variables and constants. It can be seen that the number of clusters increases linearly with a higher number of free solute atoms per unit volume in the system and decreases exponentially with increasing ΔG_r [135].

$$N_\mathrm{r} = N_0 \exp\Big(-\frac{\Delta G_\mathrm{r}}{RT}\Big) = N_\mathrm{A}[A]_\mathrm{eq} S \exp\Big(-\frac{\Delta G_\mathrm{r}}{RT}\Big) \tag{2.17}$$

Equation (2.15) is positive if the solute is undersaturated, i.e., if $S \leq 1$. Moreover, increased particle sizes increase ΔG_r further. Therefore, nucleation is not favorable. However, if the system is supersaturated, i.e., $S > 1$, an increased cluster radius leads to a decreased ΔG_r, stabilizing clusters through growth. This can be further exemplified by figure 2.12, where ΔG_r and the average number of particles N are plotted as a function of radius for a supersaturated system. The free energy increases for particles with a radius below r^*. Consequently, the system reduces energy by dissolving small clusters, while new clusters form by random collisions. This leads to a Boltzmann distribution of the number of particles for a given size, as shown in figure 2.12 (b).

Determining the critical radius can be achieved by taking the derivative with regards to r of equation (2.15) and determining when $\frac{\mathrm{d}\Delta G_\mathrm{r}}{\mathrm{d}r} = 0$. Solving the resulting equation for r results in the critical radius, given in equation (2.18). Additionally, the critical radius can be used to find the maximum excess free energy ΔG^* (see equation (2.20)), the number of particles reaching the critical radius N_{r^*} (see equation (2.20)), and the nucleation rate $\frac{\mathrm{d}N_{\mathrm{r}^*}}{\mathrm{d}t}$ (see equation (2.21)). In equation (2.21), the f_0 is introduced, consisting of a factor of stable nuclei over the total number of nuclei, and a function with variables like vibration frequency of atoms, the activation energy of diffusion, and surface area of critical nuclei.

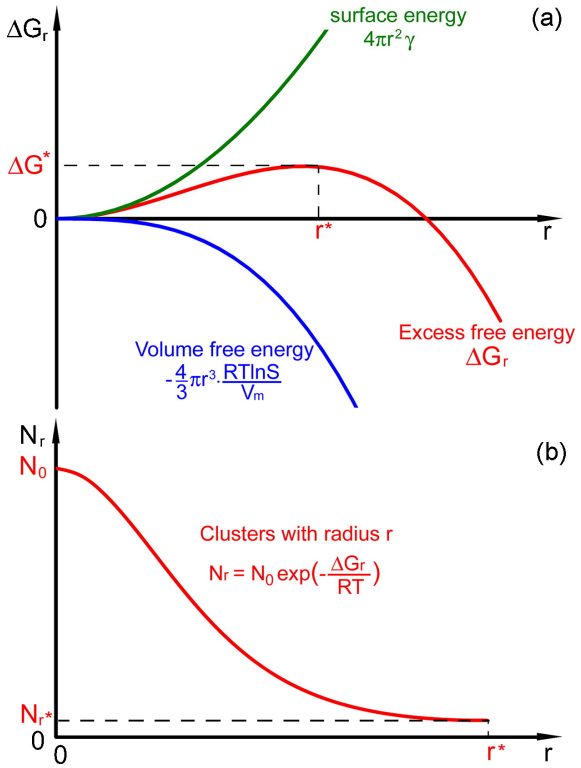

Figure 2.12: (a) The ΔG_r plotted versus the particle radius. The increase in ΔG_r for particles smaller than the critical radius is visible. (b) The average number of particles N as a function of particle radius. The figure was taken from [135], with permission.

The parameters described in equations (2.18) to (2.21) can be used to describe nucleation processes. They depend on essentially three variables, including the surface free energy (γ), reaction temperature (T), and degree of supersaturation (S). In experiments, the temperature, as well as the surface free energy, remain fixed, leaving the degree of supersaturation as the only variable. In colloidal synthesis the solute concentration changes during the reaction [135], similarly in exsolution. Nucleation and growth steps are separated to achieve a uniform particle size in colloidal synthesis [135]. Similarly, polydispersed nanoparticles form if growth and nucleation steps are not separated in exsolution.

$$r* = -\frac{2\gamma}{\Delta G_\mathrm{V}} = \frac{2\gamma V_\mathrm{m}}{RT \ln S} \tag{2.18}$$

$$\Delta G^* = \frac{16\pi\gamma^3}{3\Delta G_\mathrm{V}^2} = \frac{16\pi\gamma^3 V_\mathrm{m}^2}{3(RT \ln S)^2} \tag{2.19}$$

$$N_{r^*} = N_A[A]_{eq} S \exp\Big(-\frac{\Delta G^*}{RT}\Big) = N_A[A]_{eq} S \exp\Big(-\frac{16\pi\gamma^3 V_m^2}{3(RT)^3(\ln S)^2}\Big) \quad (2.20)$$

$$\frac{dN_{r^*}}{dt} = f_0 N_A[A]_{eq} S \exp\Big(-\frac{\Delta G^*}{RT}\Big) = f_0 N_A[A]_{eq} S \exp\Big(-\frac{16\pi\gamma^3 V_m^2}{3(RT)^3(\ln S)^2}\Big) \quad (2.21)$$

Unlike in colloidal synthesis and the above described classical nucleation theory, the change in free energy ΔG_r not only depends on ΔG_V but also on the elastic strain energy ΔG_S and the relaxation of the misfit-strain energy ΔG_{ms} [137]. Consequently, equation (2.15) has to be amended with these variables, as shown in equation (2.22). Correspondingly, equations (2.17) to (2.21) will include these additional terms to determine the parameters for a system with exsolved particles [137].

$$\Delta G_{r,\ exsolution} = 4\pi r^2\gamma + \frac{4}{3}\pi r^3(\Delta G_V + \Delta G_S + \Delta G_{ms}) \quad (2.22)$$

2.2.3 Single Perovskite Exsolution

Stoichiometric perovskites were the initial candidates studied in combination with reducible cations, including Ni^{2+}, Rh^{4+}, Ru^{2+}, Pd^{4+}, and Pt^{4+}, to synthesize the corresponding MNPs [138]. Nishihata et al. described a system with in situ grown catalysts with $LaFe_{0.57}Co_{0.38}Pd_{0.38}O_3$ where the catalyst was stable over 100 h under engine exhaust atmosphere [139]. Furthermore, Hamada et al. described the probable mechanism of self-creation of Pd particles by DFT study in the $LaFe_{1-x}Pd_xO_3$ system [130]. Co-exsolution of Fe^0 and Pd^0 has also been demonstrated for the $La_{0.8}Sr_{0.2}Fe_{0.9}Nb_{0.1}Pd_{0.04}O_{3-\delta}$ system [140]. While the enhancement was not very high, the system $La_{1-x}Sr_xCr_{1-y}Ni_yO_{3-\delta}$ showed catalytic improvements after Ni MNPs were exsolved [141]. Finally, $La_{0.5}Sr_{0.5}Ti_{1-x}Ni_xO_{3-\delta}$ was also examined for Ni exsolution [142]. Gao et al. demonstrated that Ni prefers to move to the (100)-oriented and SrTiO-terminated surfaces [143]. Nanocatalysts consisting of alloys have been

exsolved from $La_{0.6}Sr_{0.4}Fe_{0.8}Ni_{0.2}O_{3-\delta}$, resulting in Fe-Ni alloy MNPs [144] and $SrFe_{0.8}Cu_{0.1}Nb_{0.1}O_{3-\delta}$ creating Fe-Cu alloy MNPs [145].

A-site deficient perovskites have the advantage of ending in a steady cation defect-free $ABO_{3-\delta'}$ stoichiometry after exsolution. It can be shown by adjusting equation (2.13) to reflect the A-site deficiency in the starting structure resulting in equation (2.23) [105]. In addition, the exsolution of harder-to-reduce cations is possible in some cases, i.e., stable Ti cations in $La_{0.4}Sr_{0.4}TiO_3$ compositions were exsolved as TiO_2 or a reduced titanium oxide [146].

$$A_{1-x}BO_{3-\delta} + y\,H_2(g) \rightleftharpoons (1-x)ABO_{3-\delta'} + xB + yH_2O(g) \tag{2.23}$$

Neagu et al. described the effect of A-site deficiency on exsolution, stating that the creation of the oxygen vacancies leads to spontaneous B-site cation exsolution and locally regaining stoichiometry [28]. Gao et al. reported on an Sc-based A-site deficient perovskite system for Ni exsolution which exhibits good catalytic activity [129]. Recently, considerable efforts have been dedicated to the exsolution for room temperature electrocatalysis [147–152]. Zhu et al. described a system with catalytically active Ni MNPs on $La_{0.4}Sr_{0.4}Ti_{0.9}Ni_{0.1}O_{3-\delta}$ composition for hydrogen evolution reaction (HER) [153]. Li et al. presented an effective titanate system for CO_2 electrolysis with Ni and Mn co-doping [154]. Additionally, Cu has been utilized instead of Ni, i.e., $(La_{0.75}Sr_{0.25})_{0.9}(Cr_{0.5}Mn_{0.5})_{0.9}Cu_{0.1}O_{3-\delta}$ with metallic Cu on the surface characteristically effective for CO_2 electrolysis [155]. Notably, for this work, it has been previously reported that A-site excess can be detrimental to the exsolution process [156].

The termination of the oxide, i.e., the surface, plays a significant role in exsolution. Faceted surfaces create spatial inhomogeneity, resulting in preferential particle growth upon reduction. Nominal surfaces, such as those created by cleaving or polishing a surface, also lead to more uniform exsolution [25].

In addition to non-stoichiometry, the influence of lattice strain, electrical

polarization, and the gaseous environment have been studied [157]. Han et al. showed that lattice strain could result in a high degree of MNPs exsolution [158]. As shown by Myung et al., MNPs can be created within a few seconds at 900 °C by applying a voltage; hence a potential can be used for exsolution [159].

2.2.4 Double Perovskite Exsolution

The double perovskites $A_2B_2O_6$ exhibit desirable catalytical properties due to fast surface oxygen exchange kinetics, fast oxygen ion flow, and good electrical conductivity [160]. Sengodan et al. published a study on $PrBaMn_2O_{5+\delta}$ double perovskite prepared by a two-step procedure and utilized as an anode for solid oxide fuel cells (SOFCs) [113]. Moreover, Kwon et al. examined the influence of different transition metals on exsolution on $PrBaMn_{1.7}T_{0.3}O_{5+\delta}$ (T = Mn, Co, Ni, and Fe), where, i.e., Co, Ni, and Mn exsolution occurred, but no Fe exsolution did [161]. It was explained by considering the co-segregation energies of the corresponding metals and oxygen vacancies [161].

2.2.5 Current Development

In 2002, one of the earlier works on exsolution, studying the $LaFe_{0.57}Co_{0.38}Pd_{0.05}O_3$ (LFCP) for treating automotive exhaust gas, was published [139]. Early exsolution was used in the treatment of automotive exhaust gas. In both SOFCs and solid oxide electrolysis cells (SOECs), exsolution electrodes created by the reduction in gas atmospheres have been utilized [159, 162]. The Irvine group presented electrochemically driven exsolution with a similar mechanism as the thermochemically driven exsolution but on a smaller time scale [159]. Moreover, the question of where exsolution occurs was answered both by in situ experiments and calculations. MNPs nucleate inside and migrate to the surface due to asymmetric strain. The MNPs exhibit a strong interaction with

the substrate, attributed to the instantaneous construction of a socket inside the host oxide and nucleation of the unconfined particle [133, 143].

While, initially, the exsolution technique was not used outside academic works, Barnett et al. showed electrodes prepared by exsolution from strontium titanate have similar current densities to NiO/YSZ and consequently are industrially relevant [156, 163]. SOFCs' fuel elasticity and the capacity to work with non-precious metal catalysts are essential advantages, e.g., while coking can hinder the system's durability, making them industrially unsuitable, exsolved catalysts showed coking resistance because of the socketed nature, which mechanically blocks the tip-growth mechanisms [164]. Additionally, recently exsolution was used for H_2O and CO_2 electrolysis and the co-production of vital products like CH_4, CO, and H_2 [165]. Also, the exsolution of Ru in $La_{0.43}Ca_{0.37}Rh_{0.06}Ti_{0.94}O_3$ composition shows activity for co-electrolysis and co-generation [166]. Finally, it should be mentioned that Gao et al. reported A-site exsolution of Au nanoparticles [167] from $Sr_{0.995}Au_{0.005}TiO_{3-\delta}$ [167]. Moreover, Syed et al. described the bulk and surface exsolution of different Fe-rich and Fe-depleted ellipsoidal nanostructures from $La_{0.6}Sr_{0.4}FeO_3$ thin films [168]. In their work they describe four configurations of particles: surface core-shell, bulk core-shell, adjacent, and independent particles, where the core-shell structures have a metallic Fe core and a $La_xFe_yO_{3-\delta}$ shell. Adjacent particles describe situations where the Fe particle is next to a Fe-depleted $La_xFe_yO_{3-\delta}$ particle, and independent Fe particles have a very thin ($\sim$ 1 - 2 nm) $La_xFe_yO_{3-\delta}$ shell, but no larger particles nearby [168].

2.3 Galvanic Replacement Reaction

Galvanic replacement reaction (GRR), otherwise also known as immersion plating [169], can be used to create a plethora of structures, where ultrathin films and

nanoparticles are only two to mention [170]. Consequently, it is not surprising that the technique has been studied extensively over the past decades. Here, a short overview of the technique is given by first introducing a historical context, followed by the description of two distinct behaviors, the influence of the substrate, before ending the section with thermodynamic and kinetic considerations.

2.3.1 GRR in historical context

Printed circuit board technology and the metal finishing industry utilized GRR extensively, mainly using the name immersion plating [170, 171]. Studies involved not only tin/lead immersion coatings on Cu [172] but metals such as Au immersion coatings on Cu combined with Ni electroless plating [173] and Ag immersion coatings with potassium cyanide [174]. Moreover, hydrometallurgy, the retrieving of metals from a solution, has been performed and observed [175, 176].

Surface limited redox replacement (SLRR) describes a process where ultrathin epitaxial metal layers can be formed by GRR [177, 178]. The reaction involves a first step, where a monolayer of metal, hydrogen, sulfur, or iodine atoms is formed by reductive or oxidative deposition at more positive or negative potentials, respectively, than required for bulk depositions, known as underpotential deposition (upd) [179]. Subsequently, these upd layers are galvanically replaced by a more noble metal [170]. Semiconductor compounds were among the first applications for this process due to the electrochemical atomic layer epitaxy (ECALE) technique developed by Stickney and co-workers [180–183].

MNPs have been created by GRR, too. Generally, bimetallic MNPs with favorable optical, magnetic, and/or catalytic properties are formed [184]. Again, noble metals like Au, Pt, or Pd are replacing less noble metals, e.g., Cu or Ag, in these efforts [185–187]. The bimetallic MNPs have also been used in fuel cells

and/or other energy applications [185, 188–190]. Additionally, carbon-supported MNP catalysts have been created utilizing GRR [191–194].

2.3.2 Underpotential Deposition Growth and Electrochemical Etching

Works within the field of GRR fall mainly into two categories: a complete replacement of Cu, Pb, or H upd monolayer by more noble metals or a partial replacement of a metal M by layers of the more noble metal M_{noble} catalyst [170]. These two approaches are represented in figure 2.13, (A) and (B), respectively. In both cases, the noble metal in the solution is assumed to have the same valency as the metal it replaces, leading to a one-for-one substitution [170].

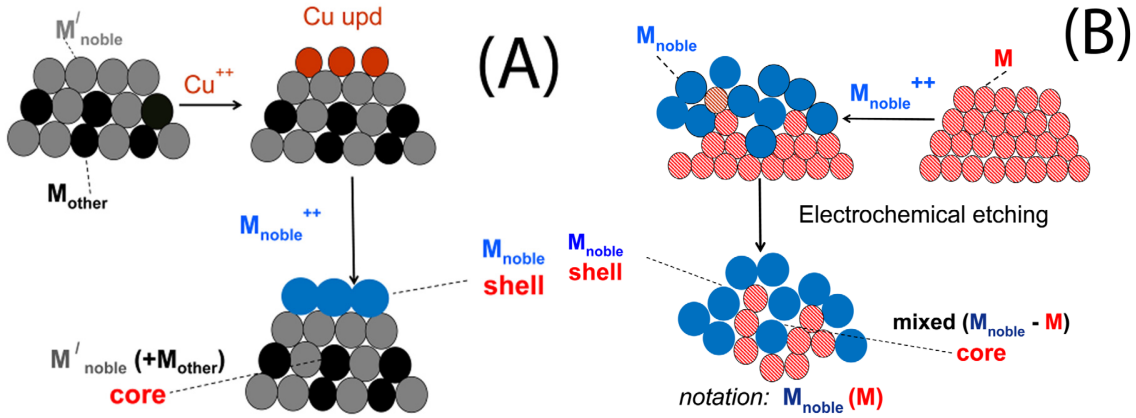

Figure 2.13: Two different mechanisms for GRR are shown. (A) shows the deposition of a Cu upd monolayer on top of a structure consisting of two different metals (M'_{noble} and M_{other}). The GRR replaces the Cu upd layer with a third metal(M^{++}_{noble}), resulting in a core-shell structure, where the latter forms the shell. (B) shows the GRR of a metal (M) by a more noble metal, M_{noble}. Effectively, this electrochemical etching process results in a plethora of different structures ranging from complete replacement to alloyed structures depending on the reaction conditions. The figure was taken from [170], under the Creative Commons Attribution License.

The first method has two slightly different growth mechanisms. Both start with a sacrificial upd layer; however, the replacement of this layer can occur

slightly differently. The first growth mechanism reflects the ideal case and leads to monolayer or sub-monolayer thick deposits of noble metals [178]. It is called the direct exchange growth mechanism and involves the direct one-for-one substitution of upd-layer atoms by the more noble metal atoms in the solution, reflecting the ideal case [178]. The second kind of growth mechanism in the upd-based method is the local cell growth mechanism. In contrast to the first, noble metals can deposit on each other while upd atoms dissolve from nearby locations. This results in thicker and incomplete layers [178]. Nonetheless, both upd-based growth mechanisms produce thin films of noble metals [178].

The second growth mechanism not only results in a top layer of noble metals but in an intimate mixture of noble and less noble metals below the surface. In fact, replacing atoms frequently occurs, allowing the formation of different morphologies, ranging from fully replaced structures to core-shell and alloy-type structures. The difference between the upd-based method and this method is that the GRR can replace not just the top layer but, theoretically, the entirety of the reactive metal substrate [170].

2.3.3 Support Type

(Photo)electrocatalysts are generally supported by a substrate, independent of whether said substrate exists in the form of another NP or a solid block [170]. However, whether the substrate is present during the GRR or not can influence the reaction. Most basic research studies utilize well-characterized smooth electrode substrates combined with upd monolayers. Figure 2.14 shows the substrate, i.e., glassy carbon (GC), with an upd-layer of metal M on top in orange, and a layer of Pt in gray, replacing parts of the metal M [170, 195, 196]. As is visible, a thin Pt layer is created in the situation on top while the bottom situation shows more replacement of the Pt inside the bulk. A difference

in standard potential between the two metals used for the upd-layers can explain the different behavior of the GRR. This will be further discussed in section 2.3.4, but generally, a more significant difference in standard potential between the metal M and the noble metal, i.e., Pt, leads to a quicker replacement and a thinner, more continuous film [195, 196].

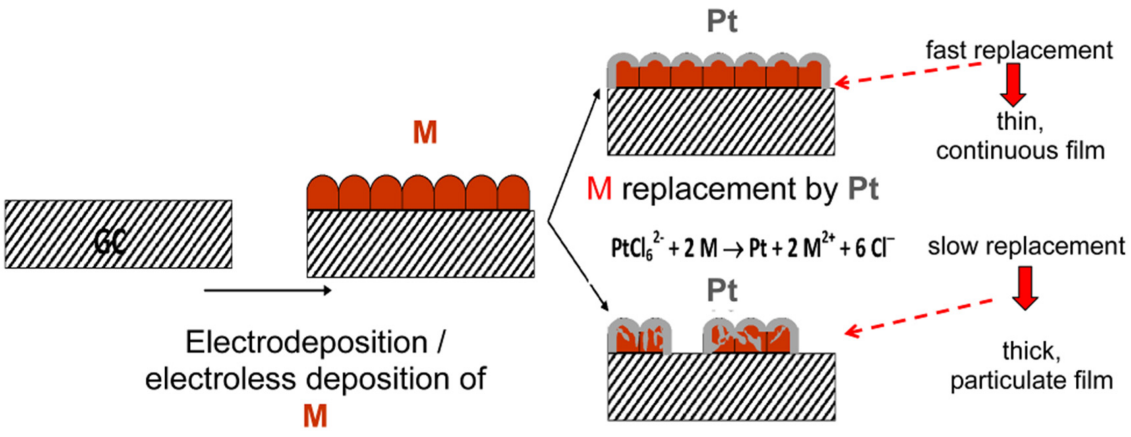

Figure 2.14: The substrate, in this case, glassy carbon (GC) covered by a layer of M. The top part depicts a substrate with a continuous M layer, where a more noble metal, i.e., Pt, replaces the top of the M-layer quickly, forming a thin Pt-film. Below a particulate layer was formed, where deposition occurred slowly, and the noble metal, i.e., Pt, penetrated the bulk. The figure was taken from [170], under the Creative Commons Attribution License.

In addition to the influence of the upd layer, the substrate on which the upd layer is deposited on can influence the deposition. Again, Pt deposition with a sacrificial metal M can be used as an example, where M is deposited as islands on carbon. While Pt partially replaces the M, as is expected, the nature of the carbon substrate, being an electronic conductor, leads to the deposition of Pt directly on carbon [197–200]. This is possible because the dissolution of nearby M releases electrons that can travel to the Pt deposition location and reduce Pt to allow metallic Pt deposits. It can be expected that this deposition seizes if the support of M is an insulator or semiconductor or if no support is present during the GRR [201–204].

2.3.4 Thermodynamic and Kinetic Considerations

Experimentally, immersing a metal (M) into a solution of a more noble metal (M_{noble}) can lead to a spontaneous reaction given in equation (2.24). Naturally, certain conditions need to be met, such as the ionic form of M needs to be stable in solution under the experimental conditions (i.e., temperature, pH, complexing agents, etc.). The GRR is driven by the difference in standard electrochemical potentials between M (E^0) and M_{noble} (E^0_{noble}), $E^0_{noble} - E^0 > 0$ [170]. The reaction can be split into two half-reactions, each focusing on one of the metals, as shown in equation (2.25) and equation (2.26) for M_{noble} and M, respectively [205].

$$M^{n+}_{noble}(aq) + \frac{n}{m}M(s) \longrightarrow M_{noble}(s) + \frac{n}{m}M^{m+}(aq) \tag{2.24}$$

$$M^{n+}_{noble}(aq) + ne^- \longleftrightarrow M_{noble}(s)\ (E^0_{noble}) \tag{2.25}$$

$$M^{m+}(aq) + me^- \longleftrightarrow M(s)\ (E^0) \tag{2.26}$$

Examples of standard electrochemical potentials of half reactions can be found in table 2.2. It is important to note that the larger the difference between the two potentials (E^0_{noble} and E^0), the more favorable the reaction is [170, 205]. Moreover, for each reaction, the actual species should be considered carefully, as the experimental conditions may allow a metal only to be present in oxide or hydroxide form [170].

Metals present as oxides, i.e., M_2O_m, or hydroxides, e.g., $M(OH))_m$, result in a decoupling of the noble metal deposition and dissolution of the metal. Instead, the deposition of the noble metal goes hand in hand with further growth of the oxides or hydroxides [170]. This results in a new reaction, given in equation (2.27).

Table 2.2: The standard electrochemical potential of selected elements relevant to this work. Data were obtained from [206] (original data from [207–209]).

Reaction	E° [V]
$Ag^{2+} + e^- \rightleftharpoons Ag^+$	1.980
$Au^{2+} + e^- \rightleftharpoons Au^+$	1.8
$Au^+ + e^- \rightleftharpoons Au$	1.692
$NiO_2 + 4\,H^+ + 2\,e^- \rightleftharpoons Ni^{2+} + 2\,H_2O$	1.678
$Au^{3+} + 3\,e^- \rightleftharpoons Au$	1.498
$Au^{3+} + 2\,e^- \rightleftharpoons Au^+$	1.401
$RuO_4 + 6\,H^+ + 4\,e^- \rightleftharpoons Ru(OH)_2^{2+} + 2\,H_2O$	1.40
$Pt^{2+} + 2\,e^- \rightleftharpoons Pt$	1.18
$RuO_2 + 4\,H^+ + 2\,e^- \rightleftharpoons Ru^{2+} + 2\,H_2O$	1.120
$RuO_4 + 8\,H^+ + 8\,e^- \rightleftharpoons Ru + 4\,H_2O$	1.038
$AuCl_4^- + 3\,e^- \rightleftharpoons Au + 4\,Cl^-$	1.002
$RuO_4 + e^- \rightleftharpoons RuO_4^-$	1.00
$Ag^+ + e^- \rightleftharpoons Ag$	0.7996
$[PtCl_4]^{2-} + 2\,e^- \rightleftharpoons Pt + 4\,Cl^-$	0.755
$[PtCl_6]^{2-} + 2\,e^- \rightleftharpoons [PtCl_4]^{2-} + 2\,Cl^-$	0.68
$Ag(ac) + e^- \rightleftharpoons Ag + (ac)^-$	0.643
$RuO_4^- + e^- \rightleftharpoons RuO_4^{2+}$	0.59
$Cu^+ + e^- \rightleftharpoons Cu$	0.521
$Ru^{2+} + 2\,e^- \rightleftharpoons Ru$	0.455
$Cu^{2+} + 2\,e^- \rightleftharpoons Cu$	0.3419
$Ru^{3+} + e^- \rightleftharpoons Ru^{2+}$	0.2487
$Cu^{2+} + e^- \rightleftharpoons Cu^+$	0.153
$2\,H^+ + 2\,e^- \rightleftharpoons H_2$	0.000
$2\,Cu(OH)_2 + 2\,e^- \rightleftharpoons Cu_2O + 2\,OH^- + H_2O$	-0.080
$Cu(OH)_2 + 2\,e^- \rightleftharpoons Cu + 2\,OH^-$	-0.222
$Ni^{2+} + 2\,e^- \rightleftharpoons Ni$	-0.257
$Cu_2O + H_2O + 2\,e^- \rightleftharpoons Cu + 2\,OH^-$	-0.360
$NiO_2 + 2\,H_2O + 2\,e^- \rightleftharpoons Ni(OH)_2 + 2\,OH^-$	-0.490
$Ni(OH)_2 + 2\,e^- \rightleftharpoons Ni + 2\,OH^-$	-0.72

$$M^{n+}_{noble} + \frac{n}{m}M + n2\,H_2O \longrightarrow M_{noble} + 2\frac{n}{2m}M_2O_m + nH^+ \tag{2.27}$$

Finally, the discussion above illustrates that there are a few essential factors to be considered in GRR. First, the phase of the metal M has to be considered [170]. Usually, consulting a Pourbaix diagram can help determine the phase. An example of a Pourbaix diagram for nickel can be seen in figure 2.15. With

the phase of the metal M determined, the second factor is the consideration of the standard potentials. The standard potentials must be corrected to their equilibrium values, meaning their exact metal ion concentration should be considered [170]. Finally, metal complexation due to ligands present in the solution has to be considered [170].

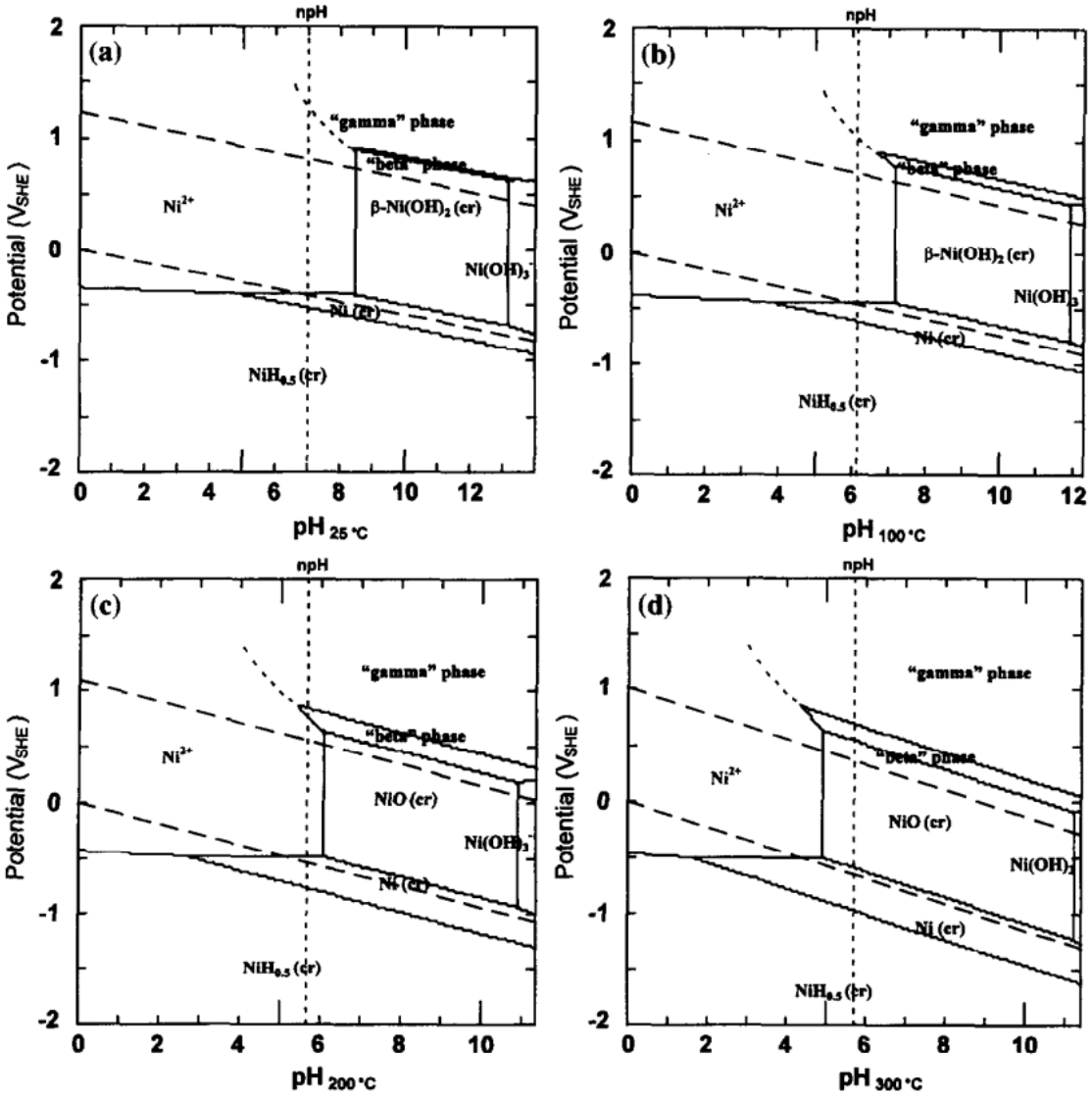

Figure 2.15: The Pourbaix diagram of Ni for 25 °C, 100 °C, 200 °C, and 300 °C. The neutral pH is indicated by a dashed line and labeled npH. The figure was taken from [210], with permission.

While thermodynamics determines whether the reaction happens, the above

considerations need to be extended by kinetic consideration to determine the speed of the reaction. There are only a handful of publications considering the speed of GRR [211–215]; however, Papaderakis et al. proposed a description analogous to corrosion kinetics [170]. They argue that GRR can essentially be viewed as corrosion, and a galvanic current density, j_{galv} can be defined in analogy to the corrosion current density, j_{corr}. The resulting expression is given in equation (2.28), where the exchange current densities for the noble metal (equation (2.25)) and metal (equation (2.26)) are given by $j_{0,\mathrm{M_{noble}}}$, and $j_{0,\mathrm{M}}$, respectively, the β_1 and β_2 are the Tafel slopes of the same reactions, and $E_e^{\mathrm{M_{noble}}} E_e^{\mathrm{M_{noble}}}$ and E_e^{M} are the equilibrium potentials. Finally, $\beta_{\mathrm{M_{noble}}}$ and β_{M} are defined by equation (2.29) and equation (2.30) [170]. Equation (2.28) suggests that in addition to the thermodynamics also, the kinetics depend on the difference in potential of the two species.

$$j_{\mathrm{galv}} = (j_{0,\mathrm{M_{noble}}})^{\beta_1} (j_{0,\mathrm{M}})^{\beta_2} \exp\left[\frac{2.3\left(E_e^{\mathrm{M_{noble}}} - E_e^{\mathrm{M}}\right)}{\beta_{\mathrm{M_{noble}}} + \beta_{\mathrm{M}}}\right] \tag{2.28}$$

$$\beta_1 = \frac{\beta_{\mathrm{M_{noble}}}}{\beta_{\mathrm{M_{noble}}} + \beta_{\mathrm{M}}} \tag{2.29}$$

$$\beta_2 = \frac{\beta_{\mathrm{M}}}{\beta_{\mathrm{M_{noble}}} + \beta_{\mathrm{M}}} \tag{2.30}$$

2.4 Photocatalysis

The enormous interest in photocatalysts originates in humanity's need for more energy and the realization that renewable energy sources must be utilized for sustainable energy production. The current renewable energy mix consists mainly of solar, wind, and hydro energy, mainly producing electricity [216]. The challenge these technologies face is energy storage, where the storage of electricity on a large scale is inefficient. Photocatalysts offer a unique solution to the problem by converting the energy of incoming photons emitted by the sun into chemical energy, for example, in the form of H_2 [217]. Like in section 2.1

and section 2.2, STO will again serve as an example material, in this case, as a photocatalyst.

Producing H_2 can be achieved using different methods, including electrolysis [218], thermolysis [219], photolysis [220], and biolysis [221]. Below, the generation of H_2 by photocatalysis will serve as an example of a photocatalytic reaction. To generate H_2 from water, i.e., drive the decomposition of water, also called water splitting, requires high energy input [222]. The energy released by water formation (equation (2.31) [222]) indicates the minimum required energy to split water.

$$O_2(g) + H_2(g) \longrightarrow H_2O(l) \qquad (\Delta G^\circ = -237.14\,\mathrm{kJ\,mol^{-1}}) \tag{2.31}$$

Hence, $237.14\,\mathrm{kJ\,mol^{-1}}$ are required to split two H_2O molecules, resulting in a roughly $1.23\,\mathrm{eV}$ per H_2O molecule. Naturally, these numbers do not take any losses into account. Utilizing UV light to split water by photoelectrochemical means was first reported by Fujishima and Honda in 1972 [223]. The most promising method of solar water splitting involves semiconductors, such as STO, and redox reactions, where the semiconductor absorbs light (equation (2.32)) and generates electrons and holes needed in the reactions (equation (2.33) and equation (2.34)).

$$\mathrm{Semiconductor} + h\nu \longrightarrow \mathrm{Semiconductor}(h^+ + e^-) \tag{2.32}$$

$$\text{Reduction:} \qquad 4\,H^+ + 4\,e^- \longrightarrow 2\,H_2(g)(\text{in acidic environment}) \tag{2.33}$$

$$\text{Oxidation:} \qquad H_2O(l) + 4\,h^+ \longrightarrow O_2(g) + 4\,H^+(\text{in acidic environment}) \tag{2.34}$$

The target efficiency of water splitting is 10% solart to hydrogen conversion efficiency under visible light and can be reached by devices (i.e., [224]), but despite the 50 years since the publication of Fujishima and Honda, the stability while performing with such high efficiency is relatively poor [222, 224]. In addition to

the target efficiency, essential requirements for a semiconductor considered for photoelectrochemical measurements have been established. These three main criteria are (i) the stability towards photocorrosion in an aqueous medium, (ii) the light sensitivity, and finally, (iii) a more electronegative conduction band (CB) related to the level of H_2 reduction and a more positive valence band related to H_2O/O_2 as well as good reaction kinetics.

Hydrogen generated by low-emission processes accounted for less than 1% of the total hydrogen production in the last three years [225]. The vast majority (more than 99%) is hydrogen production based on fossil fuels, where steam reforming of natural gas contributed with 70% and coal gasification with 30% [225]. In 2021 specifically, the vast majority of the low-emission production originates from fossil fuels with carbon capture, utilization and storage, and some from water electrolyzers (35 kt H_2 out of 1 Mt) [226]. In total, electricity and biomass technologies barely met 0.2% of the total energy demand for hydrogen production in 2021 [225]. Hence, we must increase the share of low-emission methods and a very suitable one is photocatalysis because, in principle, the only energy input is in the shape of photons.

Two principal methods can be used to generate hydrogen through photocatalysis: (i) photocatalytic water splitting [227] and (ii) photocatalytic reforming of organics [228]. The latter is again beyond the scope of this thesis. Within the former, two different approaches are established: (i.a) photoelectrolysis in PEC cells like Fujishima and Honda in 1972 [223], or (i.b) photolysis using a colloid suspension of powdered catalysts, e.g., TiO_2 [229, 230] and other ceramic powders [231]. PEC cells have the advantage of spatially isolated e^- and h^+ leading to better efficiencies by significantly reducing recombination [222]. O_2 and H_2 are also produced in different locations, reducing back reactions [232]. Alternatively, powdered photocatalysts in electrolyte can be used [233, 234].

Photoelectrochemical water splitting is a three-step process where (i) the photoabsorption occurs, leading to the generation of excited e^- and h^+ with sufficient energy to drive the reaction. (ii) The charge carriers have to be separated and migrate to the reaction sites on the surface, and, finally, (iii) reaction centers appear for both reactions [235, 236]. It should be noted that the suppression of recombination can be viewed as its own step, and the photon absorption and generation of excited e^- and h^+ can be described as two steps.

2.4.1 Band Gap Considerations

The band gap determines the energy available for the reaction and the minimum energy required by the photon to excite the electron-hole pair. Moreover, the location of the valence band edge and conduction band edge relative to the potentials of the reactions occurring must be considered [236], as stated above. In figure 2.16, the placement of multiple semiconductors can be seen relative to the redox potential of the water-splitting reaction.

Additionally, the nature of the band gap, whether the material has a direct or indirect band gap, influences the absorption of photons by the material [237]. This is exemplified when considering equation (2.35), where α is the absorption, h is Planck's constant, ν is the frequency, E_{Gap} is the band gap energy, and p is an index depending on the electronic transition responsible for the reflection [237, 238]. The value of p can be $\frac{1}{2}$ for dipole-allowed transitions occurring at a direct band gap, 2 for dipole-allowed transitions near an indirect band gap, $\frac{3}{2}$ for dipole-forbidden transitions near a direct band gap, and 3 for dipole-forbidden transitions near indirect band gaps. The latter two have suppressed dipolar transitions [237].

$$\alpha = \frac{A(h\nu - E_{\mathrm{Gap}})^p}{h\nu} \tag{2.35}$$

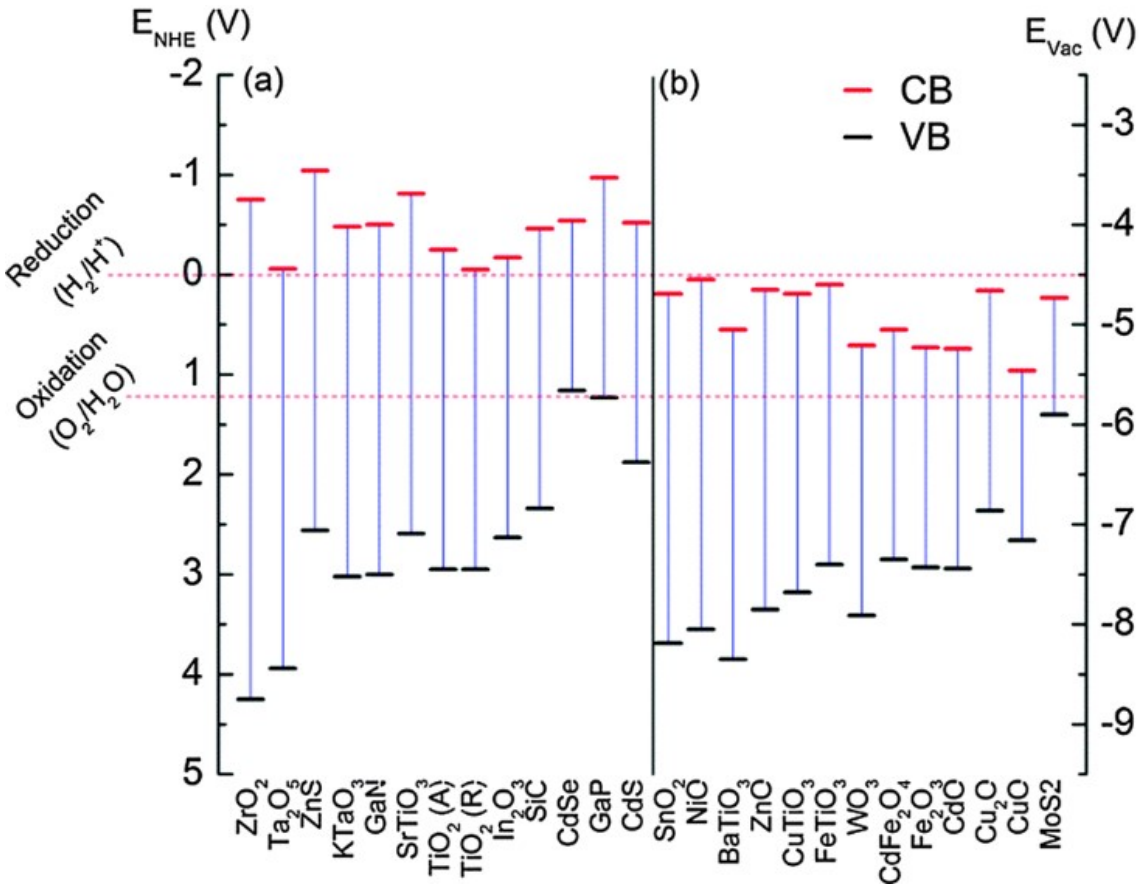

Figure 2.16: The placement of the conduction band edges (CB) and the valence band edges (VB) of multiple semiconductors relative to the reduction potential of H_2/H^+ and the oxidation potential of O_2/H_2O with respect to the normal hydrogen electrode (NHE) and the vacuum (vac). In (a), all band gaps enclose both reduction and oxidation, whereas in (b), the conduction band is too low. The figure was taken [239], with permission.

There is an apparent difference between direct and indirect band gaps; the former has conduction band edge and valence band edge at the same k-vector and the latter at different k-vectors [79]. Incoming photons carry almost no momentum; hence, the semiconductor has to provide the required momentum to allow an indirect band gap transition. Phonons provide the required momentum. Increasing the thickness of the indirect band gap semiconductor ensures that phonons and photons can interact and create an electron-hole pair [79, 240].

2.4.2 Thermodynamic Considerations

A photocatalyst in its ground state, i.e., non-illuminated, remains in a quasi-equilibrium state, where the electrons and holes have a chemical potential given by equation (2.36) and equation (2.37), respectively [241, 242]. Here, the chemical potentials are given by μ_n and μ_p, E_c and E_v are the conduction band bottom and the valence band top, respectively, k_B is the Boltzmann constant, T is the temperature, n and p are the concentrations of electrons and holes, and N_c and N_v are the effective densities of states at the conduction band bottom and valence band top, respectively [242]. Equation (2.38) describes the thermal-induced electrons and holes in non-degenerated semiconductors. They follow a Boltzmann distribution, and their product is constant [242].

$$\mu_n = E_c + k_\mathrm{B}T \ln\left(\frac{n}{N_c}\right) \tag{2.36}$$

$$\mu_p = E_v - k_\mathrm{B}T \ln\left(\frac{p}{N_v}\right) \tag{2.37}$$

$$n_0 p_0 = N_c N_v \exp\left(\frac{-E_\mathrm{Gap}}{k_\mathrm{B}T}\right) \tag{2.38}$$

$$\Delta G = G_\text{light-off} - G_\text{light-on} = -\Big|\mu_n - \mu_p\Big| = -E_\mathrm{gap} - k_\mathrm{B}T \ln\left(\frac{np}{N_c N_v}\right) \tag{2.39}$$

Thermodynamically speaking, the ΔG is defined by equation (2.39), where $G_\text{light-on}$ is the Gibbs energy of the semiconductor under illumination, and $G_\text{light-off}$ is the Gibbs free energy of the same semiconductor in the dark [241–243]. The difference in Gibbs free energy ΔG, can be seen in figure 2.17. Furthermore, an initial surge is shown in the Gibbs free energy, eventually settling on the $G_\text{light-on}$ level [241]. In a heterogeneous photocatalytic water splitting cycle that is perturbed, i.e., any imperfection of the photocatalyst, recombinations of electron-hole pairs occur, which are undesirable [242]. The recombination reaction can be described by equation (2.40) and the recombination rate by equation (2.41). The equation for the recombination rate also introduces the

recombination constant, $k_{\text{recombination}}$, which follows the Arrhenius equation shown in equation (2.42) [242, 243]. In equation (2.42), A is the pre-exponential factor, and E_{A} is the activation energy of interfacial electron transfer, as shown in figure 2.17 [241].

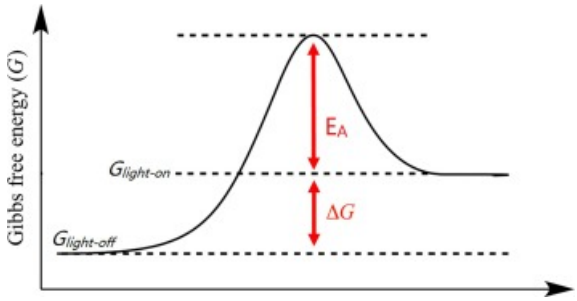

Figure 2.17: The Gibbs free energy of a photocatalyst, where $G_{\text{light-on}}$, $G_{\text{light-off}}$, and ΔG are shown. Additionally, the activation energy of the interfacial electron transfer is shown. The figure was taken from [241], with permission.

$$\text{e}^-_{\text{CB}} + \text{h}^+_{\text{VB}} \longrightarrow \text{energy loss} \tag{2.40}$$

$$r_{\text{recombination}} = k_{\text{recombination}}[\text{e}^-_{\text{CB}}][\text{h}^+_{\text{VB}}] \tag{2.41}$$

$$k_{\text{recombination}} = A \exp\Big(-\frac{E_{\text{A}}}{k_{\text{B}}T}\Big) \tag{2.42}$$

It is evident from equation (2.39) that the difference in electrochemical potential $|\mu_n - \mu_p|$ and with it, the difference in densities of electrons and holes are proportional to the driving force of the reaction. When the photocatalyst absorbs a photon, energy equal to the band gap energy (E_{Gap})is available; however, as previously elaborated, not all of it can be utilized due to inevitable losses. The entropy loss from the charges transferring is an intrinsic loss from both the conduction band electron and valence band hole and can be expressed by a total energy loss according to equation (2.43) [241, 243]. Consequently, the maximal available energy to drive the reaction is the difference between the band gap energy and the total energy loss, given by equation (2.44). This difference is also the negative of equation (2.39) [241–243].

$$T\Delta S_{\mathrm{mix}} = k_{\mathrm{B}}T\Big(\ln\frac{N_C}{n} + \ln\frac{N_V}{p}\Big) = k_{\mathrm{B}}T\ln\frac{N_cN_V}{np} \tag{2.43}$$

$$E_{\mathrm{Gap}} - T\Delta S_{\mathrm{mix}} = E_{\mathrm{Gap}} - k_{\mathrm{B}}T\ln\frac{N_cN_v}{np} = -\Delta G \tag{2.44}$$

The opposing sign of ΔG for photoexcitation (equation (2.39)) and photoredox reaction (equation (2.44)) indicate that the former is a non-spontaneous reaction and the latter is spontaneous at an excited state [241]. Consequently, photons with energy at least as large as the band gap, i.e., $h\nu \leq E_{\mathrm{Gap}}$, can excite the electron-hole pair. If the difference between losses and the band gap energy (equation (2.44)) is larger than the minimum energy required to catalyze the reaction, e.g., 1.23 eV for water splitting, the reaction will be spontaneously driven by the excited photocatalyst [241].

2.4.3 Semiconductor-Electrolyte Interface

An essential part of any photocatalyst is its interface with the electrolyte. An initial electric current flows across the junction between the electrolyte and the semiconductor upon their initial contact. The electric current seizes to flow when the Fermi energy of the electrons in the solid, E_{F}, and the redox potential of the electrolyte, E_{redox}, are equal, i.e., the system is in equilibrium [244]. However, due to the flow of electric current, a region on each side of the junction exhibits a charge distribution different from the bulk charge distribution, known as the space-charge layer [244].

$$\frac{1}{C_{\mathrm{SC}}^2} = 2\frac{\Delta\phi_{\mathrm{SC}}RT}{F}\frac{1}{\varepsilon_0\varepsilon^1 N} \tag{2.45}$$

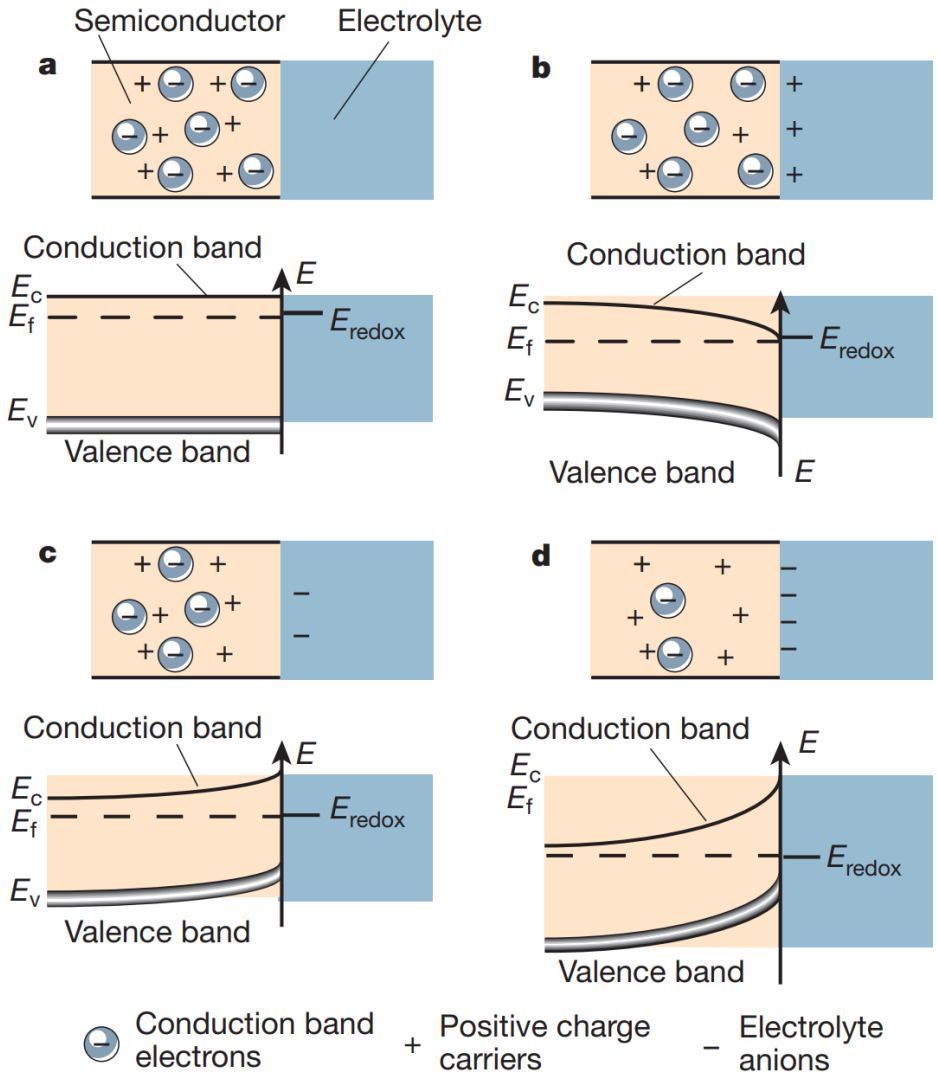

Figure 2.18: The figure shows different situations with the same n-type semiconductor, i.e., with mobile electrons, and electrolytes in contact, with different equilibration scenarios, where the upper figure shows the charge distribution and the lower the band bending. (a) The flat band potential, no charge accumulation is visible, and no band bending occurs. (b) The accumulation layer shows excess electrons on the semiconductor side and a positive charge on the electrolyte side. The bands show a downward bending towards the interface on the semiconductor side. (c) The depletion layer exhibits a lack of electrons on the semiconductor side. The bands are bent upwards towards the interface. (d) The inversion layer describes the situation where electrons have depleted below the intrinsic level, further increasing the upward band bending, leaving the semiconductor p-type at the surface. The figure was taken from [244] with permission.

The two sides of the space-charge layer, e.g., the electrolyte and the

semiconductor side, differ in their build-up. The electrolyte side consists of a double layer, where a compact (Helmholtz) layer is followed by a diffuse (Gouy-Chapman) layer [244]. While the nature of the semiconductor, i.e., p- or n-type, determines the mobile charge carrier, the Fermi level determines the band bending. Focusing on n-type semiconductors with mobile electrons, such as STO, a Fermi level of the electrode equal to the flat-band potential, no excess charge accumulates, and the bands are flat (see figure 2.18 (a)). In figure 2.18 (b), electrons accumulate on the semiconductor, and the bands bend down, whereas in (c), the space-charge layer is depleted of electrons, and the band bends upwards. Taking it to the extreme, an inversion layer can be formed, where the surface of the semiconductor is p-type while the bulk remains n-type [244]. Analogous arguments can be made for p-type photoconductors.

The energetic positions of the valence and conduction band edge can be determined by the flat band potential [244]. The capacitance of the semiconductor-electrolyte junction has to be considered to determine them. The differential capacity is established as a function of the applied voltage when a reverse bias is applied to the semiconductor. The capacity of the space-charge of the semiconductor (C_{SC}) is in series with the Helmholtz capacity layer (C_H) [244]. The space-charge capacitance can be measured using the depletion regime, where $C_H > C_{\mathrm{SC}}$. Utilizing the Mott-Schottky equation allows the determination of the space-charge capacity as a function of applied bias by equation (2.45). The Mott-Schottky is describes the ideal situation, where an ideal semiconductor with no surface states and no Fermi level pinning is considered.Here the voltage drop in the space-charge layers is given by $\Delta\phi_{\mathrm{SC}} = V - V_{\mathrm{fb}}$, R is the gas constant, F is Faraday's number, ε represents the dielectric constant of the semiconductor, ϵ_0 is the permittivity of vacuum, and ${}^1N$ represents the ionized donor dopant concentration.

2.5 Plasmonics

Photocatalysts, as introduced in section 2.4, are considered for various applications, for example, solar-to-fuel conversion, environmental remediation, organic compound formation, and synthesis of multiple compounds [245]. However, a single photocatalyst can encounter severe limitations due to, e.g., insufficient light absorption, inefficient charge separation, high charge recombination rates, and high costs, effectively preventing it from reaching commercial benchmarks [245, 246]. An alternative is to form heterostructures of two different materials, where one acts as (photo)catalyst, and the other as photosensitizer and/or light antenna. Specifically, a stable photocatalyst, such as STO, whose band gap is far wider than the ideal band gap of a photocatalyst but has high thermal stability and is resistant to photocorrosion [247], can be combined with MNPs exhibiting localized surface plasmon resonance (LSPR) to improve the photocatalytic performance [245, 248].

The surface plasmon effect has been implicitly utilized by humanity for millennia [134, 249]; however, Gustav Mie solved Maxwell's equations for spherical MNPs relatively recently in comparison [250]. After several decades of limited research, the phenomenon has steadily grown in popularity among researchers, at least in part because of its potential application in photocatalysis and photovoltaics. Today, plasmonics is widely used in research, and computational methods have been employed to tackle geometrically complex particles and the interaction between a MNP with LSPR and a semiconductor. In addition, Mie's formalism, solving Maxwell's equation for small spherical particles, has been rewritten and is barely recognizable anymore. It remains, however, the only exact solution of Maxwell's equation for any shape of MNPs. As a note, plasmonic MNPs can act as photocatalysts, too. However, with the exception of treating it as a competing mechanism to energy transfer to the semiconductor, it is beyond

the scope of this thesis.

MNPs and their optical properties have been utilized since the Roman times, e.g., the Lycurgus Cup made in the 4^{th} century AD with colloidal Au [134, 251]. The unusual optical properties have been studied over the course of centuries, among others by Michael Faraday [252], forming the basis of modern colloidal science [249]. More recently, the realization that the description of the surface plasmon absorption band structure in metals may contribute to grasping the development of the band structure in metals led to an abundance of scientific reports on the size-dependent optical properties of MNPs [249, 253–262]. It soon became clear that, while progress was made on determining the effects of defects, grain boundaries, crystallinity and polydispersity on the optical response of MNPs, the effect of surface chemical interactions was not clear [263].

2.5.1 Surface Plasmons

Experiments conducted halfway through the 20^{th} century by, among others, Ruthemann, were concerned with the bombardment of thin metallic films by fast electrons [264]. However, only the realizations of Pines and Bohm, connecting the electron density oscillation observed in electric discharges in gases and collective plasma oscillations in metals caused by long-range Coulomb interaction of valence electrons as similar, enabled an explanation of these experiments [265, 266]. The following year, Ritchie predicted the existence of self-sustained collective excitations at metal surfaces when considering characteristic energy losses of fast electrons passing through thin metal films [267]. He attributed the boundary effect to cause the appearance of a lowered loss due to the excitation of surface collective oscillations [267]. Following this, Powell and Swan showed the presence of these collective excitations in a series of electron energy loss experiments [268], and Stern and Ferrell named the quanta of these collective

excitations surface plasmons [269]. Subsequently, a plethora of studies within physics, but also in different fields, has been published. Condensed matter physics and surface physics discussed surface plasmons in a wide variety of circumstances, including the nature of Van der Waals forces [270–272], classical image potential acting between a point classical charge and a metal [273–276], the energy transfer in gas-surface interactions [277], surface energies [278–282], damping of surface vibrational modes [283, 284], the energy loss of charged particles moving outside a metal surface [285, 286], and de-excitation of adsorbed molecules [287]. Meanwhile, surface plasmons have also been topics in fields like electrochemistry [288], wetting and biosensing [289–292], scanning tunneling microscope [293], the ejection of ions from surfaces [294], nanoparticle growth [295, 296], surface plasmon microscopy [297, 298], and surface-plasmon resonance technology [299–305].

Bohm and Pines determined the quantum energy of collective plasma oscillation of a free electron gas with equilibrium density n to be $\hbar\omega_{\mathrm{p}} = \hbar\big(\frac{4\pi ne^2}{m_{\mathrm{e}}}\big)^2$, where ω_{p} symbolizes the plasmon frequency, e and m_{e} are the electron charge and mass, respectively. If a planar boundary is near, a new mode, the surface plasmon mode, appears, with a frequency equal to Ritchie's frequency (in the non-retarded region, i.e., the speed of light is large) $\omega_{\mathrm{s}} = \frac{\omega_{\mathrm{p}}}{\sqrt{2}}$ for a wave vector $\mathbf{q}$ in the range $\frac{\omega_{\mathrm{s}}}{c} \ll q \ll q_{\mathrm{F}}$, where q_{F} is the magnitude of the Fermi wave vector. With increasing wave vector, the frequency experiences some dispersion [306]. However, in the retarded region, i.e., where the phase velocity $\frac{\omega_{\mathrm{s}}}{q}$ is comparable to the speed of light, the surface plasmons couple with the free electromagnetic field.

Surface Resonance

Numerous approaches can be taken to derive meaningful equations describing plasmonic behavior. Pitarke et al. published an extensive paper discussing

the surface plasmon polaritons and localized surface plasmons in a theoretical environment, while providing experimental context showing the importance of these results [306]. Here, an abbreviated collection of the most important points mainly taken from Pitark et al. [306] will be presented.

Surface Plasmon Polaritons: Maxwell's equations for a material with dielectric function ε_i are given by equations (2.46) to (2.49), if no external field is present. Two semi-infinite media, forming an interface at $z = 0$, with dielectric functions ε_1 and ε_2, respectively, can have two sets of general solutions of equations (2.46) to (2.49), one containing s-polarized modes, and one containing p-polarized electromagnetic modes [306, 307]. The first mode restricts the electric field $\mathbf{E}$ to be parallel to the interface. The second one, on the other hand, contains the modes where the magnetic field is parallel to the interface. Utilizing an ideal surface and considering waves that propagate along the surface, s-polarized surface oscillations cannot exist, and the solution for the traveling wave must be a p-polarized electromagnetic mode. Without limitation, the x-axis can be chosen as propagation direction, and the $\mathbf{E}$ and $\mathbf{H}$ fields are then defined by equation (2.50) and equation (2.51).

$$\nabla \times \mathbf{H}_\mathrm{i} = \varepsilon_\mathrm{i} \frac{1}{c} \frac{\partial}{\partial t} \mathbf{E}_\mathrm{i} \qquad (2.46)$$

$$\nabla \cdot (\varepsilon_\mathrm{i} \mathbf{E}_\mathrm{i}) = 0 \qquad (2.47)$$

$$\nabla \times \mathbf{E}_\mathrm{i} = -\frac{1}{c} \frac{\partial}{\partial t} \mathbf{H}_\mathrm{i} \qquad (2.48)$$

$$\nabla \cdot \mathbf{H}_\mathrm{i} = 0 \qquad (2.49)$$

$$\mathbf{E}_\mathrm{i} = (E_{\mathrm{i}_x},\ 0,\ E_{\mathrm{i}_z}) \exp\big(-\kappa_\mathrm{i}|z|\big) \exp\Big[i\big(q_\mathrm{i} x - \omega t\big)\Big] \qquad (2.50)$$

$$\mathbf{H}_\mathrm{i} = (0,\ H_{\mathrm{i}_y},\ 0) \exp\big(-\kappa_\mathrm{i}|z|\big) \exp\Big[i\big(q_\mathrm{i} x - \omega t\big)\Big] \qquad (2.51)$$

In equations (2.46) to (2.51), the i is the index for the media, either 1 for $z < 0$, or 2 for $z > 0$. In equation (2.50) and equation (2.51), the q_i represents the magnitude of a wave vector parallel to the interface. Utilizing equation (2.50) and equation (2.51) in equations (2.46) to (2.49) yields equations (2.52) to (2.54).

Moreover, the boundary conditions demand that the electric and magnetic fields parallel to the surface must be continuous, ultimately yielding equations (2.55) to (2.58) when using equation (2.52) and equation (2.53) [306].

$$i\kappa_1 H_{1,y} = \frac{\omega}{c}\varepsilon_1 E_{1x} \qquad (2.52) \qquad\qquad i\kappa_2 H_{2,y} = \frac{\omega}{c}\varepsilon_2 E_{2x} \qquad (2.53)$$

$$\kappa_1 = \sqrt{q_{\mathrm{i}}^2 - \frac{\varepsilon_{\mathrm{i}}\omega^2}{c^2}} \qquad (2.54)$$

Equation (2.57) is known as the surface-plasmon condition. A direct consequence of the surface-plasmon condition is the continuity of the 2D wave vector $\mathbf{q}$, where $q_1 = q_2 = q$, leading to equation (2.58), where $\frac{\omega}{c}$ describes the magnitude of the light wave vector. Imagining the first semi-infinite medium as a metal, and the second one as a dielectric, characterized by ε_2, yields a solution with slope of $\frac{c}{\sqrt{\varepsilon_2}}$ at $q = 0$, that is monotonically increasing for increasing q [306].

$$\frac{\kappa_1}{\varepsilon_1}H_{1,y} + \frac{\kappa_2}{\varepsilon_2}H_{2,y} = 0 \qquad (2.55) \qquad\qquad H_{1,y} - H_{2,y} = 0 \qquad (2.56)$$

$$\frac{\varepsilon_1}{\kappa_1} + \frac{\varepsilon_2}{\kappa_2} = 0 \qquad (2.57) \qquad\qquad q(\omega) = \frac{\omega}{c}\sqrt{\frac{\varepsilon_1\varepsilon_2}{\varepsilon_1 + \varepsilon_2}} \qquad (2.58)$$

The solution is always smaller than $\frac{cq}{\sqrt{\varepsilon_2}}$, and is asymptotic to the value given by equation (2.59) for large q [306]. Equation (2.59) is called the non-retarded surface-plasmon condition, with $\kappa_1 = \kappa_2 = q$ substituted in equation (2.57). This is only valid as long as the phase velocity $\frac{\omega}{q} \ll c$.

$$\varepsilon_1 + \varepsilon_2 = 0 \qquad (2.59)$$

If the system is a Drude semi-infinite metal in vacuum, then $\varepsilon_2 = 1$, and, according to Ashcroft, equation (2.59) follows [308]. In equation (2.60), η is a positive infinitesimal. Utilizing equation (2.60) in equation (2.58), results in equation (2.61). The surface-plasmon polariton frequency, expressed with the plasmon frequency, is then given by equation (2.62), where the retarded region, defined by $q < \frac{\omega_{\mathrm{s}}}{c}$, couples with the free electromagnetic field, and the

non-retarded limit, defined by $q \gg \frac{\omega_s}{c}$, yields the classical nondispersive surface plasmon frequency $\omega_s = \frac{\omega_p}{\sqrt{2}}$ [306].

$$\varepsilon_1 = 1 - \frac{\omega_p^2}{\omega(\omega + i\eta)} \qquad (2.60) \qquad q(\omega) = \frac{\omega}{c}\sqrt{\frac{\omega^2 - \omega_p^2}{2\omega^2 + \omega_p^2}} \qquad (2.61)$$

$$\omega^2(q) = \frac{\omega_p}{2} + c^2q^2 - \sqrt{\frac{\omega_p^4}{4} + c^4q^4} \qquad (2.62)$$

Spatially, the electromagnetic field is characterized by the surface-plasmon decay constant κ_i perpendicular to the surface and the attenuation length $l_i = \frac{1}{\kappa_i}$. The decay constant is defined by equation (2.63), and the latter describes the length after which the electromagnetic field falls to $\frac{1}{e}$ [306].

$$\kappa_i = \frac{\omega}{c}\sqrt{-\frac{\varepsilon_i^2}{\varepsilon_1 + \varepsilon_2}} \qquad (2.63)$$

Non-retarded Surface Plasmon: In the retarded region, where $q < \frac{\omega_s}{c}$ (with $\frac{\omega_s}{c} \ll q_F$, where q_F is the magnitude of the Fermi wave vector), nonlocal effects can usually be ignored [306]. However, in the non-retarded regime, where $\frac{\omega_s}{c} < q$, and without any external source, the ω-components of the time-dependent electric and displacement fields associated with collective oscillations at a metal surface satisfy the quasi-static Maxwell's equation given in equation (2.64) or, equivalently, equation (2.65) and equation (2.66) [306]. Here, $\delta n(\mathbf{r}, \omega)$ is the fluctuating electron density associated with the surface plasmon, and $\phi(\mathbf{r}, \omega)$ is the ω component of the time-dependent scalar potential.

$$\nabla \cdot \mathbf{E}(\mathbf{r}, \omega) = -4\pi r \delta n(\mathbf{r}, \omega) \qquad (2.64)$$

$$\nabla \phi^2(\mathbf{r}, \omega) = 4\pi\delta(\mathbf{r}, \omega) \qquad (2.65)$$

$$\nabla \cdot \mathbf{D}(\mathbf{r}, \omega) = 0 \qquad (2.66)$$

Localized Surface Plasmon: Instead of semi-infinite bodies, geometries of any kind can support charge density oscillations the like of surface plasmons of planar interfaces [306]. In the long-wavelength limit, an interface separating two media with local, frequency-dependent dielectric functions ε_1 and ε_2, equation (2.67) is valid, where i again is the index for the media [306]. Simple geometrical shapes, such as spheres or cylinders, allow the explicit solution of equations (2.64) to (2.66) by utilizing equation (2.67) [306].

$$\mathbf{D}_{\mathrm{i}}(\mathbf{r},\omega) = \varepsilon_{\mathrm{i}}\mathbf{E}_{\varepsilon}i(\mathbf{r},\omega) \tag{2.67}$$

$$l\varepsilon_1 + (l+1)\varepsilon_2 = 0 \qquad \text{with } l = 1,2,3,\ldots \tag{2.68}$$

$$\omega_l = \omega_{\mathrm{p}}\sqrt{\frac{l}{2l+1}} \tag{2.69}$$

For spherical shapes, where medium 1 is the sphere and medium 2 the matrix, the planar surface-plasmon condition of equation (2.59) is replaced by equation (2.67), where l is the l-th resonance, which in turn yields, for a Drude metal sphere (ε_1 defined by equation (2.60)) in vacuum, the Mie plasmons at frequencies given in equation (2.69) [306]. If only the dipolar symmetries are considered ($l = 1$), then equation (2.69) is the well-known resonance frequency $\omega_l = \frac{\omega_{\mathrm{p}}}{\sqrt{3}}$.

2.5.2 Mie Theory

Gustav Mie solved Maxwell's equation for spherical nanoparticles in a uniform medium in 1908 [250] (Engl. [309]). The input parameters were only the particle size and the optical functions of the particle and surrounding medium. Dividing the problem into two parts, Mie treated the electromagnetic part of it from first principles and circumvented the material part by introducing phenomenological dielectric functions $\varepsilon(\omega, R)$, limiting the theory by giving no

physical insights into the materials properties [134]. Only decades later was Mie absorption interpreted in accordance with the modern concept of collective plasmon oscillations of different multipole orders [134, 310, 311].

The optical properties of a MNP are commonly expressed by absorption and scattering cross sections, σ_{abs} and σ_{sca}. These cross-sections can be used to determine the intensity loss (ΔI) of a parallel beam of incident light due to absorption and elastic scattering, and, utilizing the Beer-Lambert law, one can obtain the intensity loss for purely absorbing or scattering particles, see equation (2.70) and equation (2.71) [134]. Here, the # describes the number density of MNPs.

$$\Delta I_{\mathrm{abs}}(z) = I_0(1 - \exp\big(-\#\sigma_{\mathrm{abs}} z\big)) \tag{2.70}$$

$$\Delta I_{\mathrm{sca}}(z) = I_0(1 - \exp\big(-\#\sigma_{\mathrm{sca}} z\big)) \tag{2.71}$$

$$\sigma_{\mathrm{ext}} = \sigma_{\mathrm{abs}} + \sigma_{\mathrm{sca}} \tag{2.72}$$

$$\gamma_e = \#\sigma_{\mathrm{ext}} \tag{2.73}$$

Realistic particles, however, exhibit absorption and scattering contributions simultaneously, simplified by determining the extinction cross section (see equation (2.72)), which in turn can be related to the extinction constant γ_2 by equation (2.73) [134]. These cross sections can be expressed via series expansions by equations (2.74) to (2.76) where L is the order of the partial wave ($L = 1$: dipole, $L = 2$: quadrupole, etc.), $\mathbf{k}$ is the wavevector, and a_L and b_L are defined by equation (2.77) and equation (2.78), respectively [134].

$$\sigma_{\mathrm{ext}} = \frac{2\pi}{|\mathbf{k}|^2} \sum_{L=1}^{\infty} \big(2L+1\big)\Re\big(a_L + b_L\big) \tag{2.74}$$

$$\sigma_{\mathrm{sca}} = \frac{2\pi}{|\mathbf{k}|^2} \sum_{L=1}^{\infty} \big(2L+1\big)\big(|a_L|^2 + |b_L|^2\big) \tag{2.75}$$

$$\sigma_{\text{abs}} = \sigma_{\text{ext}} - \sigma_{\text{sca}} \tag{2.76}$$

In equation (2.77) and equation (2.78), L represents again the order of the partial wave, the size parameter is $x = |\mathbf{k}|R$ with R the radius of the particle, and $m = \frac{n_m}{n}$, where n is the complex refractive index of the particle, and n_m the real refractive index of the surrounding medium [134, 312, 313]. ψ_L and η_L are the Riccati-Bessel functions of first and third kind, respectively, and ψ'_L and η'_L their derivative with respect to the argument in the bracket [134, 312, 313].

$$a_L = \frac{m\psi_L(mx)\psi'_L(x) - \psi'_L(mx)\psi_L(x)}{m\psi_L(mx)\eta'_L(x) - \psi'_L(mx)\eta_L(x)} \tag{2.77}$$

$$b_L = \frac{\psi_L(mx)\psi'_L(x) - m\psi'_L(mx)\psi_L(x)}{\psi_L(mx)\eta'_L(x) - m\psi'_L(mx)\eta_L(x)} \tag{2.78}$$

In the quasi-static regime (i.e., $R \ll \lambda$), phase retardation and higher multipole effects can be ignored, and the Mie formula is simplified. The factors a_L and b_L in equation (2.77) and equation (2.78) are proportional to $|\mathbf{k}|R^{2L+1}$, and with $|\mathbf{k}| = \frac{\omega}{c}$ the lowest order term of equation (2.74) is then given by equation (2.79). Here, V_0 represents the particle volume, ω is the angular frequency, c is the speed of light, and ε_m, ε_1 and ε_2 are the dielectric constant of the surrounding medium and the real and imaginary dielectric function of the MNP, respectively [134, 314].

$$\sigma_{\text{ext}}(\omega) = 9\frac{\omega}{c}\varepsilon_m^{\frac{3}{2}}V_0\frac{\varepsilon_2(\omega)}{\left[\varepsilon_1(\omega) + 2\varepsilon_m\right]^2 + \varepsilon_2(\omega^2)} \tag{2.79}$$

2.5.3 Surface Plasmon Absorption Band (SPAB)

The surface plasmon absorption band (SPAB), the MNPs ultraviolet-visible spectrum, is the result of the movement of conduction electrons due to the incident electric field, resulting in the displacement of the negative and positive charges [315]. Considering equation (2.79), the SPAB can be found when $\varepsilon_1(\omega) = 2\varepsilon_m$. Elements such as Al, Mg, In, and Ga reveal strong LSPR in

the UV region, while Au, Ag, and Cu have well defined LSPR peaks in the visible region [314, 316, 317]. Ni, on the other hand, has only weak plasmonic resonance [314, 317], making Au, Ag, and Cu the preferred elements for plasmonic experiments [316, 318–322].

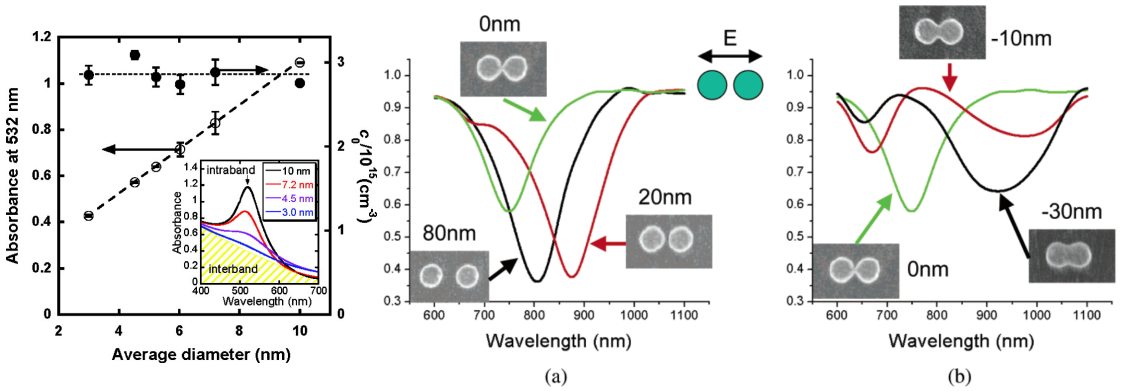

Figure 2.19: Left: The number density of solvated electrons in solutions (solid circles) at $t = 0$ is displayed. Furthermore, the absorbance at 532 nm (open circles) of 3×10^{-4} M gold nanoparticles in a 3×10^{-2} M aqueous solution, both as function of the average diameter of the Au MNPs. The inset depicts the absorption spectra of the Au MNPs with different average diameters. Middle: Pairs of Au MNPs with different distances between the two. Between pairs, there are 800 nm in the parallel direction of the pair axis and 400 nm in perpendicular direction. The dot heights were 30 nm. The distance between the two particles is indicated, where 0 nm indicates toughing particles, and their transmittance is plotted as a function of the wavelength. Right: Similar structures as in the Middle, but the distance is further reduced, widening the interconnected neck between them. Again the transmittance is plotted as a function of the wavelength for three different configurations. Figure taken from [323] (left) and [324] (middle and right), with permission.

In addition to the intrinsic materials properties like the dielectric functions of MNPs, the shape of the LSPR band depends on the size, shape, interparticle distance, etc. of the MNPs. To exemplify this, Au MNPs are considered, demonstrating the size and interparticle distance with two examples. The LSPR peak for particles with a diameter of 4.5 nm is clearly visible, increasing with increasing diameter. However, it is completely absent once the particle diameter is decreased to 3 nm, as seen in figure 2.19 (left) [323]. Furthermore, the transmittance of samples consisting of pairs of Au MNPs separated from each

other is shown in figure 2.19 (middle and right). By moving them closer together, the peak position shifts more than 100 nm depending on the configuration, while the peak splits in two once they form an interconnected neck [324].

Finally, it has also been shown that rod-shaped Au nanostructures have a transverse resonance band and a longitudinal resonance band [325]. The peak position of the former is around 520 nm, similar to that of spherical MNPs. The longitudinal resonance band position, however, is depends on the aspect ratio (length/width) [325].

2.5.4 Decay-Mechanisms in Plasmonic Metal Nanostructures

The decay of an LSPR can occur radiatively or non-radiatively [326]; an overview of four energy transfer mechanisms from a plasmonic MNP to an n-type semiconductor can be seen in figure 2.20. The decay or dephasing of the plasmon occurs rapidly, and T_2 will be used to represent the dephasing time and is defined in equation (2.80). Here, Γ_{hom} is the homogeneous line width of the surface plasmon resonance, and $\hbar$ is the reduced Planck's constant. The dephasing time can be coupled to the lifetime of a plasmon, τ_{SP}, by $T_2 = 2\tau_{\text{SP}}$ [327, 328].

$$T_2 = \frac{2\hbar}{\Gamma_{\text{hom}}} \tag{2.80}$$

$$\Gamma_{\text{hom}} = \Gamma_{\text{rad}} + \Gamma_{\text{nonrad}} \tag{2.81}$$

Because both radiative and non-radiative decay can occur, the Γ_{hom} for LSPR is defined by equation (2.81), where Γ_{rad} and Γ_{nonrad} are the radiative and non-radiative decay line width, respectively [329, 330]. In general, the former increases for a larger number of electrons, i.e., a larger size of the MNP leads to more light scattering [331]. In equation (2.82), an upper limit for Γ_{rad} is

established, where V is the volume of the structure, λ is the wavelength of the incident light, and ε_1 and ε_2 are the real and imaginary parts of the complex dielectric constant of the MNP [329]. The non-radiative decay is only dependent on the optical properties, as shown in equation (2.83), where ε_1' is the derivative of the real part of the dielectric constant of the MNP [326, 329].

$$\Gamma_{\text{rad}} \leq \frac{4\pi^2 V}{3\lambda} \frac{((\varepsilon_1 - 1)^2 - \varepsilon_2)}{\varepsilon_2} \Gamma_{\text{nonrad}} \tag{2.82}$$

$$\Gamma_{\text{nonrad}} \approx \frac{2\varepsilon_2}{\varepsilon_1'} \tag{2.83}$$

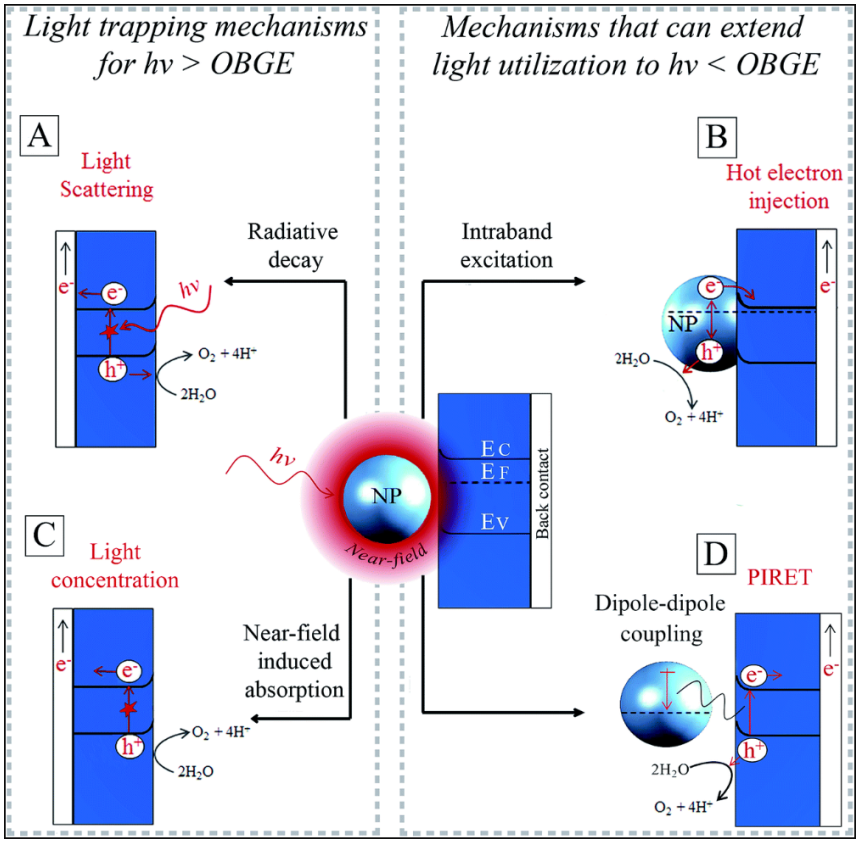

Figure 2.20: Four possible energy transfer mechanisms from a plasmonic MNP to an n-type semiconductor are displayed. (A) is light scattering, (B) is hot electron injection, (C) is light concentration, and (D) is PIRET. (A) and (C) are radiative decay mechanisms, and (B) and (D) are non-radiative ones. OBGE represents the optical band gap energy of the semiconductor, E_C is the conduction band energy, E_F the Fermi energy, and E_V the valence band energy. The figure was taken from [332] with permission from the Royal Society of Chemistry.

An example of a non-radiative dissipation of plasmon energy, hot carriers can be created via Landau damping (i.e., intra- and interband transition of electrons in metal due to the electric field induced by the plasmon resonance) within femtoseconds (1 to 100 fs) [333]. However, hot charge carriers are not the only decay mechanism.

Scattering Effects

The characteristics of scattering are dependent on the particle geometry [331, 334]. The principle behind utilizing the scattering mechanism to improve the efficiency is to optimize the incident power density by illuminating light normal to the surface and the insufficient absorption due to transmission [335]. If an incoming photon is scattered on the surface, it inevitably has to travel longer through the materials than otherwise needed. Spherical particles can scatter in both the forward direction (particles with small radii) or backward direction (particles with large radii), also known as reflection [336]. These two different scattering behaviors can be used to design devices [337–339]. Independent of the actual design, multiple scattering events are considered to improve the apparent quantum efficiency. Often the scattering effect is also referred to as light trapping or far field effect [331].

Near-Field Enhancement

LSPR occurs at a highly curved or kinked surface of a plasmonic noble metal. These surface plasmons cannot propagate, i.e., they are confined to the particle, unlike surface plasmon polariton and instead result in highly energetic local fields at the MNP surface. The degree of confinement is geometry dependent [340].

In particular, the incident wavevector and the particle dimensions determine on which surface near-field excitations occur [341]. The geometry dependency

can be further emphasized by considering that the LSPR maxima redshifts with increasing particle size, and multiple peaks emerge from complex structures [342, 343]. The proximity of two clusters can also amplify the broadband and create "hot spots" [344, 345]. The strong electromagnetic field enhances the formation rate of charge carriers, where the highly localized electric field (near field) causes interband excitation in the neighboring semiconductor, and affects the generation of electron-hole pairs [340, 346–349].

Non-radiative Transfer Mechanisms

As mentioned above, hot charge carriers can be formed by the non-radiative decay of a plasmon. In addition, plasmon-induced resonance energy transfer (PIRET, also known as PRET and RET [331]) describes a mechanism where near-field energy is non-radiatively transferred to a semiconductor via dipole-dipole interaction [350, 351].

Hot electrons, as an example of hot charge carriers, are generated through electron-electron scattering, leading to intra- and inter-band excitation of the conduction electrons [352]. Subsequently, the hot electrons from the MNP are injected into the conduction band of the semiconductor [353]. In figure 2.21, the excitation of hot electrons is shown in (b), and the injection of hot electrons in (c). As shown, only hot electrons with an energy large enough to overcome the Schottky barrier, φ_{SB}, or, with a much lower probability, electrons able to tunnel through the barrier, can be injected [354]. The Schottky barrier is defined by equation (2.84) where φ_{M} is the work function of the metal and χ_{S} is the electron affinity of the semiconductor [351, 354].

$$\varphi_{\mathrm{SB}} = \varphi_{\mathrm{M}} - \chi_{\mathrm{S}} \tag{2.84}$$

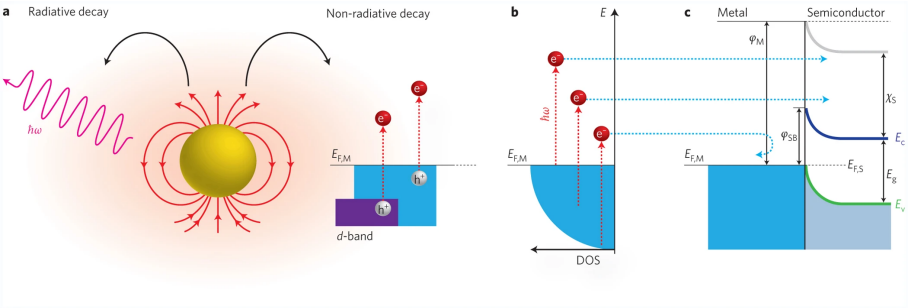

Figure 2.21: (a) LSPR decays radiatively or non-radiatively. (b) Electrons are excited above the Fermi level during non-radiative excitation. (c) Injection of hot electrons into the semiconductor if electrons have an energy high enough to cross the Schottky barrier. The figure was taken from [354], with permission.

The geometry of the MNPs affects on the energy of the hot electrons. Namely, smaller MNPs (i.e., smaller than 20 nm) typically lead to hot electrons with energy (E_{H}) ranging from $E_{\mathrm{F}} < E_H < E_{\mathrm{F}} + \hbar\omega$, whereas larger particles lead to hot electrons with energies closer to the E_{F} [355]. If the energy of the generated hot electrons is higher than the Schottky barrier, they will be injected into the conduction band [348, 355–360]. In addition to the energy requirement, the hot electron must reach the MNP surface before to relaxation [354]. Considerable emphasis has been laid on studying the timescales of generation and injection mechanisms of hot electrons [354, 361].

PIRET improves the absorption ability of the semiconductor photocatalysts below its optical band gap energy but only occurs in regions with spectral overlap between the semiconductor and MNP [350, 362, 363]. However, in contrast to hot electrons, the PIRET mechanism can occur even in the presence of an insulating layer around the MNP [350].

2.6 Concluding Remarks

Photocatalysts may not be commercially viable yet; however, Domen et al. have shown that at least scalability can already be achieved [364]. They showcased a

$100\,m^2$ photocatalytic area operating over a time period of 8 months utilizing, like in this work, STO as a photocatalyst. Domen et al. doped their photocatalyst with aluminium. STO is a wide band gap material, and they did not engineer it to absorb visible light. However, the material absorbs well in the UV range, and the quantum efficiency in the UV range was almost 100%, i.e., almost all photons were converted into products. In addition, their work showed that continuous operation of such a large scale setup can work while separating oxygen and hydrogen. Paired with the abundance of the elements within strontium titanate, STO shows great promise of up-scaling.

Scalability and efficiency are the main concern when it comes to commercial photocatalysis. The initial cost of creating the photocatalyst, as well as the running cost of the device, are determining factors. The theory introduces above can be combined into a unique synthesis route to create more efficient photocatalysts with embedded MNPs. Exsolution creates well-socketed MNPs in the bulk and on the surface, while subsequent galvanic replacement introduces a more noble, and usually considerably more scarce, metal but limited to the surface. Choosing the metal correctly to gain effects from LSPR can enhance the photoelectrochemical response of the system.

References

[1] Attfield, J. P., Lightfoot, P., and Morris, R. E. “Perovskites”. In: *Dalton Trans.* vol. 44, no. 23 (2015). Publisher: The Royal Society of Chemistry, pp. 10541–10542.

[2] Neagu, D. and Irvine, J. “4.15 – Perovskite Defect Chemistry as Exemplified by Strontium Titanate”. In: *Comprehensive Inorganic Chemistry II (Second Edition): From Elements to Applications*. Vol. 4. Journal Abbreviation: Comprehensive Inorganic Chemistry II (Second Edition): From Elements to Applications. Aug. 2013, pp. 397–415.

[3] Cowley, R. “Lattice dynamics and phase transitions of strontium titanate”. In: *Physical Review* vol. 134, no. 4A (1964), A981.

[4] Stoecker, H. et al. “Strontium titanate: From symmetry changes to functionality”. In: *Crystal Research and Technology* vol. 52, no. 1 (2017), p. 1600222.

[5] Wrighton, M. S. et al. “Strontium titanate photoelectrodes. Efficient photoassisted electrolysis of water at zero applied potential”. In: *Journal of the American Chemical Society* vol. 98, no. 10 (1976). Number: 10 Publisher: ACS Publications, pp. 2774–2779.

[6] Sunstrom, J. E., Kauzlarich, S. M., and Klavins, P. “Synthesis, structure, and properties of lanthanum strontium titanate ($La_{1-x}Sr_xTiO_3$) ($0 \leq x \leq 1$)”. In: *Chemistry of Materials* vol. 4, no. 2 (Mar. 1992). Publisher: American Chemical Society, pp. 346–353.

[7] Ohta, H. “Thermoelectrics based on strontium titanate”. In: *Materials today* vol. 10, no. 10 (2007). Publisher: Elsevier, pp. 44–49.

[8] Morgan John W. and Anders Edward. “Chemical composition of Earth, Venus, and Mercury”. In: *Proceedings of the National Academy of Sciences* vol. 77, no. 12 (Dec. 1980). Publisher: Proceedings of the National Academy of Sciences, pp. 6973–6977.

[9] Deng, Z. et al. “Octahedral connectivity and its role in determining the phase stabilities and electronic structures of low-dimensional, perovskite-related iodoplumbates”. In: *APL Materials* vol. 6, no. 11 (Nov. 2018). Publisher: American Institute of Physics, p. 114202.

[10] Gu, M. et al. “Enhancement of orbital ordering and spin polarization by controlling the dimensionality of the octahedra network”. In: *npj Quantum Materials* vol. 1 (Sept. 2016), p. 16011.

[11] Tyunina, M. et al. “Optics of epitaxial strained strontium titanate films”. In: *Applied Physics Letters* vol. 117, no. 8 (2020), p. 082901. eprint: https://doi.org/10.1063/5.0021461.

[12] Norby, T. “Proton Conductivity in Perovskite Oxides”. In: *Perovskite Oxide for Solid Oxide Fuel Cells*. Ed. by Ishihara, T. Boston, MA: Springer US, 2009, pp. 217–241.

[13] Irvine, J. T. S. “Perovskite Oxide Anodes for SOFCs”. In: *Perovskite Oxide for Solid Oxide Fuel Cells*. Ed. by Ishihara, T. Boston, MA: Springer US, 2009, pp. 167–182.

[14] Moos, R. and Hardtl, K. H. “Defect chemistry of donor-doped and undoped strontium titanate ceramics between 1000° and 1400° C”. In: *Journal of the American Ceramic Society* vol. 80, no. 10 (1997), pp. 2549–2562.

[15] Goodenough, J. B. “Electronic and ionic transport properties and other physical aspects of perovskites”. In: *Reports on Progress in Physics* vol. 67, no. 11 (2004), p. 1915.

[16] Ruddlesden, S. and Popper, P. “New compounds of the K_2NiF_4 type”. In: *Acta Crystallographica* vol. 10, no. 8 (1957), pp. 538–539.

[17] Ruddlesden, S. and Popper, P. "The compound Sr3Ti2O7 and its structure". In: *Acta Crystallographica* vol. 11, no. 1 (1958), pp. 54–55.

[18] Williams, T. et al. "On the crystal structures of $La_2Ti_2O_7$ and $La_5Ti_5O_{17}$: High-resolution electron microscopy". In: *Journal of Solid State Chemistry* vol. 93, no. 2 (1991), pp. 534–548.

[19] Howard, C. J. et al. "Crystal structures and phase transition in the system $SrTiO_3 - La_{2/3}TiO_3$". In: *Journal of Solid State Chemistry* vol. 177, no. 8 (2004), pp. 2726–2732.

[20] Howard, C. J. and Kennedy, B. J. "The orthorhombic and rhombohedral phases of-a neutron powder diffraction study". In: *Journal of Physics: Condensed Matter* vol. 11, no. 16 (1999), p. 3229.

[21] Smith, K. L. et al. "In situ radiation damage studies of $La_xSr_{1-3\frac{x}{2}}TiO_3$ perovskites". In: *Journal of Applied Physics* vol. 103, no. 8 (2008), p. 083531.

[22] Battle, P. et al. "A-site cation-vacancy ordering in $Sr_{1-3\frac{x}{2}}La_xTiO_3$: a study by HRTEM". In: *Journal of Solid State Chemistry* vol. 149, no. 2 (2000), pp. 360–369.

[23] Bednorz, J. G. and Müller, K. A. "Possible high T_c superconductivity in the Ba- La- Cu- O system". In: *Zeitschrift für Physik B Condensed Matter* vol. 64, no. 2 (1986), pp. 189–193.

[24] Kusainova, A. M. et al. "Structure–property correlations in the new ferroelectric $Bi_5PbTi_3O_{14}Cl$ and related layered oxyhalide intergrowth phases". In: *Journal of Materials Chemistry* vol. 12, no. 12 (2002), pp. 3413–3418.

[25] Neagu, D. et al. "Nano-socketed nickel particles with enhanced coking resistance grown in situ by redox exsolution". In: *Nature Communications* vol. 6, no. 1 (Sept. 2015), p. 8120.

[26] Lee, D. and Lee, H. N. "Controlling Oxygen Mobility in Ruddlesden–Popper Oxides". In: *Materials* vol. 10, no. 4 (2017).

[27] Neagu, D. "Materials and microstructures for high temperature electrochemical devices through control of perovskite defect chemistry". PhD thesis. University of St Andrews, 2013.

[28] Neagu, D. et al. "In situ growth of nanoparticles through control of non-stoichiometry". In: *Nature Chemistry* vol. 5, no. 11 (Nov. 2013), pp. 916–923.

[29] Shannon, R. D. "Revised effective ionic radii and systematic studies of interatomic distances in halides and chalcogenides". In: *Acta crystallographica section A: crystal physics, diffraction, theoretical and general crystallography* vol. 32, no. 5 (1976), pp. 751–767.

[30] Escudero, M., Irvine, J., and Daza, L. “Development of anode material based on La-substituted $SrTiO_3$ perovskites doped with manganese and/or gallium for SOFC”. In: *Journal of Power Sources* vol. 192, no. 1 (2009). CONAPPICE 2008, Zaragoza, Spain, 24-26 September 2008, pp. 43–50.

[31] Lu, C.-H. et al. “Doping and ion substitution in colloidal metal halide perovskite nanocrystals”. In: *Chem. Soc. Rev.* vol. 49 (14 2020), pp. 4953–5007.

[32] Ishihara, T. “Structure and properties of perovskite oxides”. In: *Perovskite Oxide for Solid Oxide Fuel Cells*. Springer, 2009, pp. 1–16.

[33] Ogugua, S. N., Ntwaeaborwa, O. M., and Swart, H. C. “Luminescence, structure and insight on the inversion degree from normal to inverse spinel in a $ZnAl_{(2-x)}Fe_x^{3+}O_4$ system”. In: *Boletín de la Sociedad Española de Cerámica y Vidrio* vol. 60, no. 3 (2021), pp. 147–162.

[34] Tidrow, S. C. “Mapping comparison of Goldschmidt’s tolerance factor with Perovskite structural conditions”. In: *Ferroelectrics* vol. 470, no. 1 (2014), pp. 13–27.

[35] Stoumpos, C. C. et al. “Structure–Band Gap Relationships in Hexagonal Polytypes and Low-Dimensional Structures of Hybrid Tin Iodide Perovskites”. In: *Inorganic Chemistry* vol. 56, no. 1 (2017). PMID: 27997156, pp. 56–73. eprint: https://doi.org/10.1021/acs.inorgchem.6b02764.

[36] Yadav, S. et al. “Structural correlations in the enhancement of ferroelectric property of Sr doped $BaTiO_3$”. In: *Journal of Physics: Condensed Matter* vol. 32, no. 44 (2020), p. 445402.

[37] Dabrowski, B. et al. “Tolerance factor rules for $Sr_{1-x-y}Ca_xBa_yMnO_3$ perovskites”. In: *Journal of Solid State Chemistry* vol. 170, no. 1 (2003), pp. 154–164.

[38] Woodward, P. M. “Octahedral tilting in perovskites. I. Geometrical considerations”. In: *Acta Crystallographica Section B: Structural Science* vol. 53, no. 1 (1997), pp. 32–43.

[39] Woodward, P. M. “Octahedral tilting in perovskites. II. Structure stabilizing forces”. In: *Acta Crystallographica Section B: Structural Science* vol. 53, no. 1 (1997), pp. 44–66.

[40] Howard, C. J. and Stokes, H. T. “Group-theoretical analysis of octahedral tilting in perovskites”. In: *Acta Crystallographica Section B: Structural Science* vol. 54, no. 6 (1998), pp. 782–789.

[41] Lufaso, M. W. and Woodward, P. M. “Jahn–Teller distortions, cation ordering and octahedral tilting in perovskites”. In: *Acta Crystallographica Section B: Structural Science* vol. 60, no. 1 (2004), pp. 10–20.

[42] Xiang, H. et al. “Rules and mechanisms governing octahedral tilts in perovskites under pressure”. In: *Physical Review B* vol. 96, no. 5 (2017), p. 054102.

[43] Hui, S. and Petric, A. "Electrical properties of yttrium-doped strontium titanate under reducing conditions". In: *Journal of the Electrochemical Society* vol. 149, no. 1 (2001), J1.

[44] Eng, H. W. et al. "Investigations of the electronic structure of d0 transition metal oxides belonging to the perovskite family". In: *Journal of Solid State Chemistry* vol. 175, no. 1 (2003), pp. 94–109.

[45] Wolfram, T. and Ellialtioglu, S. *Electronic and optical properties of d-band perovskites*. Cambridge University Press, 2006.

[46] Slater, P. et al. "High-temperature powder neutron diffraction study of the oxide ion conductor $La_{0.9}Sr_{0.1}Ga_{0.8}Mg_{0.2}O_{2.85}$". In: *Journal of Solid State Chemistry* vol. 139, no. 1 (1998), pp. 135–143.

[47] Kennedy, B. J., Howard, C. J., and Chakoumakos, B. C. "Phase transitions in perovskite at elevated temperatures-a powder neutron diffraction study". In: *Journal of Physics: Condensed Matter* vol. 11, no. 6 (1999), p. 1479.

[48] Kennedy, B. et al. "Structural characterization of the perovskite series $La_{1-x}Sr_xCr_{1-x}Ti_xO_3$". In: *Journal of Solid State Chemistry* vol. 155, no. 2 (2000), pp. 455–457.

[49] Howard, C. J. and Stokes, H. T. "Structures and phase transitions in perovskites–a group-theoretical approach". In: *Acta Crystallographica Section A: Foundations of Crystallography* vol. 61, no. 1 (2005), pp. 93–111.

[50] Carpenter, M. A. et al. "Structural relationships and a phase diagram for (Ca,Sr)TiO_3 perovskites". In: *Journal of Physics: Condensed Matter* vol. 18, no. 48 (Nov. 2006), pp. 10725–10749.

[51] Zhang, Z. et al. "Structures and phase diagram for the system $CaTiO_3$ – $La_{2/3}TiO_3$". In: *Journal of Solid State Chemistry* vol. 180, no. 3 (2007), pp. 1083–1092.

[52] Liu, X., Hong, R., and Tian, C. "Tolerance factor and the stability discussion of ABO_3-type ilmenite". In: *Journal of Materials Science: Materials in Electronics* vol. 20, no. 4 (2009), pp. 323–327.

[53] Onishi, T. "Perovskites: Application and Structure". In: *Ferroelectric Perovskites for High-Speed Memory*. Springer, 2022, pp. 19–36.

[54] Attfield, J. "'A'cation control of perovskite properties". In: *Crystal engineering* vol. 5, no. 3-4 (2002), pp. 427–438.

[55] Garcia-Fernandez, P. et al. "Key role of covalent bonding in octahedral tilting in perovskites". In: *The Journal of Physical Chemistry Letters* vol. 1, no. 3 (2010), pp. 647–651.

[56] Howard, C. J., Kennedy, B. J., and Woodward, P. M. "Ordered double perovskites–a group-theoretical analysis". In: *Acta Crystallographica Section B: Structural Science* vol. 59, no. 4 (2003), pp. 463–471.

[57] Hodges, J. et al. “Evolution of oxygen-vacancy ordered crystal structures in the perovskite series $Sr_nFe_nO_{3n-1}$ (n= 2, 4, 8, and∞), and the relationship to electronic and magnetic properties”. In: *Journal of Solid State Chemistry* vol. 151, no. 2 (2000), pp. 190–209.

[58] Glazer, A. M. “The classification of tilted octahedra in perovskites”. In: *Acta Crystallographica Section B: Structural Crystallography and Crystal Chemistry* vol. 28, no. 11 (1972), pp. 3384–3392.

[59] Glazer, A. “A brief history of tilts”. In: *Phase Transitions* vol. 84, no. 5-6 (2011), pp. 405–420.

[60] Anderson, M. T., Vaughey, J. T., and Poeppelmeier, K. R. “Structural similarities among oxygen-deficient perovskites”. In: *Chemistry of materials* vol. 5, no. 2 (1993), pp. 151–165.

[61] Stølen, S., Bakken, E., and Mohn, C. E. “Oxygen-deficient perovskites: linking structure, energetics and ion transport”. In: *Physical Chemistry Chemical Physics* vol. 8, no. 4 (2006), pp. 429–447.

[62] Poeppelmeier, K., Leonowicz, M., and Longo, J. “$CaMnO_{2.5}$ and $Ca_2MnO_{3.5}$: New oxygen-defect perovskite-type oxides”. In: *Journal of Solid State Chemistry* vol. 44, no. 1 (1982), pp. 89–98.

[63] Asenath-Smith, E., Misture, S. T., and Edwards, D. D. “Structural behavior and thermoelectric properties of the brownmillerite system $Ca_2(Zn_xFe_{2-x})O_5$”. In: *Journal of Solid State Chemistry* vol. 184, no. 8 (2011), pp. 2167–2177.

[64] Shaula, A. et al. “Ionic conductivity of brownmillerite-type calcium ferrite under oxidizing conditions”. In: *Solid State Ionics* vol. 177, no. 33-34 (2006), pp. 2923–2930.

[65] D’Hondt, H. et al. “Tetrahedral chain order in the $Sr_2Fe_2O_5$ brownmillerite”. In: *Chemistry of Materials* vol. 20, no. 22 (2008), pp. 7188–7194.

[66] Alonso, J. et al. “A structural and magnetic study of the defect perovskite from high-resolution neutron diffraction data”. In: *Journal of Physics: Condensed Matter* vol. 9, no. 30 (1997), p. 6417.

[67] Canales-Vázquez, J. et al. “Studies on the Reorganization of Extended Defects with Increasing n in the Perovskite-Based $La_4Sr_{n-4}Ti_nO_{3n+2}$ Series”. In: *Advanced Functional Materials* vol. 15, no. 6 (2005), pp. 1000–1008.

[68] Aurivillius, B. “Mixed bismuth oxides with layer lattices”. In: *Ark. Kemi.* vol. 1 (1949), p. 499.

[69] Jacobson, A., Johnson, J. W., and Lewandowski, J. “Interlayer chemistry between thick transition-metal oxide layers: synthesis and intercalation reactions of $K[Ca_2Na_{n-3}Nb_nO_{3n+1}](3 \leq n \leq 7)$”. In: *Inorganic chemistry* vol. 24, no. 23 (1985), pp. 3727–3729.

[70] Bowden, M., Jefferson, D., and Brown, I. "Determination of Layer Structure in $Sr_{1-x}La_xTiO_{3+0.5x}$ ($0< x< 1$) Compounds by High-Resolution Electron Microscopy". In: *Journal of Solid State Chemistry* vol. 117, no. 1 (1995), pp. 88–96.

[71] Harvey, E. J. et al. "Characterisation of the $(Y_{1-x}La_x)_2Ti_2O_7$ system by powder diffraction and nuclear magnetic resonance methods". In: *Journal of Materials Chemistry* vol. 16, no. 48 (2006), pp. 4665–4674.

[72] Housecroft, C. and Sharpe, A. *Inorganic Chemistry*. Pearson, 2018.

[73] Wolfram, T., Kraut, E., and Morin, F. "d-Band Surface States on Transition-Metal Perovskite Crystals: I. Qualitative Features and Application to $SrTiO_3$". In: *Physical Review B* vol. 7, no. 4 (1973), p. 1677.

[74] Zimmermann, R. et al. "Electronic structure systematics of 3d transition metal oxides". In: *Journal of Electron Spectroscopy and related phenomena* vol. 96, no. 1-3 (1998), pp. 179–186.

[75] Ellialtioğlu, Ş. and Wolfram, T. "Electronic density of states for the perovskites". In: *Physical Review B* vol. 15, no. 12 (1977), p. 5909.

[76] Luo, W. et al. "Structural and electronic properties of n-doped and p-doped Sr Ti O 3". In: *Physical Review B* vol. 70, no. 21 (2004), p. 214109.

[77] Spinelli, A. et al. "Electronic transport in doped SrTiO 3: Conduction mechanisms and potential applications". In: *Physical Review B* vol. 81, no. 15 (2010), p. 155110.

[78] Jourdan, M., Blümer, N., and Adrian, H. "Superconductivity of SrTiO". In: *The European Physical Journal B-Condensed Matter and Complex Systems* vol. 33, no. 1 (2003), pp. 25–30.

[79] Kittel, C., McEuen, P., and McEuen, P. *Introduction to solid state physics*. Vol. 8. Wiley New York, 1996.

[80] Ishihara, T. et al. "Oxide ion conductivity in doped Ga based perovskite type oxide". In: *Solid State Ionics* vol. 86 (1996), pp. 197–201.

[81] Huang, K., Tichy, R. S., and Goodenough, J. B. "Superior perovskite oxide-ion conductor; strontium-and magnesium-doped $LaGaO_3$: I, phase relationships and electrical properties". In: *Journal of the American ceramic society* vol. 81, no. 10 (1998), pp. 2565–2575.

[82] Goodenough, J. B. "Oxide-ion electrolytes". In: *Annual review of materials research* vol. 33, no. 1 (2003), pp. 91–128.

[83] Kim, N. and Grey, C. P. "Probing oxygen motion in disordered anionic conductors with 17O and 51V MAS NMR spectroscopy". In: *Science* vol. 297, no. 5585 (2002), pp. 1317–1320.

[84] Kharton, V., Marques, F., and Atkinson, A. "Transport properties of solid oxide electrolyte ceramics: a brief review". In: *Solid State Ionics* vol. 174, no. 1-4 (2004), pp. 135–149.

[85] Yashima, M. “Crystal structures, structural disorders and diffusion paths of ionic conductors from diffraction experiments”. In: *Solid State Ionics* vol. 179, no. 21-26 (2008), pp. 797–803.

[86] Norby, T. *Defects and Transport in Crystalline Materials*. Oslo, Norway, 2018.

[87] De Souza, R. “Oxygen diffusion in SrTiO3 and related perovskite oxides”. In: *Advanced Functional Materials* vol. 25, no. 40 (2015), pp. 6326–6342.

[88] Neagu, D. and Irvine, J. T. “Enhancing electronic conductivity in strontium titanates through correlated A and B-site doping”. In: *Chemistry of materials* vol. 23, no. 6 (2011), pp. 1607–1617.

[89] Tao, S. and Irvine, J. T. “A redox-stable efficient anode for solid-oxide fuel cells”. In: *Nature materials* vol. 2, no. 5 (2003), pp. 320–323.

[90] Ishihara, T. “Oxide Ion Conductivity in Perovskite Oxide for SOFC Electrolyte”. In: *Perovskite Oxide for Solid Oxide Fuel Cells*. Ed. by Ishihara, T. Boston, MA: Springer US, 2009, pp. 65–93.

[91] Kilner, J. A., Berenov, A., and Rossiny, J. “Diffusivity of the Oxide Ion in Perovskite Oxides”. In: *Perovskite Oxide for Solid Oxide Fuel Cells*. Ed. by Ishihara, T. Boston, MA: Springer US, 2009, pp. 95–116.

[92] Mogensen, M. et al. “Factors controlling the oxide ion conductivity of fluorite and perovskite structured oxides”. In: *Solid State Ionics* vol. 174, no. 1-4 (2004), pp. 279–286.

[93] Goodenough, J. B., Ruiz-Diaz, J., and Zhen, Y. “Oxide-ion conduction in $Ba_2In_2O_5$ and $Ba_3In_2MO_8$ (M= Ce, Hf, or Zr)”. In: *Solid State Ionics* vol. 44, no. 1-2 (1990), pp. 21–31.

[94] Chanthanumataporn, M. et al. “Electrical reduction of perovskite electrodes for accelerating exsolution of nanoparticles”. In: *Electrochimica Acta* vol. 306 (2019), pp. 159–166.

[95] Islam, M. S. and Davies, R. A. “Atomistic study of dopant site-selectivity and defect association in the lanthanum gallate perovskite”. In: *Journal of Materials Chemistry* vol. 14, no. 1 (2004), pp. 86–93.

[96] Dai, H. et al. “The relationship of structural defect–redox property–catalytic performance of perovskites and their related compounds for CO and NOx removal”. In: *Catalysis today* vol. 90, no. 3-4 (2004), pp. 231–244.

[97] Liang, R. et al. “Superconductivity, magnetism and oxygen nonstoichiometry of $Ba_2Y(Cu_{1-x}M_x)_3O_y$ (M= Zn and Ni)”. In: *Physica C: Superconductivity* vol. 170, no. 3-4 (1990), pp. 307–314.

[98] Coey, J., Viret M, v., and Von Molnar, S. “Mixed-valence manganites”. In: *Advances in physics* vol. 48, no. 2 (1999), pp. 167–293.

[99] Dabrowski, B. et al. “Oxygen content and structures of $La_{1-x}Ca_xMnO_{3+d}$ as a function of synthesis conditions”. In: *Journal of Solid State Chemistry* vol. 146, no. 2 (1999), pp. 448–457.

[100] Slater, P. R., Fagg, D. P., and Irvine, J. T. "Synthesis and electrical characterisation of doped perovskite titanates as potential anode materials for solid oxide fuel cells". In: *Journal of Materials Chemistry* vol. 7, no. 12 (1997), pp. 2495–2498.

[101] McColm, T. and Irvine, J. "Structural and property investigations of Strontium Galloniobate". In: *Solid state ionics* vol. 152 (2002), pp. 615–623.

[102] Vashook, V. et al. "Synthesis, crystal structure, oxygen stoichiometry, and electrical conductivity of $La_{1-a}Ca_aCr_{0.2}Ti_{0.8}O_{3-\delta}$". In: *Solid State Ionics* vol. 158, no. 3-4 (2003), pp. 317–325.

[103] Blennow, P. et al. "Defect and electrical transport properties of Nb-doped $SrTiO_3$". In: *Solid State Ionics* vol. 179, no. 35-36 (2008), pp. 2047–2058.

[104] Ruiz-Morales, J. C. et al. "Disruption of extended defects in solid oxide fuel cell anodes for methane oxidation". In: *Nature* vol. 439, no. 7076 (2006), pp. 568–571.

[105] Islam, Q. A. et al. "Nanoparticle exsolution in perovskite oxide and its sustainable electrochemical energy systems". In: *Journal of Power Sources* vol. 492 (Apr. 2021), p. 229626.

[106] Meng, Y. et al. "Novel high ionic conductivity electrolyte membrane based on semiconductor $La_{0.65}Sr_{0.3}Ce_{0.05}Cr_{0.5}Fe_{0.5}O_{3-\delta}$ for low-temperature solid oxide fuel cells". In: *Journal of Power Sources* vol. 421 (May 2019), pp. 33–40.

[107] Shamsi, J. et al. "Metal Halide Perovskite Nanocrystals: Synthesis, Post-Synthesis Modifications, and Their Optical Properties". In: *Chemical Reviews* vol. 119, no. 5 (Mar. 2019). Publisher: American Chemical Society, pp. 3296–3348.

[108] Zhang, Y. et al. "Ferroelectric and Piezoelectric Effects on the Optical Process in Advanced Materials and Devices". In: *Advanced Materials* vol. 30, no. 34 (Aug. 2018). Publisher: John Wiley & Sons, Ltd, p. 1707007.

[109] Zhu, H., Zhang, P., and Dai, S. "Recent Advances of Lanthanum-Based Perovskite Oxides for Catalysis". In: *ACS Catalysis* vol. 5, no. 11 (Nov. 2015). Publisher: American Chemical Society, pp. 6370–6385.

[110] Wei, Y., Cheng, Z., and Lin, J. "An overview on enhancing the stability of lead halide perovskite quantum dots and their applications in phosphor-converted LEDs". In: *Chemical Society Reviews* vol. 48, no. 1 (2019). Publisher: The Royal Society of Chemistry, pp. 310–350.

[111] Kang, K.-N. et al. "Co_3O_4 Exsolved Defective Layered Perovskite Oxide for Energy Storage Systems". In: *ACS Energy Letters* vol. 5, no. 12 (Dec. 2020). Publisher: American Chemical Society, pp. 3828–3836.

[112] Tang, C. et al. "Towards efficient use of noble metals via exsolution exemplified for CO oxidation". In: *Nanoscale* vol. 11, no. 36 (2019). Publisher: The Royal Society of Chemistry, pp. 16935–16944.

[113] Sengodan, S. et al. “Layered oxygen-deficient double perovskite as an efficient and stable anode for direct hydrocarbon solid oxide fuel cells”. In: *Nature Materials* vol. 14, no. 2 (Feb. 2015), pp. 205–209.

[114] Kim, S. et al. “Strategy for Enhancing Interfacial Effect of Bifunctional Electrocatalyst: Infiltration of Cobalt Nanooxide on Perovskite”. In: *Advanced Materials Interfaces* vol. 5, no. 12 (June 2018). Publisher: John Wiley & Sons, Ltd, p. 1800123.

[115] Cargnello M. et al. “Exceptional Activity for Methane Combustion over Modular Pd@CeO_2 Subunits on Functionalized Al_2O_3”. In: *Science* vol. 337, no. 6095 (Aug. 2012). Publisher: American Association for the Advancement of Science, pp. 713–717.

[116] Munnik, P., Jongh, P. E. de, and Jong, K. P. de. “Recent Developments in the Synthesis of Supported Catalysts”. In: *Chemical Reviews* vol. 115, no. 14 (July 2015). Publisher: American Chemical Society, pp. 6687–6718.

[117] Meille, V. “Review on methods to deposit catalysts on structured surfaces”. In: *Applied Catalysis A: General* vol. 315 (Nov. 2006), pp. 1–17.

[118] Tang, C. et al. “Trends and prospects of bimetallic exsolution”. In: *Chemistry–A European Journal* vol. 27, no. 22 (2021), pp. 6666–6675.

[119] Guerrero-Caballero, J. et al. “A Performant Dry Reforming Catalytic System Elaborated from the Reductive Decomposition of $BaNi_2V_2O_8$”. In: *ChemistrySelect* vol. 1, no. 18 (2016), pp. 5633–5637.

[120] Cao, P. et al. “Atomic-Scale Insights into Nickel Exsolution on $LaNiO_3$ Catalysts via In Situ Electron Microscopy”. In: *The Journal of Physical Chemistry C* vol. 126, no. 1 (2021), pp. 786–796.

[121] Kousi, K. et al. “Emergence and future of exsolved materials”. In: *Small* vol. 17, no. 21 (2021), p. 2006479.

[122] Liu, S. et al. “Producing ultrastable Ni-ZrO_2 nanoshell catalysts for dry reforming of methane by flame synthesis and Ni exsolution”. In: *Chem Catalysis* (2022).

[123] Padi, S. P. et al. “Coke-free methane dry reforming over nano-sized NiO-CeO_2 solid solution after exsolution”. In: *Catalysis Communications* vol. 138 (2020), p. 105951.

[124] Joo, S. et al. “The first observation of Ni nanoparticle exsolution from YSZ and its application for dry reforming of methane”. In: *Materials Reports: Energy* vol. 1, no. 2 (2021), p. 100021.

[125] Yang, Y., Li, J., and Sun, Y. “The metal/oxide heterointerface delivered by solid-based exsolution strategy: A Review”. In: *Chemical Engineering Journal* (2022), p. 135868.

[126] Kim, Y. H. et al. “Shape-shifting nanoparticles on a perovskite oxide for highly stable and active heterogeneous catalysis”. In: *Chemical Engineering Journal* vol. 441 (2022), p. 136025.

[127] Švarcová, S. et al. "Structural instability of cubic perovskite $Ba_xSr_{1-x}Co_{1-y}Fe_yO_{3-\delta}$". In: *Solid State Ionics* vol. 178, no. 35-36 (2008), pp. 1787–1791.

[128] Otto, S.-K. et al. "Exsolved nickel nanoparticles acting as oxygen storage reservoirs and active sites for redox CH_4 conversion". In: *ACS Applied Energy Materials* vol. 2, no. 10 (2019), pp. 7288–7298.

[129] Gao, Y. et al. "From material design to mechanism study: nanoscale Ni exsolution on a highly active A-site deficient anode material for solid oxide fuel cells". In: *Nano Energy* vol. 27 (2016), pp. 499–508.

[130] Hamada, I. et al. "A density functional theory study of self-regenerating catalysts $LaFe_{1-x}M_xO_{3-y}$ (M= Pd, Rh, Pt)". In: *Journal of the American Chemical Society* vol. 133, no. 46 (2011), pp. 18506–18509.

[131] Tsekouras, G., Neagu, D., and Irvine, J. T. "Step-change in high temperature steam electrolysis performance of perovskite oxide cathodes with exsolution of B-site dopants". In: *Energy & Environmental Science* vol. 6, no. 1 (2013), pp. 256–266.

[132] Oh, T.-S. et al. "Evidence and Model for Strain-Driven Release of Metal Nanocatalysts from Perovskites during Exsolution". In: *The Journal of Physical Chemistry Letters* vol. 6, no. 24 (Dec. 2015). Publisher: American Chemical Society, pp. 5106–5110.

[133] Neagu, D. et al. "In situ observation of nanoparticle exsolution from perovskite oxides: from atomic scale mechanistic insight to nanostructure tailoring". In: *ACS nano* vol. 13, no. 11 (2019), pp. 12996–13005.

[134] Kreibig, U. and Vollmer, M. *Optical Properties of Metal Clusters*. Springer Berlin Heidelberg, 2013.

[135] Peng, Z. and Yang, H. "Designer platinum nanoparticles: Control of shape, composition in alloy, nanostructure and electrocatalytic property". In: *Nano today* vol. 4, no. 2 (2009), pp. 143–164.

[136] Liu, F. et al. "Analysis of solid state phase transformation kinetics: models and recipes". In: *International materials reviews* vol. 52, no. 4 (2007), pp. 193–212.

[137] Han, H. et al. "Lattice strain-enhanced exsolution of nanoparticles in thin films". In: *Nature communications* vol. 10, no. 1 (2019), pp. 1–8.

[138] Katz, M. B. et al. "Reversible precipitation/dissolution of precious-metal clusters in perovskite-based catalyst materials: Bulk versus surface redispersion". In: *Journal of catalysis* vol. 293 (2012), pp. 145–148.

[139] Nishihata, Y. et al. "Self-regeneration of a Pd-perovskite catalyst for automotive emissions control". In: *Nature* vol. 418, no. 6894 (July 2002), pp. 164–167.

[140] Li, J. et al. "A Highly Efficient and Robust Perovskite Anode with Iron–Palladium Co-exsolutions for Intermediate-Temperature Solid-Oxide Fuel Cells". In: *ChemSusChem* vol. 11, no. 15 (2018), pp. 2593–2603.

[141] Sauvet, A. and Irvine, J. "Catalytic activity for steam methane reforming and physical characterisation of $La_{1-x}Sr_xCr_{1-y}Ni_yO_{3-\delta}$". In: *Solid State Ionics* vol. 167, no. 1-2 (2004), pp. 1–8.

[142] Arrivé, C. et al. "Exsolution of nickel nanoparticles at the surface of a conducting titanate as potential hydrogen electrode material for solid oxide electrochemical cells". In: *Journal of power sources* vol. 223 (2013), pp. 341–348.

[143] Gao, Y. et al. "Energetics of nanoparticle exsolution from perovskite oxides". In: *The journal of physical chemistry letters* vol. 9, no. 13 (2018), pp. 3772–3778.

[144] Liu, S., Liu, Q., and Luo, J.-L. "Highly stable and efficient catalyst with in situ exsolved Fe–Ni alloy nanospheres socketed on an oxygen deficient perovskite for direct CO_2 electrolysis". In: *Acs Catalysis* vol. 6, no. 9 (2016), pp. 6219–6228.

[145] Lan, R. et al. "A perovskite oxide with high conductivities in both air and reducing atmosphere for use as electrode for solid oxide fuel cells". In: *Scientific reports* vol. 6, no. 1 (2016), pp. 1–8.

[146] Neagu, D. and Irvine, J. T. "Structure and properties of $La_{0.4}Sr_{0.4}TiO_3$ ceramics for use as anode materials in solid oxide fuel cells". In: *Chemistry of Materials* vol. 22, no. 17 (2010), pp. 5042–5053.

[147] Hua, B. et al. "A coupling for success: controlled growth of Co/CoO_x nanoshoots on perovskite mesoporous nanofibres as high-performance trifunctional electrocatalysts in alkaline condition". In: *Nano Energy* vol. 32 (2017), pp. 247–254.

[148] Wang, Y. et al. "Enhanced overall water electrolysis on a bifunctional perovskite oxide through interfacial engineering". In: *Electrochimica Acta* vol. 318 (2019), pp. 120–129.

[149] Zhu, K. et al. "Perovskites decorated with oxygen vacancies and Fe–Ni alloy nanoparticles as high-efficiency electrocatalysts for the oxygen evolution reaction". In: *Journal of Materials Chemistry A* vol. 5, no. 37 (2017), pp. 19836–19845.

[150] Islam, Q. A., Majee, R., and Bhattacharyya, S. "Bimetallic nanoparticle decorated perovskite oxide for state-of-the-art trifunctional electrocatalysis". In: *Journal of Materials Chemistry A* vol. 7, no. 33 (2019), pp. 19453–19464.

[151] Zhang, Y.-Q. et al. "In situ grown cobalt phosphide (CoP) on perovskite nanofibers as an optimized trifunctional electrocatalyst for Zn–air batteries and overall water splitting". In: *Journal of Materials Chemistry A* vol. 7, no. 46 (2019), pp. 26607–26617.

[152] Bian, J. et al. "Oxygen deficient $LaMn_{0.75}Co_{0.25}O_{3-\delta}$ nanofibers as an efficient electrocatalyst for oxygen evolution reaction and zinc–air batteries". In: *Inorganic Chemistry* vol. 58, no. 12 (2019), pp. 8208–8214.

[153] Zhu, Y. et al. “Synergistically enhanced hydrogen evolution electrocatalysis by in situ exsolution of metallic nanoparticles on perovskites”. In: *Journal of Materials Chemistry A* vol. 6, no. 28 (2018), pp. 13582–13587.

[154] Li, Y. et al. “Efficient carbon dioxide electrolysis based on perovskite cathode enhanced with nickel nanocatalyst”. In: *Electrochimica Acta* vol. 153 (2015), pp. 325–333.

[155] Li, H. et al. “Chromate cathode decorated with in-situ growth of copper nanocatalyst for high temperature carbon dioxide electrolysis”. In: *International journal of hydrogen energy* vol. 39, no. 36 (2014), pp. 20888–20897.

[156] Zhu, T. et al. “Exsolution and electrochemistry in perovskite solid oxide fuel cell anodes: Role of stoichiometry in $Sr(Ti,Fe,Ni)O_3$”. In: *Journal of Power Sources* vol. 439 (2019), p. 227077.

[157] Kwon, O. et al. “Review on exsolution and its driving forces in perovskites”. In: *Journal of Physics: Energy* vol. 2, no. 3 (2020), p. 032001.

[158] Sengodan, S. et al. “Layered oxygen-deficient double perovskite as an efficient and stable anode for direct hydrocarbon solid oxide fuel cells”. In: *Nature materials* vol. 14, no. 2 (2015), pp. 205–209.

[159] Myung, J.-h. et al. “Switching on electrocatalytic activity in solid oxide cells”. In: *Nature* vol. 537, no. 7621 (2016), pp. 528–531.

[160] Kim, G. et al. “Rapid oxygen ion diffusion and surface exchange kinetics in $PrBaCo_2O_{5+x}$ with a perovskite related structure and ordered A cations”. In: *Journal of Materials Chemistry* vol. 17, no. 24 (2007), pp. 2500–2505.

[161] Kwon, O. et al. “Exsolution trends and co-segregation aspects of self-grown catalyst nanoparticles in perovskites”. In: *Nature communications* vol. 8, no. 1 (2017), pp. 1–7.

[162] Nenning, A. and Fleig, J. “Electrochemical XPS investigation of metal exsolution on SOFC electrodes: Controlling the electrode oxygen partial pressure in ultra-high-vacuum”. In: *Surface Science* vol. 680 (2019), pp. 43–51.

[163] Zhu, T. et al. “Ni-substituted $Sr(Ti,Fe)O_3$ SOFC anodes: achieving high performance via metal alloy nanoparticle exsolution”. In: *Joule* vol. 2, no. 3 (2018), pp. 478–496.

[164] Zubenko, D., Singh, S., and Rosen, B. A. “Exsolution of Re-alloy catalysts with enhanced stability for methane dry reforming”. In: *Applied Catalysis B: Environmental* vol. 209 (2017), pp. 711–719.

[165] Lv, H. et al. “In situ exsolved $FeNi_3$ nanoparticles on nickel doped $Sr_2Fe_{1.5}Mo_{0.5}O_{6-\delta}$ perovskite for efficient electrochemical CO_2 reduction reaction”. In: *Journal of Materials Chemistry A* vol. 7, no. 19 (2019), pp. 11967–11975.

[166] Kyriakou, V. et al. “Symmetrical exsolution of Rh nanoparticles in solid oxide cells for efficient syngas production from greenhouse gases”. In: *ACS Catalysis* vol. 10, no. 2 (2019), pp. 1278–1288.

[167] Gao, Y. et al. “In Situ exsolved Au nanoparticles from perovskite oxide for efficient epoxidation of styrene”. In: *Journal of Materials Chemistry A* vol. 9, no. 16 (2021), pp. 10374–10384.

[168] Syed, K. et al. “Bulk and surface exsolution produces a variety of Fe-rich and Fe-depleted ellipsoidal nanostructures in La 0.6 Sr 0.4 FeO 3 thin films”. In: *Nanoscale* vol. 14, no. 3 (2022), pp. 663–674.

[169] Magagnin, L., Maboudian, R., and Carraro, C. “Gold deposition by galvanic displacement on semiconductor surfaces: effect of substrate on adhesion”. In: *The Journal of Physical Chemistry B* vol. 106, no. 2 (2002), pp. 401–407.

[170] Papaderakis, A. et al. “Electrocatalysts prepared by galvanic replacement”. In: *Catalysts* vol. 7, no. 3 (2017), p. 80.

[171] Walsh, D. E., Milad, G., and Gudeczauskas, D. “Final finish: printed circuit boards”. In: *Metal Finishing* vol. 101, no. 1 (2003), pp. 25–26.

[172] Couble, E. C. et al. “Immersion, Non-electrolytic Tin/lead Plating Process”. In: *Circuit World* (1992).

[173] Milad, G. and Mayes, R. “Electroless nickel/immersion gold finishes for application to surface mount technology: A regenerative approach”. In: *Metal finishing* vol. 96, no. 1 (1998), pp. 42–46.

[174] Blair, A. “Silver plating”. In: *Metal Finishing* vol. 100 (2002), pp. 284–290.

[175] Davenport, W. G. et al. *Extractive metallurgy of copper*. Elsevier, 2002.

[176] Petala, M. et al. “Silver deposition on stainless steel container surfaces in contact with disinfectant silver aqueous solutions”. In: *Applied Surface Science* vol. 396 (2017), pp. 1067–1075.

[177] Brankovic, S. R. and Zangari, G. “Electrochemical surface processes and opportunities for material synthesis”. In: *Electrochemical Engineering across Scales: From Molecules to Processes* (2015), pp. 59–106.

[178] Dimitrov, N. “Recent advances in the growth of metals, alloys, and multilayers by surface limited redox replacement (SLRR) based approaches”. In: *Electrochimica acta* vol. 209 (2016), pp. 599–622.

[179] Herrero, E., Buller, L. J., and Abruña, H. D. “Underpotential deposition at single crystal surfaces of Au, Pt, Ag and other materials”. In: *Chemical Reviews* vol. 101, no. 7 (2001), pp. 1897–1930.

[180] Gregory, B. W., Suggs, D. W., and Stickney, J. L. “Conditions for the deposition of CdTe by electrochemical atomic layer epitaxy”. In: *Journal of the Electrochemical Society* vol. 138, no. 5 (1991), p. 1279.

[181] Gregory, B. W. and Stickney, J. L. “Electrochemical atomic layer epitaxy (ECALE)”. In: *Journal of electroanalytical chemistry and interfacial electrochemistry* vol. 300, no. 1-2 (1991), pp. 543–561.

[182] Villegas, I. and Stickney, J. L. “Preliminary studies of GaAs deposition on Au (100),(110), and (111) surfaces by electrochemical atomic layer epitaxy”. In: *Journal of the Electrochemical Society* vol. 139, no. 3 (1992), p. 686.

[183] Suggs, D. W. et al. “Formation of compound semiconductors by electrochemical atomic layer epitaxy”. In: *Journal of Vacuum Science & Technology A: Vacuum, Surfaces, and Films* vol. 10, no. 4 (1992), pp. 886–891.

[184] Xia, X. et al. “25th Anniversary Article: Galvanic replacement: a simple and versatile route to hollow nanostructures with tunable and well-controlled properties”. In: *Advanced Materials* vol. 25, no. 44 (2013), pp. 6313–6333.

[185] Zhao, M. and Crooks, R. M. “Intradendrimer exchange of metal nanoparticles”. In: *Chemistry of Materials* vol. 11, no. 11 (1999), pp. 3379–3385.

[186] Park, J.-I. and Cheon, J. “Synthesis of “solid solution” and “core-shell” type cobalt- platinum magnetic nanoparticles via transmetalation reactions”. In: *Journal of the American Chemical Society* vol. 123, no. 24 (2001), pp. 5743–5746.

[187] Shon, Y.-S. et al. “Monolayer-protected bimetal cluster synthesis by core metal galvanic exchange reaction”. In: *Langmuir* vol. 18, no. 10 (2002), pp. 3880–3885.

[188] Liu, B., Liao, S., and Liang, Z. “Core-shell structure: The best way to achieve low-Pt fuel cell electrocatalysts”. In: *Progress in Chemistry* vol. 23, no. 5 (2011), p. 852.

[189] Lai, X., Halpert, J. E., and Wang, D. “Recent advances in micro-/nano-structured hollow spheres for energy applications: From simple to complex systems”. In: *Energy & Environmental Science* vol. 5, no. 2 (2012), pp. 5604–5618.

[190] Adzic, R. R. et al. “Platinum monolayer fuel cell electrocatalysts”. In: *Topics in Catalysis* vol. 46, no. 3 (2007), pp. 249–262.

[191] Cappillino, P. J. et al. “Atomic-layer electroless deposition: A scalable approach to surface-modified metal powders”. In: *Langmuir* vol. 30, no. 16 (2014), pp. 4820–4829.

[192] Sasaki, K. et al. “Recent advances in platinum monolayer electrocatalysts for oxygen reduction reaction: Scale-up synthesis, structure and activity of Pt shells on Pd cores”. In: *Electrochimica Acta* vol. 55, no. 8 (2010), pp. 2645–2652.

[193] Khateeb, S. et al. “Fuel cell performance of palladium-platinum core-shell electrocatalysts synthesized in gram-scale batches”. In: *Journal of the Electrochemical Society* vol. 163, no. 7 (2016), F708.

[194] Zhu, S. et al. “The role of citric acid in perfecting platinum monolayer on palladium nanoparticles during the surface limited redox replacement reaction”. In: *Journal of The Electrochemical Society* vol. 163, no. 12 (2016), p. D3040.

[195] Tegou, A. et al. “Oxygen reduction at platinum-and gold-coated copper deposits on glassy carbon substrates”. In: *Journal of Electroanalytical Chemistry* vol. 608, no. 1 (2007), pp. 67–77.

[196] Tegou, A. et al. “Oxygen reduction at platinum-and gold-coated iron, cobalt, nickel and lead deposits on glassy carbon substrates”. In: *Journal of Electroanalytical Chemistry* vol. 623, no. 2 (2008), pp. 187–196.

[197] Podlovchenko, B. I. et al. “Effect of copper deposit morphology on the characteristics of a Pt (Cu)/C-catalyst obtained by galvanic displacement”. In: *Mendeleev Communications* vol. 22, no. 4 (2012), pp. 203–205.

[198] Geboes, B. et al. “Surface and electrochemical characterisation of a Pt-Cu/C nano-structured electrocatalyst, prepared by galvanic displacement”. In: *Applied Catalysis B: Environmental* vol. 150 (2014), pp. 249–256.

[199] Mintsouli, I. et al. “Pt–Ni carbon-supported catalysts for methanol oxidation prepared by Ni electroless deposition and its galvanic replacement by Pt”. In: *Journal of solid state electrochemistry* vol. 17, no. 2 (2013), pp. 435–443.

[200] Mintsouli, I. et al. “Pt-Cu electrocatalysts for methanol oxidation prepared by partial galvanic replacement of Cu/carbon powder precursors”. In: *Applied Catalysis B: Environmental* vol. 136 (2013), pp. 160–167.

[201] Georgieva, J. et al. “Methanol oxidation and photo-oxidation at Pt/WO3 electrocatalysts on graphite substrates”. In: *Journal of Electroanalytical Chemistry* vol. 727 (2014), pp. 135–140.

[202] Georgieva, J. et al. “Pt (Ni) electrocatalysts for methanol oxidation prepared by galvanic replacement on TiO2 and TiO2–C powder supports”. In: *Journal of Electroanalytical Chemistry* vol. 754 (2015), pp. 65–74.

[203] Mintsouli, I. et al. “Methanol oxidation at platinized copper particles prepared by galvanic replacement”. In: *Journal of Electrochemical Science and Engineering* vol. 6, no. 1 (2016), pp. 17–28.

[204] Teng, X., Du, W., and Wang, Q. “Synthesis of Pt–Containing Metals Alloy and Hybrid Nanowires and Investigation of Electronic Structure Using Synchrotron-Based X-Ray Absorption Techniques”. In: *Nanowires-Fundamental Research*. IntechOpen, 2011.

[205] Cobley, C. M. and Xia, Y. “Engineering the properties of metal nanostructures via galvanic replacement reactions”. In: *Materials Science and Engineering: R: Reports* vol. 70, no. 3-6 (2010), pp. 44–62.

[206] Vanysek, P. *Table of Standard Chemical Potentials: Learning Commons.* 2022.

[207] Milazzo, G., Caroli, S., and Braun, R. D. "Tables of standard electrode potentials". In: *Journal of The Electrochemical Society* vol. 125, no. 6 (1978), p. 261C.

[208] Bard, A., Parsons, R., and Jordan, J. "Standard Potentials in Aqueous Solution, Marcel Dekker, Inc., New York 1985." In: ().

[209] Bratsch, S. G. "Standard electrode potentials and temperature coefficients in water at 298.15 K". In: *Journal of Physical and Chemical Reference Data* vol. 18, no. 1 (1989), pp. 1–21.

[210] Beverskog, B. and Puigdomenech, I. "Revised Pourbaix diagrams for nickel at 25 - 300 °C". In: *Corrosion Science* vol. 39, no. 5 (1997), pp. 969–980.

[211] Dimitrov, N., Vasilic, R., and Vasiljevic, N. "A kinetic model for redox replacement of UPD layers". In: *Electrochemical and solid-state letters* vol. 10, no. 7 (2007), p. D79.

[212] Gokcen, D., Bae, S.-E., and Brankovic, S. R. "Kinetics of metal deposition via surface-limited redox replacement reaction". In: *ECS Transactions* vol. 35, no. 21 (2011), p. 11.

[213] Gokcen, D., Bae, S.-E., and Brankovic, S. R. "Reaction kinetics of metal deposition via surface limited red-ox replacement of underpotentially deposited metal monolayers". In: *Electrochimica Acta* vol. 56, no. 16 (2011), pp. 5545–5553.

[214] Bulut, E. et al. "Reaction kinetics of metal deposition via surface limited redox replacement of underpotentially deposited monolayer studied by surface reflectivity and open circuit potential measurements". In: *Journal of The Electrochemical Society* vol. 164, no. 4 (2017), p. D159.

[215] Mkwizu, T. S. and Cukrowski, I. "Physico–chemical Modelling of Adlayer Phase Formation via Surface–limited Reactions of Copper in Relation to Sequential Electrodeposition of Multilayered Platinum on Crystalline Gold". In: *Electrochimica Acta* vol. 147 (2014), pp. 432–441.

[216] Alrikabi, N. "Renewable energy types". In: *Journal of Clean Energy Technologies* vol. 2, no. 1 (2014), pp. 61–64.

[217] Wenderich, K. and Mul, G. "Methods, mechanism, and applications of photodeposition in photocatalysis: a review". In: *Chemical reviews* vol. 116, no. 23 (2016). Publisher: ACS Publications, pp. 14587–14619.

[218] Zeng, K. and Zhang, D. "Recent progress in alkaline water electrolysis for hydrogen production and applications". In: *Progress in Energy and Combustion Science* vol. 36, no. 3 (June 2010), pp. 307–326.

[219] Steinfeld, A. "Solar hydrogen production via a two-step water-splitting thermochemical cycle based on Zn/ZnO redox reactions". In: *International Journal of Hydrogen Energy* vol. 27, no. 6 (June 2002), pp. 611–619.

[220] Momeni, M. M. and Ghayeb, Y. “Fabrication, characterization and photoelectrochemical behavior of Fe – TiO_2 nanotubes composite photoanodes for solar water splitting”. In: *Journal of Electroanalytical Chemistry* vol. 751 (Aug. 2015), pp. 43–48.

[221] Turn, S. et al. “An experimental investigation of hydrogen production from biomass gasification”. In: *International Journal of Hydrogen Energy* vol. 23, no. 8 (Aug. 1998), pp. 641–648.

[222] Phoon, B. L. et al. “Recent developments of strontium titanate for photocatalytic water splitting application”. In: *A Special Issue on Advanced Hydrogen Production Technologies* vol. 44, no. 28 (May 2019), pp. 14316–14340.

[223] Fujishima, A. and Honda, K. “Electrochemical Photolysis of Water at a Semiconductor Electrode”. In: *Nature* vol. 238, no. 5358 (July 1972), pp. 37–38.

[224] Jacobsson, T. J. et al. “A monolithic device for solar water splitting based on series interconnected thin film absorbers reaching over 10% solar-to-hydrogen efficiency”. In: *Energy & Environmental Science* vol. 6, no. 12 (2013), pp. 3676–3683.

[225] Agency, I. E. *Hydrogen Supply*. 2022. URL: %5Curl%7Bhttps://www.iea.org/reports/hydrogen-supply%7D (visited on 10/12/2012).

[226] Agency, I. E. *Global Hydrogen Review 2022*. Paris, 2022.

[227] Abe, R. “Recent progress on photocatalytic and photoelectrochemical water splitting under visible light irradiation”. In: *Journal of Photochemistry and Photobiology C: Photochemistry Reviews* vol. 11, no. 4 (2010). Publisher: Elsevier, pp. 179–209.

[228] Kondarides, D. I. et al. “Hydrogen production by photo-induced reforming of biomass components and derivatives at ambient conditions”. In: *Catalysis Letters* vol. 122, no. 1 (2008). Publisher: Springer, pp. 26–32.

[229] Kraeutler, B. and Bard, A. J. “Heterogeneous photocatalytic preparation of supported catalysts. Photodeposition of platinum on titanium dioxide powder and other substrates”. In: *Journal of the American Chemical Society* vol. 100, no. 13 (June 1978). Publisher: American Chemical Society, pp. 4317–4318.

[230] Schrauzer, G. and Guth, T. “Photolysis of water and photoreduction of nitrogen on titanium dioxide”. In: *Journal of the American Chemical Society* vol. 99, no. 22 (2002). Publisher: ACS Publications, pp. 7189–7193.

[231] Reber, J. F. and Meier, K. “Photochemical production of hydrogen with zinc sulfide suspensions”. In: *The Journal of Physical Chemistry* vol. 88, no. 24 (1984), pp. 5903–5913.

[232] Meda, L. and Abbondanza, L. “Materials for photo-electrochemical water splitting”. In: *Reviews in Advanced Sciences and Engineering* vol. 2, no. 3 (2013), pp. 200–207.

[233] Liao, C.-H., Huang, C.-W., and Wu, J. C. “Hydrogen production from semiconductor-based photocatalysis via water splitting”. In: *Catalysts* vol. 2, no. 4 (2012), pp. 490–516.

[234] Jiang, D. et al. “Photoelectrochemical behaviour of methanol oxidation at nanoporous TiO_2 film electrodes”. In: *Journal of Photochemistry and Photobiology A: Chemistry* vol. 144, no. 2-3 (2001), pp. 197–204.

[235] Zhukovskii, Y. F. et al. “First principle evaluation of photocatalytic suitability for TiO_2-based nanotubes”. In: *Semiconductor Photocatalysis-Materials, Mechanisms and Applications*. IntechOpen, 2016.

[236] Ismail, A. A. and Bahnemann, D. W. “Photochemical splitting of water for hydrogen production by photocatalysis: A review”. In: *Solar Energy Materials and Solar Cells* vol. 128 (2014), pp. 85–101.

[237] Landi Jr, S. et al. “Evaluation of band gap energy of TiO_2 precipitated from titanium sulphate”. In: *Physica B: Condensed Matter* (2022), p. 414008.

[238] Joshi, G. et al. “Band gap determination of Ni-Zn ferrites”. In: *Bulletin of Materials Science* vol. 26, no. 4 (2003), pp. 387–389.

[239] Babu, V. J. et al. “Review of one-dimensional and two-dimensional nanostructured materials for hydrogen generation”. In: *Physical Chemistry Chemical Physics* vol. 17, no. 5 (2015), pp. 2960–2986.

[240] Simon, S. H. *The Oxford solid state basics*. OUP Oxford, 2013.

[241] Ng, K. H. et al. “Photocatalytic water splitting for solving energy crisis: Myth, Fact or Busted?” In: *Chemical Engineering Journal* vol. 417 (2021), p. 128847.

[242] Liu, B. et al. “Thermodynamic and kinetic analysis of heterogeneous photocatalysis for semiconductor systems”. In: *Physical Chemistry Chemical Physics* vol. 16, no. 19 (2014), pp. 8751–8760.

[243] Salvador, P. “Semiconductors’ photoelectrochemistry: a kinetic and thermodynamic analysis in the light of equilibrium and nonequilibrium models”. In: *The Journal of Physical Chemistry B* vol. 105, no. 26 (2001), pp. 6128–6141.

[244] Grätzel, M. “Photoelectrochemical cells”. In: *Nature* vol. 414, no. 6861 (Nov. 2001), pp. 338–344.

[245] Wu, N. “Plasmonic metal–semiconductor photocatalysts and photoelectrochemical cells: a review”. En. In: *Nanoscale* vol. 10, no. 6 (Feb. 2018). Publisher: The Royal Society of Chemistry, pp. 2679–2696.

[246] Walter, M. G. et al. “Solar Water Splitting Cells”. In: *Chemical Reviews* vol. 110, no. 11 (Nov. 2010). Publisher: American Chemical Society, pp. 6446–6473.

[247] Hara, S. et al. “Hydrogen and oxygen evolution photocatalysts synthesized from strontium titanate by controlled doping and their performance in two-step overall water splitting under visible light”. In: *The Journal of Physical Chemistry C* vol. 116, no. 33 (2012), pp. 17458–17463.

[248] Foerster, B. et al. “Interfacial States Cause Equal Decay of Plasmons and Hot Electrons at Gold–Metal Oxide Interfaces”. In: *Nano Letters* vol. 20, no. 5 (May 2020). Number: 5 Publisher: American Chemical Society, pp. 3338–3343.

[249] Mulvaney, P. “Surface Plasmon Spectroscopy of Nanosized Metal Particles”. In: *Langmuir* vol. 12, no. 3 (Jan. 1996). Publisher: American Chemical Society, pp. 788–800.

[250] Mie, G. “Beiträge zur Optik trüber Medien, speziell kolloidaler Metallösungen”. In: *Annalen der Physik* vol. 330, no. 3 (Jan. 1908). Publisher: John Wiley & Sons, Ltd, pp. 377–445.

[251] Savage, G. *Glass and Glassware*. Octopus Books, 1973.

[252] Faraday, M. “X. The Bakerian Lecture. —Experimental relations of gold (and other metals) to light”. In: *Philosophical Transactions of the Royal Society of London* vol. 147 (Jan. 1857). Publisher: Royal Society, pp. 145–181.

[253] Scott, A. B., Smith, W. A., and Thompson, M. A. “Alkali Halides Colored by Colloidal Metal”. In: *The Journal of Physical Chemistry* vol. 57, no. 8 (Aug. 1953). Publisher: American Chemical Society, pp. 757–761.

[254] Doremus, R. H. “Optical Properties of Small Silver Particles”. In: *The Journal of Chemical Physics* vol. 42, no. 1 (Jan. 1965). Publisher: American Institute of Physics, pp. 414–417.

[255] Doyle, W. T. “Absorption of Light by Colloids in Alkali Halide Crystals”. In: *Physical Review* vol. 111, no. 4 (Aug. 1958). Publisher: American Physical Society, pp. 1067–1072.

[256] Römer, H. and Fragstein, C. v. “Bestimmung des Absorptionskoeffizienten und des Brechungsquotienten von kolloidalem Gold”. In: *Zeitschrift für Physik* vol. 163, no. 1 (Feb. 1961), pp. 27–43.

[257] Perenboom, J., Wyder, P., and Meier, F. “Electronic properties of small metallic particles”. In: *Physics Reports* vol. 78, no. 2 (Nov. 1981), pp. 173–292.

[258] Papavassiliou, G. “Optical properties of small inorganic and organic metal particles”. In: *Progress in Solid State Chemistry* vol. 12, no. 3 (Jan. 1979), pp. 185–271.

[259] Kreibig, U. “Electronic properties of small silver particles: the optical constants and their temperature dependence”. In: *Journal of Physics F: Metal Physics* vol. 4, no. 7 (July 1974). Publisher: IOP Publishing, pp. 999–1014.

[260] Fragstein, C. von and Schoenes, F. J. "Absorptionskoeffizient und Brechungsindex feinster Goldkugeln im nahen Ultrarot". In: *Zeitschrift für Physik* vol. 198, no. 5 (Oct. 1967), pp. 477–493.

[261] Kreibig, U. "Lattice defects in small metallic particles and their influence on size effects". In: *Zeitschrift für Physik B Condensed Matter* vol. 31, no. 1 (Mar. 1978), pp. 39–47.

[262] Yanase, A. and Komiyama, H. "In situ observation of oxidation and reduction of small supported copper particles using optical absorption and X-ray diffraction". In: *Surface Science* vol. 248, no. 1 (May 1991), pp. 11–19.

[263] Kreibig, U. and Genzel, L. "Optical absorption of small metallic particles". In: *Surface Science* vol. 156 (June 1985), pp. 678–700.

[264] Ruthemann, G. "Elektronenbremsung an Röntgenniveaus". In: *Die Naturwissenschaften* vol. 30, no. 9 (Feb. 1942), pp. 145–145.

[265] Pines, D. and Bohm, D. "A Collective Description of Electron Interactions: II. Collective vs Individual Particle Aspects of the Interactions". In: *Physical Review* vol. 85, no. 2 (Jan. 1952). Publisher: American Physical Society, pp. 338–353.

[266] Pines, D. "Collective Energy Losses in Solids". In: *Reviews of Modern Physics* vol. 28, no. 3 (July 1956). Publisher: American Physical Society, pp. 184–198.

[267] Ritchie, R. H. "Plasma Losses by Fast Electrons in Thin Films". In: *Physical Review* vol. 106, no. 5 (June 1957). Publisher: American Physical Society, pp. 874–881.

[268] Powell, C. J. and Swan, J. B. "Origin of the Characteristic Electron Energy Losses in Aluminum". In: *Physical Review* vol. 115, no. 4 (Aug. 1959). Publisher: American Physical Society, pp. 869–875.

[269] Stern, E. A. and Ferrell, R. A. "Surface Plasma Oscillations of a Degenerate Electron Gas". In: *Physical Review* vol. 120, no. 1 (Oct. 1960). Publisher: American Physical Society, pp. 130–136.

[270] Inglesfield, J. E. and Wikborg, E. "The Van der Waals interaction between metals". In: *Journal of Physics F: Metal Physics* vol. 5, no. 8 (Aug. 1975). Publisher: IOP Publishing, pp. 1475–1489.

[271] Zaremba, E. and Kohn, W. "Van der Waals interaction between an atom and a solid surface". In: *Physical Review B* vol. 13, no. 6 (Mar. 1976). Publisher: American Physical Society, pp. 2270–2285.

[272] Sernelius, B. E. "Effects of spatial dispersion on electromagnetic surface modes and on modes associated with a gap between two half spaces". In: *Physical Review B* vol. 71, no. 23 (June 2005). Publisher: American Physical Society, p. 235114.

[273] Feibelman, P. J. "Inclusion of dynamics in the ion-metal surface interaction. I". In: *Surface Science* vol. 27, no. 3 (Oct. 1971), pp. 438–450.

[274] Ritchie, R. “Surface plasmons and the image force in metals”. In: *Physics Letters A* vol. 38, no. 3 (Jan. 1972), pp. 189–190.

[275] Ray, R. and Mahan, G. “Dynamical image charge theory”. In: *Physics Letters A* vol. 42, no. 4 (Dec. 1972), pp. 301–302.

[276] Šunjic, M., Toulouse, G., and Lucas, A. “Dynamical corrections to the image potential”. In: *Solid State Communications* vol. 11, no. 12 (Dec. 1972), pp. 1629–1631.

[277] Gadzuk, J. W. and Metiu, H. “Theory of electron-hole pair excitations in unimolecular processes at metal surfaces. I. X-ray edge effects”. In: *Physical Review B* vol. 22, no. 6 (Sept. 1980). Publisher: American Physical Society, pp. 2603–2613.

[278] Schmit, J. and Lucas, A. “Plasmon theory of the surface energy of metals — II. Transition metals”. In: *Solid State Communications* vol. 11, no. 3 (Aug. 1972), pp. 419–422.

[279] Schmit, J. and Lucas, A. “Plasmon theory of the surface energy of metals — I”. In: *Solid State Communications* vol. 11, no. 3 (Aug. 1972). Number: 3, pp. 415–418.

[280] Wikborg, E. and Inglesfield, J. E. “Collective Modes and Ground State Energy of the Semi-infinite Electron Gas”. In: *Physica Scripta* vol. 15, no. 1 (Jan. 1977). Publisher: IOP Publishing, pp. 37–55.

[281] Lang, N. and Sham, L. “Exchange-correlation in inhomogeneous systems—a comment on the surface energy problem”. In: *Solid State Communications* vol. 17, no. 5 (Sept. 1975), pp. 581–584.

[282] Langreth, D. C. and Perdew, J. P. “Exchange-correlation energy of a metallic surface: Wave-vector analysis”. In: *Physical Review B* vol. 15, no. 6 (Mar. 1977). Number: 6 Publisher: American Physical Society, pp. 2884–2901.

[283] Chabal, Y. J. and Sievers, A. J. “High-Resolution Infrared Study of Hydrogen (1×1) on Tungsten (100)”. In: *Physical Review Letters* vol. 44, no. 14 (Apr. 1980). Number: 14 Publisher: American Physical Society, pp. 944–947.

[284] Persson, B. N. J. and Ryberg, R. “Vibrational Phase Relaxation at Surfaces: CO on Ni(111)”. In: *Physical Review Letters* vol. 54, no. 19 (May 1985). Number: 19 Publisher: American Physical Society, pp. 2119–2122.

[285] Echenique, P. M. and Pendry, J. B. “Absorption profile at surfaces”. In: *Journal of Physics C: Solid State Physics* vol. 8, no. 18 (Sept. 1975). Number: 18 Publisher: IOP Publishing, pp. 2936–2942.

[286] Echenique, P. M. et al. “Semiclassical image potential at a solid surface”. In: *Physical Review B* vol. 23, no. 12 (June 1981). Number: 12 Publisher: American Physical Society, pp. 6486–6493.

[287] Ueba, H. “Theory of core-hole-decay dynamics of adsorbates on metal surfaces: Role of the $2\pi^*$ level of a chemisorbed CO molecule”. In: *Physical Review B* vol. 45, no. 7 (Feb. 1992). Number: 7 Publisher: American Physical Society, pp. 3755–3768.

[288] Knoll, W. “Interfaces and Thin Films as seen by Bound Electromagnetic Waves”. In: *Annual Review of Physical Chemistry* vol. 49, no. 1 (Oct. 1998). Number: 1 Publisher: Annual Reviews, pp. 569–638.

[289] Herminghaus, S. et al. “Hydrogen and helium films as model systems of wetting”. In: *Annalen der Physik* vol. 509, no. 6 (Jan. 1997). Number: 6 Publisher: John Wiley & Sons, Ltd, pp. 425–447.

[290] Malmqvist, M. “Biospecific interaction analysis using biosensor technology”. In: *Nature* vol. 361, no. 6408 (Jan. 1993). Number: 6408, pp. 186–187.

[291] Braguglia, C. “Biosensors: an outline of general principles and application”. In: *Chemical and biochemical engineering quarterly* vol. 12, no. 4 (1998). Number: 4, pp. 183–190.

[292] Chien, F.-C. and Chen, S.-J. “A sensitivity comparison of optical biosensors based on four different surface plasmon resonance modes”. In: *Optical Biosensing* vol. 20, no. 3 (Oct. 2004). Number: 3, pp. 633–642.

[293] Berndt, R., Gimzewski, J. K., and Johansson, P. “Inelastic tunneling excitation of tip-induced plasmon modes on noble-metal surfaces”. In: *Physical Review Letters* vol. 67, no. 27 (Dec. 1991). Number: 27 Publisher: American Physical Society, pp. 3796–3799.

[294] Shea, M. J. and Compton, R. N. “Surface-plasmon ejection of Ag^+ ions from laser irradiation of a roughened silver surface”. In: *Physical Review B* vol. 47, no. 15 (Apr. 1993). Number: 15 Publisher: American Physical Society, pp. 9967–9970.

[295] Jin Rongchao et al. “Photoinduced Conversion of Silver Nanospheres to Nanoprisms”. In: *Science* vol. 294, no. 5548 (Nov. 2001). Number: 5548 Publisher: American Association for the Advancement of Science, pp. 1901–1903.

[296] Jin, R. et al. “Controlling anisotropic nanoparticle growth through plasmon excitation”. In: *Nature* vol. 425, no. 6957 (Oct. 2003). Number: 6957, pp. 487–490.

[297] Rothenhäusler, B. and Knoll, W. “Surface–plasmon microscopy”. In: *Nature* vol. 332, no. 6165 (Apr. 1988). Number: 6165, pp. 615–617.

[298] Flätgen Georg et al. “Two-Dimensional Imaging of Potential Waves in Electrochemical Systems by Surface Plasmon Microscopy”. In: *Science* vol. 269, no. 5224 (Aug. 1995). Number: 5224 Publisher: American Association for the Advancement of Science, pp. 668–671.

[299] Gordon, J. and Ernst, S. “Surface plasmons as a probe of the electrochemical interface”. In: *Surface Science* vol. 101, no. 1 (Dec. 1980). Number: 1, pp. 499–506.

[300] Liedberg, B., Nylander, C., and Lunström, I. “Surface plasmon resonance for gas detection and biosensing”. In: *Sensors and Actuators* vol. 4 (Jan. 1983), pp. 299–304.

[301] Schuster, S. C. et al. “Assembly and function of a quaternary signal transduction complex monitored by surface plasmon resonance”. In: *Nature* vol. 365, no. 6444 (Sept. 1993). Number: 6444, pp. 343–347.

[302] Schuck, P. “Reliable determination of binding affinity and kinetics using surface plasmon resonance biosensors”. In: *Current Opinion in Biotechnology* vol. 8, no. 4 (Aug. 1997). Number: 4, pp. 498–502.

[303] Homola, J., Yee, S. S., and Gauglitz, G. “Surface plasmon resonance sensors: review”. In: *Sensors and Actuators B: Chemical* vol. 54, no. 1 (Jan. 1999). Number: 1, pp. 3–15.

[304] Mendelsohn Andrew R. and Brent Roger. “Protein Interaction Methods-Toward an Endgame”. In: *Science* vol. 284, no. 5422 (June 1999). Number: 5422 Publisher: American Association for the Advancement of Science, pp. 1948–1950.

[305] Green, R. J. et al. “Surface plasmon resonance analysis of dynamic biological interactions with biomaterials”. In: *Biomaterials* vol. 21, no. 18 (Sept. 2000). Number: 18, pp. 1823–1835.

[306] Pitarke, J. M. et al. “Theory of surface plasmons and surface-plasmon polaritons”. In: *Reports on Progress in Physics* vol. 70, no. 1 (Dec. 2006). Publisher: IOP Publishing, pp. 1–87.

[307] Greiner, W. *Klassische Elektrodynamik*. Europa-Nr. Deutsch, 2008.

[308] Ashcroft, N. and Mermin, N. *Solid State Physics*. Cengage., 2020.

[309] Mie, G. *Contributions to the optics of turbid media, particularly of colloidal metal solutions*. Contributions to the optics of turbid media, particularly of colloidal metal solutions Transl. into English from Ann. Phys. (Leipzig), v. 25, no. 3, 1908 p 377-445. Feb. 1976.

[310] Kreibig, U. and Zacharias, P. “Surface plasma resonances in small spherical silver and gold particles”. In: *Zeitschrift für Physik A Hadrons and nuclei* vol. 231, no. 2 (1970), pp. 128–143.

[311] Kreibig, U., Schmitz, B., and Breuer, H. “Separation of plasmon-polariton modes of small metal particles”. In: *Physical Review B* vol. 36, no. 9 (1987), p. 5027.

[312] Sinzig, J. et al. “Binary clusters: homogeneous alloys and nucleus-shell structures”. In: *Zeitschrift für Physik D Atoms, Molecules and Clusters* vol. 26, no. 1 (1993), pp. 242–245.

[313] Sinzig, J. and Quinten, M. “Scattering and absorption by spherical multilayer particles”. In: *Applied Physics A* vol. 58, no. 2 (1994), pp. 157–162.

[314] Zhao, J. et al. “Localized surface plasmon resonance for enhanced electrocatalysis”. In: *Chemical Society Reviews* (2021).

[315] Slistan-Grijalva, A. et al. “Classical theoretical characterization of the surface plasmon absorption band for silver spherical nanoparticles suspended in water and ethylene glycol”. In: *Physica E: Low-dimensional Systems and Nanostructures* vol. 27, no. 1-2 (2005), pp. 104–112.

[316] Li, S. et al. “Recent advances in plasmonic nanostructures for enhanced photocatalysis and electrocatalysis”. In: *Advanced Materials* vol. 33, no. 6 (2021), p. 2000086.

[317] Kim, S. et al. “Nonnoble-Metal-Based Plasmonic Nanomaterials: Recent Advances and Future Perspectives”. In: *Advanced Materials* vol. 30, no. 42 (2018), p. 1704528.

[318] Liz-Marzán, L. M. “Tailoring surface plasmons through the morphology and assembly of metal nanoparticles”. In: *Langmuir* vol. 22, no. 1 (2006), pp. 32–41.

[319] Zhang, Y. et al. “Surface-plasmon-driven hot electron photochemistry”. In: *Chemical reviews* vol. 118, no. 6 (2017), pp. 2927–2954.

[320] Gellé, A. and Moores, A. “Plasmonic nanoparticles: Photocatalysts with a bright future”. In: *Current Opinion in Green and Sustainable Chemistry* vol. 15 (2019). Nanocatalysis Special Issue on the Green and Sustainable Chemistry Conference, Berlin, May 2018, pp. 60–66.

[321] Dongare, P. D. et al. “A 3D Plasmonic Antenna-Reactor for Nanoscale Thermal Hotspots and Gradients”. In: *ACS nano* vol. 15, no. 5 (2021), pp. 8761–8769.

[322] Nilsson, S. et al. “Probing the role of grain boundaries in single Cu nanoparticle oxidation by in situ plasmonic scattering”. In: *Physical Review Materials* vol. 6, no. 4 (2022), p. 045201.

[323] Yamada, K., Miyajima, K., and Mafuné, F. “Thermionic emission of electrons from gold nanoparticles by nanosecond pulse-laser excitation of interband”. In: *The Journal of Physical Chemistry C* vol. 111, no. 30 (2007), pp. 11246–11251.

[324] Atay, T., Song, J.-H., and Nurmikko, A. V. “Strongly interacting plasmon nanoparticle pairs: from dipole- dipole interaction to conductively coupled regime”. In: *Nano letters* vol. 4, no. 9 (2004), pp. 1627–1631.

[325] Myroshnychenko, V. et al. “Modelling the optical response of gold nanoparticles”. In: *Chemical Society Reviews* vol. 37, no. 9 (2008), pp. 1792–1805.

[326] Melikyan, A. and Minassian, H. “On surface plasmon damping in metallic nanoparticles”. In: *Applied Physics B* vol. 78, no. 3 (2004), pp. 453–455.

[327] Heilweil, E. and Hochstrasser, R. “Nonlinear spectroscopy and picosecond transient grating study of colloidal gold”. In: *The Journal of chemical physics* vol. 82, no. 11 (1985), pp. 4762–4770.

[328] Klar, T. et al. “Surface-plasmon resonances in single metallic nanoparticles”. In: *Physical Review Letters* vol. 80, no. 19 (1998), p. 4249.

[329] Munechika, K. et al. “Plasmon line widths of single silver nanoprisms as a function of particle size and plasmon peak position”. In: *The Journal of Physical Chemistry C* vol. 111, no. 51 (2007), pp. 18906–18911.

[330] Sönnichsen, C. et al. “Drastic reduction of plasmon damping in gold nanorods”. In: *Physical review letters* vol. 88, no. 7 (2002), p. 077402.

[331] Jang, Y. H. et al. “Plasmonic solar cells: from rational design to mechanism overview”. In: *Chemical reviews* vol. 116, no. 24 (2016), pp. 14982–15034.

[332] Valenti, M. et al. “Plasmonic nanoparticle-semiconductor composites for efficient solar water splitting”. In: *Journal of Materials Chemistry A* vol. 4, no. 46 (2016), pp. 17891–17912.

[333] Li, X., Xiao, D., and Zhang, Z. “Landau damping of quantum plasmons in metal nanostructures”. In: *New Journal of Physics* vol. 15, no. 2 (2013), p. 023011.

[334] Eustis, S. and El-Sayed, M. A. “Why gold nanoparticles are more precious than pretty gold: noble metal surface plasmon resonance and its enhancement of the radiative and nonradiative properties of nanocrystals of different shapes”. In: *Chemical society reviews* vol. 35, no. 3 (2006), pp. 209–217.

[335] Ferry, V. E. et al. “Light trapping in ultrathin plasmonic solar cells”. In: *Optics express* vol. 18, no. 102 (2010), A237–A245.

[336] Mokkapati, S. et al. “Resonant nano-antennas for light trapping in plasmonic solar cells”. In: *Journal of Physics D: Applied Physics* vol. 44, no. 18 (2011), p. 185101.

[337] Lee, Y.-Y. et al. “Light-trapping performance of silicon thin-film plasmonics solar cells based on indium nanoparticles and various TiO2 space layer thicknesses”. In: *Japanese Journal of Applied Physics* vol. 53, no. 6S (2014), 06JE11.

[338] Morawiec, S. et al. “Broadband photocurrent enhancement in a-Si: H solar cells with plasmonic back reflectors”. In: *Optics express* vol. 22, no. 104 (2014), A1059–A1070.

[339] Tan, H. et al. “Plasmonic light trapping in thin-film silicon solar cells with improved self-assembled silver nanoparticles”. In: *Nano letters* vol. 12, no. 8 (2012), pp. 4070–4076.

[340] Linic, S., Christopher, P., and Ingram, D. B. “Plasmonic-metal nanostructures for efficient conversion of solar to chemical energy”. In: *Nature materials* vol. 10, no. 12 (2011), pp. 911–921.

[341] Hutter, E. and Fendler, J. H. “Exploitation of localized surface plasmon resonance”. In: *Advanced materials* vol. 16, no. 19 (2004), pp. 1685–1706.

[342] Chen, H. et al. “Gold nanorods and their plasmonic properties”. In: *Chemical Society Reviews* vol. 42, no. 7 (2013), pp. 2679–2724.

[343] Sohn, K. et al. “Construction of evolutionary tree for morphological engineering of nanoparticles”. In: *ACS nano* vol. 3, no. 8 (2009), pp. 2191–2198.

[344] Barman, T. et al. “Plasmonic hot hole generation by interband transition in gold-polyaniline”. In: *Scientific reports* vol. 5, no. 1 (2015), pp. 1–5.

[345] Hoa, X. D., Kirk, A., and Tabrizian, M. “Towards integrated and sensitive surface plasmon resonance biosensors: A review of recent progress”. In: *Biosensors and bioelectronics* vol. 23, no. 2 (2007), pp. 151–160.

[346] Callahan, D. M., Munday, J. N., and Atwater, H. A. “Solar cell light trapping beyond the ray optic limit”. In: *Nano letters* vol. 12, no. 1 (2012), pp. 214–218.

[347] Erwin, W. R. et al. “Light trapping in mesoporous solar cells with plasmonic nanostructures”. In: *Energy & Environmental Science* vol. 9, no. 5 (2016), pp. 1577–1601.

[348] Atwater, H. A. and Polman, A. “Plasmonics for improved photovoltaic devices”. In: *Materials for sustainable energy: a collection of peer-reviewed research and review articles from Nature Publishing Group* (2011), pp. 1–11.

[349] Zhang, L., Herrmann, L. O., and Baumberg, J. J. “Size dependent plasmonic effect on BiVO4 photoanodes for solar water splitting”. In: *Scientific reports* vol. 5, no. 1 (2015), pp. 1–12.

[350] Cushing, S. K. et al. “Photocatalytic activity enhanced by plasmonic resonant energy transfer from metal to semiconductor”. In: *Journal of the American Chemical Society* vol. 134, no. 36 (2012), pp. 15033–15041.

[351] Abouelela, M. M., Kawamura, G., and Matsuda, A. “A review on plasmonic nanoparticle-semiconductor photocatalysts for water splitting”. In: *Journal of Cleaner Production* vol. 294 (2021), p. 126200.

[352] Ma, X.-C. et al. “Energy transfer in plasmonic photocatalytic composites”. In: *Light: Science & Applications* vol. 5, no. 2 (2016), e16017–e16017.

[353] Verma, A. et al. “Enhanced photoelectrochemical response of plasmonic Au embedded BiVO 4/Fe 2 O 3 heterojunction”. In: *Physical Chemistry Chemical Physics* vol. 19, no. 23 (2017), pp. 15039–15049.

[354] Clavero, C. “Plasmon-induced hot-electron generation at nanoparticle/metal-oxide interfaces for photovoltaic and photocatalytic devices”. In: *Nature Photonics* vol. 8, no. 2 (2014), pp. 95–103.

[355] Govorov, A. O., Zhang, H., and Gun’ko, Y. K. “Theory of photoinjection of hot plasmonic carriers from metal nanostructures into semiconductors and surface molecules”. In: *The Journal of Physical Chemistry C* vol. 117, no. 32 (2013), pp. 16616–16631.

[356] Amidani, L. et al. “Probing Long-Lived Plasmonic-Generated Charges in TiO2/Au by High-Resolution X-ray Absorption Spectroscopy”. In: *Angewandte Chemie International Edition* vol. 54, no. 18 (2015), pp. 5413–5416.

[357] Sá, J. et al. “Direct observation of charge separation on Au localized surface plasmons”. In: *Energy & Environmental Science* vol. 6, no. 12 (2013), pp. 3584–3588.

[358] Knight, M. W. et al. “Embedding plasmonic nanostructure diodes enhances hot electron emission”. In: *Nano letters* vol. 13, no. 4 (2013), pp. 1687–1692.

[359] Tian, Y. and Tatsuma, T. “Plasmon-induced photoelectrochemistry at metal nanoparticles supported on nanoporous TiO 2”. In: *Chemical communications*, no. 16 (2004), pp. 1810–1811.

[360] Wu, K. et al. “Efficient hot-electron transfer by a plasmon-induced interfacial charge-transfer transition”. In: *Science* vol. 349, no. 6248 (2015), pp. 632–635.

[361] Brongersma, M. L., Halas, N. J., and Nordlander, P. “Plasmon-induced hot carrier science and technology”. In: *Nature nanotechnology* vol. 10, no. 1 (2015), pp. 25–34.

[362] Kochuveedu, S. T. et al. “Revolutionizing the FRET-based light emission in core-shell nanostructures via comprehensive activity of surface plasmons”. In: *Scientific reports* vol. 4, no. 1 (2014), pp. 1–8.

[363] Li, J. et al. “Plasmon-induced resonance energy transfer for solar energy conversion”. en. In: *Nature Photonics* vol. 9, no. 9 (Sept. 2015), pp. 601–607.

[364] Nishiyama, H. et al. “Photocatalytic solar hydrogen production from water on a 100-m2 scale”. In: *Nature* vol. 598, no. 7880 (2021), pp. 304–307.

Chapter 3

Methodology

In this work, powder and thin film samples are presented. The synthesis of the powders is briefly summarized in section 3.1. The manufacturing of thin film samples with well-socketed plasmonically active MNPs will be described below. The workflow will be represented by order of appearance of the different sections.

3.1 Powder Synthesis: Nanoparticles on Particles

Appropriate precursor powders were utilized, e.g., lanthanum oxide (La_2O_3, Sigma Aldrich, CAS: 1312-81-8), strontium carbonate ($SrCO_3$, 99 % + 1% Ba, Johnson Matthey GmbH, CAS: 1633-05-2), titanium dioxide (TiO_2, anatase, Sigma Aldrich, CAS:1317-70-0), and nickel nitrate hexahydrate (99.999%, Sigma Aldrich, CAS: 13478-00-7) for Ni-doped LSTO. Powders prepared for Paper I were mixed with acetone and ultrasonicated. Subsequently, the acetone was evaporated and pressed into a pellet. The pellet was calcined at 1000 °C for 12 h and afterwards crushed, and ball milled at 250 rpm for 2 h in isopropanol. The isopropanol was evaporated before the powder was pressed into a pellet and sintered at 1100 °C for 12 h before the crushing and ball-milling were repeated, and the dried powder was pressed into a pellet and calcined for a third time at 1200 °C. The subsequent exsolution occurred either in a ProboStat^{TM} (NorECs AS, Norway) under continuous H_2 flow or in combination with CaH_2. The temperature and time varied for exsolution in H_2. The CaH_2 and sample were mixed and pressed into a loose pellet (minimal pressure in the coldpress

(Atlas Manual Hydraulic Press 15T, Specac)) before being sealed inside an ampule. Exsolution occurred by keeping the ampule at 600 °C for 72 h. The CaO and remaining CaH_2 were removed by washing the powder in a methanolic solution containing 0.1 M NH_4Cl. Galvanic replacement occurred in a solution of 1×10^{-3} M HCl, 1×10^{-3} M$HAuCl_4$, and 1×10^{-3} M polyvinylpyrrolidone (PVP) at 80 °C.

Powders presented in chapter 5, however, were mixed in isopropanol and ball milled for 3 h at 300 rpm in an agate jar with agate balls instead of ultrasonicated. The isopropanol was evaporated, and the powder was calcined in a crucible at 900 °C for 5 h. Subsequently, the powders were ball milled again for 3 h at 300 rpm in isopropanol and dried. The powder was pressed in a pellet and sintered at 1000 - 1100 °C for 12 h. The pellet was crushed, and ball milled for a final time for 3 h at 300 rpm in isopropanol, and dried. Exsolution was performed in a ProboStat^{TM} (NorECs AS, Norway) at 800 - 900 °C for 10 - 12 h under a continuous flow of H_2. The higher temperature and longer duration were chosen because the number of particles incrased. Subsequent galvanic replacement typically occurred in a solution with 1×10^{-3} M of an appropriate metal complex and 0.1 M perchloric acid ($HClO_4$), typically at 80 °C.

3.2 Thin Film Synthesis: From Pellet to Thin Films with Particles

The pellet serving as the target in the pulsed laser deposition (PLD) determines the stoichiometry of the thin film. Thus, local variations in stoichiometry within the pellet can have a significant influence on the stoichiometry of the thin film, while the density and diameter determine how many depositions can be run with the same pellet. Creating a pellet starts by weighing the correct amount of precursor powders. For A-site excess N̦-doped pellets typically strontium

carbonate ($SrCO_3$, 99 % + 1% Ba, Johnson Matthey GmbH, CAS 1633-05-2), titanium dioxide (TiO_2, anatase, Sigma Aldrich, CAS:1317-70-0), and nickel nitrate hexahydrate (99.999%, Sigma Aldrich, CAS: 13478-00-7) were used. The powders were mixed and ball-milled in an agate jar with agate balls for 3 h at 300 rpm in H_2O.

The ball milled samples were dried in a heating cabinet at 120 °C before being calcined at 450 °C for 4 h. The resulting powder was mixed with binder (B60/B709, mixed with ethyl acetate type, 17 drops per gram of powder) by mortar and pestle, and a dye of 20 mm was used to press the powder into a pellet. 13.26 N m^{-2} of pressure was applied by a coldpress (Atlas Manual Hydraulic Press 15T, Specac). The green body was placed on sacrificial powder inside an alumina crucible and covered with sacrificial powder. Subsequently, the pellet was sintered at 1100 °C for 12 h. The resulting pellets had a uniform color indicating a uniform stoichiometry across the entire pellets.

3.2.1 Thin Film Deposition

PLD has many degrees of freedom to deposit a thin film successfully. The key advantages of the PLD technique for this work are stoichiometric transfer of the material, the ability to grow adherent and epitaxial films at lower substrate temperatures than other methods, and the ease with which the desired targets can be synthesized [1, 2]. The targets utilized were made based on the desired stoichiometry of the thin film. The substrates to deposit the films on were unless otherwise indicated, Si (001) n-type wafers (Si, N<100>, 2", Si-mat). The strength of the laser and position of the focusing lens were set such that the plasma plume grazed the substrate. The particular machine (Surface-Tec system, laser: Coherent COMPex Pro 205F, KrF, wavelength: 248 nm) utilized during this work allowed up to four targets simultaneously in the deposition

chamber. Moreover, four substrate positions can be chosen. However, when depositing multiple samples simultaneously, cross-deposition will occur.

The distance between the substrate and the target was kept at 9 cm. This allowed for the most uniform thickness but, unfortunately, also the most cross-deposition. In figure 3.1, a Si-wafer with a $Sr_{1.07}Ti_{0.93}Ni_{0.07}O_{3\pm\delta}$ thin film is shown, where four times 10'000 shots were deposited. The alignment of the PLD creates circular areas of uniform thickness, where the difference in the colors visible in the figure indicates slightly different thicknesses. The substrate temperature was set to be 600 °C, a temperature stable during deposition and generally allowing for crystalline growth. A film thickness of 500-1000 nm was achieved by depositing a total of 20'000 laser pulses with a repetition rate of 5 to 10 Hz. The targets were rotated with 5 rpm during the deposition. Individual targets were used for multiple depositions, where the surface before to every deposition was flattened by mechanically grinding the target until the surface was flat.

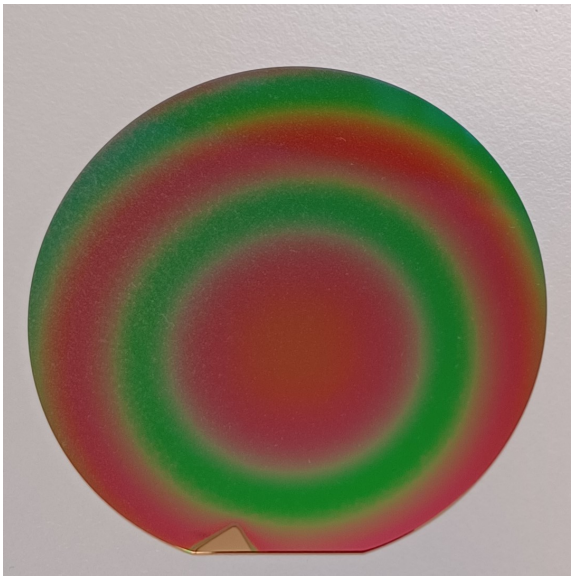

Figure 3.1: A Si wafer covered with a thin film of $Sr_{1.07}Ti_{0.93}Ni_{0.07}O_{3\pm\delta}$ before exsolution. The diameter of the wafer is 2". The color difference indicates a thickness difference.

3.2.2 Post-Deposition Annealing and Exsolution

Some thin films were post-annealed after deposition. The annealing typically occurred before exsolution and was conducted at 900 °C in ambient pressure and atmosphere. The purpose of post-deposition annealing was to homogenize the thin films before exsolution. These samples are mainly considered in Paper III.

Exsolution of thin films was conducted in the ProboStat^{TM} (NorECs AS, Norway) at 800 °C. The reducing atmosphere was either a continuous flow of HArmix (5 % H_2 and 95 % Ar) or pure H_2. For safety reasons, the system was flushed by Ar for 15 minutes before starting exsolution and similarly for 15 minutes after the furnace reached room temperature. Additionally, multiple exsolution times, referring to the time the sample was kept at 800 °C, were studied. The heating and cooling rates were $\pm$ 5 °C min^{-1}. However, the furnace could not follow the cooling rate below temperatures of $\sim$ 250 °C, leading to a slower cooling rate. Subsequently, the freshly exsolved thin films were used in GRR as quickly as possible or stored in ambient conditions.

3.2.3 Galvanic Replacement

The GRR of nanoparticles in thin films was conducted in a double-jacketed glass connected to a thermostated water bath. The temperature set was at 80 °C, with the replacement solution reaching 77 °C. The appropriate replacement solution contained Pt, Ag, or Au based on the desired experiment. In contrast to the powder samples previously discussed by X. Kang [3], much shorter replacement times were used for thin films, ranging from 5 s to 90 s. After GRR, the samples were rinsed with de-ionized H_2O, dried in air, and stored in ambient conditions for analysis.

3.3 Electron Energy Loss Spectroscopy (EELS)

Electron energy loss spectroscopy is a technique frequently utilized to study LSPRs of MNPs [4]. LSPR has been introduced above, but for its characterization, especially with regard to photons and electrons, it is important to mention that certain modes are optically dark while others are bright. Optically dark modes typically cannot radiate into the far field and have longer lifetimes than bright modes [5–7]. In literature, however, the definition is not always applied. In the quasistatic regime, only modes with a non-zero dipole moment are bright modes and coupled to the farfield and scatter [4, 8]. In contrast, if the particle size increases and becomes comparable to the wavelength, higher-order modes can couple the MNP to the far field without a dipole mode present [4]. Importantly, optical dark modes can be excited by electrons and by altered far-field sources, e.g., dipole sources [9], evanescent excitation [10], radially polarized light [11], non-normal incidence [12] or retardation effects [13].

Two different techniques can be utilized to study LSP of MNPs. They both include EELS and are called energy filtered transmission electron microscopy (EFTEM) and spectrum image (SI) mode in STEM [4]. The former results in images with high spatial resolution and fast acquisition times, while the latter yields high-energy resolution maps [4]. In SI STEM, an EEL spectrum can be acquired for every pixel in a region of interest, and a hyperspectral cube consisting of the energy loss probability $\Gamma(E, x, y)$ can be assembled [14]. Selecting an energy range and creating an image results in an energy-filtered SI, also known as EELS map [4]. While this is similar to EFTEM data, in this work EELS map is exclusively used for energy-filtered SI, and EFTEM will not be discussed further.

The first EELS maps of plasmonic MNPs were reported in 2007 [15], and relatively quickly, these maps have become routine results in LSPR mapping

today [4]. The acceleration voltage set during the experiment ranges typically from 60 - 300 kV resulting in relativistic electrons with de Broglie wavelengths on the picometer scale [4]. The electron beam is usually monochromated and focused by electromagnetic lenses resulting in a subnanometer monochromatic probe [16, 17]. Aberration correctors typically allow the formation of sub-angstrom probes [18, 19]. The zero-loss peak (ZLP) consisting of unscattered or elastically scattered electrons influences the quality of the EELS map. The full width at half-maximum (FWHM) is a typical measure of the quality of the ZLP [4]. Additionally, while performing the EELS experiments for every pixel, a high angle annular dark-field detector (HAADF) is usually utilized to collect structural information [4].

3.3.1 Post Experimental Data Analysis

SI STEM experiments result in a wealth of data. Analyzing the data is a critical step to gain understand the system [4]. In the following essential steps are illustrated that are used during the analysis. It is assumed that all ZLPs are well aligned.

Normalization of the Spectra

An EELS ZLP of a spectrum obtained in vacuum and one from a pixel on the material result in different heights of the ZLP (as seen in figure 3.2 (a)). The cause is the scattering of the electrons by the material to positions outside the EEL spectrometer aperture [4]. By normalizing the individual EEL spectra, the data becomes interpretable due to the proportionality to the EEL probability. The probability is the number of electrons divided by the total number of incident electrons. Treating an experimental EEL spectrum, the ZLP height serves as the denominator, while the EEL spectrum is the numerator. Figure 3.2 (d) shows

the difference in resulting EELS maps.

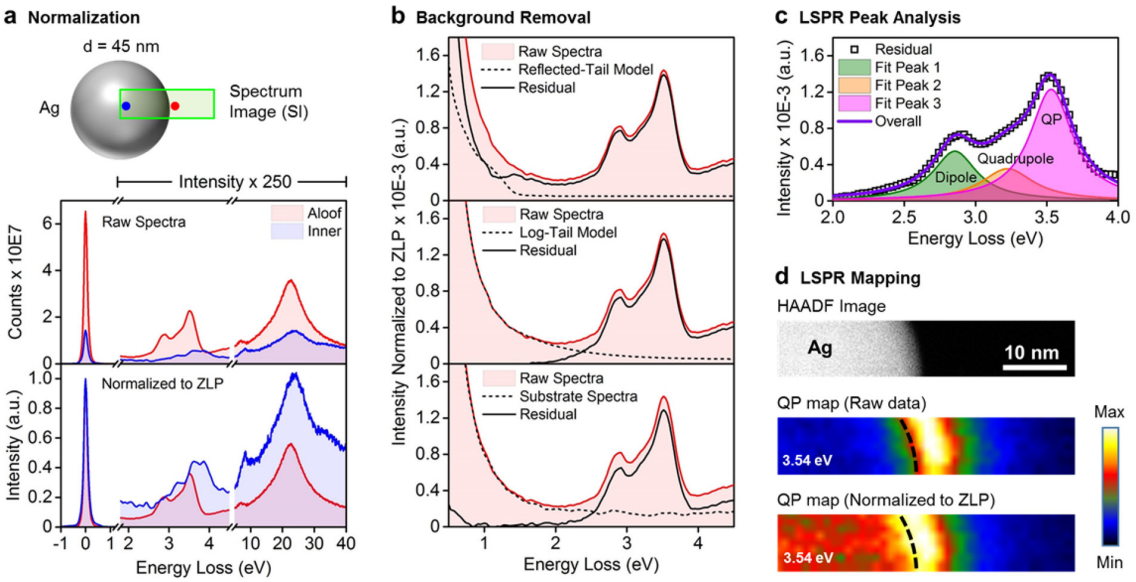

Figure 3.2: (a) The Ag particle examined in the rest of the figure is shown with the SI region of interest. Moreover, two non-normalized raw spectra and two normalized spectra are compared. (b) Three different fitting models were used where the top panel shows the reflected-tail model, the middle panel displays the logarithmic fitting of a section of the ZLP, and the bottom panel shows the use of a reference spectrum. (c) shows the fitting of the resulting normalized and background subtracted spectra with a Lorentzian for the dipole, quadrupole, and quasiplanar mode. (d) The HAADF image, as obtained EELS map and normalized EELS map of the region of interest. The figure was taken from [4], with permission.

Background Removal

The LSPR signal can be masked by a variety of different signals, including the tail of the ZLP, bulk plasmons, Cherenkov radiation, transition radiation, and inter- and intraband transitions [14, 17, 20]. Cherenkov radiation was avoided by performing the measurements at 60 kV acceleration voltage. Analyzing the LSPR peak properly requires the removal of the background caused by these additional signals. This can be achieved by using models reflecting, i.e., the ZLP shape like the reflected-tail (seen in figure 3.2 (b), top panel), Gaussian, or combined Gaussian and Lorentzian models. These models may not remove the

background completely because the ZLP is not symmetric, and contributions from the sample may not be accounted for [4]. Alternatively, a model dealing with just the tail can be used (as seen in figure 3.2 (b), middle panel), where a logarithmic function was fitted to a region (0.9 - 1.5 eV) and subtracted. Finally, EEL spectra obtained from different regions of the sample, so-called "blank" spectra, are used to subtract the background as seen in figure 3.2 (b), bottom panel. [4, 21–24].

Peak Analysis

Extracting the individual peaks can be both challenging and significant. If LSPR modes are confined to small energy ranges, peak fitting must be used, while direct measurements of energy, amplitude, and line width are achievable for other modes [4]. A fitting with a Lorentzian is shown in figure 3.2 (c), where the quasiplanar (QP) mode represents multiple higher-order modes appearing as a single peak due to line-width broadening and peak aggregation [22, 25, 26]. Scripts utilized in this thesis can be found in [27].

3.4 Additional Characterization

The characterization of the thin films was achieved by a plethora of techniques. Among them are electron microscopy, X-ray diffraction (XRD), X-ray photoelectron spectroscopy (XPS), photoelectrochemical (PEC) measurements, and scanning electron microscopy (SEM).

The electron microscope used was a FEI Titan G2 60-300 instrument, able to perform STEM and high-resolution EELS. The instrument is equipped with a CEOS DCOR corrector for the probe forming lenses, a Wien-filter monochromator, a Gatan 965 Quantum EELS spectrometer, and the FEI Super-X EDS detector. Typically, structural and chemical characterization of samples

were carried out at an acceleration voltage of 300 kV, with a probe convergence semi-angle of 21 mrad. The inner collection semi-angle of the HAADF, DF4, and DF2 detector were 101, 22, and 9 mrad, respectively. Surface plasmon mapping was conducted at an acceleration voltage of 60 kV, with varying energy resolution.

The analysis of the electron microscopy data was conducted utilizing the Velox software by Thermo Fisher Scientific^{TM}, the DigitalMicrograph Software by Gatan, and custom-made python codes utilizing, among other packages, hyperspy [28].

The XRD measurements were performed on a Bruker D8 (Cu K_{α_1}, Bragg-Brentano), typically measuring from 10 or 20° to 90°. Diffrac.Eva by Bruker was used to analyze the XRD data if not stated otherwise. The SEM images were obtained utilizing two SEMs. The first was the Hitachi SU8230 ultra-high resolution cold-field emission SEM, equipped with a secondary electron (SE) detector under an acceleration voltage of 5 kV). The second was a FEI QUanta 200 FEG SEM, equipped with a SE detector and backscatter detector at a gun acceleration voltage of 20 kV.

An Ivium Vertex potentiostat/galvanostat in a standard three-electrode set-up was used to perform the photoelectrochemical measurements if not stated otherwise. The electrolyte, reference and counter electrode are indicated for each measurement, but in general a Pt sheet was used as the counter electrode and a saturated calomel electrode (SCE) as the reference. All measurements were performed under one sun illumination by a Newport Oriel® LCS-100 solar simulator. The solar simulator used a 100 W ozone-free xenon lamp and an AM 1.5G filter. The intensity was regularly calibrated by a monocrystalline Si PV reference cell (Newport 91150V-KG5). The potentials were corrected against the appropriate electrode (see individual measurements).

References

[1] Ogugua, S. N., Ntwaeaborwa, O. M., and Swart, H. C. "Latest development on pulsed laser deposited thin films for advanced luminescence applications". In: *Coatings* vol. 10, no. 11 (2020), p. 1078.

[2] Bao, Q. et al. "Pulsed laser deposition and its current research status in preparing hydroxyapatite thin films". In: *Applied Surface Science* vol. 252, no. 5 (2005), pp. 1538–1544.

[3] Kang, X. *Novel nanostructured materials for energy applications*. eng. Vol. no. 2465. Series of dissertations submitted to the Faculty of Mathematics and Natural Sciences, University of Oslo (trykt utgave). Oslo: Department of Chemistry, Faculty of Mathematics and Natural Sciences, University of Oslo, 2021.

[4] Wu, Y., Li, G., and Camden, J. P. "Probing Nanoparticle Plasmons with Electron Energy Loss Spectroscopy". In: *Chemical Reviews* vol. 118, no. 6 (2018). PMID: 29215265, pp. 2994–3031. eprint: https://doi.org/10.1021/acs.chemrev.7b00354.

[5] Chu, M.-W. et al. "Probing Bright and Dark Surface-Plasmon Modes in Individual and Coupled Noble Metal Nanoparticles Using an Electron Beam". In: *Nano Letters* vol. 9, no. 1 (2009). PMID: 19063614, pp. 399–404. eprint: https://doi.org/10.1021/nl803270x.

[6] Barrow, S. J. et al. "Mapping Bright and Dark Modes in Gold Nanoparticle Chains using Electron Energy Loss Spectroscopy." In: *Nano Letters* vol. 14, no. 7 (2014). PMID: 24955651, pp. 3799–3808. eprint: https://doi.org/10.1021/nl5009053.

[7] Zhang, S. et al. "Substrate-Induced Fano Resonances of a Plasmonic Nanocube: A Route to Increased-Sensitivity Localized Surface Plasmon Resonance Sensors Revealed". In: *Nano Letters* vol. 11, no. 4 (2011). PMID: 21410217, pp. 1657–1663. eprint: https://doi.org/10.1021/nl200135r.

[8] Movsesyan, A. et al. "Hybridization and dehybridization of plasmonic modes". In: *The Journal of Physical Chemistry C* vol. 125, no. 1 (2020), pp. 724–731.

[9] Liu, M. et al. "Excitation of Dark Plasmons in Metal Nanoparticles by a Localized Emitter". In: *Phys. Rev. Lett.* vol. 102 (10 Mar. 2009), p. 107401.

[10] Yang, S.-C. et al. "Plasmon Hybridization in Individual Gold Nanocrystal Dimers: Direct Observation of Bright and Dark Modes". In: *Nano Letters* vol. 10, no. 2 (2010). PMID: 20058898, pp. 632–637. eprint: https://doi.org/10.1021/nl903693v.

[11] Gómez, D. E. et al. "The Dark Side of Plasmonics". In: *Nano Letters* vol. 13, no. 8 (2013). PMID: 23802620, pp. 3722–3728. eprint: https://doi.org/10.1021/nl401656e.

[12] Zhou, W. and Odom, T. W. "Tunable subradiant lattice plasmons by out-of-plane dipolar interactions". In: *Nature Nanotechnology* vol. 6, no. 7 (July 2011), pp. 423–427.

[13] Myroshnychenko, V. et al. "Modelling the optical response of gold nanoparticles". In: *Chemical Society Reviews* vol. 37, no. 9 (2008), pp. 1792–1805.

[14] Williams, D. B. and Carter, C. B. "Transmission electron microscopy". In: *Systematic Materials Analysis* vol. 4 (1978), pp. 407–432.

[15] Nelayah, J. et al. "Mapping surface plasmons on a single metallic nanoparticle". In: *Nature Physics* vol. 3, no. 5 (2007), pp. 348–353.

[16] Essers, E. et al. "Energy resolution of an Omega-type monochromator and imaging properties of the MANDOLINE filter". In: *Ultramicroscopy* vol. 110, no. 8 (2010), pp. 971–980.

[17] Fultz, B. and Howe, J. M. *Transmission electron microscopy and diffractometry of materials*. Springer Science & Business Media, 2012.

[18] Krivanek, O., Lovejoy, T., and Dellby, N. *Aberration-corrected STEM for atomic-resolution imaging and analysis*. 2015.

[19] Pennycook, S. J. et al. "Atomic-resolution spectroscopic imaging: past, present and future". In: *Journal of electron microscopy* vol. 58, no. 3 (2009), pp. 87–97.

[20] Egerton, R. F. *Electron energy-loss spectroscopy in the electron microscope*. Springer Science & Business Media, 2011.

[21] Li, G. et al. "Spatially mapping energy transfer from single plasmonic particles to semiconductor substrates via STEM/EELS". In: *Nano Letters* vol. 15, no. 5 (2015), pp. 3465–3471.

[22] Bosman, M. et al. "Surface plasmon damping quantified with an electron nanoprobe". In: *Scientific reports* vol. 3, no. 1 (2013), pp. 1–7.

[23] Jarausch, K. and Leonard, D. N. "Three-dimensional electron microscopy of individual nanoparticles". In: *Journal of electron microscopy* vol. 58, no. 3 (2009), pp. 175–183.

[24] Wu, Y. et al. "Electron energy loss spectroscopy study of the full plasmonic spectrum of self-assembled Au–Ag alloy nanoparticles: Unraveling size, composition, and substrate effects". In: *ACS Photonics* vol. 3, no. 1 (2016), pp. 130–138.

[25] Li, G. et al. "Examining substrate-induced plasmon mode splitting and localization in truncated silver nanospheres with electron energy loss spectroscopy". In: *The Journal of Physical Chemistry Letters* vol. 6, no. 13 (2015), pp. 2569–2576.

[26] Aizpurua, J., Rivacoba, A., and Apell, S. "Electron-energy losses in hemispherical targets". In: *Physical Review B* vol. 54, no. 4 (1996), p. 2901.

[27] Both, K. G. *Ph.D. Code Collection*. Version 2.0.4.

[28] Peña, F. de la et al. *hyperspy/hyperspy: Release v1.7.2*. Version v1.7.2. Sept. 2022.

Chapter 4

Introduction to Papers

Following this chapter, the main papers of this work are presented. In Paper I the growing need to control and tune metal nanoparticles (MNPs) to increase their stability and effectiveness, especially for photo- and electrochemical energy conversion applications, are addressed. As introduced in section 2.2, exsolved particles remain in their initial location and structural arrangement even when being re-shaped because they are well anchored. In Paper I, the galvanic replacement method is utilized, allowing the manufacturing of a wealth of new hybrid nanostructures with a potentially high degree of tailorability while being simpler and safer than most other methods. The resulting NiAu bimetallic nanostructures were supported on the $LaSrTiO_3$ and showed enhanced activity in plasmon-assisted photoelectrochemical water oxidation reactions. The photoelectrochemical performance increased starting from Ni-doped $LaSrTiO_3$ to exsolved $LaSrTiO_3$, and finally, with the best performance of Au MNPs introduced by GRR. The particles were observed by scanning transmission electron microscopy (STEM), where in situ experiments were used to visualize the structural evolution of the bimetallic structures. Computational simulations provided mechanistic insights and correlated the surface plasmon resonance effects with structural features. To showcase the generality of the approach, NiPt bimetallic nanoparticles were created with a low Pt loading on highly reduced $LaSrTiO_3$. The Pt-powders exhibited good stability under galvanostatic operation at $-10\,\mathrm{mA\,cm^{-2}}$, and an overpotential of $-320\,\mathrm{mV}$ versus RHE at $-10\,\mathrm{mA\,cm^{-2}}$, representing a high electrocatalytic activity toward the hydrogen

evolution reaction, while utilizing 40 times less platinum than commercially available Pt-C.

In Paper II, the focus is on plasmonically active nanoparticles on an A-site excess $SrTiO_3$ thin film. The absorption range of photocatalysts can be extended by utilizing plasmonically active nanoparticles. These particles do not need to be catalytically active themselves; instead, they introduce the possibility to absorb photons with lower energies in wide band gap photocatalysts. In Paper II the focus is on A-site $SrTiO_3$ doped with Ni in the form of thin films. The Ni was exsolved, and the surface Ni MNPs were replaced by Au by means of GRR. In comparison to Paper I, exsolution occurred at lower times and in less reducing atmospheres, i.e., HArmix. Moreover, the GRR times decreased significantly from 10 min to somewhere between 5 to 90 s while replacing the nickel completely. The resulting structures showed well-socketed Au nanoparticles of variable sizes on the surface. Replacing Ni with Au had a positive effect for the intermediate reaction time lengths and resulting medium particle sizes while being detrimental for the short and long replacement times. Again STEM was utilized to determine the structures of the thin films, and EELS mapping is presented. Complementary computational results are presented additionally. The main mechanism of the samples is suggested as hot electron injection based on the plasmon peak position.

Paper III focuses on exsolution in thin films. Exsolution becomes an increasingly attractive technique to form MNPs embedded in a matrix. However, the phenomenon is predominantly studied in A-site deficient and stoichiometric perovskite powders. A-site excess Ni-doped $SrTiO_3$ thin films are studied. These thin films, while all deposited in an oxygen-rich atmosphere, have different thicknesses. Some samples were annealed at 900 °C before exsolution, while the others were not, to study the impact of pre-annealing on exsolution. Like in Paper II, exsolution was carried out at 800 °C but the length at the target

temperature, as well as the reduction gas, e.g., H_2 or HArmix, were varied. All samples showed exsolution, even within the bulk. In Paper II, the less reducing atmosphere led to more metallic Ni XPS peaks, and here we have shown that the particle sizes is independent of the gas. The annealing before exolution lowered the number of particles while the size of the particles increased. It is suggested that the appearance of columnar structures within the thin film during exsolution is necessary for the exsolution process. Additionally, the process of forming larger crystal domains lower the critical radii of exsolved MNPs, while a pre-existing structure forces higher critical radii.

To investigate the exsolution behavior away from the thin film surface and thin film - substrate interface, three-layer thin film structures are utilized, where the bottom and top layer are A-site excess $SrTiO_3$ without any nickel doping. The middle layer, however, has the same doping level as in the single layer thin films. No annealing before exsolution was utilized for multilayer structures, and HArmix was used to create the reducing atmosphere. The time of exsolution was varied, where the time at 800 °C ranged from 0 min, immediate cooling upon reaching the target temperature, to 600 min. The resulting thin films had a columnar structure, with Ni particles outside the original doping zone. Yet, the overall doping of the STO of the originally undoped layers remained low. It is concluded that the nickel particles themselves diffuse within the thin film. The columnar structure may assist this movement in both the surface and interface direction. The study of the thin films is an effort to establish the impact of different conditions during the synthesis and processing of the thin films.

Finally, it is worth mentioning that in appendix A and appendix B, two publications are included as appendices that neither concern themselves with exsolution nor plasmonics. However, appendix A is included because of the pulsed laser deposition work. The influence of the deposition atmosphere as well

as thin film thickness were important parameters during this work. Appendix B concerns itself with galvanic deposition, a reaction not unlike GRR. The work includes a first version of the code later utilized in Paper I.

Papers

Paper I

Galvanic Restructuring of Exsolved Nanoparticles for Plasmonic and Electrocatalytic Energy Conversion

Xiaolan Kang, Vilde Mari Reinertsen, Kevin Gregor Both, Augustinas Galeckas, Thomas Aarholt, Øystein Prytz, Truls Norby, Dragos Neagu, Athanasios Chatzitakis*

Published in *Small*, June 2022, volume 18, issue 29, pp. 2201106. DOI: https://doi.org/10.1002/smll.202201106.

X.K. acknowledges support by the China Scholarship Council (201806060141). A.C. and Ø.P. acknowledge The Research Council of Norway for support through the projects PH2ON (288320), and FUNCTION (287729), respectively. Support to the Norwegian Center for Transmission Electron Microscopy was also acknowledged (NORTEM 197405/F50). D.N. gratefully acknowledges the Royal Society for the grant RGS/R1/211253.

RESEARCH ARTICLE

NANO · MICRO small
www.small-journal.com

Galvanic Restructuring of Exsolved Nanoparticles for Plasmonic and Electrocatalytic Energy Conversion

*Xiaolan Kang, Vilde Mari Reinertsen, Kevin Gregor Both, Augustinas Galeckas, Thomas Aarholt, Øystein Prytz, Truls Norby, Dragos Neagu, and Athanasios Chatzitakis**

There is a growing need to control and tune nanoparticles (NPs) to increase their stability and effectiveness, especially for photo- and electrochemical energy conversion applications. Exsolved particles are well anchored and can be re-shaped without changing their initial location and structural arrangement. However, this usually involves lengthy treatments and use of toxic gases. Here, the galvanic replacement/deposition method is used, which is simpler, safer, and leads to a wealth of new hybrid nanostructures with a higher degree of tailorability. The produced NiAu bimetallic nanostructures supported on $SrTiO_3$ display exceptional activity in plasmon-assisted photoelectrochemical (PEC) water oxidation reactions. In situ scanning transmission electron microscopy is used to visualize the structural evolution of the plasmonic bimetallic structures, while theoretical simulations provide mechanistic insight and correlate the surface plasmon resonance effects with structural features and enhanced PEC performance. The versatility of this concept in shifting catalytic modes to the hydrogen evolution reaction is demonstrated by preparing hybrid NiPt bimetallic NPs of low Pt loadings on highly reduced $SrTiO_3$ supports. This powerful methodology enables the design of supported bimetallic nanomaterials with tunable morphology and catalytic functionalities through minimal engineering.

1. Introduction

Metallic nanoparticles (NPs) are crucial in a broad range of applications, such as catalysis, photo-catalysis, plasmonics, electronics, sensors, and photovoltaics.[1] Generally, their properties and targeted functionalities can be tuned by adjusting parameters such as structure, morphology, and composition.[2] More specifically, bimetallic NPs exhibit unique properties outperforming their monometallic counterparts, as is the case for Ir–Ru bimetallic composites, which are efficient and stable electrocatalysts for the oxygen evolution reaction (OER) in acidic solutions.[1b] Another example is Pd–Ag bimetallic structures, which can increase the selectivity in the hydrogenation of ethylene compared to the widely used Pd or Ag monomers, a fact attributed to modulation of hydrogen adsorption on Pd in the composites.[3] Bimetallic composites involving plasmonic metals, like Au, Ag, Cu, and Al are of particular interest because of the localized surface plasmon resonance (LSPR) effect,[4] which renders them important photosensitizers in semiconductor-supported systems for photocatalytic and photoelectrochemical (PEC) applications.[5] Recently, the antenna–reactor effect has been demonstrated, in which plasmonic NPs (antenna) induce a localized field that can significantly enhance the catalytic reaction rates on adjacent NPs (reactor).[6] This system has the advantage of combining the optical response of plasmonically active metals and the catalytic abilities of catalytically active metals.

The synthesis of such supported multi-metallic NPs with targeted structural features is hence of great importance, but very challenging. Most of the approaches developed so far involve co-reduction or co-precipitation, in situ exsolution, galvanic replacement reaction (GRR), Ostwald ripening and Kirkendall effects.[2d,7] Among them, GRR stands out due to its simplicity and versatility in engineering the metallic nanostructures in terms of composition, morphology, structure, etc.[8] GRR is a chemical process in which one metal often referred to as the sacrificial template is oxidized by the ions of another metal. The standard reduction potential difference between the sacrificial and depositing metals provides the driving force for the galvanic deposition of the desired metallic element.[9]

X. Kang, K. G. Both, T. Norby, A. Chatzitakis
Centre for Materials Science and Nanotechnology
Department of Chemistry
University of Oslo
Gaustadalléen 21, Oslo NO-0349, Norway
E-mail: athanasios.chatzitakis@smn.uio.no
V. M. Reinertsen, A. Galeckas, T. Aarholt, Ø. Prytz
Centre for Materials Science and Nanotechnology
Department of Physics
University of Oslo
P. O. Box 1048 Blindern, Oslo NO-0316, Norway
D. Neagu
Department of Chemical and Process Engineering
University of Strathclyde
75 Montrose St, Glasgow G1 1XJ, UK
The ORCID identification number(s) for the author(s) of this article can be found under https://doi.org/10.1002/smll.202201106.

DOI: 10.1002/smll.202201106

In situ exsolution is a facile process to prepare well-defined and anchored supported NPs. In this process, the catalytically active metal elements are initially dissolved into the host oxide lattice during the crystallization process, and then partly exsolved from the support upon subsequent reductive conditions.[10] Exsolved metallic NPs with lower reduction potentials are excellent templates for subsequent GRR reactions and the formation of new structures and enhanced functionalities.

Here we show how the combination of two powerful methods as in situ exsolution and galvanic replacement forms a new method of chemical (solid-ion reaction) restructuring and hybridization of supported bimetallic NPs. These new and otherwise impossible to form exotic nanostructures supported on perovskite oxides ($SrTiO_3$) have tunable catalytic functionalities and are prepared with minimal engineering requirements.[8b,11] Specifically, we deposit through the galvanic replacement reaction plasmonic Au nano-islands on exsolved Ni NPs and both experimental evidence and modeling data correlate the improved PEC water splitting performance to the localized surface plasmon resonance of Au, as well as to the synergetic effect between Ni and Au in the form of antenna–reactor. We shift the catalytic activity of the parent compound by galvanically depositing Pt that forms Pt nano-needles with superior hydrogen evolution rate (HER) activity, approaching that of commercial Pt/C in alkaline media, with considerably lower Pt loadings.

2. Results

2.1. Crystal Structures and the Evolution of As-Prepared Samples

An overview of the different synthesis conditions and the corresponding obtained structures is schematically presented in **Figure 1**. La- and Ni- co-doped, A-site deficient $SrTiO_3$ ($La_{0.6}Sr_{0.2}Ti_{0.9}Ni_{0.1}O_{3-x}$ – LSTN, refer also to Note S1, Supporting Information) was first reduced in H_2 atmosphere (rLSTN) or in the presence of CaH_2 (rLSTN-CaH_2) to get Ni exsolution. We have previously studied the reduction of TiO_2 in the presence of CaH_2 and we showed that heavily reduced TiO_2 nanotube films with metallic conductivity could be obtained.[12] Motivated by this, we successfully exsolved Ni NPs in the presence of CaH_2 at as low temperatures as 600 °C. Then, the galvanic replacements were done by exposing rLSTN to a Au (III) complex solution (rLSTNAu) and the rLSTN-CaH_2 to a Pt (IV) solution to form, respectively, ladybug-like NiAu bimetallic and hedgehog-like NiPt supported, hybrid nanostructures. In this way, we can tune the electrocatalytic activity of the parent compound from plasmon-assisted photoelectrocatalytic water splitting to electrocatalysis for the HER. Details of the synthesis steps are given in the supporting information (SI), but the main structures are discussed below.

We examined the crystal structures of the as-synthesized LSTN, rLSTN, and rLSTNAu samples by X-ray diffraction (XRD). As displayed in **Figure 2**a, the XRD patterns of these three samples are almost identical (single phase cubic structure, $Pm\bar{3}m$) showing a high degree of crystallinity, that indicates the stability of LSTN upon high temperature chemical reduction and galvanic replacement reactions. The characteristic peak of metallic Ni at ≈44.5° (inset II) is detectable in the XRD patterns of rLSTN and rLSTNAu but not in the LSTN, as expected. After the galvanic replacement reaction with the Au (III) complex solution, a new peak is detected at ≈38.3° (inset I) of the rLSTNAu sample, which is indexed to cubic metallic Au.[13]

Dopants (Ni and La) and deficiencies (A-site deficiency and oxygen non-stoichiometry) deliberately introduced in these compositions to promote exsolution, led to a slight distortion to the perovskite structure. A close examination of the (222) reflection (≈86.4°, inset IV, cubic primitive cell) shows a small shoulder peak at higher angle, indicating the increased pseudocubic unit cell parameter (a_p) and lattice distortion after Ni doping. Such a shoulder peak becomes invisible after reduction, but a peak-shifting of both the (202) (≈67.9°, inset III) and (222) reflections toward lower angles is observed for the rLSTN and rLSTNAu samples. The lattice parameters were estimated by Rietveld refinement ($Pm\bar{3}m$, a_p (LSNT): 3.8969 Å, a_p (rLSNT): 3.8978 Å, refer to Figure S1, Supporting Information for fitted data), where the slight lattice expansion after reduction can be attributed to the egress of Ni dopants from the parent lattice accompanied by the formation of oxygen vacancies. Besides, the Ti^{4+} radius in the oxidized LSTN is generally 0.605 Å, while the reduced rLSTN contains traces of Ti^{3+} with an ionic radius of 0.670 Å, further expanding of the cell parameters.[14]

Figure 2b–f displays the microstructures of the as-prepared samples. LSTN shows a relatively smooth surface, as seen in Figure 2b, but after reduction, nano-sized particles are exsolved, resulting in a rough surface of rLSTN (Figure 2c). The scanning transmission electron microscopy (STEM) image and the corresponding energy dispersive spectroscopy (EDS) mapping of rLSTN (Figure 1g and inset) further confirm the homogeneous dispersion of Ni NPs on the perovskite surface. The exsolution on both surface and grain boundaries are observed in the rLSTN sample, which exhibits major differences in terms of NPs size and population: the exsolved NPs inside the grain are much smaller and more numerous compared to the ones on the surface, which reflects different nucleation and growth rates, maybe related to strain associated with the NPs growing within the bulk. More scanning electron microscope (SEM) images corresponding to additional investigations showing exsolved particles of different sizes and surface population relative to changes in reduction temperature and duration are presented in Figure S2 (Supporting Information), while bulk exsolution SEM images are shown in Figure S3 (Supporting Information). Previous studies have already shown this phenomenon and suggested that embedding metal NPs within non-metallic crystal lattices improves the electronic transport in a manner analogous to substitutional aliovalent doping.[15]

Figure 2d–f give an overview of the obtained NiAu bimetallic NPs anchored on the surface of the perovskite hosts after the galvanic replacement reaction. We emphasize that the freshly-made sample shows a ladybug-like morphology, where many small Au NPs (≈2 nm) decorate one Ni particle (Figure 2d), as well as an antenna–reactor-like structure (Figure 2e). The ladybug structure is of high surface energy and a coalescence of the Au NPs takes place, evolving to a nanoflower structure (Figure 2f; Figure S4, Supporting Information) under ambient conditions, typically in the range of several hours to a few days

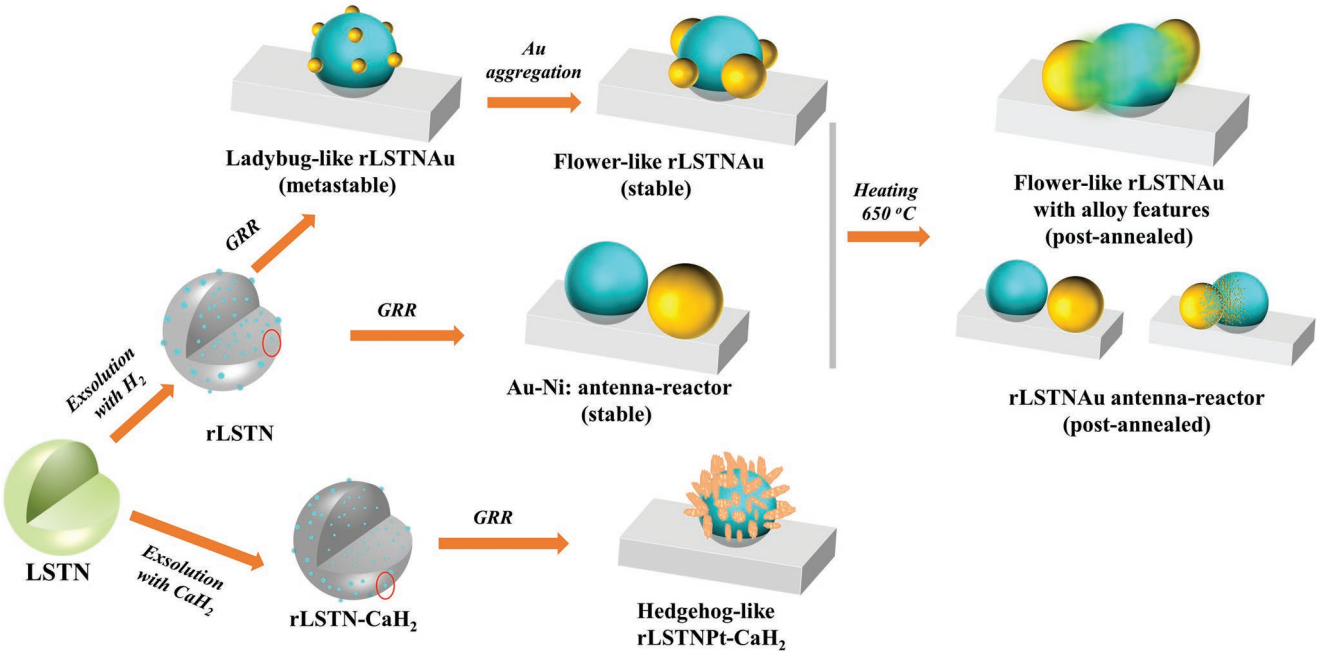

Figure 1. Schematic representation of the observed evolution of NiAu and NiPt bimetallic NPs. Ni exsolution was achieved in H_2 atmosphere (rLSTN) or by CaH_2 (rLSTN-CaH_2). The exsolved Ni NPs were partly replaced by Au or Pt to obtain a mixture of ladybug-like and antenna–reactor rLSTNAu and hedgehog-like rLSTNPt-CaH_2 structures, respectively. The ladybug-like rLSTNAu evolved into the flower-like structure. A subsequent short-time thermal treatment further evolved the different structures, inducing slight alloy features.

after the material is exposed to air. A characteristic STEM image and accompanying energy dispersive spectroscopy (EDS) analysis of a NiAu nanoflower structure can be seen in Figure 2h,i. Additional SEM images of all the structures are shown categorized in Figure S5 (Supporting Information), also being transformed into the corresponding color plots of Figure S6 (Supporting Information). From the color plots we were able to extract the Au and Ni NPs sizes distribution, which are summarized by category in Figure S7 (Supporting Information). In general, we see that the diameter of the Au NPs increases from the ladybug to the flower-like and to the post-annealed structures. The antenna–reactor structures contain the largest in diameter Au NPs and our analysis indicates that the ratio between flower-like:antenna–reactor in both the pre and post annealed rLSTNAu is ≈5:1. Finally, the Au NPs appear overall larger than the Ni NPs, which is expected as they are partially covered by Au NPs.

2.2. Structural Evolution of the rLSTNAu and In Situ Scanning Transmission Electron Microscopy Studies

Structures in the forms of hollow structures, core–shell, yolk–shell, and alloys are the general products of GRR,[8b] but the unique metastable ladybug and flower-like shapes in this study are new. Controlling the selective formation of these structures is challenging, but this creates a new landscape in the synthesis of supported multi-metallic NPs. Currently, they might have derived from i) the high degree of bulk immiscibility between Ni and Au caused by the large lattice mismatch (≈15.7%) and the weak adhesive interaction,[16] and/or ii) corrosion pits on the native and naturally occurring surface oxides/hydroxide on the Ni NPs,[17] as it can also be seen in Figure S8 (Supporting Information), which shows the presence of oxygen on the Ni NP. In spite of the large difference in the reduction potential between metallic Ni and $AuCl_4^-$, Ni atoms first have to migrate through the self-passivating oxide shell, reach the surface and then participate in GRR, which significantly increases the energy barrier. Therefore, the growth of the Au nucleus into a nanoparticle becomes more favorable than forming core-shell or alloy structures on the amorphous surface of Ni oxide. Alternatively, the acidity of the GRR solution may etch away the native oxide/hydroxide layer and form corrosion pits that cause the galvanic Au deposition in the ladybug-like form.

Furthermore, the antenna–reactor-like structure might originate from the coalescence of smaller Au NPs as for the flower-like ones, but only resulting in one Au NP next to the Ni NP. Another possible explanation could be that rLSTN is also participating in the GRR. We have recently shown that when heavily reduced TiO_2 (black TiO_2) was immersed in a solution of Pt (IV) ions, then a spontaneous deposition of well-formed Pt NPs occurred.[18] Our experimental evidence as well as density functional theory (DFT) studies suggest that neutral oxygen vacancies donate electrons to Pt (IV) that consequently grows to Pt NPs of an average diameter of 2 nm. Similarly, this may be the case with the rLSTN sample and nucleation site adjacent to the Ni NPs. Extracting the mechanism behind these transformations, as well as the stabilization of the high energy ladybug-like structures requires further studies.

To gain a better insight into the structural evolution of the rLSTNAu sample (Figure 2), we subjected it to thermal annealing under high vacuum using an in situ sample holder

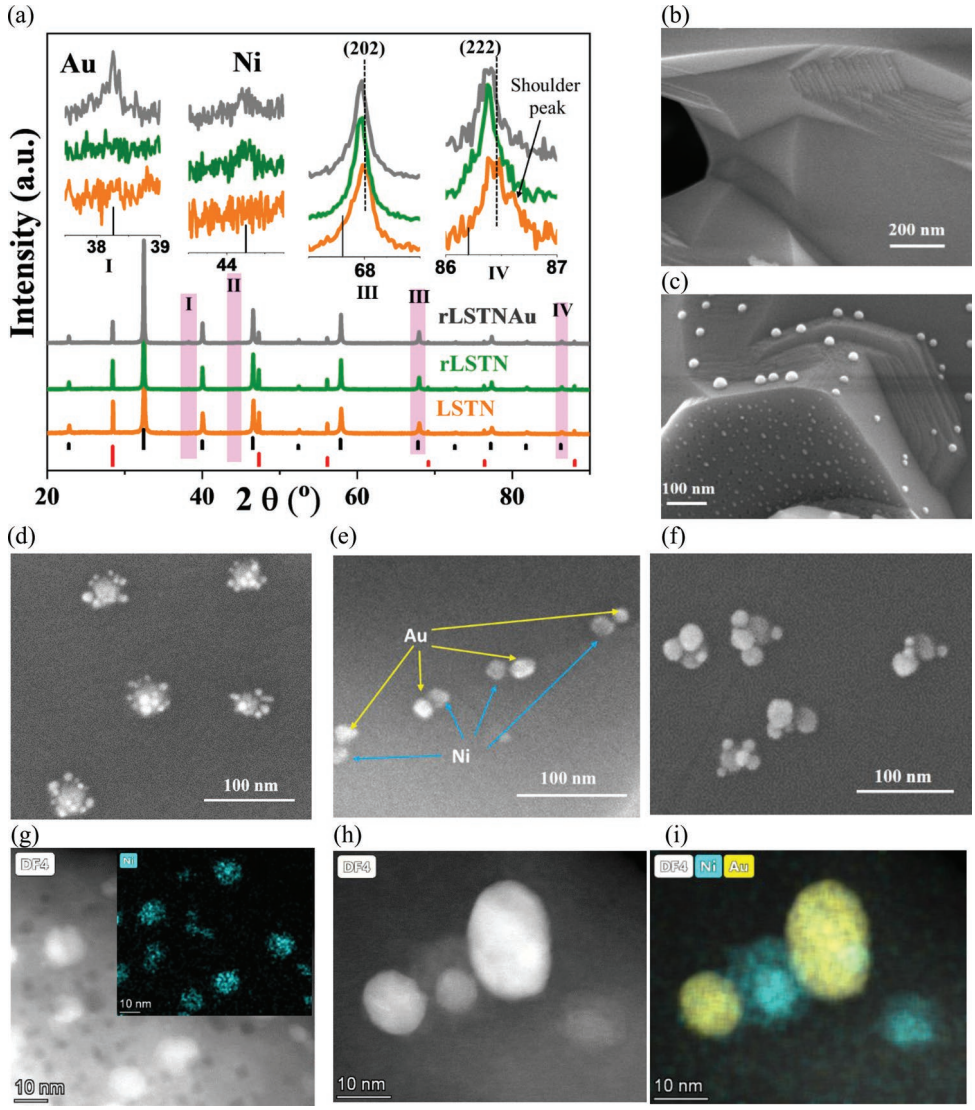

Figure 2. Structural characterization of the nano-engineered LSTN precursor material. a) XRD patterns of LSTN, rLSTN, and rLSTNAu. All the diffractograms are normalized on a scale from 0 to 1. Insets are the enlarged peaks in the specified 2θ angles. The lines underneath the XRD patterns denote the expected peak positions of $SrTiO_3$ (cubic, ICSD 65088, in black) and Si (cubic, ICSD 257794, in red), b) SEM images of LSTN before and c) after exsolution (rLSTN) at 900 °C. d) rLSTNAu after GRR in the metastable ladybug structure. e) rLSTNAu antenna–reactor structure. f) rLSTNAu flower-like structure. g) DF-STEM image of rLSTN and the corresponding EDS mapping of Ni (inset). h) STEM-DF4 pattern of NiAu nanocomposite embedded on perovskite surface, i) the corresponding EDS mapping of the flower-like NiAu structure.

for STEM. It is well-known that binary nanocrystals with various structures (e.g., alloy, core-shell and heterostructure) generally display distinct physical and chemical properties, which further give rise to different performance during reactions.[19] In our case and as displayed in **Figure 3** and Figure S4 (Supporting Information), the flower-like shape gradually developed also a NiAu alloy-containing structure in the post annealed rLSTNAu sample.[20]

The magnified STEM-DF images and the EDS mapping displayed in Figure 3 reveal that Ni and Au NPs stand side by side before heat treatment. It is noted that the snapshots were taken during this dynamic process, reflecting more accurately the structural changes occurring. As the temperature increases to 200 °C, the structural change of Ni and Au NPs is insignificant. A coalescence between particles occurred at 300 °C, where Au appears to diffuse on the surface of rLSTN and wrap around the Ni NPs. A more significant reconstruction begins at 400 °C with an Au layer partially covering the Ni surface. This wrapping might be attributed to the removal of oxygen atoms from the thin NiO layer, leading to the amorphous reconstruction of Ni and Au atoms with partial interdiffusion between Au and Ni atoms.

The above observations demonstrate the outstanding anchorage of exsolved Ni at the perovskite surface, as well as the simple yet intriguing reconstruction of Au around Ni particles. Finally, and already at 600 °C, a partial diffusion of Au atoms into the Ni NPs is seen, accompanied by a slight alloying morphology at higher temperatures (650 °C).[19,20]

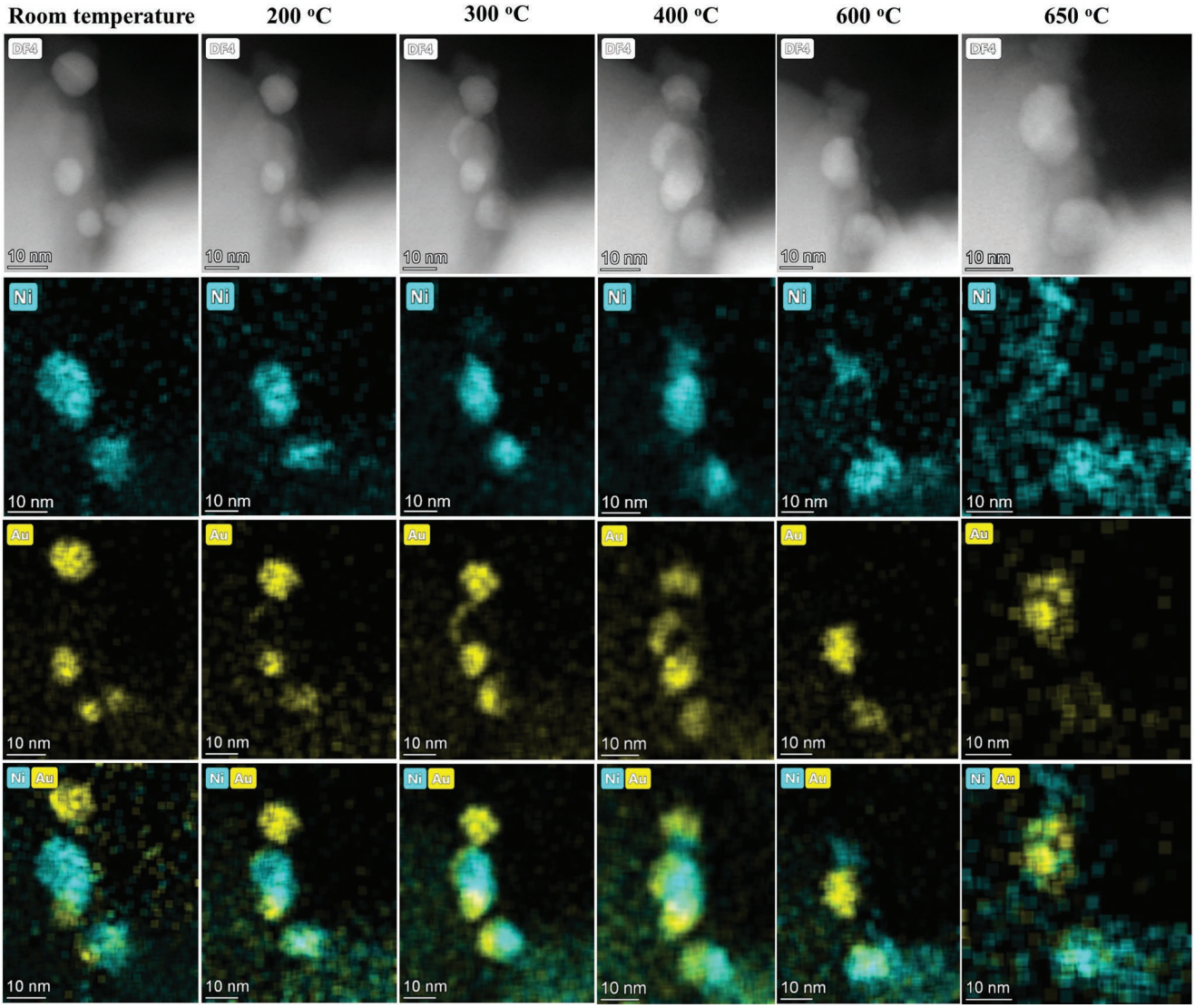

Figure 3. Real time observations via in situ STEM of the temperature-dependent NiAu NPs reconstruction on the perovskite surface. Au has a higher atomic number than Ni and appears brighter in the STEM-DF mode. A series of STEM DF frames and the corresponding EDS maps of the selected NiAu particles on the rLSTN surface with different temperatures are given. The temperature ramp rate was ≈100 °C s^{-1}, and the snapshots were taken after staying after equilibrating at the specific temperatures for a few seconds. Yellow, Au; cyan, and Ni.

2.3. Photoelectrochemical Activity of Post-Annealed rLSTNAu

We studied the PEC water electrolysis performance of the supported NiAu system in 1 M KOH electrolyte under simulated 1 sun illumination and compared it against the LSTN and rLSTN samples. A set of linear sweep voltammograms (LSVs) were recorded, as shown in **Figure 4**a. The photocurrent response during intermittent illumination of constant intervals was spike-free, especially at applied potential >0.5 versus reversible hydrogen electrode (RHE), indicating a good charges carriers separation efficiency in all the samples. On the other hand, the photocurrent density of the rLSTNAu sample (containing both the mixed flower-like and antenna–reactor-like structures) reached 140 mA cm^{-2} at 1.23 V (vs RHE), which is 2.2 and 2.5 times, higher than in the LSTN and rLSTN samples, respectively. To compare the activity of rLSTN and LSTN, we repeated the LSV tests several times with electrodes made in different batches. Statistically, we observed that the improvement of charge current is not obvious after Ni exsolution, which means Ni alone has limited efficacy toward PEC water splitting. The intrinsic defects induced during the reduction process of rLSTN are likely becoming trapping centers for charge annihilation, which may also undermine photocatalytic activities.[21] On the other hand, our novel and facile introduction of Au greatly improved the PEC performance.

We conducted additional PEC measurements in order to further investigate the semiconducting properties of the samples and the interfacial electrochemistry during photoelectrocatalytic testing. Mott–Schottky (M–S) measurements were employed to study the basic mechanism behind the increase in photocurrent density, considering that the slope in the M–S plot is inversely proportional to the donor concentration (N_D) in the

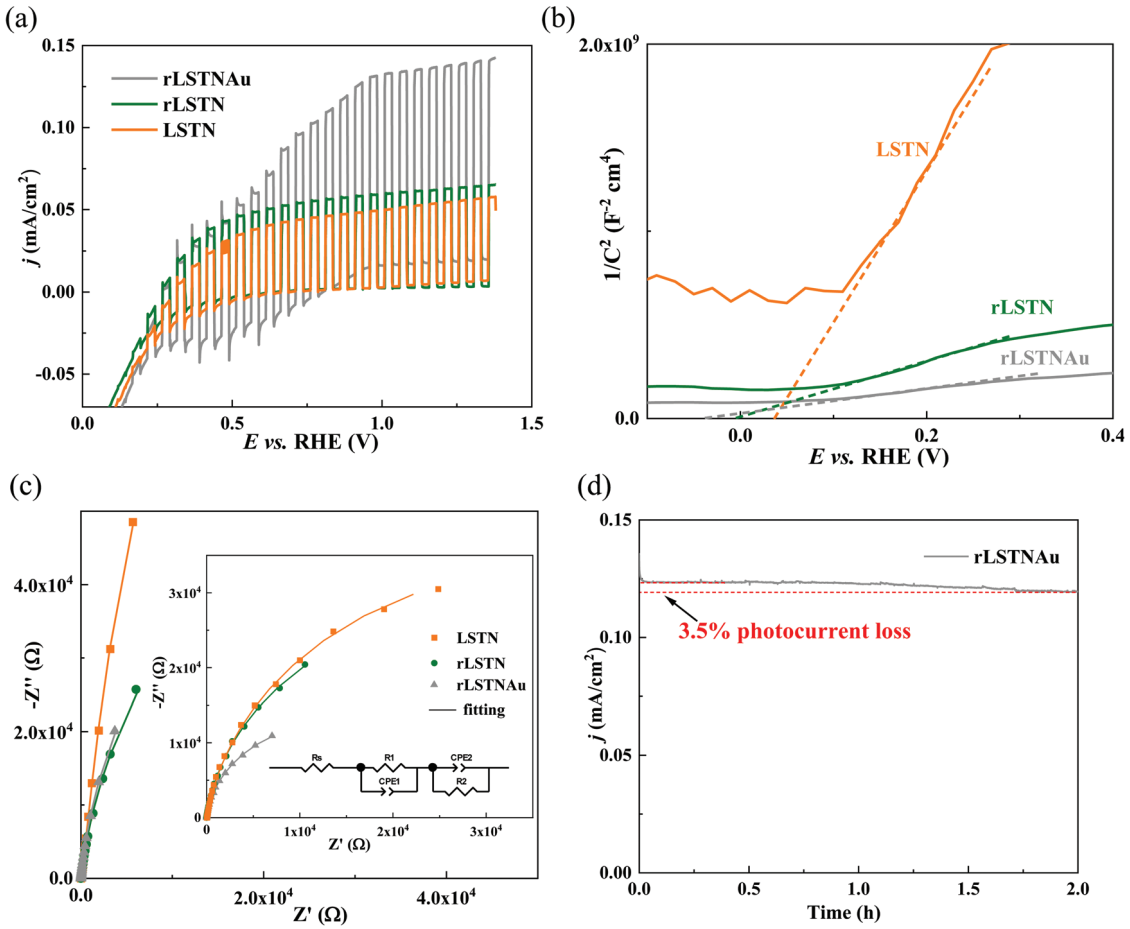

Figure 4. PEC performance of LSTN, rLSTN and rLSTNAu. a) Linear-sweep voltammograms from 0–1.38 V (vs RHE), b) Mott-Schottky plots obtained at 1000 Hz, c) Nyquist plots under dark and illumination (inset) conditions at a bias potential of 1.23 V (vs RHE) under a frequency range from 10^5 to 0.1 Hz with an amplitude of 10 mV. The inset shows also the equivalent circuit used to fit the raw data. d) The chronoamperometric test under 1 sun illumination at 1.23 V (vs RHE) for 2 h.

semiconductor, and the intercept reflects the flat band potential (V_{fb}).[22] M–S plots in Figure 4b indicate the *n*-type conductivity of the as-prepared samples with a positive slope and an S-shape of the curves. Table S1 (Supporting Information) summarizes the slopes and intercept values from the M–S plots. The results show that the donor concentration increased significantly after Ni exsolution (decreasing slope values), which means the electronic properties of the LSTN semiconductor are efficiently improved. The addition of Au further increased the donor density, accompanied by a slight shift of the flat band potential to more negative values (from 60 to –70 mV vs RHE). This means that the Fermi level (E_F) is slightly shifted to more negative energy levels by reduction and exsolution, as well as subsequent Au deposition, altering the intrinsic energy levels of the semiconducting substrate. Together with the plasmonic activity and the improved charge separation in the flower- and antenna–reactor-like structures the PEC performance is enhanced.

To further study and understand the interfacial PEC reaction kinetics and the charge carriers' separation efficiency, electrochemical impedance spectroscopy (EIS) and incident-photon-to-current-efficiency (IPCE) measurements were conducted at an applied potential of 1.23 V versus RHE under dark and illuminated conditions. IPCE measurements given in Figure S9 (Supporting Information) clearly show that the highest IPCE along the whole spectrum range was achieved on the rLSTNAu photoanode. EIS measurements represented by the Nyquist plots of Figure 4c, indicate that the low frequency resistances are much larger in dark conditions than under illumination, representative of slow or even blocking electrode process kinetics.[23] Upon illumination, the low frequency resistances for rLSTN with Ni exsolution is smaller than that of pristine LSTN photoanode, while rLSTNAu shows the smallest resistance (see Table S1, Supporting Information) for the deconvoluted resistance and capacitance data). Therefore, the supported NiAu bimetallic structure possesses the strongest separation efficiency of electron-hole pairs, which is a key factor for high PEC performance. This is also assessed in terms of stability under potentiostatic conditions in strongly alkaline media. As it is seen in Figure 4d, the photocurrent retains 97% of its initial value after 2 h of constant illumination. We performed an additional stability testing and as shown in Figure S10 (Supporting Information), a 10% degradation is observed after 24 h of constant illumination, increasing to 33% after 48 h. These

results indicate a very promising stability of the supported NiAu bimetallic photoanode under strongly alkaline conditions, but further studies are needed to elucidate the degradation mechanism.

3. Mechanistic Insights and Shift in Catalytic Activity

3.1. Structure-Plasmonic Property Correlations

To provide mechanistic insights in the superior PEC performance of the galvanically restructured rLSTN, the plasmonic behavior of the supported NiAu system in the antenna–reactor-like and flower-like structures (will be referred to as "configurations" in the simulations) was studied. Electron energy loss spectroscopy (EELS) was employed and complemented by both Metal NanoParticle Boundary Element Method (MNPBEM) and Finite Difference Time Domain (FDTD) simulations as displayed in **Figure 5**. The dielectric constant of La-doped $SrTiO_3$ (LSTO), as found by Duan et al. for $La_{0.625}Sr_{0.375}TiO_3$,[24] was used in the simulations under the assumption that after Ni exsolution, our substrate, LSTN, is close to LSTO.

The HAADF image and the EDS mapping of Figure 5a depict one Au nanoparticle with a diameter of 21 nm adjacent to a Ni nanoparticle of 16 nm in diameter, a unique configuration considered as antenna–reactor.[6,25] Their relative position on the LSTN particle is given in Figure 5a, together with the region that the EELS spectra were recorded (Figure 5b,c). We observe a prominent excitation from the Au NP (antenna), especially at ≈2.4 eV in the region around the Au NP, but also around the adjacent Ni NP (reactor), as well as between them. This is more evident when looking at the color maps, which represent the number of electrons having lost energy between 2.38 and 2.40 eV, and 2.40 and 2.42 eV, respectively (Figure 5c and Video S1, Supporting Information of EELS spectrum with energies between 1.40 and 4.00 eV).

Figure 5d shows the simulated loss probability (P_{loss}) map of a Au NP on an LSTO NP at energies close to the LSPR energy of Au in vacuum. The highest loss in the simulated map is found at the edge of the Au NP pointing away from LSTO. This is similar to what the experimental EELS map shows. Furthermore, Figure 5e shows the P_{loss} map of a Ni and Au NPs touching at 1.85 eV and not touching at 2.4 eV. Most of the loss is clearly around the Au NP at 2.4 eV, while for the touching case, there is an additional mode at 1.85 eV which has the highest loss at the part of the particle diametrically opposite from their intersect. The average simulated P_{loss} spectra in 5f, from the areas marked in 5e, show an LSPR peak in both the Au and the Ni NPs at the Au's LSPR energy (2.4 eV) for both the touching case and the not touching case. The peak at 2.4 eV in the Ni NP in both simulations and the measured EELS spectra indicate that the energy absorption of the Ni nanoparticle is enhanced due to the adjacent Au NP. The absence of gap between the particles does not seem to change the absorption in Ni due to the main Au plasmon peak at 2.4 eV. The appearance of the extra peak at 1.85 eV was investigated with additional simulations and its energy was found to be dependent on the amount of overlap between the particles. In Figure S11 (Supporting Information) the peak is shifted between 1.65 and 2.00 eV, indicating that a small change in the particles' overlap will shift the peak energy significantly.

Additional simulations confirm the antenna–reactor effect due to the electromagnetic coupling effect between Au and Ni NPs.[26] An increase in absorption is present both for a Ni NPs in water and surrounded by water but embedded on LSTO (Figure 5g,h), a configuration that closely resembles the PEC experiments. The absorption of the Ni reactor increases with increasing Au size and decreasing inter-particle distance (Figures S12 and S13, Supporting Information). Moreover, we observe that the absorption in the Au NP is also increased by the presence of the Ni NP (Figure 5i). It seems that the presence of the Ni NP can compensate for the lower absorption when Au is embedded on LSTO compared to only surrounded by water. A possible explanation for the lower Au absorption when embedded in LSTO is that an energy transfer occurs from the excited Au NPs to the immediate surroundings of LSTO, visualized as a broadening and lowering of the LSPR peak. Although the Ni NPs are expected to have a NiO_x shell (refer to Figure S8, Supporting Information), especially under anodic PEC water splitting conditions, FDTD simulations still indicate a strong antenna–reactor effect of Au on a core-shell Ni-NiO NP (Figure S12, Supporting Information). Interestingly, we see that the absorption cross section of the Ni NP with an oxide layer is larger than a Ni NP without an oxide layer, here shown for the extreme case with an oxide thickness of 3 nm.

In the flower-like configuration, which is expected to contribute to the PEC performance in synergy with the antenna–reactor one, Au NPs grow around the Ni particle with some of the Au NPs being in direct contact with Ni (Figure S4, Supporting Information). Therefore, FDTD simulations were done for Ni NPs that are surrounded by a random number of Au NPs of different sizes, in accordance with the SEM and STEM observations (Figure 2; Figures S4–S7, Supporting Information). In a hypothetical situation where the Ni NPs are removed, the simulations indicate that the absorption is higher and the Q-factor is larger than that in the presence of Ni NPs (Figure S14, Supporting Information) but the difference is small. Although any antenna–reactor effects are not expected due to electron tunneling,[26] we did see electron energy losses in the Ni NPs earlier at ≈1.85 and 2.40 eV (simulations), but also in the EELS spectra (experimental data) in Figure S15 (Supporting Information) and corresponding EELS (Video S1, Supporting Information). Based on these experimental evidences we can conclude that the charge transfer between the two metals does not completely hinder absorption in either NP. A similar system where the antenna NPs/single atoms are in contact with the reactor have been reported by Zhou et al., in a CuRu, antenna(Cu)–reactor(Ru) system.[6a] More importantly, our calculations in Figure S14e–g (Supporting Information) show that the electric field is boosted when Au NPs approach each other as compared to isolated ones. Therefore, the plasmonic flower-like and antenna–reactor hybrid structures, which can now be facilely realized and further developed through our reported methodology, can produce more effective photocatalysts than singly supported plasmonic NPs.

To complement our EELS and simulation studies with additional experimental evidence, we conducted diffuse-reflectance

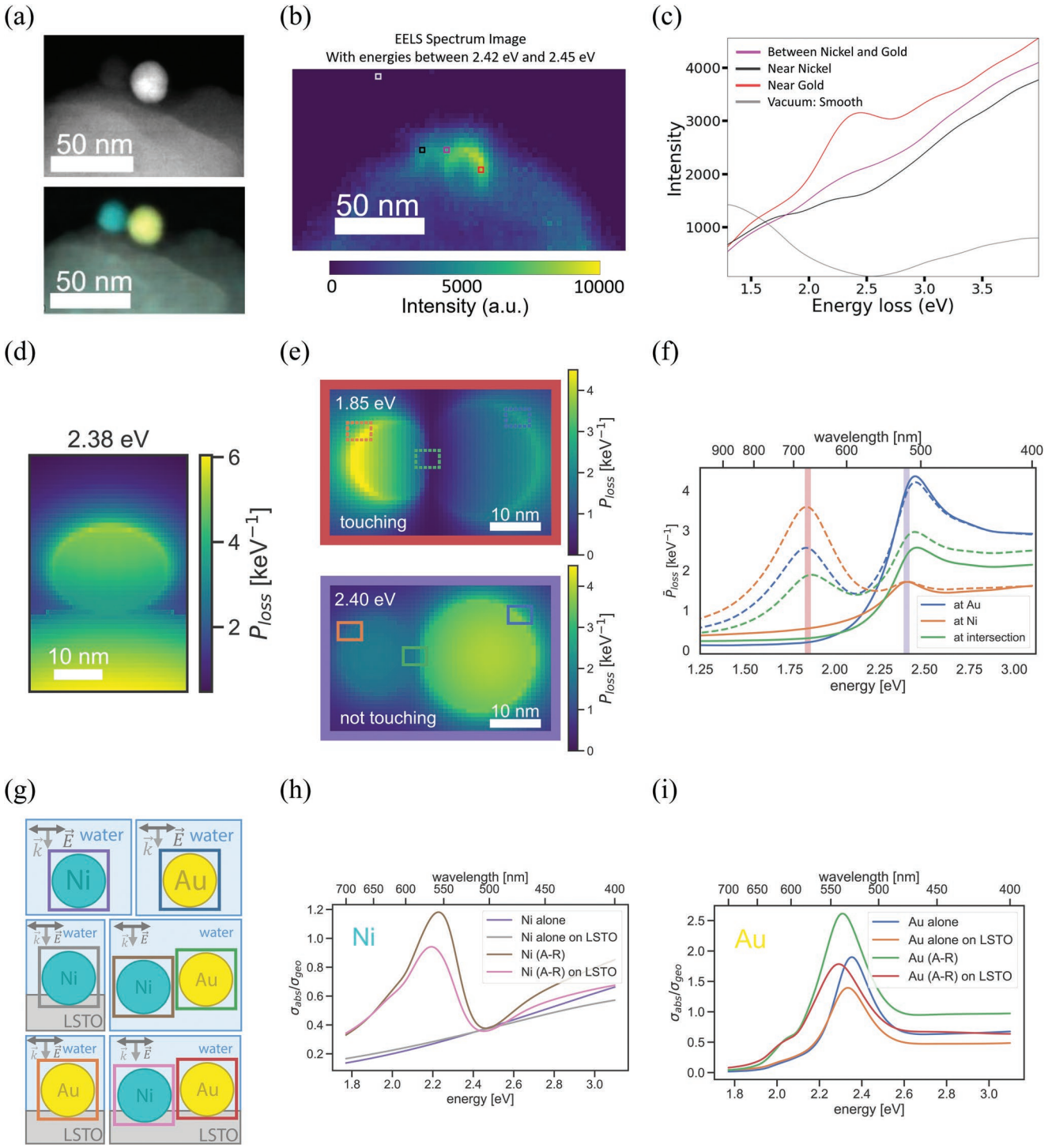

Figure 5. EELS and MNPBEM and FDTD simulations. a) HAADF-STEM and the corresponding EDS image of rLSTNAu in a bimetallic antenna–reactor-like configuration. b) EELS map at energy of Au LSPR mode, i.e., ≈2.4 eV. c) EELS spectral components of the specific antenna–reactor configuration at positions shown in (b). Simulated loss probability maps of d) Au on LSTO NP (diameter 100 nm) near LSPR energy and e) simulated loss map of Ni NP (left) and Au NP (right) touching (i.e., the Au NP is pertruding into the Ni NP) at 1.85 eV and with a small gap (1 nm) at 2.40 eV. f) Simulated loss probability spectra at positions marked in (e), the touching case (dashed lines) and the not touching case (solid lines). g) Different configurations used to calculate absorption cross-sections of example antenna–reactor. The absorption cross-sections normalized by the geometrical cross-section for Ni and Au NPs in different situations are shown in h) and i), respectively.

spectroscopy (DRS), steady-state photoluminescence (PL), and time-resolved photoluminescence (TRPL) measurements (**Figure 6**).

The differential DRS spectra of Figure 6a show the increased extinction in the visible region with maximum at ≈2.4 eV, a direct

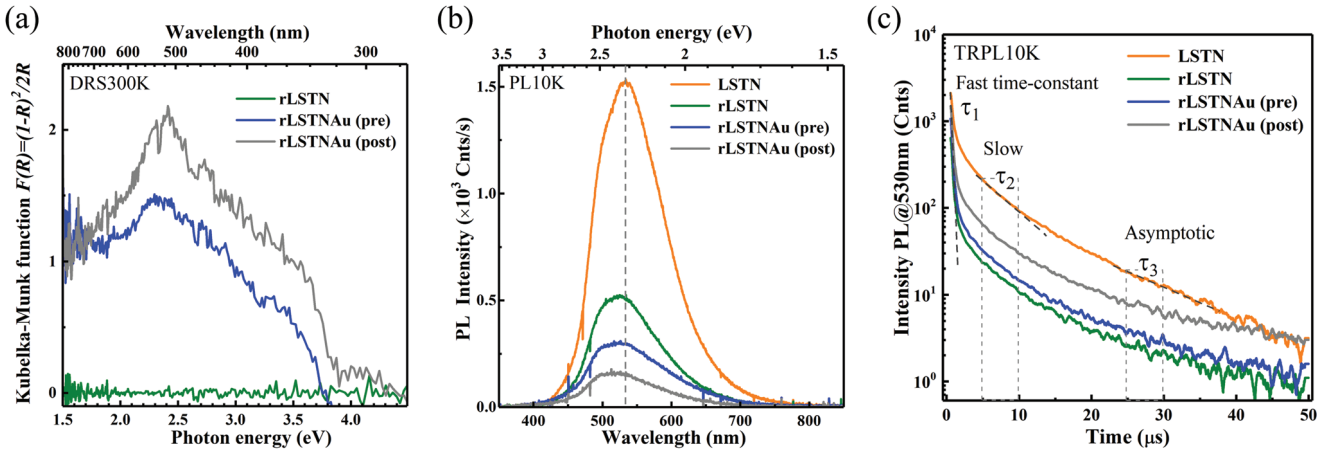

Figure 6. Optical absorption and emission properties of LSTN, rLSTN, rLSTNAu (pre annealed) and post-annealed rLSTNAu. a) Kubelka–Munk function (absorbance) derived from differential diffuse-reflectance with reference to rLSTN ($R_{diff} = R_{\#} / R_{rLSTN}$), b) steady-state PL emission spectra obtained at 10 K, c) TRPL transients revealing non-exponential dynamics of the photo-excited carrier recombination ascribed by three decay time constants.

proof of plasmonic effect due to Au incorporation that appears further enhanced by postannealing. The results are consistent with the fact that excitation of LSPR in Au NPs results in an extreme concentration of light and an enhanced electric field around the nanostructures, leading to the significant enhancement in absorption and scattering efficiencies for photons at the resonant energy.[27] As our experimental particle structures have a large variety of overlapping between the particles, as well as sizes, we do not expect to see a distinct peak at 1.85 eV in measurements like PL or DRS. Instead, the differently overlapping particles might result in a broad peak or shoulder in the region ≈1.6 to 2.0 eV, but we do not see such evidence clearly. This could be attributed to a) increased overlap between Ni and Au NPs and/or b) increasing ratio between the radius of Ni and Au NPs (Figure S11, Supporting Information), red-shifting their peak energy. On the other hand, the magnitude of each contribution is currently unknown and necessitates further studies. The steady-state PL spectra in Figure 6b show that the Au incorporation leads to significant decrease of the quantum efficiency as compared to LSTN. The likely cause of the quenched PL is that the photoexcited electrons from the conduction band of LSTN are being transferred of to the Fermi level of the Au NPs, the plasmonic absorption region of which overlaps with that of LSTN emission. The dynamics of this mechanism is elucidated by the TRPL measurements (Figure 6c). The shortest lifetime (τ_1) observed for rLSTN-Au (Table S4, Supporting Information) might be associated either with extra non-radiative pathway due to deterioration of crystallinity upon Au incorporation (which is unlikely according to the XRD analyses), or to plasmonic effect leading to LSPR-enhanced charge transfer between the Au NPs and LSTN. More information and additional DRS and TRPL results can be found in Note S2, Figures S26 and S27 and Table S4 (Supporting Information).

3.2. Shift of Catalytic Activity to Hydrogen Evolution Reaction with NiPt Bimetallic NPs

In order to generalize our method, we galvanically hybridized Ni NPs with platinum (Pt) through the GRR method for the synthesis of a hydrogen evolving catalyst. We remind that in this case a highly conducting substrate material is desired, therefore the reduction of LSTN was done in the presence of CaH_2 (refer to experimental and electrochemical activity of rLSTNPt part in Figures S16–S23, Supporting Information). Impedance measurements confirm that the conductivity of the reduced LSTN by CaH_2 (rLSTN-CaH_2) is greatly improved compared to the LSTN, as well as rLSTN (Figure S17, Supporting Information). As displayed by the SEM, HAADF-STEM, and EDS analyses of **Figure 7**a,b, Pt deposits grow on the Ni NPs with a morphology similar to a hedgehog-like structure. It is noted that the rLSTN-Pt sample shows also a hedgehog-like structure as seen in Figure S18 (Supporting Information). Compared to our plasmonic NiAu structures, the lattice mismatch of Ni and Pt is smaller (≈11%), with a less significant difference in electronegativity and atomic radius, which results in a narrowed miscibility gap. Therefore, unlike Au that tends to form isolated NPs, Pt is more likely to grow around the Ni NPs, and the inter-diffusion of Ni and Pt atoms at their interface should happen easier. The obtained hybrid NiPt hedgehog-like structure shows an exceptional improvement of the electrochemical performance of the rLSTNPt sample for the HER in 0.1 M KOH. An overpotential of −320 mV versus RHE at 10 mA cm^{-2} represents a high electrocatalytic activity toward the HER approaching that of the state-of-art and commercial Pt-C HER catalyst. The Tafel slope of 135 mV dec^{-1} indicates the Volmer reaction as the rate determining step, which is also the case for the Pt-C with a Tafel slope of 114 mV dec^{-1}. The superior performance of the Pt-C is attributed to the much higher Pt content and superior conductivity of carbon. The peak in the underpotential deposition region of hydrogen atoms (UPD-H) was used in acidic conditions (0.1 M $HClO_4$),[28] and the estimated electrochemically active surface area (ECSA) of Pt-C is ≈1.2 cm^2, while for rLSTNPt-CaH_2 is only ≈0.03 cm^2, that can be directly correlated to a significantly lower Pt amount (factor of 40) in the rLSTNPt-CaH_2.

To further support this, we estimated the double layer capacitance, which is a direct measure of the ECSA, in the non-faradaic region by cyclic voltammetry (CV) and impedance

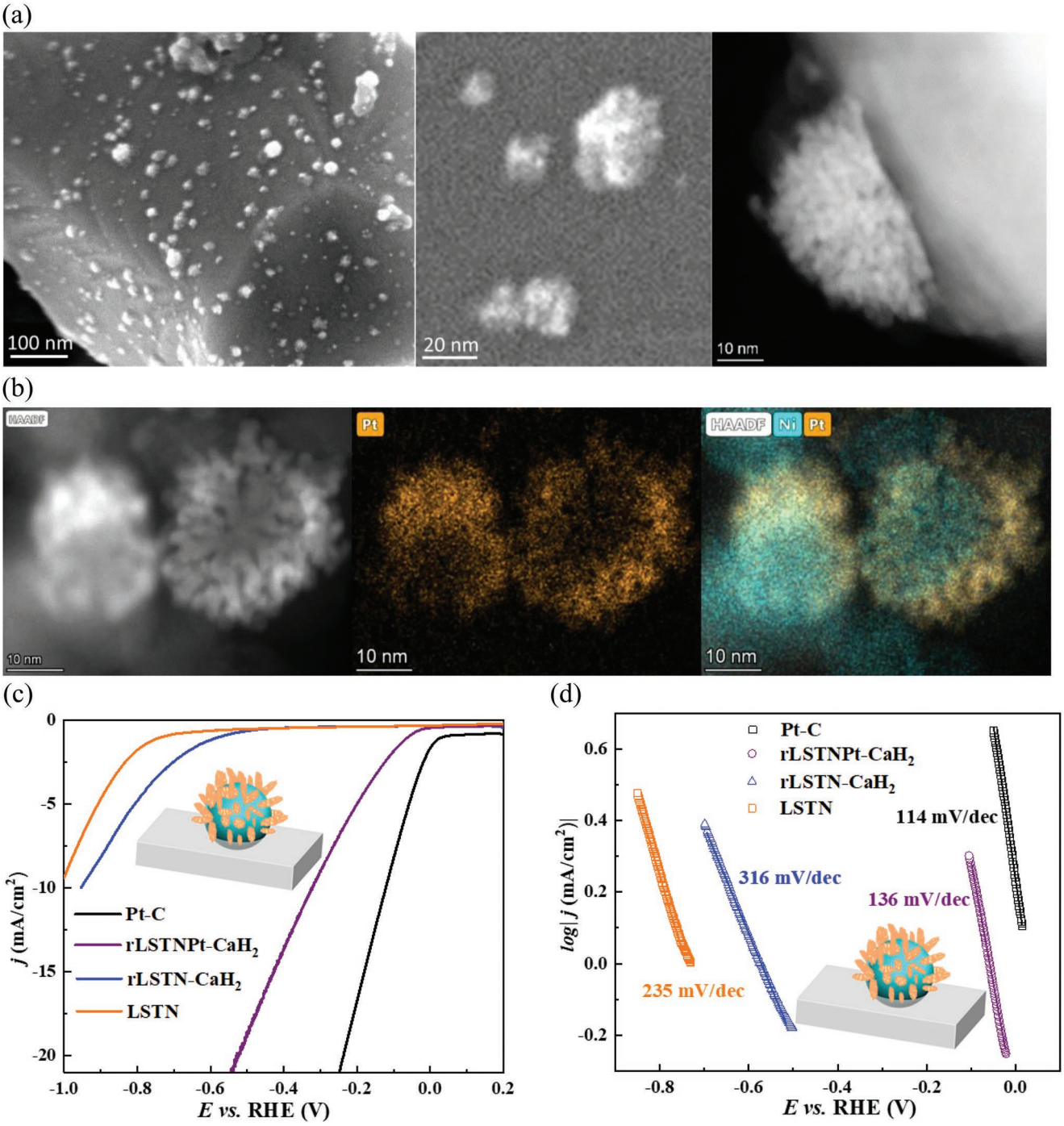

Figure 7. Structural observations and electrochemical performance of Pt-nano-engineered LSTN. a) SEM images of rLSTN-CaH_2 after reduction with CaH_2 at 600 °C, showing the exsolved Ni NPs. b) HAADF-STEM images and EDS maps of rLSTNPt-CaH_2 after galvanic replacement with $PtCl_6^-$ in 0.1 M $HClO_4$, revealing the coexistence of Ni and Pt in a hedgehog-like morphology. c) LSV curves and d) Tafel slopes of the perovskite-based samples and the commercial Pt-C electrocatalyst. The potential scanning rate was 10 mV s^{-1} in 0.1 M KOH electrolyte.

spectroscopy. Table S3 (Supporting Information) shows that both methods give the same trends in double layer capacitances between the LSTN-based and Pt-C samples. Notably, a factor of ≈24 by the CV method indicates again the much larger ECSA of the Pt-C, which can also be seen in its nanostructure (Figure S24, Supporting Information). Finally, rLSTNPt-CaH_2 shows good stability under galvanostatic operation at –10 mA cm^{-2}, and a 20% increase in the overpotential is seen after 48 h of operation in 0.1 M KOH (Figure S25, Supporting Information). A partial loss of powder from the carbon support is also responsible for the overpotential increase and apparent instability of the material.

4. Conclusions

This work introduces a new method to prepare functional bimetallic hybrid nanostructures supported on perovskite surfaces, such as on $SrTiO_3$, with minimal engineering and high catalytic versatility. In situ metal exsolution followed by galvanic replacement and deposition can easily stir the catalytic activity from plasmonic photocatalysis (NiAu NPs supported on LSTN) to hydrogen evolving cathodes (NiPt NPs supported on LSTN), by merely deciding on composition of the galvanic replacement solution. Our approach opens up tremendous opportunities in the synthesis of well-adhered and supported bi- or multi-metallic, catalytically active NPs of improved activity and tunable properties and structures. Optimization of the different synthesis parameters will further improve the control for targeted hybrid structures, like core-shell, antenna–reactor, and multi-metallic alloys with the desired catalytic properties beyond water splitting through minimal engineering and amounts of both precious and non-critical elements.

5. Experimental Section

Synthesis of Supported Ni-Based Bimetallic Catalysts: The samples were synthesized by a modified solid-state route using high purity precursors, including $Ni(NO_3)_2{\cdot}6H_2O$, La_2O_3 (dried at 800 °C), $SrCO_3$, and TiO_2 (both dried at 300 °C). The dried powders were weighed while hot (nickel nitrate was cold) in the appropriate stoichiometric ratios for the composition $La_{0.6}Sr_{0.2}Ti_{0.9}Ni_{0.1}O_{3-x}$ and mixed in a beaker with acetone. The mixture underwent ultrasonic treatment to break down agglomerates. The acetone was evaporated under continuous stirring to ensure further homogenization, and then the powder was pressed into a pellet and calcined at 1000 °C for 12 h. The calcined powder was crushed and ball-milled for 2 h at 250 rpm, and then pressed into a pellet again for the second sintering at 1100 °C for 12 h. The final perovskite powders were prepared by repeating the above step for the third time calcination at 1200 °C for 10 h.

The exsolution process was carried out in a ProboStat cell (NORECS, Norway) under continuous pure H_2 gas flow at atmospheric pressure and calcined at various temperatures, the resulting sample was donated as rLSTN. The Ni exsolution was also achieved for the first time by mixing LSTN powder and CaH_2 in a molar ratio of 1:3 (rLSTN-CaH_2). Then the mixture was pelletized and put in an ampoule, which was sealed under vacuum ($<5.0 \times 10^{-2}$ bar). The sample was heated at 600 °C for 3 days, and then washed in methanol containing 0.1 M NH_4Cl to remove the CaO and the excess CaH_2.

The bimetallic nanostructures were prepared via a facile galvanic replacement reaction. Typically, the freshly prepared exchange solution containing 2.5 mL gold ion precursor (1×10^{-3} M HCl + 1×10^{-3} M $HAuCl_4$, pH = 3) and 1 mL PVP (1×10^{-3} M) was deaerated by N_2 bubbling for 20 min at 80 °C. Then, the as-synthesized rLSTN powders were dispersed into the solution, during which the spontaneous Ni dissolution and Au deposition occurred:

$$3Ni + 2AuCl_4^- \rightarrow 2Au + 3Ni^{2+} + 8Cl^- \quad (1)$$

The standard chemical potential of $AuCl_4^-$ ($E^0(AuCl_4^-/Au)$ = 1.002 V vs the standard hydrogen electrode (SHE)) was much higher than Ni (E^0 (Ni^{2+}/Ni) = − 0.257 V vs SHE), rendering a very fast replacement. The reaction lasted for only 1 min, and was quenched immediately by cold deionized water. The final powders (rLSTNAu) were collected and washed with deionized water. The removal of oxygen and a moderate acidic atmosphere during replacement reaction were crucial for efficient and fast noble metal deposition, avoiding the more favorable oxygen reduction reaction (E^0 (O_2/H_2O) = 1.23 V vs SHE) or even the possible competitive hydrogen evolution reaction (E^0 (H^+/H_2) = 0 V vs SHE). The elevated temperature and a short reaction period not only enhanced the reaction kinetics, but also ensured the decoration of those tiny Au nanocrystals on the Ni surface instead of aggregating.

In order to obtain rLSTNPt-CaH_2 from rLSTN-CaH_2 powders, the $HAuCl_4$ solution was replaced with a H_2PtCl_6 solution. Considering the different standard chemical potentials,

$$E^0(PtCl_6^{2-}/Pt) = 0.744 \text{ V vs SHE} \quad (2)$$

the time was adjusted to 5 min to ensure a sufficient reaction.

Characterizations: The phase purity and crystal structure of the prepared perovskites as well as bimetallic nanostructures were confirmed by room temperature X-ray diffraction (XRD, Bruker D8 Discover, Cu $K_{\alpha 1}$, Bragg-Brentano). Si powders were used to correct the instrumental peak-shifting. Rietveld refinement analysis was conducted using Topas software. The following parameters were gradually unlocked and refined: background (Chebyshev coefficient, 5–9 terms), peak shape, unit cell parameters, atomic coordinates, site occupancies, thermal displacement parameters, and microstrain. The pseudocubic perovskite cell parameter a_p (*A*) was calculated as: $a_p = \sqrt[3]{\frac{V}{4}}$, where *V* is the volume of the perovskite unit cell calculated from Rietveld refinement. Scanning electron microscopy (SEM, Hitachi SU8230 ultra-high resolution cold-field emission SEM equipped with a secondary electron (SE) detector under an acceleration voltage of 5 kV) was used to image the series of nanostructures, calculating the particle size distribution and population. As the ladybug structure was metastable and quickly evolved to the flower-like (see Section 2.1), SEM for the ladybug was done right after the high temperature reduction process.

STEM and high-resolution EELS were performed using an FEI Titan G2 60–300 instrument. The instrument was equipped with a CEOS DCOR corrector for the probe forming lenses, a Wien-filter monochromator, a Gatan 965 Quantum EELS spectrometer, and the FEI Super-X EDS detector. For structural and chemical characterization, the instrument was operated at an accelerating voltage of 300 kV, with a probe convergence semi-angle of 21 mrad. The inner collection semi-angle was 101, 22, and 9 mrad for the HAADF, DF4, and DF2 detector, respectively. Surface plasmon mapping was done at 60 kV with an energy resolution of ≈110 meV as measured using the full-width-half-maximum (FWHM) of the zero loss peak. In situ heating experiments were performed using the Protochips Fusion 350 double-tilt sample stage. The stage utilizes resistive ceramic heating chips, each individually calibrated by the manufacturer to an accuracy of better than 5%. A stability better than 0.01 °C is guaranteed by the manufacturer. The temperature uniformity across the viewing area of the chip is better than 99.5%, and the displacement after a temperature ramp of 325 °C was <7 nm, with an ultimate drift rate of 0.5 nm min^{-1}. It is important to note that all the specifications were stated by the manufacturer, and were not individually verified.

The EELS maps were analyzed using a custom made Python code, utilizing the hyperspy package.[29] The zero-loss peaks were aligned to 0 eV, and the energy resolution determined by measuring the FWHM. Subsequently, the background was subtracted for each individual plot, fitted to a suitable energy range. A Gaussian filter with a width matching the energy resolution was used to deconvolute the spectra further. To visualize the peaks in the energy loss spectra for all pixels, an integration was performed over a tiny energy range. This range was set to three times the energy resolution. The integrated values were plotted as contour plot using the matplotlib library,[30] and the videos (Videos S1 and S2, Supporting Information) were made by combining the individual frames. Moreover, individual spectra from marked pixels were plotted.

The optical absorption properties were investigated at room temperature by means of DRS using EVO-600 (Thermo Fisher Scientific, Inc.) UV–Vis spectrophotometer. The emission properties were attained by steady-state PL measurements carried out at 10 K in a CCS450 (Janis Research Company, LLC) closed-cycle He refrigerator system and using a 325 nm wavelength He–Cd cw-laser as an excitation source

(power density <10 W cm^{-2}). The luminescence was collected by a microscope and analyzed by USB4000 (Ocean Optics, Inc.) fiber-optic spectrometer with a spectral resolution below 2 nm. The recombination and trapping dynamics of the photo-excited carriers were assessed by TRPL measurements performed at 10 K by employing 372 nm wavelength ps-laser (PicoQuant LDH375, 50 ps-pulsed 2mW @40MHz) as an excitation source. The selected spectral region was filtered out from the total PL signal using imaging spectrograph (HORIBA Jobin Yvon, iHR320) and registered by photon counting system (PicoQuant NanoHarp250, Becker&Hickl PMC100).

Catalyst Performance Evaluation: PEC measurements were performed on a standard three-electrode set up with NaOH (1 M, pH 13.6) as the electrolyte, Hg/HgO and a platinum foil as the reference electrode and counter electrode, respectively. The working electrodes containing the investigated catalysts were prepared as follows: adding 100 mg of powder in a mixture of 2.5 mL water, 1.25 mL isopropanol, and 30 µL of 5 wt.% Nafion, followed by the sonication for 3 h to obtain a homogeneous ink. Applying 50 µL of ink on the Ti foil (1 cm^2) by the drop-cast method and then anneal at 600 °C under an inert atmosphere for 0.5 h to achieve the stable reconstructed nanostructure, in addition to a better adhesion with the Ti foil substrate. All the tests were conducted by a Gamry Reference 3000 potentiostat, under 1 sun simulated solar light from a Newport Oriel LCS-100 solar simulator equipped with a 100 W ozone-free xenon lamp and an AM 1.5G filter. The light intensity was regularly calibrated by a monocrystalline Si PV reference cell (Newport 91150V-KG5). All over potentials are corrected against the RHE taking into account that water electrolysis takes place thermodynamically at 1.23 V versus RHE. Therefore, the potentials were corrected versus RHE according to the Nernst Equation:

$$E_{RHE} = E_{meas.} + 0.059\ V \times pH + 0.121\ V \quad (3)$$

Photocurrent at the applied bias of 1.23 V vs RHE was measured as a function of wavelength for the calculation of IPCE with the following equation:

$$IPCE = \frac{j_p 1240}{\lambda I_0} \quad (4)$$

where j_p is the photocurrent density (mA cm^{-2}), λ is wavelength of the incident light in nm, and I_0 is the wavelength dependent intensity of incident light (mW cm^{-2}).

The electrochemical measurements were also carried out following a similar procedure with the above PEC test. A rotating disc electrode (RDE) with glassy carbon (GC) as the tip (RDE710 Rotating Electrode from Gamry Instruments) was used as the working electrode, a standard Hg/HgO as the reference and a graphite rod as the counter electrodes. The supporting electrolyte was 0.1 M aqueous KOH solution. The RDE was coated with the as-prepared catalyst ink according to the procedure suggested by S. Jung et al.[31] The inks were drop-cast on the GC tip (0.196 cm^2) by applying 4 µL of ink and then dried for 10 min at 60 °C. This procedure resulted in the loading of ≈0.5 mg of the electrocatalyst on the GC. For long-term stability experiments, the same amount of powder (≈0.5 mg) was loaded by drop-casting on C paper of a nominal surface area of 1 cm^2 with a mass loading of 0.5 mg cm^{-2}.

Simulation Details: The simulations of surface plasmons excited by a light source were performed with Ansys Lumerical's FDTD software, which uses the FDTD method to solve Maxwell's equations. The source used was the Total field/Scattered field (TSFS) source and the absorption was calculated using the frequency-domain field and power monitors. The monitors were placed as indicated in the illustration in Figure 5g. The electric field of the plane wave source was parallel to the surface of LSTO and pointing from one NP to the other in the cases with two NPs. The simulation region was meshed using a nonuniform mesh with a mesh size of 0.8 nm (A-R) and 0.75 nm (flower) within the TSFS source region. One simulation of the antenna–reactor configuration with mesh size 0.5 nm was tested and resulted in a peak height change of 3% for Ni and 1% for Au. This test-simulation gave an absorption peak energy blue-shift for Ni of 0.02 eV, and for the Au absorption spectra, a small change in shape where the small peak at lower energies, ≈2 eV, became less prominent. The same test simulation was done for one of the flower-configurations which resulted in a 3% change in peak height and a less prominent peak at 2 eV. The rest of the region was meshed automatically with mesh accuracy 4. Conformal variant 0 was used and all boundaries were set to be absorbing using perfectly matched layers.

The simulations of surface plasmons excited by an electron beam source, i.e., the calculation of P_{loss}, were done using MNPBEM.[32] The simulations were performed with a retarded solver and using curved particle boundaries. The Au, Ni and LSTO NPs were made using the trispheresegment-function. In the antenna–reactor (A–R) configuration, the Ni (Au) sphere surface was discretized using 21 (32) mesh points for theta and 16 (24) for phi. While for the Au NP on a LSTO NP and the touching A–R configuration the amount of overlap between the NPs was defined with an overlap angle of 0.2 π and 0.1 π from the center of the Au NP, respectively (see Figure S11, Supporting Information for an overlap angle explanation). The surfaces of the spheres were discretized using 21 mesh points for theta and 16 for phi. The segment representing the boundary between the Au and the LSTO was defined with 16 mesh points for phi and 6 for theta. For the EELS simulations it had a beam size of 0.32 and a velocity that corresponded to 60 keV. The dielectric functions used for Au and Ni within FDTD was from Lumerical's database which has them from the CRC Handbook of Chemistry and Physics, and the one used for LSTO was extracted using WebPlotDigitalizer developed by Rohatgi.[24,33] The same dielectric function for LSTO was used within the MNPBEM simulations, but for Au and Ni dielectric functions from Johnson and Christy were used.[34]

Supporting Information

Supporting Information is available from the Wiley Online Library or from the author.

Acknowledgements

X.K. acknowledges support by the China Scholarship Council (201806060141). A.C. and Ø.P. acknowledge The Research Council of Norway for support through the projects PH2ON (288320), and FUNCTION (287729), respectively. Support to the Norwegian Center for Transmission Electron Microscopy was also acknowledged (NORTEM 197405/F50). D.N. gratefully acknowledges the Royal Society for the grant RGS/R1/211253.

Conflict of Interest

The authors declare no conflict of interest.

Author Contributions

X.K. synthesized all materials, performed experiments and wrote the original draft. V.M.R. performed all calculations and contributed to writing, review, and editing. K.G.B. performed TEM and EELS measurements and analyses, did the color plots and particle size analyses and contributed to writing, review and editing. A.G. performed and analyzed all DRS and PL measurements. T.A. performed TEM and in situ TEM measurements. Ø.P. did supervision and contributed insights to TEM and EELS. T.N. did supervision, provided resources, and contributed to review and editing. D.N. provided insights and contributed to writing, review, and editing and A.C. conceptualized and supervised the work, did project management and administration, provided insights and contributed to writing, review, and editing.

Data Availability Statement

The data that support the findings of this study are available from the corresponding author upon reasonable request.

Keywords

antenna–reactor, electrocatalysis, exsolution, galvanic replacement, hybrid nanoparticles, photocatalysis, plasmons

Received: February 19, 2022
Revised: May 7, 2022
Published online:

[1] a) C. H. Wu, C. Liu, D. Su, H. L. Xin, H.-T. Fang, B. Eren, S. Zhang, C. B. Murray, M. B. Salmeron, *Nat. Catal.* **2019**, *2*, 78; b) N. Danilovic, R. Subbaraman, K. C. Chang, S. H. Chang, Y. Kang, J. Snyder, A. P. Paulikas, D. Strmcnik, Y. T. Kim, D. Myers, V. R. Stamenkovic, N. M. Markovic, *Angew. Chem. Int. Ed. Engl.* **2014**, *53*, 14016; c) X.-Z. Song, L. Qiao, K.-M. Sun, Z. Tan, W. Ma, X.-L. Kang, F.-F. Sun, T. Huang, X.-F. Wang, *Sens. Actuators, B* **2018**, *256*, 374.

[2] a) J. E. Bruno, N. S. Dwarica, T. N. Whittaker, E. R. Hand, C. S. Guzman, A. Dasgupta, Z. Chen, R. M. Rioux, B. D. Chandler, *ACS Catal.* **2020**, *10*, 2565; b) W. Zhan, J. Wang, H. Wang, J. Zhang, X. Liu, P. Zhang, M. Chi, Y. Guo, Y. Guo, G. Lu, S. Sun, S. Dai, H. Zhu, *J. Am. Chem. Soc.* **2017**, *139*, 8846; c) C. H. Wu, C. Liu, D. Su, H. L. Xin, H.-T. Fang, B. Eren, S. Zhang, C. B. Murray, M. B. Salmeron, *Nat. Catal.* **2018**, *2*, 78; d) J. Ahn, L. Zhang, D. Qin, *ChemNanoMat* **2019**, *6*, 5.

[3] Q. Zhang, J. Li, X. Liu, Q. Zhu, *Appl. Catal., A* **2000**, *197*, 221.

[4] a) R. Reichert, Z. Jusys, R. J. Behm, *J. Phys. Chem. C* **2015**, *119*, 24750; b) K. Awazu, M. Fujimaki, C. Rockstuhl, J. Tominaga, H. Murakami, Y. Ohki, N. Yoshida, T. Watanabe, *J. Am. Chem. Soc.* **2008**, *130*, 1676.

[5] S. Wang, Y. Gao, S. Miao, T. Liu, L. Mu, R. Li, F. Fan, C. Li, *J. Am. Chem. Soc.* **2017**, *139*, 11771.

[6] a) L. Zhou, J. M. P. Martirez, J. Finzel, C. Zhang, D. F. Swearer, S. Tian, H. Robatjazi, M. Lou, L. Dong, L. Henderson, P. Christopher, E. A. Carter, P. Nordlander, N. J. Halas, *Nat. Energy* **2020**, *5*, 61; b) D. F. Swearer, H. Zhao, L. Zhou, C. Zhang, H. Robatjazi, J. M. P. Martirez, C. M. Krauter, S. Yazdi, M. J. McClain, E. Ringe, E. A. Carter, P. Nordlander, N. J. Halas, *Proc. Natl. Acad. Sci. USA* **2016**, *113*, 8916.

[7] E. González, J. Arbiol, V. F. Puntes, *Science* **2011**, *334*, 1377.

[8] a) G. G. Li, Z. Wang, H. Wang, *ChemNanoMat* **2020**, *6*, 998; b) X. Xia, Y. Wang, A. Ruditskiy, Y. Xia, *Adv. Mater.* **2013**, *25*, 6313.

[9] A. Papaderakis, N. Pliatsikas, C. Prochaska, G. Vourlias, P. Patsalas, D. Tsiplakides, S. Balomenou, S. Sotiropoulos, *J. Phys. Chem. C* **2016**, *120*, 19995.

[10] D. Neagu, G. Tsekouras, D. N. Miller, H. Menard, J. T. Irvine, *Nat. Chem.* **2013**, *5*, 916.

[11] a) A. G. M. da Silva, T. S. Rodrigues, S. J. Haigh, P. H. C. Camargo, *Chem. Commun.* **2017**, *53*, 7135; b) J. Zhang, M.-R. Gao, J.-L. Luo, *Chem. Mater.* **2020**, *32*, 5424; c) J. H. Kim, J. K. Kim, J. Liu, A. Curcio, J. S. Jang, I. D. Kim, F. Ciucci, W. Jung, *ACS Nano* **2021**, *15*, 81.

[12] X. Liu, P. Carvalho, M. N. Getz, T. Norby, A. Chatzitakis, *J. Phys. Chem. C* **2019**, *123*, 21931.

[13] S. Krishnamurthy, A. Esterle, N. C. Sharma, S. V. Sahi, *Nanoscale Res. Lett.* **2014**, *9*, 627.

[14] G. Tsekouras, D. Neagu, J. T. S. Irvine, *Energy Environ. Sci.* **2013**, *6*, 256.

[15] K. Kousi, D. Neagu, L. Bekris, E. I. Papaioannou, I. S. Metcalfe, *Angew. Chem.* **2020**, *132*, 2531.

[16] S.-B. Duan, R.-M. Wang, *Rare Met.* **2016**, *36*, 229.

[17] C. R. Stilhano Vilas, Boas, J. M. Sturm, W. T. E. van den Beld, F. Bijkerk, *Materialia* **2021**, *20*, 101203.

[18] A. Touni, X. Liu, X. Kang, P. A. Carvalho, S. Diplas, K. G. Both, S. Sotiropoulos, A. Chatzitakis, *ChemSusChem* **2021**, *14*, 4993.

[19] C. Cai, S. Han, W. Liu, K. Sun, L. Qiao, S. Li, X. Zu, *Appl. Catal., B* **2020**, 260.

[20] a) S. Zhou, H. Yin, V. Schwartz, Z. Wu, D. Mullins, B. Eichhorn, S. H. Overbury, S. Dai, *ChemPhysChem* **2008**, *9*, 2475; b) H. Nishikawa, D. Kawamoto, Y. Yamamoto, T. Ishida, H. Ohashi, T. Akita, T. Honma, H. Oji, Y. Kobayashi, A. Hamasaki, T. Yokoyama, M. Tokunaga, *J. Catal.* **2013**, *307*, 254; c) M. Schnedlitz, M. Lasserus, R. Meyer, D. Knez, F. Hofer, W. E. Ernst, A. W. Hauser, *Chem. Mater.* **2018**, *30*, 1113; d) G. Zhao, J. Huang, Z. Jiang, S. Zhang, L. Chen, Y. Lu, *Appl. Catal., B* **2013**, *140–141*, 249.

[21] B. Liu, X. Zhao, J. Yu, I. P. Parkin, A. Fujishima, K. Nakata, *J. Photochem. Photobiol., C* **2019**, *39*, 1.

[22] a) M. Tayebi, A. Tayyebi, B.-K. Lee, *Catal. Today* **2019**, *328*, 35; b) C. Fleischer, A. Chatzitakis, T. Norby, *Mater. Sci. Semicond. Process.* **2018**, *88*, 186.

[23] T. Lopes, L. Andrade, H. A. Ribeiro, A. Mendes, *Int. J. Hydrogen Energy* **2010**, *35*, 11601.

[24] Y. Duan, P. Ohodnicki, B. Chorpening, G. Hackett, *J. Solid State Chem.* **2017**, *256*, 239.

[25] C. Zhang, H. Zhao, L. Zhou, A. E. Schlather, L. Dong, M. J. McClain, D. F. Swearer, P. Nordlander, N. J. Halas, *Nano Lett.* **2016**, *16*, 6677.

[26] K. Sytwu, M. Vadai, J. A. Dionne, *Adv Phys X* **2019**, *4*,1619480

[27] F. Wang, Y. R. Shen, *Phys. Rev. Lett.* **2006**, *97*, 206806.

[28] P. Daubinger, J. Kieninger, T. Unmussig, G. A. Urban, *Phys. Chem. Chem. Phys.* **2014**, *16*, 8392.

[29] F. de la Peña, E. Prestat, V. Tonaas Fauske, P. Burdet, T. Furnival, P. Jokubauskas, J. Lähnemann, M. Nord, T. Ostasevicius, K. E. MacArthur, D. N. Johnstone, M. Sarahan, J. Taillon, T. Aarholt, V. Migunov, A. Eljarrat, J. Caron, T. Poon, S. Mazzucco, B. Martineau, S. Somnath, T. Slater, C. Francis, N. Tappy, M. Walls, N. Cautaerts, F. Winkler, G. Donval, v1.6.4 ed., Zenodo, **2021**.

[30] J. D. Hunter, *Comput. Sci. Eng.* **2007**, *9*, 90.

[31] S. Jung, C. C. L. McCrory, I. M. Ferrer, J. C. Peters, T. F. Jaramillo, *J. Mater. Chem. A* **2016**, *4*, 3068.

[32] a) U. Hohenester, A. Trügler, *Comput. Phys. Commun.* **2012**, *183*, 370; b) U. Hohenester, *Comput. Phys. Commun.* **2014**, *185*, 1177; c) J. Waxenegger, A. Trügler, U. Hohenester, *Comput. Phys. Commun.* **2015**, *193*, 138.

[33] a) D. W. Lynch, R. Rosei, J. H. Weaver, *Solid State Commun.* **1971**, *9*, 2195; b) A. Rohatgi, WebPlotDigitizer, Pacifica, CA, USA **2021**; c) J. R. Rumble, *CRC Handb. Chem. phys.*, CRC Press, Boca Raton, FL **2017**.

[34] a) P. B. Johnson, R. W. Christy, *Phys. Rev. B* **1972**, *6*, 4370; b) P. B. Johnson, R. W. Christy, *Phys. Rev. B* **1974**, *9*, 5056.

Paper II

Ni-doped A-site excess SrTiO3 thin films modified with Au nanoparticles by a thermodynamically-driven restructuring for plasmonic activity

Kevin G. Both, Vilde M. Reinertsen, Thomas M. Aarholt, Ingvild J. T. Jensen, Dragos Neagu, Øystein Prytz, Truls Norby, Athanasios Chatzitakis*

Submitted to *Catalysis Today*
Special Issue: SPEA 11

II

The Research Council of Norway is acknowledged for the support to the Norwegian Center for Transmission Electron Microscopy (NORTEM, no 197405/F50), the NANO2021 researcher project FUNCTION (no. 287729) and FRINATEK project PH2ON (288320).

Ni-doped A-site excess $SrTiO_3$ thin films modified with Au nanoparticles by a thermodynamically-driven restructuring for plasmonic activity

Authors

Kevin G. Both,[1] Vilde M. Reinertsen,[2] Thomas M. Aarholt,[2] Ingvild J. T. Jensen,[3] Dragos Neagu,[4] Øystein Prytz,[2] Truls Norby,[1] Athanasios Chatzitakis[1*]

Affiliations

(1) Centre for Materials Science and Nanotechnology, Department of Chemistry, University of Oslo, Gaustadalléen 21, NO-0349 Oslo, Norway

(2) Centre for Materials Science and Nanotechnology, Department of Physics, University of Oslo, P. O. Box 1048 Blindern, NO-0316, Oslo, Norway

(3) SINTEF Materials Physics, Forskningsveien 1, NO-0373 Oslo, Norway

(4) Department of Chemical and Process Engineering, University of Strathclyde, 75 Montrose St, G1 1XJ, Glasgow, United Kingdom

[*]corresponding author: athanasios.chatzitakis@smn.uio.no

Abstract

Plasmonically active nanoparticles offer a promising pathway to extend the absorption range of photocatalysts. While not necessarily catalytically active themselves, these particles allow the absorption of lower energy photons in wide band gap photocatalysts. Here, we present A-site excess $SrTiO_3$ thin films, doped with Ni, where through a subsequent exsolution process we created well socketed Ni nanoparticles in the surface of $SrTiO_3$. These were galvanically replaced by Au, resulting in well-socketed Au nanoparticles with variable size on the surface, depending on the galvanic replacement time. Photoelectrochemical measurements and electron energy loss spectroscopy revealed the improved photoresponse of the thin films by plasmonic activity of the nanoparticles. The energy of the plasmon peak suggests that the main improvement results from the injection of hot charge carriers. Our study opens new avenues for the design and synthesis of the next generation of photocatalytic materials.

1. Introduction

The continued interest in renewable energy sources has led to a plethora of directions to improve the energy harvest efficiency and the energy storage [1–8]. One approach is the utilization of photons to obtain a chemical product by converting the photon energy to chemical energy via a photocatalyst. Photocatalysts are widely investigated for many applications, such as water splitting, environmental remediation, and other uses, each one with specific requirements [2,3,9]. For example, solar water splitting requires a semiconductor with a bandgap of at least 1.23 eV, and taking into account any additional overpotential due to kinetic and thermodynamic losses, this results in an ideal band gap energy of 1.8 – 2.3 eV [2,3,10]. Another key requirement for practical applications is stability, where most stable semiconductors have a bandgap larger than 2.3 eV, ultimately limiting their light absorption capacity, and, consequently, their efficiency [2,3,11]. A promising pathway to enhance the light absorption capacity of a photocatalyst is to combine it with materials exhibiting plasmonic activity. Transfer of photon induced plasmonic energy to the semiconductor can amplify the photoconversion from photonic to chemical energy [12].

The localized surface plasmon resonance (LSPR) is generated on metal nanoparticles (MNPs) on the surface of a semiconductor photocatalyst upon illumination [2]. These MNPs can act as light absorbing antennas or photosensitizers [12], where MNPs and their nanostructures with dimensions significantly smaller than the wavelength of light will have a narrow absorption

bands in the visible range of the spectrum [13]. The energy of the LSPR can be transferred from the MNP to the semiconductor by three major mechanisms: (i) light scattering/trapping, (ii) plasmon-induced energy transfer (PIRET), and (iii) hot electron injection [8,11]. The effectiveness of the three decay mechanisms for each particle is directly dependent on its size, shape and chemical composition [2,14]. The size distribution, surface states, surface coverage, and surrounding environment of these nanoparticles influence the bandwidth, peak height and position of the absorption maximum [13,15,16], making them ideal for photosensitization of semiconductors [17]. Hence, to predict the results across a macroscopic sample it is imperative to control the size distribution and shape of the particles. The combination of plasmonic MNPs and the semiconductor, forming a heterojunction, affects the photoconversion by introducing four different effects: (i) strong light absorption, (ii) intensive far-field light scattering, (iii) abundant hot carrier generation, and (iv) plasmonic heating effects [2,9,12,13,17]. The short lifetime of the excited intraband transitions remains a challenge for the effective utilization of the plasmonic energy of MNPs [2].

We have recently presented a new synthesis method for supported, well-adhered MNPs [18] and here we extend our method to thin films and A-site excess defective perovskite oxides. We wanted to generalize the concept of exsolution beyond A-site deficient and stoichiometric perovskite by utilizing A-site excess perovskites. A-site excess perovskites typically have Ruddlesden-Popper (RP) interlayers to accommodate the excess A-site ions. In contrast to A-site deficient perovskites there are no inherent A-site vacancies and lower amounts or most likely non-existent oxygen vacancies in the perovskite-like blocks on the RP phase. This creates a host matrix in which metal exsolution is potentially less thermodynamically driven by evolution towards a stoichiometric variant compared to A-site deficient structures [19]. However, A-site excess perovskite might bring kinetic improvements owing to improved ion diffusion in the interlayer region, potentially leading to better control over particle distribution and their “socketing” depth in the surface of the host semiconductor. Exsolving gold (Au) on A-site excess strontium (STO, $Sr_{1+x}Ti_{1-x}Ni_xO_3$) is considered unfeasible due to the difficulty of dissolving Au in ionic state in a host perovskite oxide due to the size-coordination preference of Au ions compared to those of typical A or B ions. Meanwhile, the exsolution of nickel (Ni) particles has been studied extensively [20–22], but Ni does not have significant plasmonic activity [14]. However, plasmonically active Au particles can be introduced by galvanic replacement reaction (GRR) where Ni particles serve as template for Au.

Our method can introduce well-adhered and distributed Au MNPs by galvanically replacing existing MNPs of Ni formed through exsolution that are "socketed" in the surface of the host perovskite material. This electroless process utilizes Ni as the sacrificial template, which is oxidized by a solution containing Au ions. The latter are reduced and deposited on the surface of the template, replacing the original, "socketed" Ni particles [23–26]. The major advantage is that Au MNPs can by this method be embedded in the perovskite surface, a process otherwise very difficult. Partially embedded Au MNPs on glass substrates through a melting procedure have previously been reported to show enhanced stability, while still being able to create charge carriers where they are needed, mainly near the oxide surface, in order to drive chemical reactions [27,28]. We have studied the latter by means of Finite-Difference Time-Domain (FDTD) and our result indicate a strong relation between light absorption efficiency and depth of the socketed Au MNPs in the surface of A-site excess $SrTiO_3$ thin films.

2. Experimental

A pellet of Ni-doped, A-site excess strontium titanate ($Sr_{1.07}Ti_{0.93}Ni_{0.07}O_{3-\delta}$, STO(Ni)) was prepared by the solid-state reaction method. The appropriate amounts of precursor powders ($SrCO_3$ 99%, (1% Ba) Johnson Matthey GmbH, CAS: 1633-05-2; TiO_2, anatase, Sigma Aldrich, CAS:1317-70-0; and $Ni(NO_3)_2 \cdot 6H_2O$, 99.999%, Sigma Aldrich, CAS: 13478-00-7) were weighed to obtain 2.5 g of STO(Ni), powder. The precursors were crushed and ball milled in an agate jar with agate balls for 3 h at 300 rpm in de-ionized water (DI H_2O), dried under stirring and subsequently calcined at 450 ℃ for 4 h. The calcined powder was crushed and again ball milled in DI H_2O, dried, pressed to a pellet of 20 mm in diameter, and finally sintered at 1100 ℃ for 12 h.

The pellet was used as target to deposit STO(Ni) films on silicon (Si) wafers by pulsed laser deposition (PLD, Surface-Tec system, laser: Coherent COMPex Pro 205F, KrF, wavelength: 248 nm) at 600 ℃ substrate temperature. The chamber was evacuated, and oxygen gas was used to reach a pressure of 0.005 mbar throughout the process. The target was irradiated with 3.0 J cm^{-2} at a repetition rate of 10 Hz with the distance between the target and substrate being 9 cm. A total of 20,000 shots were applied.

The deposited thin films were then placed in a ProboStat™ sample holder cell (NorECs AS, Norway) in a hydrogen/argon mix (5% H_2, 95% Ar, HArmix) atmosphere. After an initial flushing for 15 min at room temperature, the temperature was raised to 800 ℃, with a ramp rate of 5 ℃ min^{-1} and kept at 800 ℃ for 30 min before it was cooled down to room temperature

with 5 °C min^{-1}. The described procedure leads to samples with the highest Ni metal signal in XPS (see Fig. S1a). Unless otherwise stated this procedure was followed and the reduced thin films with Ni MNPs will be referred to as STONi.

While the sample was cooling, a solution of 1 mM $HAuCl_4$ in 1 mM HCl was heated to 77 °C in a double jacketed beaker connected to a thermostated water bath. The STONi samples were then immediately transferred from the ProboStat™ to the solution, and kept there for 5 s, 30 s and 90 s, thereafter denoted as samples STONiAu5s, STONiAu30s, and STONiAu90s, respectively. Subsequently, each sample was removed for the replacement solution, rinsed with DI H_2O, dried in air, and stored under ambient conditions for analysis.

The analysis consisted of electron microscopy (scanning electron microscopy (SEM) and scanning transmission electron microscopy (STEM), Fei Tecnai-G2 60-300 instrument), including the Energy-Dispersive X-ray Spectroscopy (EDS) and Electron Energy Loss Spectroscopy (EELS), X-ray Photoelectron Spectroscopy (XPS, Kratos Axis Ultra DLD, monochromated A1 Kα), X-ray Diffraction (XRD, Bruker D8 Discover, Cu $K_{\alpha 1}$, Bragg-Brentano), and photoelectrochemical (PEC) measurements (the sample architecture and experimental setup are shown in Fig. S2, while the supplementary text contains additional details for the STEM, SEM and XPS analyses). PEC measurements were performed with an Ivium Vertex potentiostat/galvanostat in a standard three-electrode set up (Fig. S2a) in 0.5 M Na_2SO_4 (pH = 7.5) as the electrolyte, a saturated calomel electrode (SCE) and a platinum foil as the reference and counter electrodes, respectively. Details for the preparation of the working electrodes can be found in Fig. S2b. All PEC tests were performed under 1 sun simulated solar light, supplied by a Newport Oriel® LCS-100 solar simulator, equipped with a 100 W ozone-free xenon lamp and an AM 1.5G filter. The light intensity was regularly calibrated by a monocrystalline Si PV reference cell (Newport 91150V-KG5). All potentials were corrected against the reversible hydrogen electrode (RHE) according to Equation 1:

$$E_{RHE} = E_{meas.} + 0.059 \times pH + 0.242\ V \quad (1)$$

The FDTD calculations were performed in the Ansys Lumerical FDTD Solutions software [29] using the total-field/scattered-field (TFSF) source. A mesh size between 0.2 and 0.8 nm was used, depending on the size and depth of the nanoparticle, in a mesh override region covering the TFSF source region. The number was chosen to be smaller for smaller particles and particles with a smaller depth since these result in geometrical details of small sizes. A non-uniform mesh with a mesh accuracy of 4 was used for the rest of the simulation region, which spanned

1000 nm in every direction. Perfectly matched layers with 8 layers were used as boundary conditions together with two symmetry planes to decrease the computed region. Also, conformal variant 1 was used. The absorption was calculated from a square box of monitors positioned around the MNP, which implies that the absorption includes the STO encapsulated by the box near the MNP surface. Two different permittivity data used to model both Au [30,31], and Ni [32,33] which are all from Lumerical's Material Database [34] that has the data from CRC Handbook of Chemistry & Physics, Handbook of optical Constants of Solids I – III by E. Palik and Johnson and Christy. Two different permittivity data were also employed for STO; one was extracted from ab initio calculations, i.e., Duan et al. [35] with the help of WebPlotDigitizer [36], and the other was from Dodge [37].

3. Results and Discussion

The structure of the resulting thin films was studied before and after the GRR step by STEM, XRD and SEM. Fig. 1 shows multiple bright field STEM (BF-STEM) images combined with EDS maps, where the Si substrate is at the bottom of each image. In Fig. 1a, a bright field (BF) image overlayed with Ni EDS of STO(Ni) is shown. No columnar growth of the film is seen – the film appears nanocrystalline – and no Ni-rich areas are visible, implying high homogeneity. The XRD measurement of a non-exsolved thin film (Fig. 2a, black line) also shows no distinct peaks beyond the ones attributed to the substrate (Si). Fig. 1(b-e) show the BF overlayed with Ni and Au EDS of STONi, STONiAu90s, STONiAu30s, and STONiAu5s samples, respectively. Here, a columnar structure of the thin film and Ni particles in all the thin films is clearly visible (see also Fig. S3–S5). Au particles are on top, or located in macro-pores, where the Au-solution was able to penetrate the thin film during GRR. The longer the galvanic replacement reaction, the larger the Au MNPs were. The diameters of the original Ni particles were less than 25 nm, while the Au MNPs in the studied areas were 10 – 25 nm, 20 – 50 nm and > 40 nm in diameter, for the STONiAu5s, STONiAu30s and STONiAu90s samples, respectively. Moreover, for the longest replacement time the particles took a non-spherical shape (Fig. 1c), yielding multiple absorption peaks in the low-loss spectra of the EELS data, depending on the location of the beam as we will show later. Backscatter electron (BSE), top-view SEM images (Fig. S6) indicate the presence of Au in the STONiAu5s, STONiAu30s and STONiAu90s samples (bright nanoparticles). They also indicate an increase in the MNPs' density and average size from the STONiAu5s to the STONiAu30s, while no significant increase in their density is seen in the STONiAu90s. This agrees well with the shape change of

the MNPs in this sample, indicating that most, if not all of the initially exsolved Ni MNPs were replaced by Au already in the STONiAu30s sample and further grown in STONiAu90s.

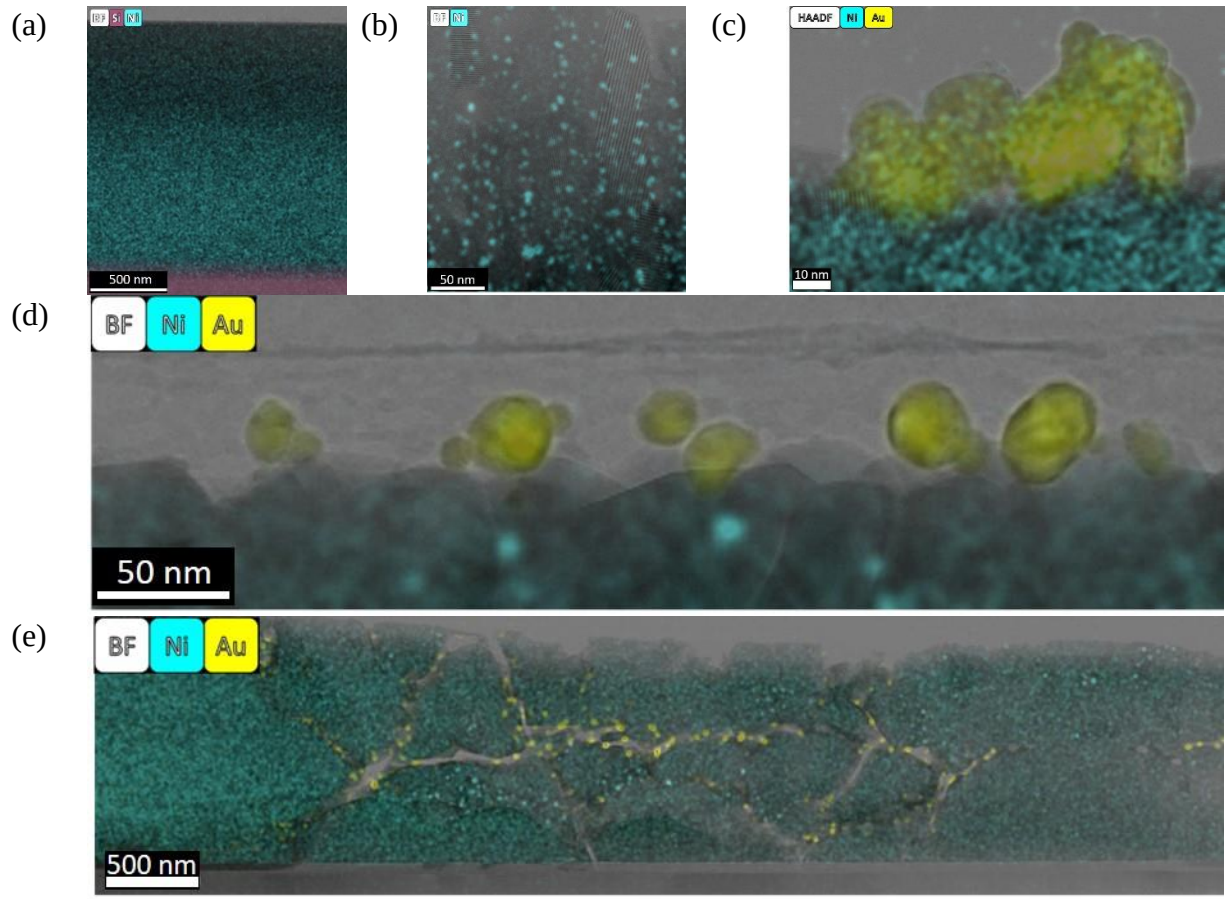

Figure 1: BF-STEM cross sectional images with overlayed Si, Ni and Au EDS of (a) STO(Ni), (b) STONi, (c) STONiAu90s, (d) STONiAu30s and (e) STONiAu5s. Additional high resolution STEM images of STONiAu5s can be found in Fig. S7 in the SI.

The XRD patterns in Fig. 2a show the diffraction patterns of the as-deposited, exsolved and galvanically replaced STNOAu5s, STNOAu30s, STNOAu90s thin films. The absence of any peak but the substrate peaks in the non-exsolved sample indicates either a nanocrystalline or amorphous sample. The BF-STEM images in Fig. 1(a-e) confirm that non-exsolved and exsolved samples are different in that the columnar structure appears only in samples exsolved at 800 ℃, but not in the non-exsolved specimen (see also Fig. S8–S13). The noticeable exceptions are peaks attributed to the Si substrate, see Fig. S8. All the exsolved patterns show a multitude of peaks, including peaks of $SrTiO_3$ (PDF 01-070-8508), with secondary phases identified as $3SrO{\cdot}SiO_2$ (PDF 00-010-0026), the RP phase Sr_2TiO_4 (PDF 00-039-1471), TiO_2 (PDF 01-070-8501), and naturally the Si substrate (PDF 01-078-6300). The secondary phases may form locally due to favorable interaction with the substrate ($3SrO{\cdot}SiO_2$), or local stoichiometry (Sr_2TiO_4, TiO_2). STO peaks are present and are the most dominant ones after the Si peaks in all the samples. Their relative height and the absence of various peaks from different

patterns indicate that the growth of crystal domains is only experiencing a weak templating effect by the substrate. In summary, the XRD and STEM images show exsolution in all thin films, independently of the different crystal orientations and phases present.

In Fig. 2b, the XPS measurements of a STO(Ni) and STONi exsolved in HArmix for 30 min are presented. The XPS results are indicative of the formation of metallic Ni (853 eV) in the reduced sample when compared to the as deposited one, in which no metallic Ni was detected. As expected, the metallic Ni peak is decreasing in intensity (Fig. 2b) while the Au 4f double peak is increasing (Fig. 2c) with increasing immersion times during GRR, in good agreement with the increase in the Au particle size. The Au 4f peaks shift to higher binding energies for increasing Au particle size. The shapes of the peaks are similar and hence do not suggest that the shift is caused by chemical phase changes. Differential effects of charge compensation on the Au MNPs and the STO substrate could be an explanation (see details of the measurements in supplementary note 2). More work is needed to determine the physical significance of the observed shift in the Au 4f peaks relative to the STO peaks.

(a)

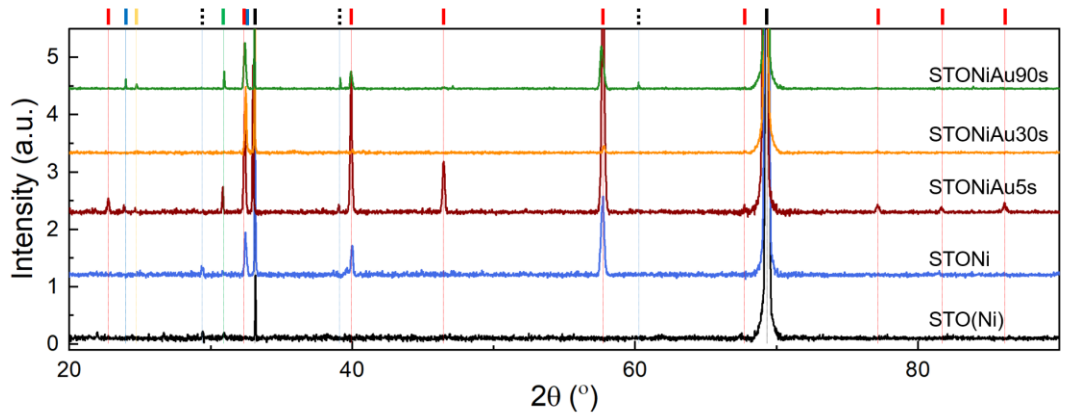

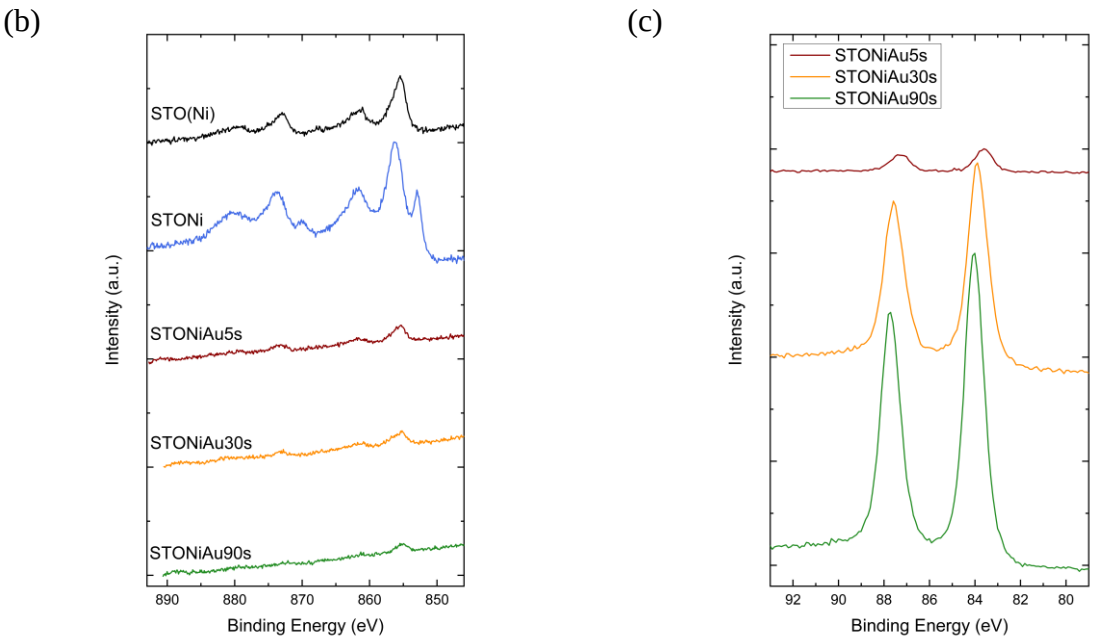

Figure 2: (a) XRD for the STO(Ni), STONi, STONiAu5s, STONiAu30s, and STONiAu90s. The lines on top mark Si (substrate, black, PDF 01-078-6300), $SrTiO_3$ (red, PDF 01-070-8508), $3SrO{\cdot}SiO_2$ (green, PDF 00-0390-1471), Sr_2TiO_4 (dark blue PDF 00-039-1371), and TiO_2 (yellow, PDF 01-070-8501). Peaks of unknown phases are marked with dotted black lines. (b) XPS spectra of Ni 2p for STO(Ni), STONi, STONiAu5s, STONiAu30s, and STONiAu90s. (c) XPS spectra of Au 4f of STONiAu5s, STONiAu30s, and STONiAu90s.

The PEC performances of the different samples were studied by linear sweep voltammetry (LSV) in 0.5 M Na_2SO_4 (pH=7.5) and the results are shown in Fig. 3. While the STO(Ni) thin film exhibits a clear generation of photocurrent as is expected for STO, the photocurrent density of samples with Ni and Au particles varies. For the STNOAu5s sample (Fig. 3c) the photoresponse is hardly noticeable, with the photocurrent being much lower than the STO(Ni). The STNOAu30s sample (Fig. 3a), on the other hand, has a large photocurrent generation. The STNOAu90s sample (Fig. 3d) exhibits prominent recombination spikes, like STO(Ni) (Fig. S14) and STONi (Fig. 3b), indicating a strong charge carrier recombination. While these increased recombination spikes can be an indication of a thermal decay of the plasmons and provide direct evidence of larger PEC capacity, i.e., larger light absorption properties of the plasmonically active samples, their appearance in STO(Ni), STONi and STONiAu90s suggests that they are a property of the deposited film.

The steady state PEC responses at 0.785 V versus RHE (table S1) of the different samples suggest that the reduction of STO during exsolution decreases the PEC response. The generally low photocurrent densities are attributed to the non-conducting nature of the substrate and the millimeter range that the charge carriers must move in order to reach the Ag contact. The results show that small Au MNPs increase the steady state response compared to the just exsolved

sample (table S1, samples STONi and STONiAu5s), while larger Au MNPs did not have the same effect (table S1, samples STONi and STONiAu90s). Thus, intermediate Au MNPs size (20-50 nm) as found in the STONiAu30s showed the best performance among all samples, indicating the importance in the size of the plasmonically active MNPs. The higher PEC response suggests that a measurable portion of the photogenerated surface plasmons decay by creating an electron hole pair that can be separated. Chronoamperometric measurements at 0.8 and 1.0 V vs RHE (Fig. S15) are in good agreement with the LSV curves, further showcasing the superiority of the STONiAu30s sample. It is noted that these performances correspond to a duplicate series of these five samples.

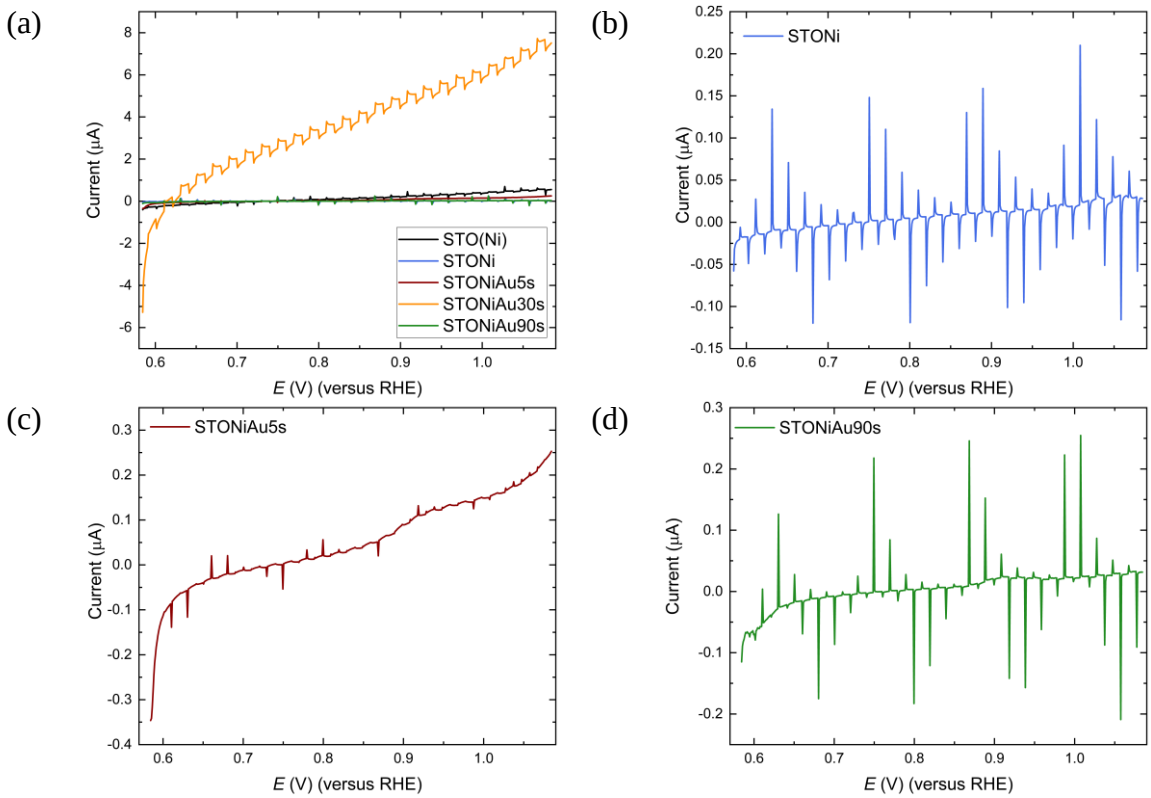

Figure 3: (a) LSV performances of all samples under chopped illumination conditions in 0.5 M Na_2SO_4. LSVs from (a) but at narrower potentials for (b) STONi, (c) STONiAu5s, and (d) STONiAu90s. Scan rate 5 mV s^{-1}.

To further investigate the size effects of Au MNPs EELS studies have been performed on individual particles and their surroundings [38]. Fig. 4 and Fig. S16 include particles from STONiAu5s, STONiAu30s, and STONiAu90s. The shape of the particles can be seen in the STEM images. EELS maps with selected energy ranges are shown in the EELS map column. The energy ranges are 1.505–1.520 eV for the STNOAu90s, 2.35–2.40 eV for the STNOAu30s and STNOAu5s. They were selected based on the most dominant peak in the given map. EELS spectra of selected pixels, indicated with colored frames in the maps are presented in the EELS graph column. These graphs reiterate that the peak around 1.5 eV dominates the spectra for the

STNOAu90s sample, with minor peaks between 1.9 eV and 2.4 eV. On the other hand, for the STNO30s and STNO5s samples, which showed improved PEC activity the spectra exhibit one peak at 2.4 eV, which is the expected peak for the plasmonic activity of Au MNPs [14].

The position of the peaks in all samples suggest that the major mechanism for charge carriers transfer between the plasmonically active MNPs and the STO is hot charge carriers transfer. The spectral overlap between Au MNPs and STO determines the PIRET response [2], which is very limited as our calculations indicate in Fig. S17, while scattering/trapping would only increase the chances of exciting an electron-hole pair by photons with an energy larger than the band gap of STO. Additionally, the positions of the EELS peaks in all samples suggest that the major mechanism by which the plasmonic energy is utilized is either local heating or hot charge carrier transfer between the plasmonically active MNPs and the STO. The hot charge carrier transfer is then suggested as the main mechanism for energy transfer between the plasmonic MNPs and STO, although a combination of hot charge carriers and local heating cannot be conclusively excluded.

STEM (HAADF)	**EELS map**	**EELS graph**
STONiAu5s		
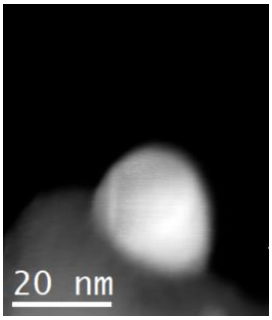	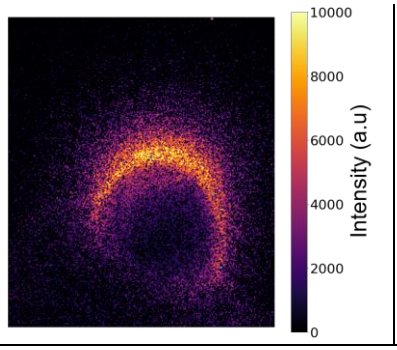	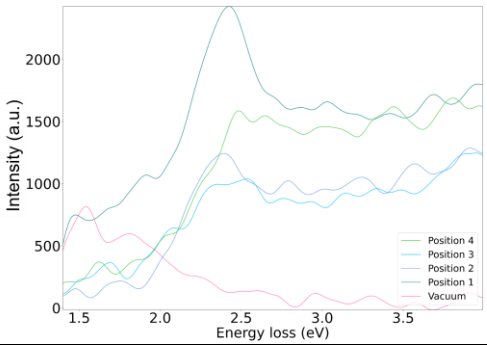
STONiAu30s		
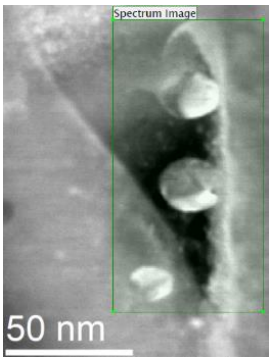	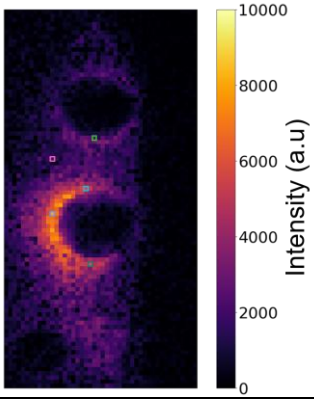	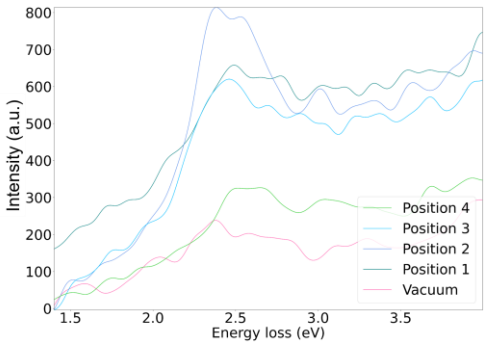
STONiAu90s		

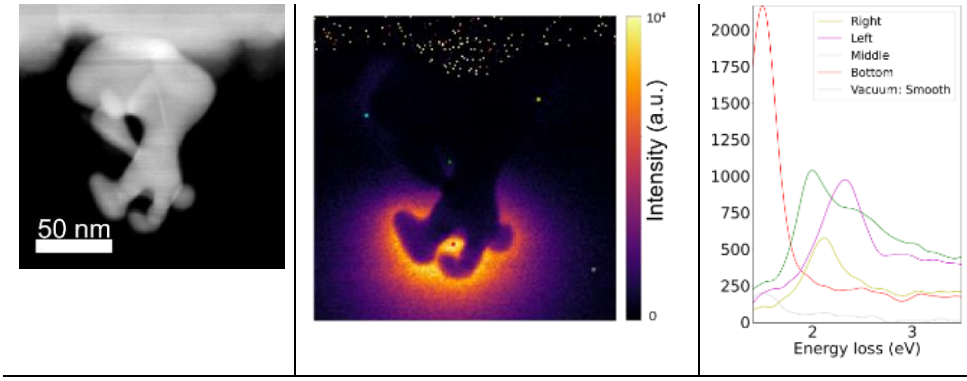

Figure 4: STEM HAADF images of Au particles on STNOAu5s, STNOAu30s, and STNOAu90s samples, with the corresponding EELS map and EEL spectra from the selected pixels in each image.

4. Calculations

Computational studies in the form of FDTD calculations [29] of Au and Ni MNPs with randomly selected dimeters between 10 nm and 30 nm were performed to study the effect of embedding the MNPs. In these calculations, the centers of the spheres were placed at different depths compared to the surface of STO (Fig. 5a). The study revealed two important findings: First, Au particles showed enhanced absorption in comparison to Ni particles located at the same depth (Fig. 5b). Second, particles with their center buried in STO have increased absorption compared to the particles with their center at or above the STO surface (Fig. 5c, and total absorptions given in Fig. S18). We believe the increased absorption is due to a red-shift of the peak (Fig. S19), bringing it away from interband transitions (at 2.4 eV [14]) that lead to damping. Consequently, we predict that partially buried particles as a result of exsolution and GRR, show an enhanced absorption cross section compared to deposited particles (physical deposition, photodeposition and other such methods). Moreover, we also calculated absorption cross section of deposited particles compare to embedded particles, i.e. ‘dome’-particles (Fig. 5b). Dome particles were defined as spherical MNPs with a flat interface with STO (Fig. 5a). Here, the depth refers to the position of the flat interface and the results show that the absorption is similar for the dome particles and the spherical particles (particles with 0% in Fig. 5a). Finally, burying a particle deeper inside the surface also increases the interface area between the MNP and the STO, which has been shown to increase the probability of hot charge carrier injection [39]. Metal exsolution is an appropriate method for controlling the “socketing” depth of a particle and control over this process will be of great importance for the design of highly efficient, plasmonically active photocatalysts.

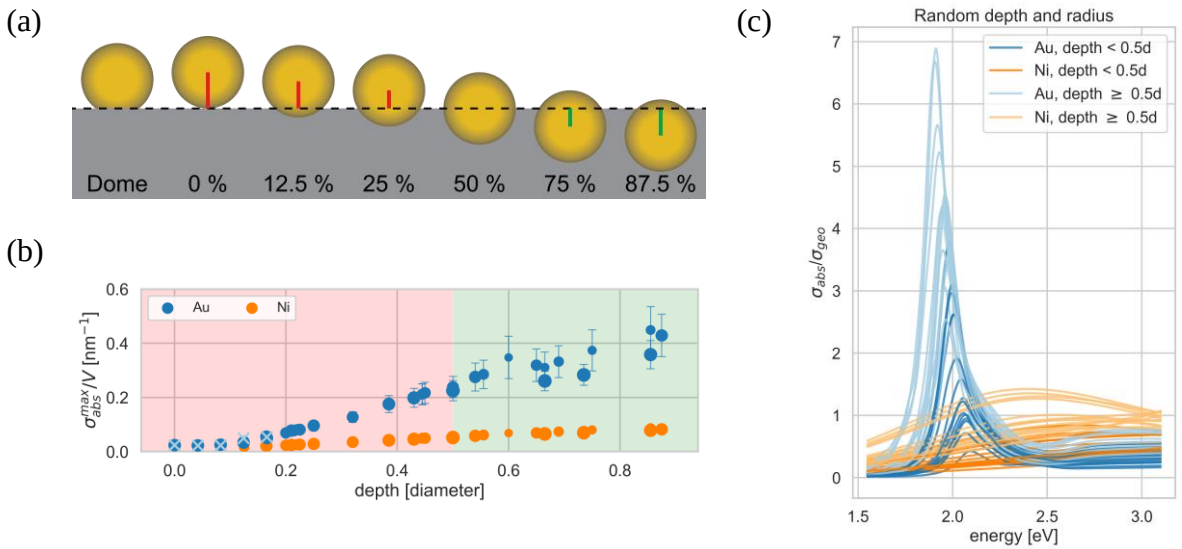

Figure 5: (a) Illustration of the sphere placements for the calculations. (b) Absorption cross sections normalized with the geometrical cross section for Ni and Au particles on STO located at different depths. (c) Maximum absorption cross section per volume against the depth of the particle both for Ni and Au. The marker-size reflects the size of the nanoparticle in the particular simulation. Additional calculations of dome-type Au particles are shown as light blue crosses. The error bars show the spread of the peak height with different permittivity data for the metal and STO (see also Fig. S20). The spread is so small for Ni that the error bars are smaller than the marker.

5. Conclusions

Our methodology enables the formation of well-socketed Au MNPs of various sizes and shapes created by galvanic replacement of exsolved Ni by Au ions on A-site excess STO thin films. We demonstrated that the shape and size of the particles lead to differences in EELS mapping. Specifically, large non-spherical particles as observed in sample STONiAu90s exhibit multiple peaks that ultimately decrease the PEC activity, while spherical particles as in STONiAu5s and STONiAu30s have a singular peak around 2.4 eV, and improved PEC activity. This suggests that an intermediate size distribution of Au MNPs, allows the dominant energy transfer mechanism from MNP to STO that is found to occur through hot charge carriers transfer. Our FDTD calculations highlighted that embedded particles can heavily improve the absorption cross section than particles on the surface of the photocatalyst, reflecting the need to create well-socketed, plasmonically active particles not only to improve their stability, but also their plasmonic response. This is now possible through our method of metal exsolution and galvanic replacement and efforts to gain control over particles' "socketing" depth, size and distribution will open the way for the next generation of photocatalytic materials.

Acknowledgements

The Research Council of Norway is acknowledged for the support to the Norwegian Center for Transmission Electron Microscopy (NORTEM, no 197405/F50), the NANO2021 researcher project FUNCTION (no. 287729) and FRINATEK project PH2ON (288320).

CRediT

Kevin G. Both: Methodology, Validation, Formal analysis, Investigation, Visualization, Writing – Original Draft, Review and Editing **Vilde M. Reinertsen:** Methodology, Validation, Formal analysis, Investigation, Visualization, Writing Review and Editing **Thomas M. Aarholt:** Investigation, Formal analysis, Writing Review and Editing **Ingvild J. T. Jensen:** Investigation, Writing Review and Editing **Dragos Neagu:** Methodology, Writing Review and Editing **Øystein Prytz:** Resources, Writing – Review and Editing, Supervision **Truls Norby:** Resources, Writing – Review and Editing, Supervision **Athanasios Chatzitakis:** Conceptualization, Methodology, Investigation, Writing – Original Draft, Review and Editing, Visualization, Supervision, Project administration, Funding acquisition

References

[1] D. Ravelli, D. Dondi, M. Fagnoni, A. Albini, Photocatalysis. A multi-faceted concept for green chemistry, Chem. Soc. Rev. 38 (2009) 1999–2011. https://doi.org/10.1039/B714786B.

[2] N. Wu, Plasmonic metal–semiconductor photocatalysts and photoelectrochemical cells: a review, Nanoscale. 10 (2018) 2679–2696. https://doi.org/10.1039/C7NR08487K.

[3] M.G. Walter, E.L. Warren, J.R. McKone, S.W. Boettcher, Q. Mi, E.A. Santori, N.S. Lewis, Solar Water Splitting Cells, Chem. Rev. 110 (2010) 6446–6473. https://doi.org/10.1021/cr1002326.

[4] G.L. Soloveichik, Battery Technologies for Large-Scale Stationary Energy Storage, Annu. Rev. Chem. Biomol. Eng. 2 (2011) 503–527. https://doi.org/10.1146/annurev-chembioeng-061010-114116.

[5] E. Kabir, P. Kumar, S. Kumar, A.A. Adelodun, K.-H. Kim, Solar energy: Potential and future prospects, Renew. Sustain. Energy Rev. 82 (2018) 894–900. https://doi.org/10.1016/j.rser.2017.09.094.

[6] D.J. Willis, C. Niezrecki, D. Kuchma, E. Hines, S.R. Arwade, R.J. Barthelmie, M. DiPaola, P.J. Drane, C.J. Hansen, M. Inalpolat, J.H. Mack, A.T. Myers, M. Rotea, Wind energy research: State-of-the-art and future research directions, Renew. Energy. 125 (2018) 133–154. https://doi.org/10.1016/j.renene.2018.02.049.

[7] H. Andersen, K. Xu, D. Malyshkin, R. Strandbakke, A. Chatzitakis, A highly efficient electrocatalyst based on double perovskite cobaltites with immense intrinsic catalytic activity for water oxidation, Chem. Commun. 56 (2020) 1030–1033. https://doi.org/10.1039/C9CC08765F.

[8] M.M. Momeni, Y. Ghayeb, N. Moosavi, Preparation of Ni–Pt/Fe–TiO2 nanotube films for photoelectrochemical cathodic protection of 403 stainless steel, Nanotechnology. 29 (2018) 425701.

[9] Q. Zhang, D.T. Gangadharan, Y. Liu, Z. Xu, M. Chaker, D. Ma, Recent advancements in plasmon-enhanced visible light-driven water splitting, J. Materiomics. 3 (2017) 33–50. https://doi.org/10.1016/j.jmat.2016.11.005.
[10] M. Volokh, G. Peng, J. Barrio, M. Shalom, Carbon Nitride Materials for Water Splitting Photoelectrochemical Cells, Angew. Chem. Int. Ed. 58 (2019) 6138–6151. https://doi.org/10.1002/anie.201806514.
[11] M. Ben-Naim, R.J. Britto, C.W. Aldridge, R. Mow, M.A. Steiner, A.C. Nielander, L.A. King, D.J. Friedman, T.G. Deutsch, J.L. Young, T.F. Jaramillo, Addressing the Stability Gap in Photoelectrochemistry: Molybdenum Disulfide Protective Catalysts for Tandem III–V Unassisted Solar Water Splitting, ACS Energy Lett. 5 (2020) 2631–2640. https://doi.org/10.1021/acsenergylett.0c01132.
[12] J. Li, Z. Lou, B. Li, Engineering plasmonic semiconductors for enhanced photocatalysis, J. Mater. Chem. A. 9 (2021) 18818–18835. https://doi.org/10.1039/D1TA04541E.
[13] E. Hutter, J.H. Fendler, Exploitation of Localized Surface Plasmon Resonance, Adv. Mater. 16 (2004) 1685–1706. https://doi.org/10.1002/adma.200400271.
[14] U. Kreibig, M. Vollmer, Optical Properties of Metal Clusters, Springer Berlin Heidelberg, 2013. https://books.google.no/books?id=6WrrCAAAQBAJ.
[15] S. Underwood, P. Mulvaney, Effect of the Solution Refractive Index on the Color of Gold Colloids, Langmuir. 10 (1994) 3427–3430. https://doi.org/10.1021/la00022a011.
[16] M.E. Stewart, C.R. Anderton, L.B. Thompson, J. Maria, S.K. Gray, J.A. Rogers, R.G. Nuzzo, Nanostructured Plasmonic Sensors, Chem. Rev. 108 (2008) 494–521. https://doi.org/10.1021/cr068126n.
[17] M.M. Abouelela, G. Kawamura, A. Matsuda, A review on plasmonic nanoparticle-semiconductor photocatalysts for water splitting, J. Clean. Prod. 294 (2021) 126200. https://doi.org/10.1016/j.jclepro.2021.126200.
[18] X. Kang, V.M. Reinertsen, K.G. Both, A. Galeckas, T. Aarholt, Ø. Prytz, T. Norby, D. Neagu, A. Chatzitakis, Galvanic Restructuring of Exsolved Nanoparticles for Plasmonic and Electrocatalytic Energy Conversion, Small. n/a (2022) 2201106. https://doi.org/10.1002/smll.202201106.
[19] G. Tsekouras, D. Neagu, J.T.S. Irvine, Step-change in high temperature steam electrolysis performance of perovskite oxide cathodes with exsolution of B-site dopants, Energy Environ. Sci. 6 (2013) 256–266. https://doi.org/10.1039/C2EE22547F.
[20] F.N. Agüero, A.M. Beltrán, M.A. Fernández, L.E. Cadús, Surface nickel particles generated by exsolution from a perovskite structure, J. Solid State Chem. 273 (2019) 75–80. https://doi.org/10.1016/j.jssc.2019.02.036.
[21] D. Neagu, T.-S. Oh, D.N. Miller, H. Ménard, S.M. Bukhari, S.R. Gamble, R.J. Gorte, J.M. Vohs, J.T.S. Irvine, Nano-socketed nickel particles with enhanced coking resistance grown in situ by redox exsolution, Nat. Commun. 6 (2015) 8120. https://doi.org/10.1038/ncomms9120.
[22] T.-S. Oh, E.K. Rahani, D. Neagu, J.T.S. Irvine, V.B. Shenoy, R.J. Gorte, J.M. Vohs, Evidence and Model for Strain-Driven Release of Metal Nanocatalysts from Perovskites during Exsolution, J. Phys. Chem. Lett. 6 (2015) 5106–5110. https://doi.org/10.1021/acs.jpclett.5b02292.
[23] X. Xia, Y. Wang, A. Ruditskiy, Y. Xia, 25th Anniversary Article: Galvanic Replacement: A Simple and Versatile Route to Hollow Nanostructures with Tunable and Well-Controlled Properties, Adv. Mater. 25 (2013) 6313–6333. https://doi.org/10.1002/adma.201302820.
[24] S.E. Skrabalak, J. Chen, Y. Sun, X. Lu, L. Au, C.M. Cobley, Y. Xia, Gold Nanocages: Synthesis, Properties, and Applications, Acc. Chem. Res. 41 (2008) 1587–1595. https://doi.org/10.1021/ar800018v.

[25] C.M. Cobley, Y. Xia, Engineering the properties of metal nanostructures via galvanic replacement reactions, Mater. Sci. Eng. R Rep. 70 (2010) 44–62. https://doi.org/10.1016/j.mser.2010.06.002.
[26] Y. Sun, B.T. Mayers, Y. Xia, Template-Engaged Replacement Reaction: A One-Step Approach to the Large-Scale Synthesis of Metal Nanostructures with Hollow Interiors, Nano Lett. 2 (2002) 481–485. https://doi.org/10.1021/nl025531v.
[27] S. Zhu, D. Wang, Photocatalysis: Basic Principles, Diverse Forms of Implementations and Emerging Scientific Opportunities, Adv. Energy Mater. 7 (2017) 1700841. https://doi.org/10.1002/aenm.201700841.
[28] R.S. Moirangthem, M.T. Yaseen, P.-K. Wei, J.-Y. Cheng, Y.-C. Chang, Enhanced localized plasmonic detections using partially-embedded gold nanoparticles and ellipsometric measurements, Biomed Opt Express. 3 (2012) 899–910. https://doi.org/10.1364/BOE.3.000899.
[29] https://www.lumerical.com/, n.d. https://www.lumerical.com/.
[30] C.G. Olson, D.W. Lynch, J.H. Weaver, (n.d.). unpublished.
[31] P.B. Johnson, R.W. Christy, Optical Constants of the Noble Metals, Phys Rev B. 6 (1972) 4370–4379. https://doi.org/10.1103/PhysRevB.6.4370.
[32] D.W. Lynch, R. Rosei, J.H. Weaver, Infrared and visible optical properties of single crystal Ni at 4K, Solid State Commun. 9 (1971) 2195–2199. https://doi.org/10.1016/0038-1098(71)90629-6.
[33] E.D. Palik, Handbook of optical constants of solids, Academic press, 1998.
[34] Material Database in FDTD and MODE, (n.d.). https://support.lumerical.com/hc/en-us/articles/360034394614-Material-Database-in-FDTD-and-MODE.
[35] Y. Duan, P. Ohodnicki, B. Chorpening, G. Hackett, Electronic structural, optical and phonon lattice dynamical properties of pure- and La-doped SrTiO3: An ab initio thermodynamics study, J. Solid State Chem. 256 (2017) 239–251. https://doi.org/10.1016/j.jssc.2017.09.016.
[36] A. Rohatgi, WebPlotDigitizer, 2020. https://automeris.io/WebPlotDigitizer.
[37] M.J. Dodge, Refractive Index, in M. J. Weber (ed.), Handbook of Laser Science and Technology, Volume IV, Optical Material: Part 2, (as cited in Handbook of Optics, 3rd edition, Vol. 4. McGraw-Hill 2009)., CRC Press, Boca Raton, 1986.
[38] R.F. Egerton, Scattering delocalization and radiation damage in STEM-EELS, Ondrej Krivanek Res. Life EELS Aberration Corrected STEM. 180 (2017) 115–124. https://doi.org/10.1016/j.ultramic.2017.02.007.
[39] X.-C. Ma, Y. Dai, L. Yu, B.-B. Huang, Energy transfer in plasmonic photocatalytic composites, Light Sci. Appl. 5 (2016) e16017–e16017.

Supplementary Information (SI)

Ni-doped A-site excess $SrTiO_3$ thin films modified with Au nanoparticles by a thermodynamically-driven restructuring for plasmonic activity

Authors

Kevin G. Both,[1] Vilde M. Reinertsen,[2] Thomas M. Aarholt,[2] Ingvild J. T. Jensen,[3] Dragos Neagu,[4] Øystein Prytz,[2] Truls Norby,[1] Athanasios Chatzitakis[1*]

Affiliations

(1) Centre for Materials Science and Nanotechnology, Department of Chemistry, University of Oslo, Gaustadalléen 21, NO-0349 Oslo, Norway
(2) Centre for Materials Science and Nanotechnology, Department of Physics, University of Oslo, P. O. Box 1048 Blindern, NO-0316, Oslo, Norway
(3) SINTEF Materials Physics, Forskningsveien 1, 0373 Oslo, Norway
(4) Department of Chemical and Process Engineering, University of Strathclyde, 75 Montrose St, G1 1XJ, Glasgow, United Kingdom

[*]corresponding author: athanasios.chatzitakis@smn.uio.no

1. Supplementary Figures

(a) (b)

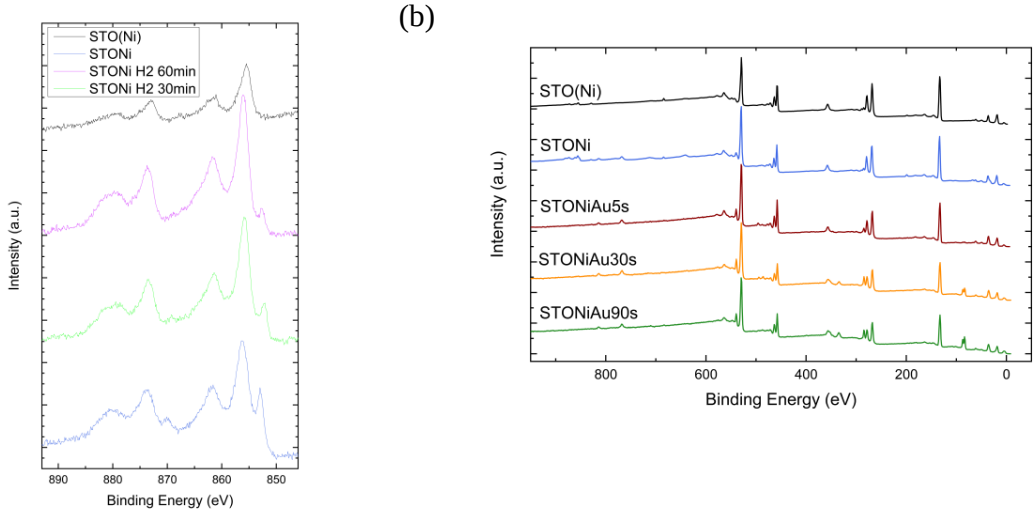

Figure S1: (a) XPS of samples exsolved under different conditions. (b) XPS investigation spectra of STO(Ni), STONi, STNONiAu5s, STONiAu30s, and STONiAu90s.

(a) (b)

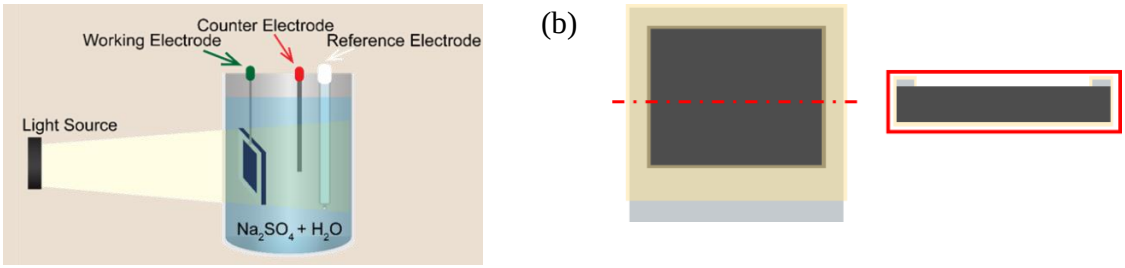

Figure S2: (a) Sketch of the photoelectrochemical setup. (b) Sketch of the working electrodes of a nominal area of 0.12 cm^2; on the left a top view and on the right a cross section. STO(Ni), STONi and series of STONiAu electrodes were prepared as follows: Conductive Ag ink was used to paint a frame around the center part of the device, serving as contact. Subsequently, epoxy was used to insulate the Ag contact and substrate from the environment. In dark the sample, grey the silver contacts, and yellow the epoxy.

(a)

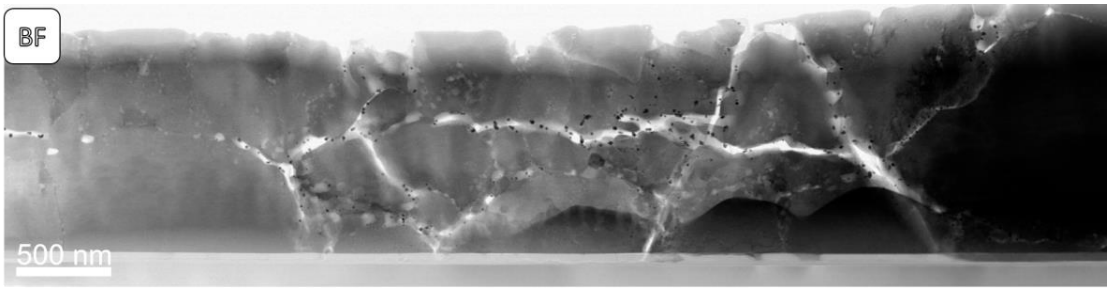

(b)

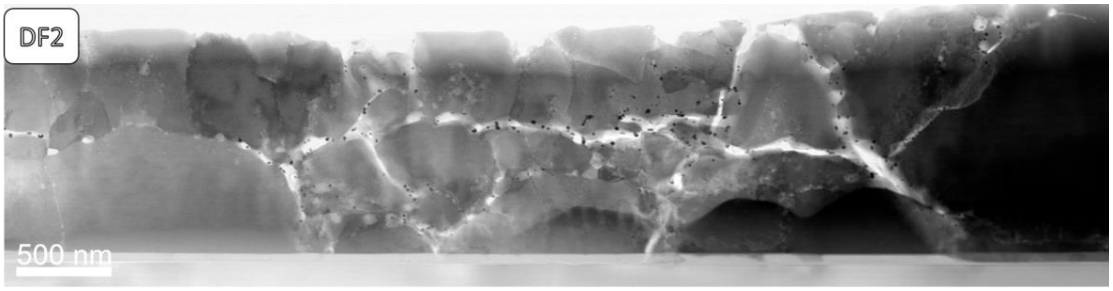
DF2
500 nm

(c)

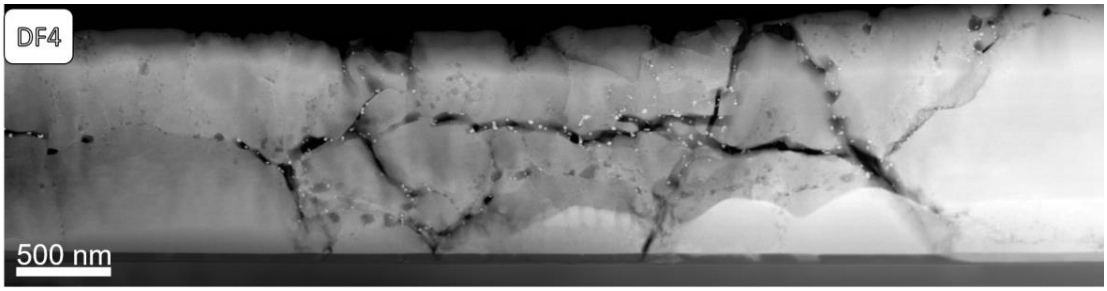
DF4
500 nm

(d)

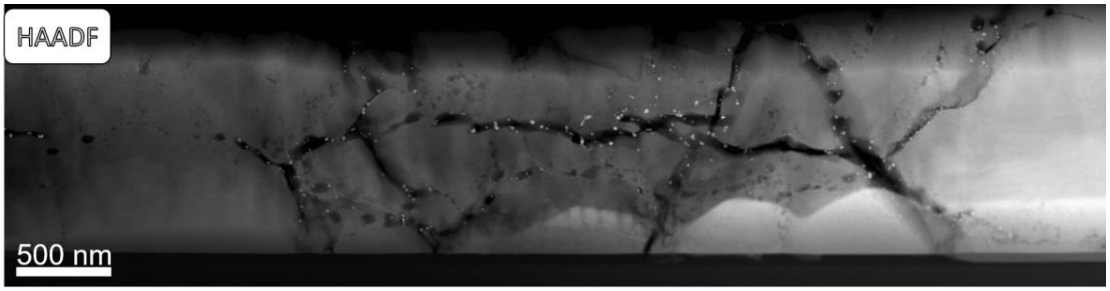
HAADF
500 nm

(e)

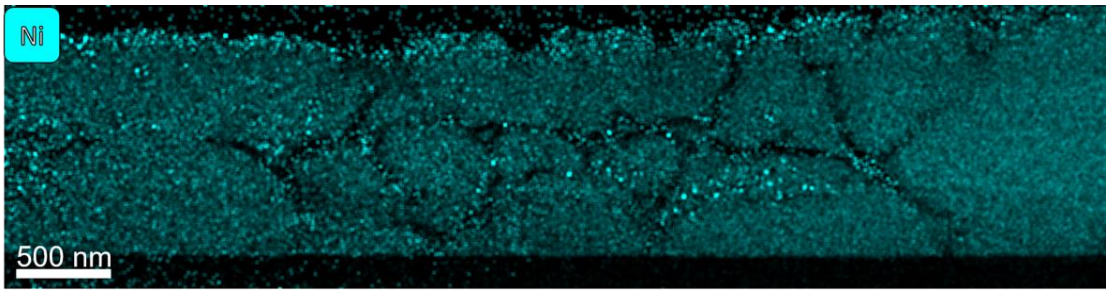
Ni
500 nm

(f)

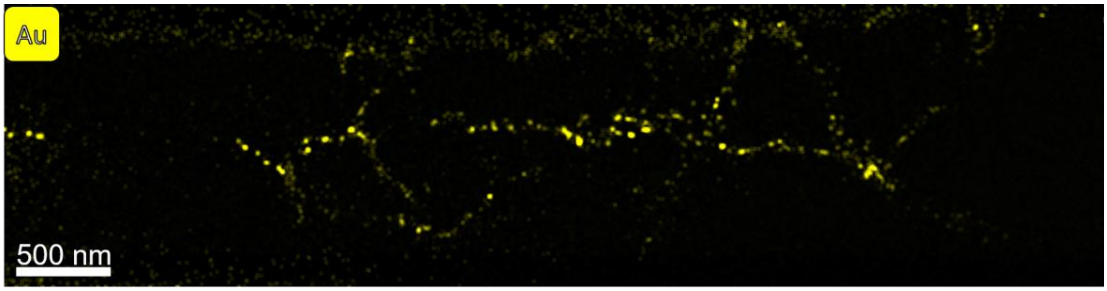
Au
500 nm

(g)

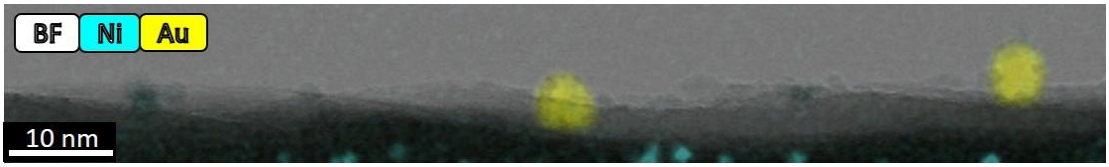
BF
Ni
Au
10 nm

Fig. S3: The BF (a), DF2 (b), DF4 (c), and HAADF (d) images, respectively, and the EDS maps of Ni (e) and Au (f) of the STONiAu5s sample.

(a)

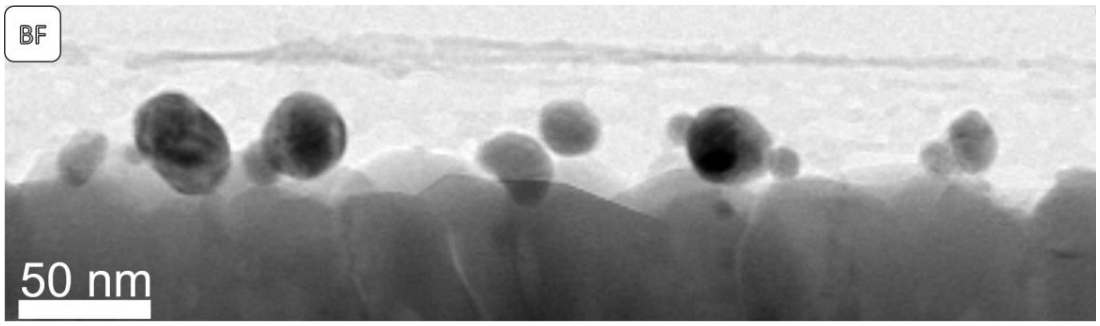

(b)

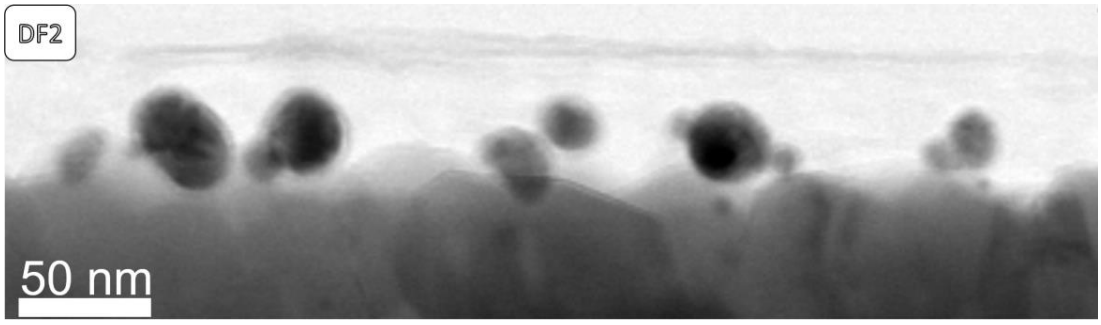

(c)

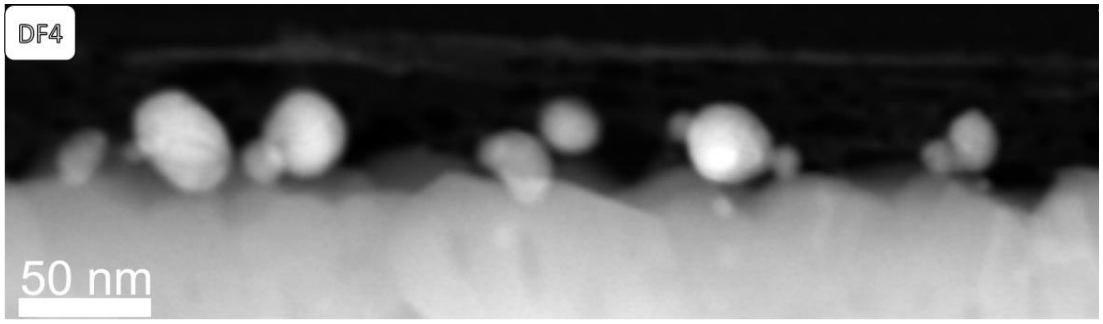

(d)

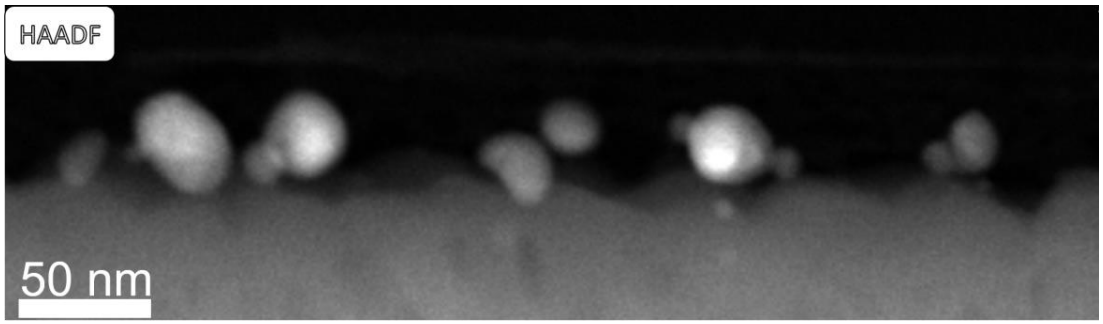

(e)

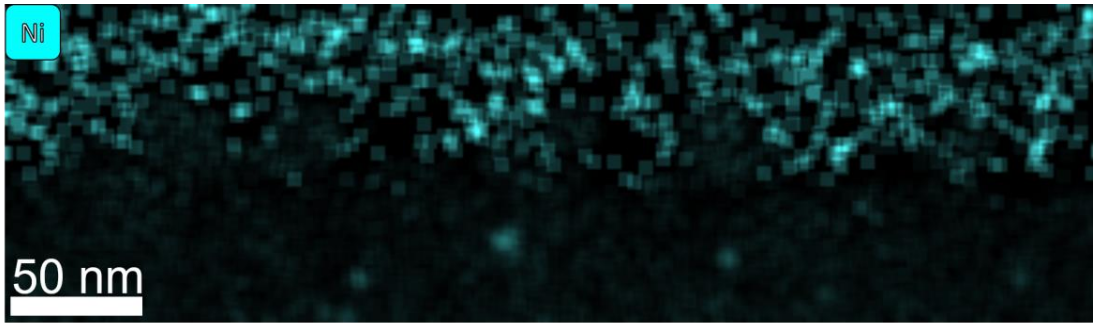

(f)

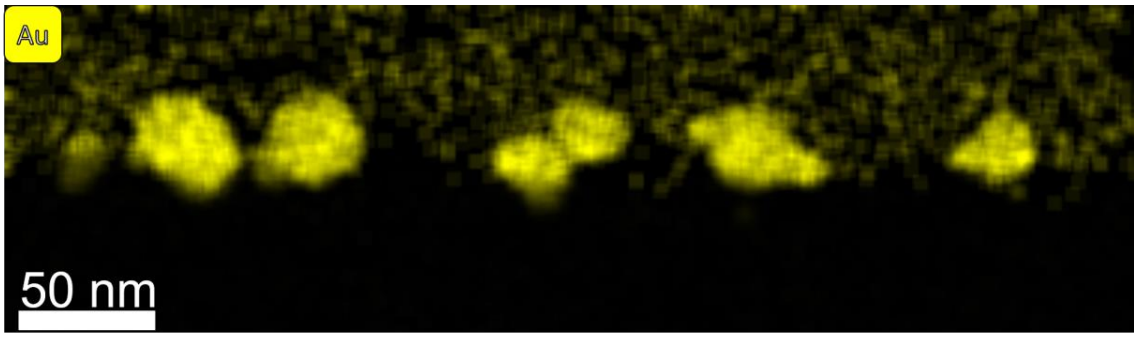

Fig. S4: The BF (a), DF2 (b), DF (4) (c), and HAADF (d) images, respectively, and the EDS maps of Ni (e) and Au (f) of the STONiAu30s sample.

(a)

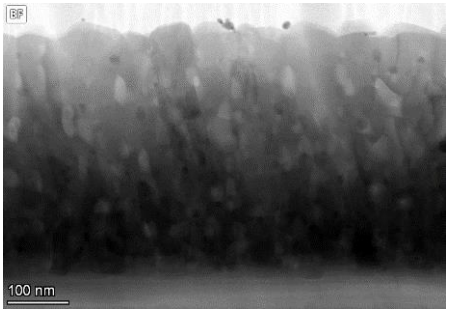

(b)

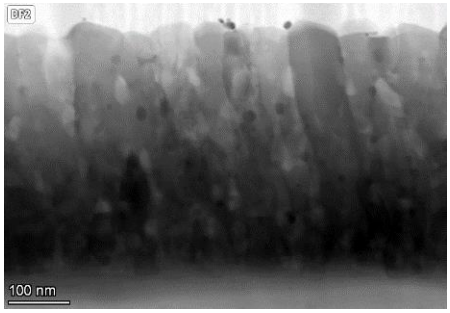

(c)

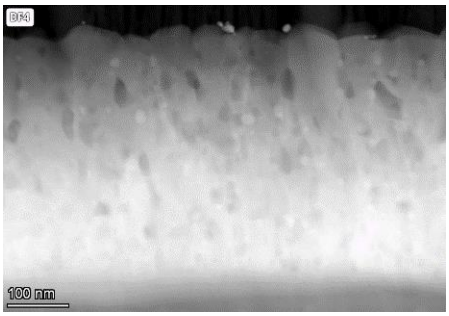

(d)

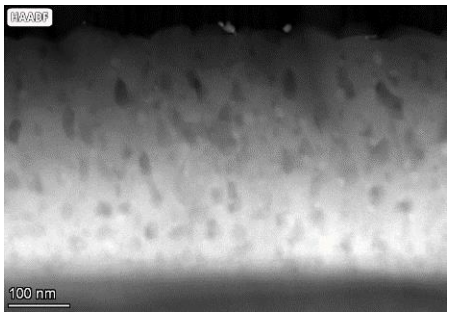

(e) 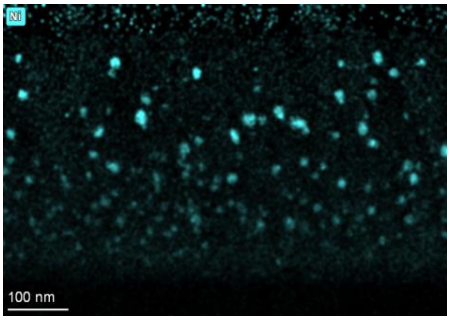

(f) 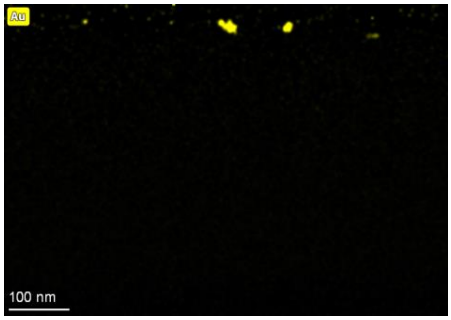

Fig. S5: Lower magnification BF (a), DF2 (b), DF (4) (c), and HAADF (d) images, respectively, and the EDS maps (e) of Ni and Au (f) of the STONiAu90s sample.

(a) 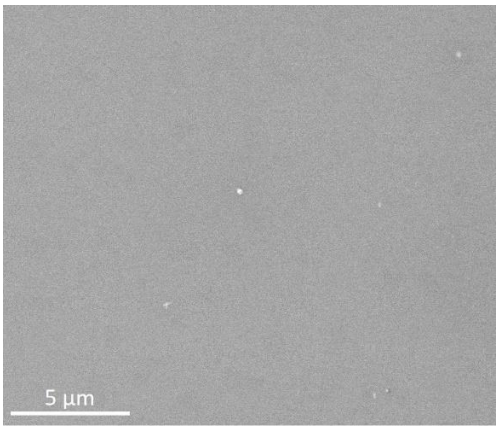

(b) 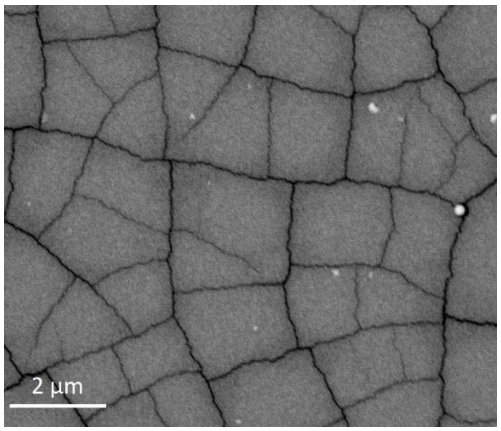

(c) 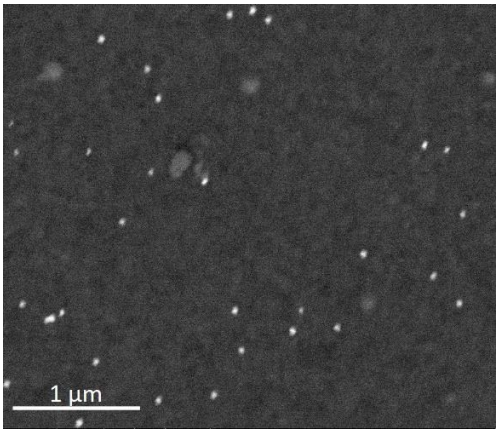

(d) 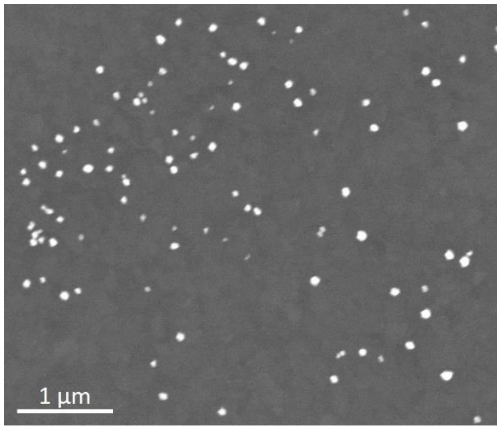

(e)

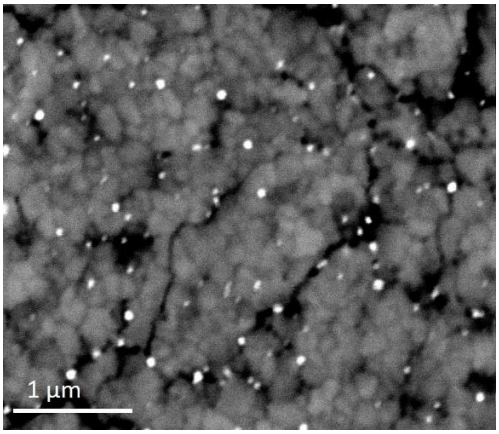

Fig. S6: Backscatter electron SEM images of (a) STO(Ni), (b) STONi, (c) STONiAu5s, (d) STONiAu30s, and (e) STONiAu90s thin films.

(a)

(b)

(c)

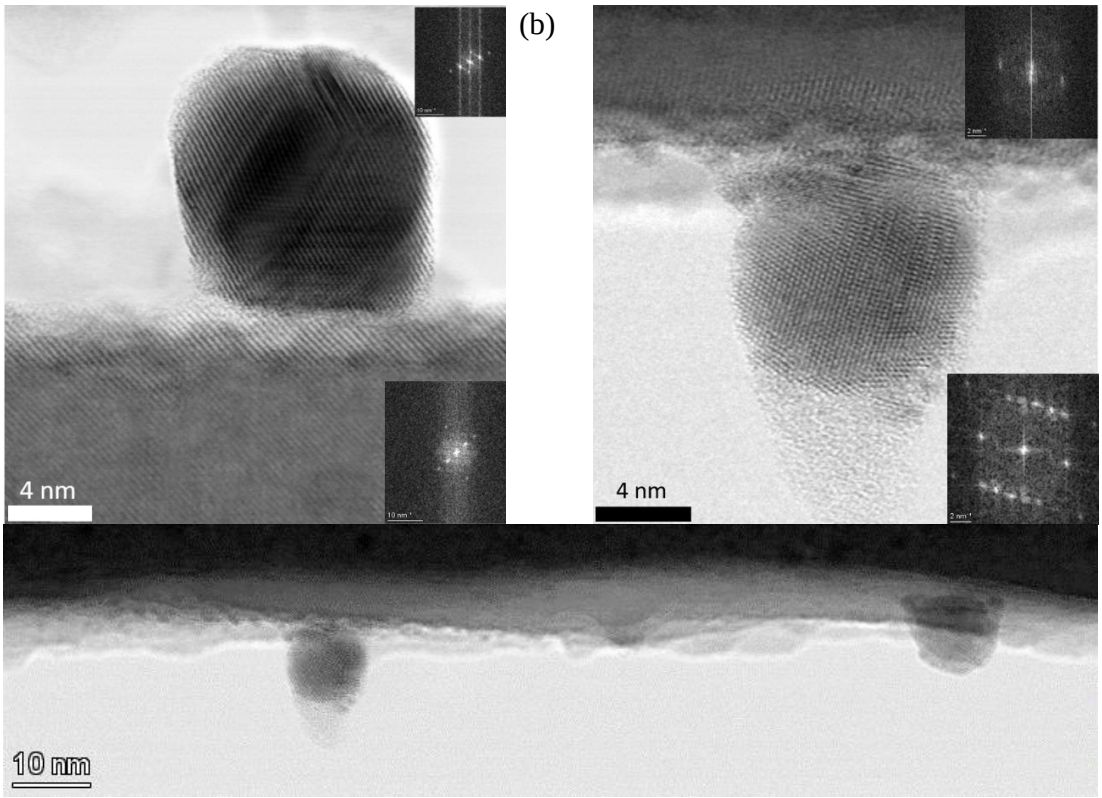

Fig. S7: (a) HR-STEM BF image of a Au particle of the STONiAu5s sample with Fast Fourier Transformation (FFT) insets of the particle and thin film, showing a slight angle mismatch. (b) Another HR-STEM BF image of a Au particle of the STONiAu5s sample, with FFT, showing almost no angle mismatch. (c) The particle in (b, on the left) together with an additional particle on the same thin film grain with different orientation.

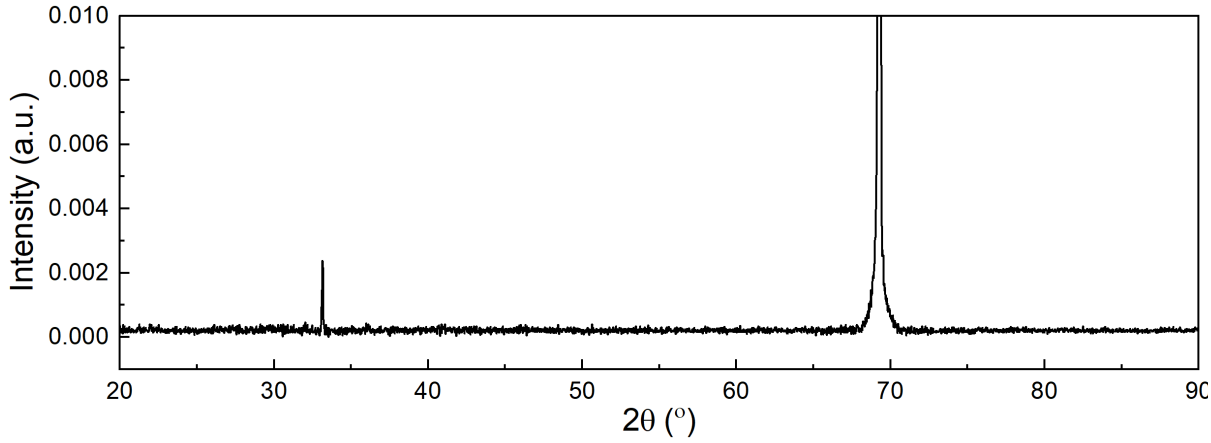

Fig. S8: XRD pattern of the substrate.

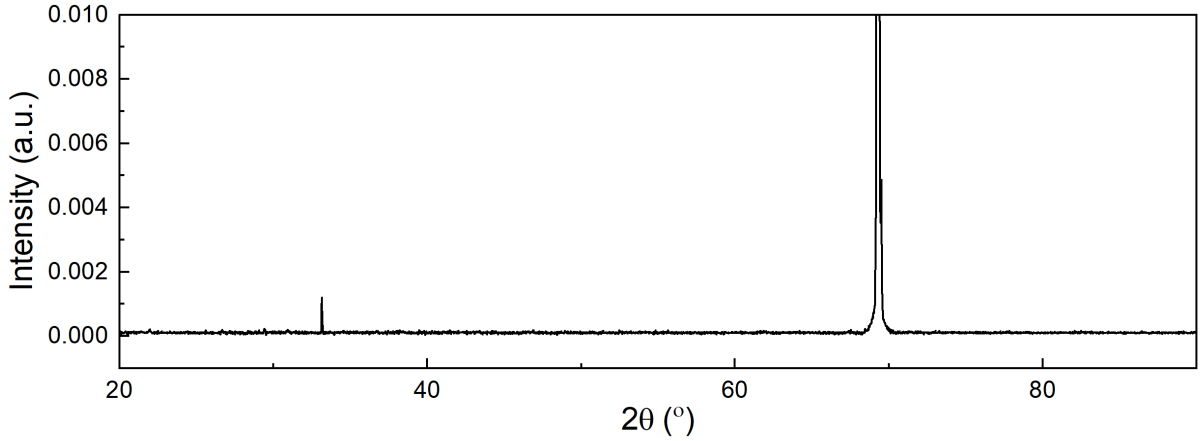

Fig. S9: XRD pattern of the STO(Ni).

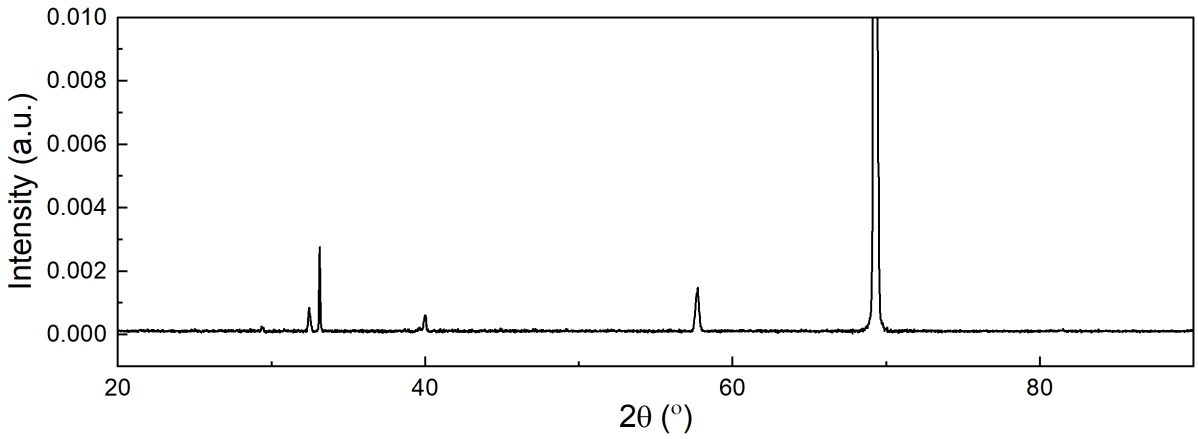

Fig. S10: XRD pattern of the STONi film.

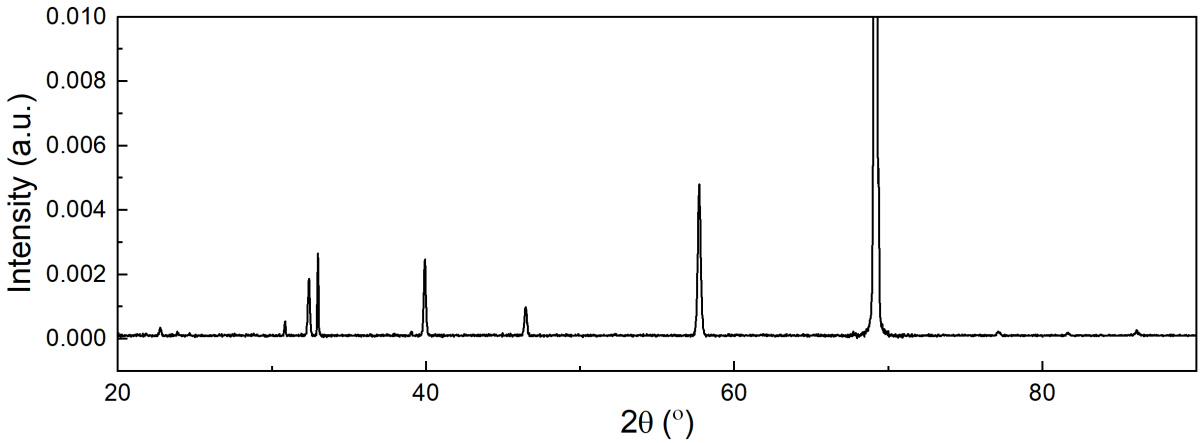

Fig. S11: XRD pattern of the STONiAu5s film.

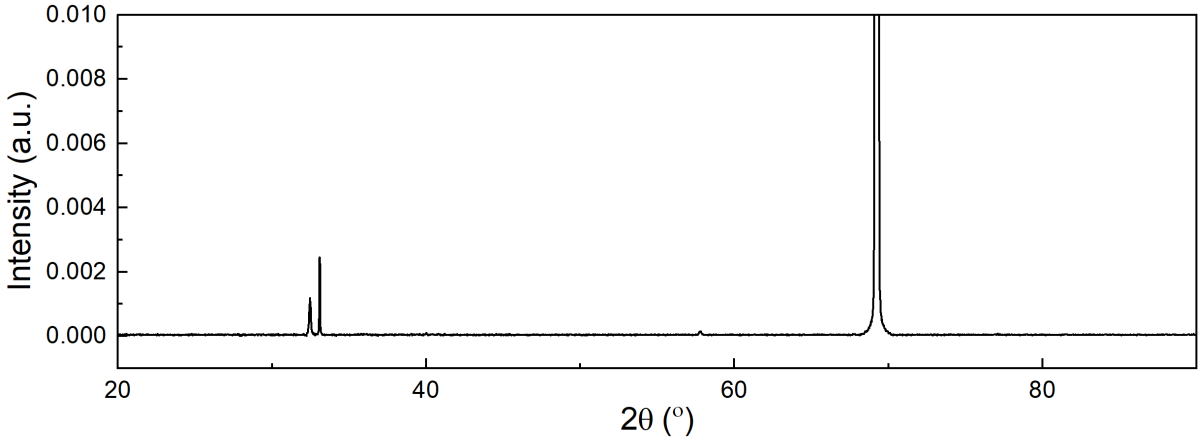

Fig. S12: XRD pattern of STONiAu30s.

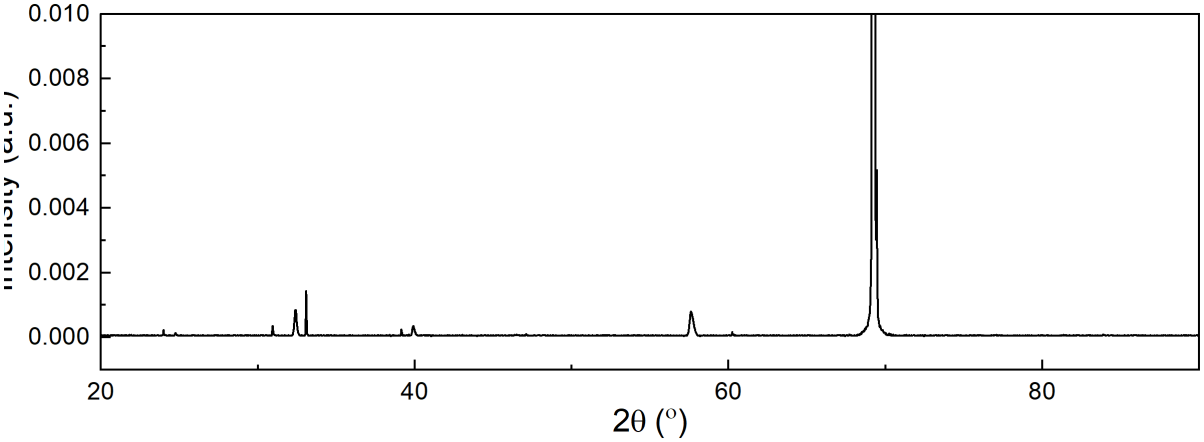

Fig. S13: XRD pattern of STONiAu90s thin film.

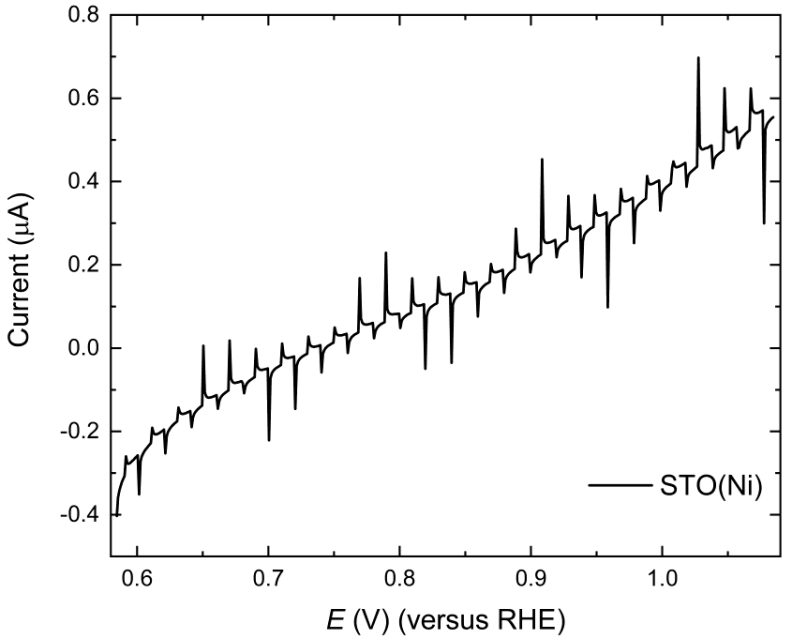

Fig. S14: LSV sweep of STO(Ni).

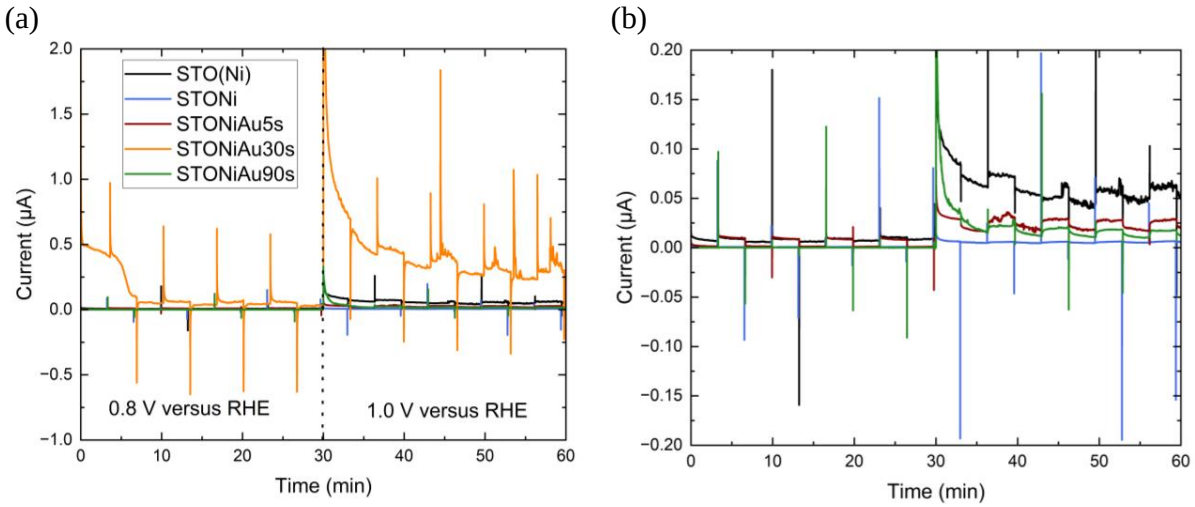

Fig. S15: (a) Chronoamperometric measurements at 0.8 and 1.0 V versus RHE in 0.5 M Na_2SO_4. (b) Higher magnification of (a) in which the comparatively giant response of STONiAu30s is removed to highlight the rest of the samples. The PEC response of all the samples agrees well with the LSV curves of Fig. 3 and they also show good stability under intermittent illumination in the studied time period.

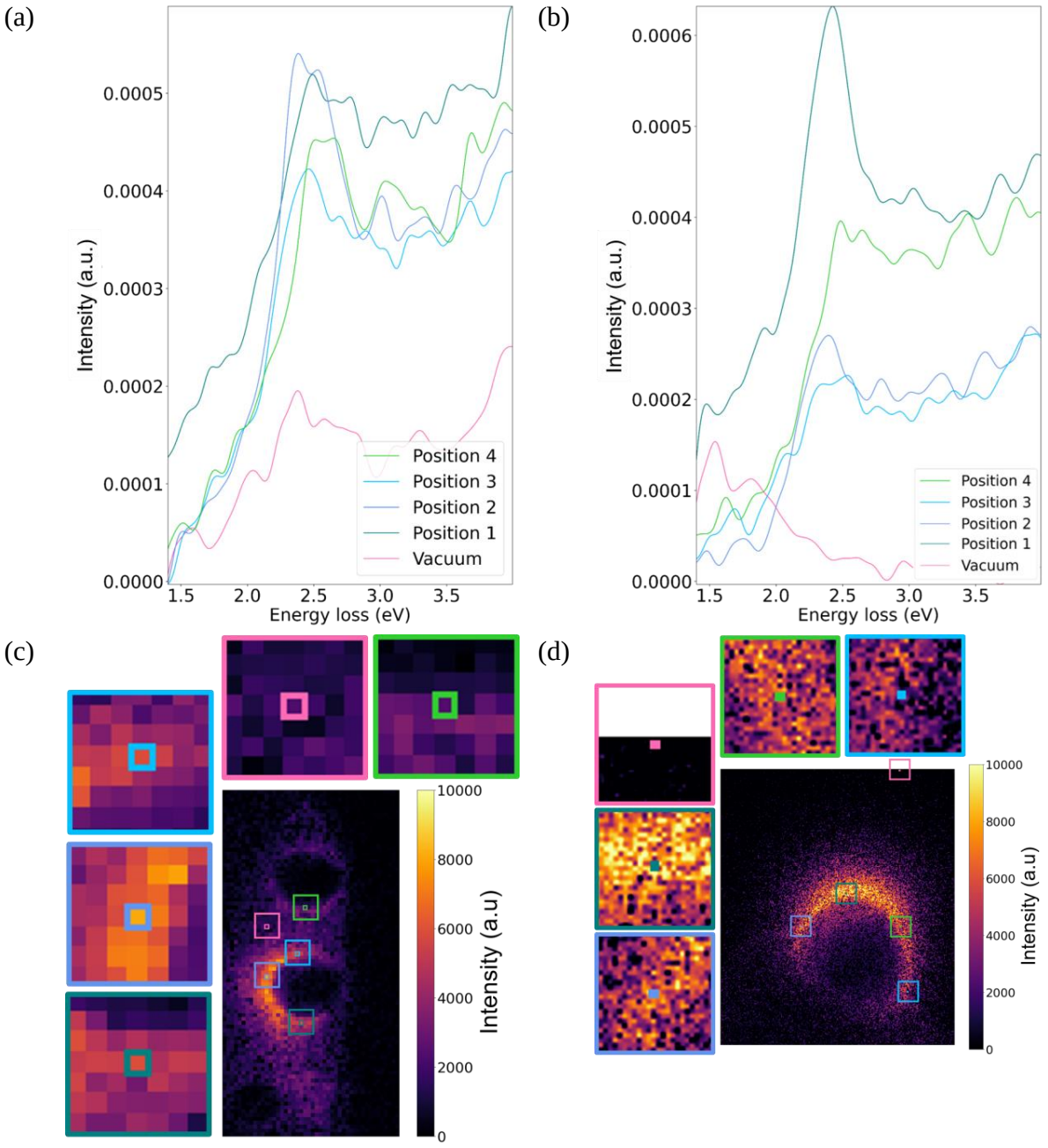
(a)
(b)
(c)
(d)
Intensity (a.u.)
Energy loss (eV)
Position 4
Position 3
Position 2
Position 1
Vacuum
Intensity (a.u)

(e)

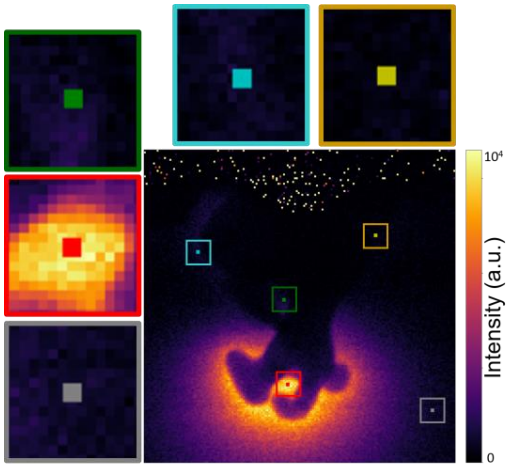

Fig. S16: (a) The EELS spectra of 5 pixels of STONiAu30s normalized with their respective zero-loss peak. (b) The EELS spectra of 5 pixels of STONiAu5s normalized with their respective zero-loss peak. (c) The EELS map of STONiAu30s with zoomed in pixels. (d) The EELS map of STONiAu5s with zoomed in pixels. (e) The EELS map of STONiAu90s with zoomed in pixels.

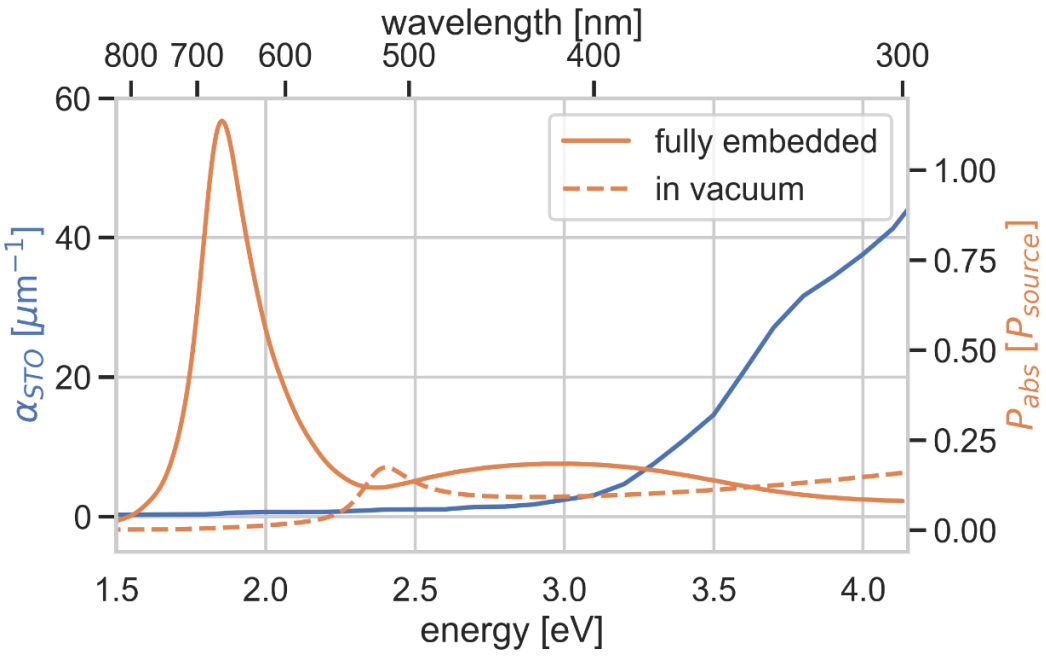

Fig. S17: Spectral overlap between Au (orange; solid in STO, dashed in vacuum) and STO (blue). The power absorbed, P_{abs}, was calculated using the permittivity data of Au to get only the absorption in Au when the particle was totally embedded in STO. This was accomplished using an analysis group within the Ansys Lumerical FDTD software. The absorption coefficient of STO, α_{STO}, was calculated from the permittivity of STO using $2E\kappa/\hbar c$ where E is the energy in eV, κ is

the imaginary part of the refractive index of STO obtained from the permittivity, c is the speed of light and $\hbar$ is the reduced Planck's constant.

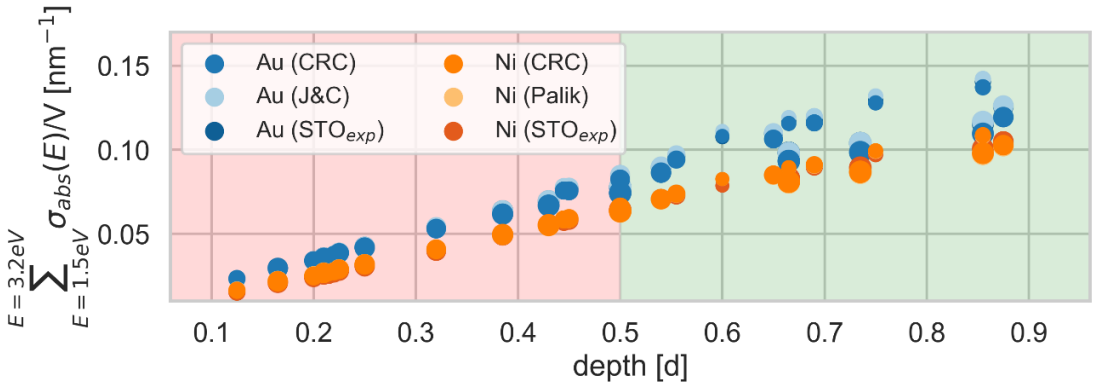

Fig S18: Summation of the area underneath the peaks (from 1.5 eV to 3.2 eV in Fig. 5c) versus the depth in diameter for Ni and Au MNPs. The figure shows the area included underneath the peaks in Fig. 5c, describing the total absorption instead of the peak position and height in the interval from 1.5 eV to 3.2 eV. Generally, plasmonic metals have a high Q-factor, i.e., a well-defined peak (like Au in Fig. 5c), while, i.e., Ni has a low Q-factor or broad peak (like Ni in Fig. 5c). To describe the system more accurately, both the peak and the total absorption have to be considered. In Fig. S19 the peak positions are shown, in Fig. S20 the peak maxima are described, and here are the total absorptions. The peak positions decrease in energy, while the maxima increase for more buried MNPs, independent of the metal (Au or Ni). Moreover, as demonstrated here, the total absorption also increases, making buried MNPs preferable. "CRC" denotes the permittivity data taken from CRC Handbook of Chemistry & Physics, "Palik" permittivity data taken from the Handbook of optical Constants of Solids I – III and "J&C" permittivity data taken from [2] and finally "STO_{exp}" are experimentally found permittivity data.

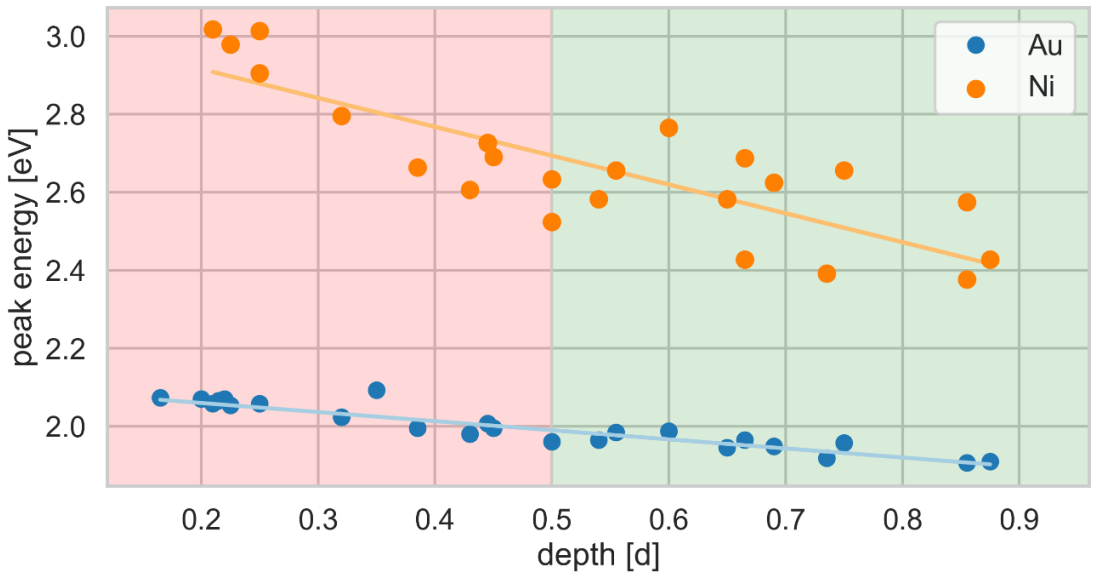

Fig. S19: Peak energy versus depth in diameter for Ni (orange) and Au (blue) MNPs on/in STO.

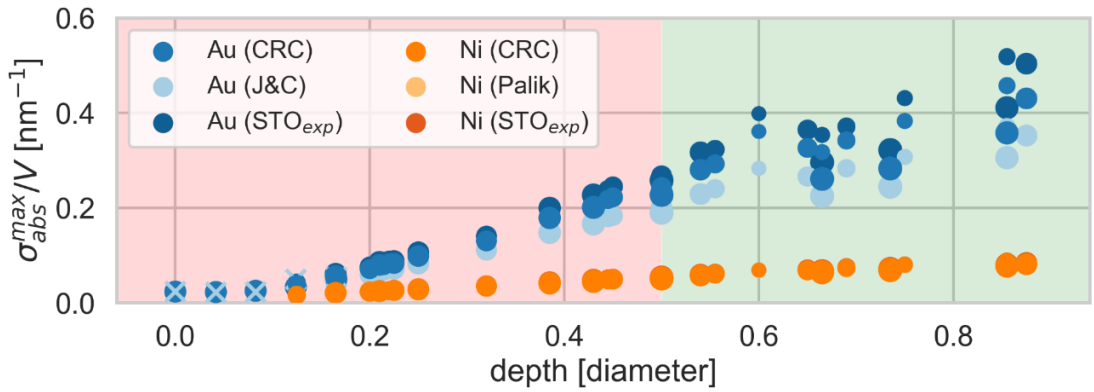

Fig. S20: Maximum absorption cross-section divided by the volume of the particle versus the depth in diameter for Ni and Au particles for different permittivity data ([1–4]). Crosses mark calculation points for domes. “CRC” denotes the data taken from CRC Handbook of Chemistry & Physics, “Palik” data taken from the Handbook of optical Constants of Solids I – III and “J&C” data taken from [2] and finally “STO$_{exp}$“ are experimentally found data.

2. Supplementary Tables

Table S1: The mean photocurrent of four LSV sweeps for each sample taken at On 0795 V – Off 0.785 V vs RHE. The standard deviation of the mean is given as error.

Sample	**Photocurrent [nA]**
STO(Ni)	25.9 ± 0.6
STONi	2.8 ± 0.3
STONiAu5s	5.7 ± 0. 2
STONiAu30s	481 ± 6.2
STONiAu90s	1.5 ± 0.1

3. Supplementary Text

Supplementary note 1:

A FEI Titan G2 60-300 instrument was used to perform STEM and high-resolution EELS. A CEOS DCOR corrector for the probe forming lenses, a Wien-filter monochromator, a Gatan 965 Quantum EELS spectrometer and a FEI Super-X EDS detector were installed on the instrument. The instrument was operated at 300 kV acceleration voltage for structural and chemical characterization, with a probe convergence of 21 mrad. The HAADF, DF4, and DF2 have 101, 22, and 9 mrad, respectively, as inner collection semi-angle. Surface plasmon mapping was done at 60 kV with an energy resolution of ≈110 meV as measured using the full-width-half-maximum (FWHM) of the zero loss peak. The top-view images of Fig. S6 were observed with scanning electron microscopy (SEM) using a FEI Quanta 200F FEG-ESEM microscope at an acceleration voltage of 20 kV using the back-scattering detector.

Supplementary note 2:

Additional XPS Details: The samples were characterized by X-ray photoelectron spectroscopy (XPS) using a Kratos Axis Ultra DLD spectrometer, with monochromated Al Kα radiation (hν = 1486.6 eV). Survey spectra were measured using step size 1 eV and pass energy (PE) 160 eV, while high-resolution spectra were measured using step size 0.1 eV and PE 40 eV. Charge compensation was applied via a low energy electron flood gun. The energy axis was calibrated by using the position of the Ti 2p component of STO previously reported at 458.4 eV [5].

Supplementary note 3:

Figure 5b shows that the maximum absorption in Au is larger than Ni when one compares the results for a certain depth and size, e.g. at a depth of 0.6 times the diameter, d, the maximum absorption in Au is approximately 0.35 nm^{-1} compared to Ni at 0.1 nm^{-1}. For very low depths, the maximum absorption difference is not as prominent. However, from Fig. 5c the shape of the absorption peaks from particles with depth < 0.5d shows that Au has a peak with higher quality factor. The higher quality factor implies that the plasmon is less dampened for Au compared to Ni. In addition to the maximum absorption being higher for Au, the total absorption within the spectral region below the STO band gap is also higher for Au than Ni (Fig. S17).

4. Reference

[1] C.G. Olson, D.W. Lynch, J.H. Weaver, (n.d.). unpublished.

[2] P.B. Johnson, R.W. Christy, Optical Constants of the Noble Metals, Phys Rev B. 6 (1972) 4370–4379. https://doi.org/10.1103/PhysRevB.6.4370.

[3] D.W. Lynch, R. Rosei, J.H. Weaver, Infrared and visible optical properties of single crystal Ni at 4K, Solid State Commun. 9 (1971) 2195–2199. https://doi.org/10.1016/0038-1098(71)90629-6.

[4] E.D. Palik, Handbook of optical constants of solids, Academic press, 1998.

[5] Ji, L., McDaniel, M., Wang, S. *et al.* A silicon-based photocathode for water reduction with an epitaxial $SrTiO_3$ protection layer and a nanostructured catalyst. *Nature Nanotech* **10**, 84–90 (2015). https://doi.org/10.1038/nnano.2014.277

Paper III

Exsolution of Ni Nanoparticles in A-site Excess STO Thin Films I: Thin Film Properties

Kevin G. Both*

Manuscript

* More authors may be included when they have had the full possibility to check, accept, and take full responsibility of all contents of the manuscript. Their contributions to the work are listed in the Credits at the end of the manuscript.

Chapter 5

Additional Experiments and Summarizing Discussion

In the following sections, results of experiments relevant to the topic of the thesis are presented that are not included in previous chapters. Additionally, a summarizing discussion is given based on the results presented in the papers and in this chapter. The additional samples include strontium titanate (STO) thin films and powders doped with Cu, Ru, Ag, and Fe.

5.1 Copper Doping, Galvanic Replacement by Silver, and Plasmon Response

A-site excess STO doped with Cu ($Sr_{1.07}Ti_{0.93}Cu_{0.07}O_{3\pm\delta}$) has been synthesized by a modified approach of [1] and as highlighted in Paper I. The powder was synthesized by mixing stoichiometric amounts of precursors by ball milling for 3 h at 300 rpm in isopropanol. Subsequently, the powder was dried and calcined at 1000 °C for 5 h. The resulting powder was ball-milled again for 3 h for 300 rpm in isopropanol and dried in the heating cabinet before being pressed into a pellet and sintered at 1100 °C. The pellet was crushed, and the obtained powder was ball-milled for a third time under the same conditions and dried. The exsolution process was carried out in H_2 for 12 h, creating Cu metal nanoparticles (MNPs).

Part of the obtained powder was utilized in a galvanic replacement reaction (GRR), where Ag MNPs were created. The GRR was conducted by submerging

the powders in a silver acetate solution (10^{-3} M $AgCH_3CO_2$ and 0.1 M $HClO_4$) for 10 min. The main difference between this method and the one in [1] is the use of ball-milling instead of ultrasonication and the calcination as powder instead of as pellet.

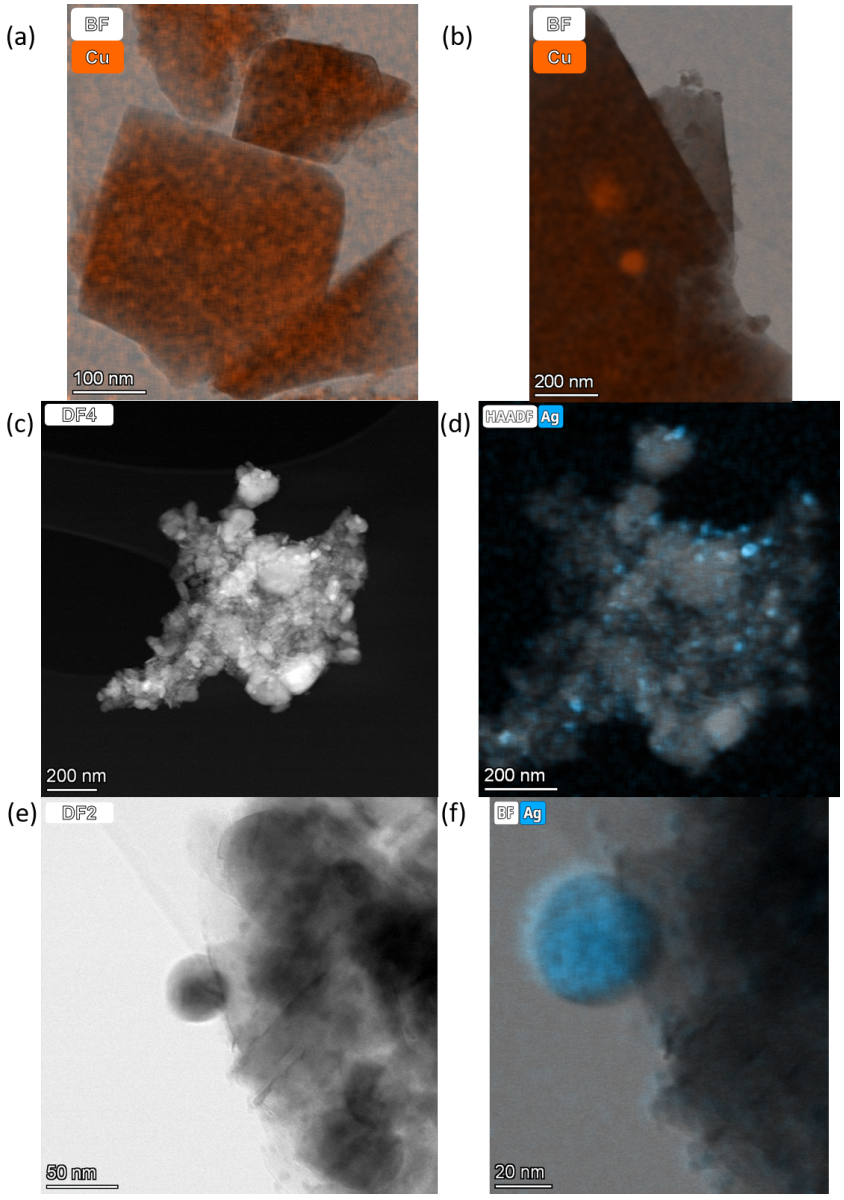

Figure 5.1: (a) A BF STEM image overlayed with Cu EDX of nonexsolved $Sr_{1.07}Ti_{0.93}Cu_{0.07}O_{3\pm\delta}$. (b) A BF STEM image overlayed with Cu EDX of exsolved $Sr_{1.07}Ti_{0.93}Cu_{0.07}O_{3\pm\delta}$. (c) A DF4 image of $Sr_{1.07}Ti_{0.93}Cu_{0.07}O_{3\pm\delta}$, exsolved and galvanically replaced by Ag. (d) An overlay of a HAADF image and EDX map of Ag of the same STO particle as in (c). (e) A small particle on the side of the STO matrix is shown by a DF2 image. (f) The BF image and EDX map of Ag of the same particle as in (e).

The nanoparticles can be seen in figure 5.1, where (a) shows the powder before exsolution, and (b) shows the exsolved Cu particles on STO. The images in (c-f) are of the replaced STO and include Ag. Specifically, (c) shows a DF4 image of an STO particle, whereas (d) shows the corresponding HAADF image overlayed with the Ag EDX map. In (e), a DF2 image of a particle is shown and (f) shows the corresponding BF image with an Ag EDX map. The STO particle is covered in Ag MNPs where the selected one (shown in (e, f)) is about 50 nm in diameter, appearing spherical.

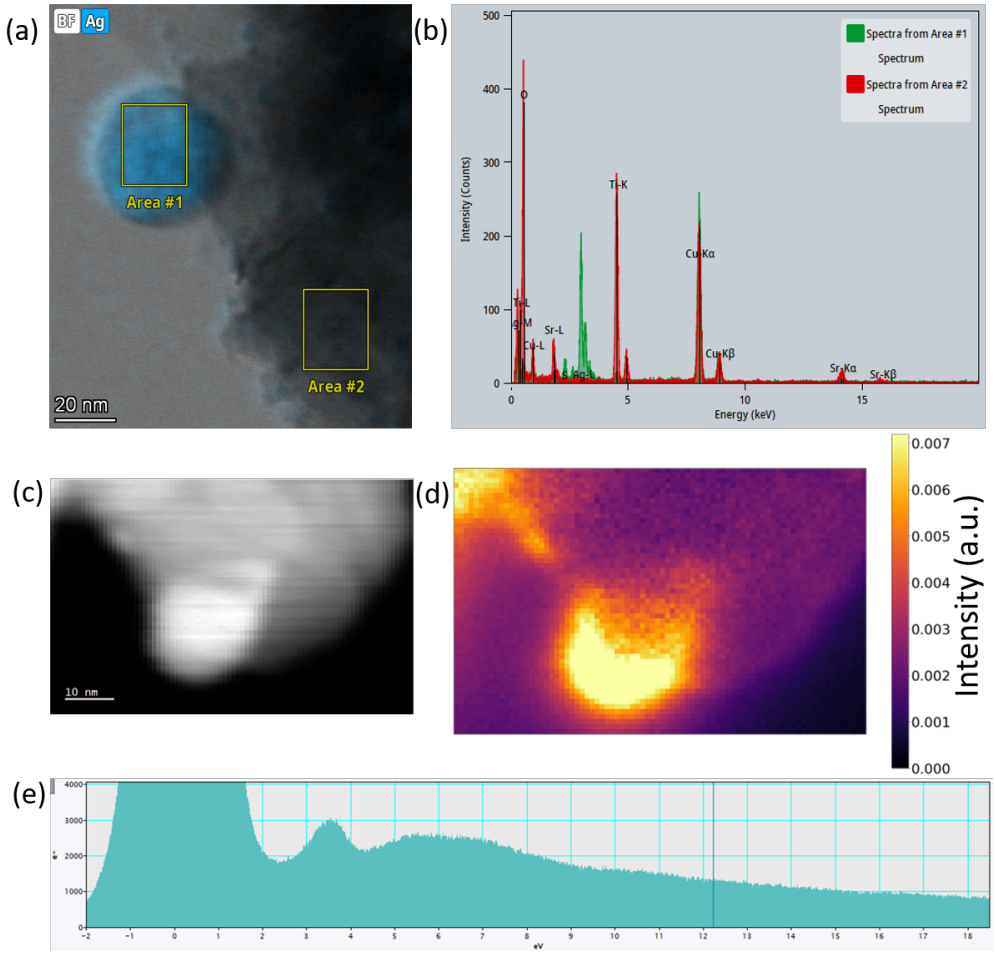

Figure 5.2: (a) The same particle as in figure 5.1 (d), but two boxes indicate the origin of the EDX spectra in (b). (b) The EDX spectra where green represents the spectra of the particle, and red the spectrum of the matrix. (d) The normalized plasmon map of the Ag particle in (c) is shown for the energy range from 3.48 - 3.51 eV.

In contrast to the Ni MNPs replaced by Au in Paper I and Paper II, it is rather challenging to determine the amount of Cu left by EDX. This is due to the experimental setup, where the background Cu signal is very high due to the copper grid and other copper sources within the TEM. In contrast, detecting the presence of Ag, as seen in figure 5.2 (a,b) is achievable and confirms that the GRR reaction took place, further generalizing the combination of exsolution and GRR as a pathway to introduce noble MNPs, in addition to the ones presented in Paper I and Paper II.

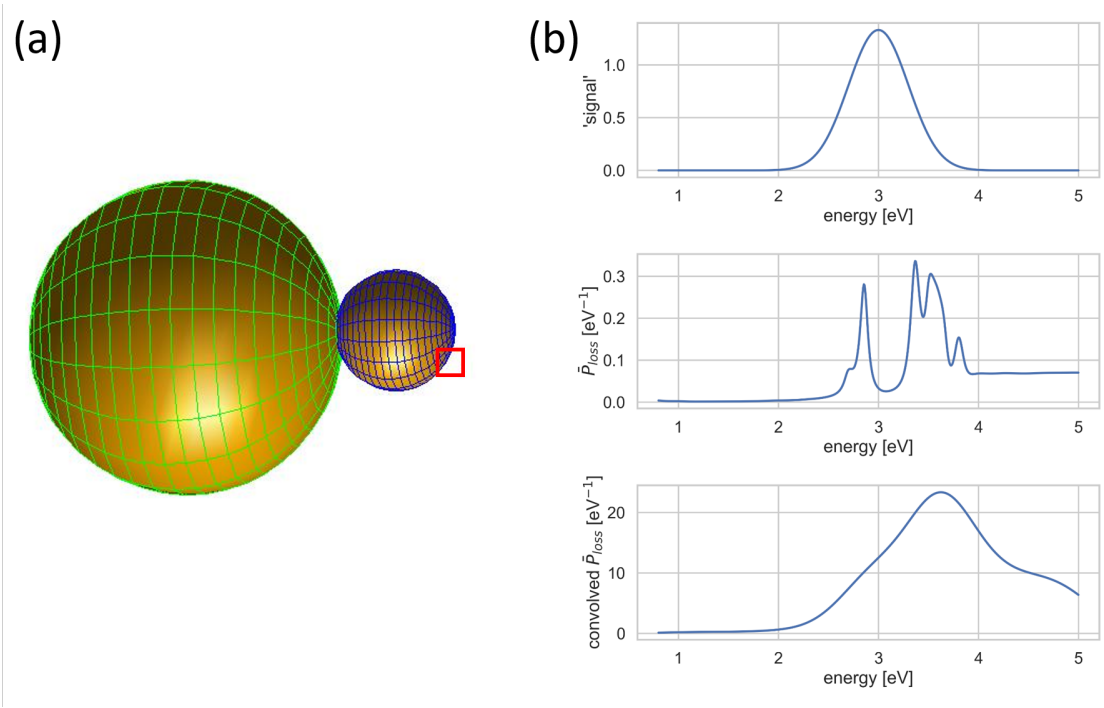

Figure 5.3: (a) The small Ag sphere on top of a larger STO sphere used in the determination of the electron energy loss probability. (b) Top: The Gaussian used to deconvolute the (middle) calculated electron energy loss probability, resulting in the (bottom) deconvoluted absorption loss probability. The calculations were performed with the metal nanoparticle boundary element method and simulate EEL. The orange square indicates which area was scanned by the simulation beam with a 5×5 grid. The average response is plotted in (b). This is similar to the method used in Paper I.

Cu and Ag are both materials with observable surface plasmonic responses,

as introduced in section 2.5. Experimentally, the observation of the Cu localized surface plasmon resonance (LSPR) by EELS is challenging, and not part of this work. In addition to the LSPR maps of Au in Paper I and Paper II, plasmon maps for an Ag particle were obtained; one is displayed in figure 5.2 (c-e). The HAADF image of the Ag MNP is shown in (c), the corresponding plasmon map for the energy range from 3.48 - 3.51 eV in (d), and the EEL spectrum in (e). A singular peak can be seen around 3.5 eV in (e). To confirm the shape and position of the peak, theoretical calculations were employed. They revealed that an Ag MNP on STO should yield multiple peaks. Specifically, the electron loss probability of a small Ag particle slightly embedded in a larger STO sphere is shown in figure 5.3 ((b), middle), with four distinct peaks and a shoulder on the left side of the lowest energy peak. Using a Gaussian signal given in figure 5.2 ((b), top) based on the full width at half-maximum of the experiment zero loss peak, the electron loss probability was convoluted and figure 5.2 ((b), bottom) resulted. The peak is similar in shape and position to the experimentally observed peak, including a shoulder just below 3 eV in both calculated and measured spectra. However, confirmation that structures like the one in figure 5.2 yield multiple experimental peaks was not obtained in this work due to experimental constraints, such as the limited energy resolution at the time of the experiments.

In general, the LSPR band shape and peak position varied with changes in geometry and elemental composition of the MNPs, and with the change of environment, as expected from the theory presented in section 2.5. The single particles of a single element can have varying degrees of spectral overlap, as seen in figure 5.4. Furthermore, as shown in Paper II, the absorption increases if Au MNPs are buried inside the STO matrix, similar to the absorption for Ag, Au, and Cu. For Cu and, as will be shown below, for Ag, the burying can be achieved by exsolution, leading to bulk MNPs. However, the exsolution of

Au particles is extremely difficult. Introducing Au via GRR not only serves to socket the particles well but also to enhance the loss probability. It should be noted that a spherical Au MNP slightly embedded into STO has a single peak, while the Ag MNP displayed multiple peaks in calculations. Experimentally, the spherical particles display only one peak, but the energy resolution of the EELS map of the Ag MNP is not good enough to distinguish between the peaks. More complex structures, like in Paper II, have multiple peaks.

As introduced in section 2.5, the absorption of energy via plasmonically active structures is only part of the requirements to enhance a photocatalytic system. The other part is the decay mechanism. For Au MNPs and STO, hot charge carrier injection is most probably the dominant mechanism, as argued in Paper II. The spectral overlap between the Au MNPs and STO is very limited; hence the plasmon-induced resonance energy transfer (PIRET) mechanism is minimal. However, a combination of hot charge carriers and local heating cannot be excluded. The Cu MNPs and STO overlap is very similar to the Au particle STO overlap and a similar argument can be made for the copper system.

The Ag MNPs and STO system are slightly different, where particles in vacuum have a large overlap with STO and embedded a relatively small one. Hence, particles on the surface have a larger overlap than particles in the bulk, and the importance of the PIRET mechanism decreases from surface particles to bulk particles. This creates a more complex decay environment, where it is impossible to determine the dominant decay mechanism with the experiments presented in this work. Typically, an insulating layer around the MNPs would prevent hot charge carriers from being injected into the matrix while, the PIRET mechanism can still excite an electron-hole pair even with an insulating layer of up to 25 nm around the MNPs [2]. Unfortunately, with exsolution and GRR, introducing an insulating layer between the MNPs and the matrix is impractical.

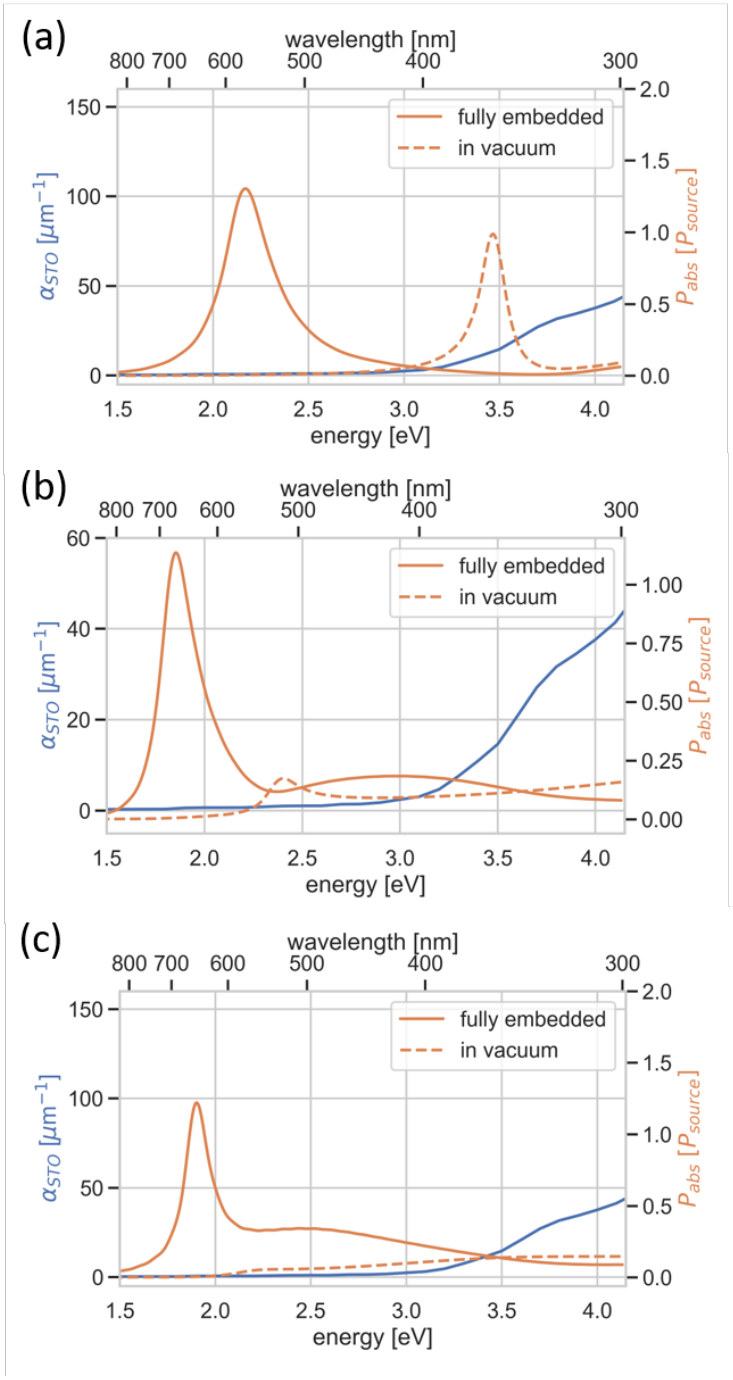

Figure 5.4: All three graphs show the spectral overlap between STO (blue) and a nanoparticle in vacuum (dashed orange line) or a fully embedded nanoparticle (solid orange line) of the same material. The graphs use the results for Ag (a), Au (b), and Cu (c). The calculations are performed with FDTD.

A second configuration, the two-particle system of two different elements as observed in Paper I can come in different forms as elaborated in that publication.

If the two spheres do not touch, theoretical calculations suggest only one peak in the loss probability spectra. However, if they are touching, two peaks are expected. This holds true for all positions, i.e., near the Au MNP, near the Ni MNP, and between the two. Experimentally, the single peak situation has been observed, indicating that the particles were touching. These particle systems can be utilized as antenna reactor plasmonic photocatalysts, i.e., like the ones described in [3, 4], but with a simpler synthesis method.

5.2 Galvanic Replacement Reaction and Secondary Particle Formation

The secondary particle formation, i.e., the formation of particles because of GRR, results in two different general configurations. Either the particles are completely replaced, i.e., in Paper II, and no sacrificial MNPs are found on the surface, or more complex structures, such as in the case of Paper I, with noble MNPs and sacrificial MNPs are obtained. The most apparent difference between the two, besides their stoichiometry, is one set being thin film samples and the other powder samples; however, closer examination of other samples like the one in figure 5.1 reveals that A-site excess STO powders also have complete replacement of the initial surface MNPs. A second difference is the use of polyvinylpyrrolidone (PVP) which was only used in Paper I but not in Paper II or any of the additional experiments. Consequently, either the stoichiometry of the STO or the presence of PVP results in different degrees of electrochemical etching process described in section 2.3.

The bimetallic nanostructures observed in this work appear not as single alloys, but rather as two regions, i.e., a Ni- and a Au-rich region. The Hume-Rothery substitutional solubility rules predict that two metals which have a different type of lattice structure, an atomic size difference of more than 15%,

and a high chemical affinity have lower solubility [5]. Furthermore, if the ratio between the valence electrons to atom is different, the metal with the lower valency will have a higher solubility and vice versa [5]. In table 5.1, the relevant details for atoms used in GRR are given. Ni has the same lattice structure and is 13.89% smaller than Au, while the lattice parameter of Ni ($a = 0.3524\,\text{nm}$) is 13.63% smaller than of Au ($a = 0.408\,\text{nm}$).

Table 5.1: The type of lattice structure, metallic radii [6], electronegativity, and ratio between valence electrons to atoms for different elements exsolved and used in GRR in this work, including Ni, Cu, Ag, and Au.

Element	Lattice	Size [pm]	Electronegativity [7]	Ratio
Ag	FCC	144	1.93	2
Au	FCC	144	2.54	1
Cu	FCC	128	1.9	1
Ni	FCC	124	1.91	2
Pt	FCC	139	2.28	1

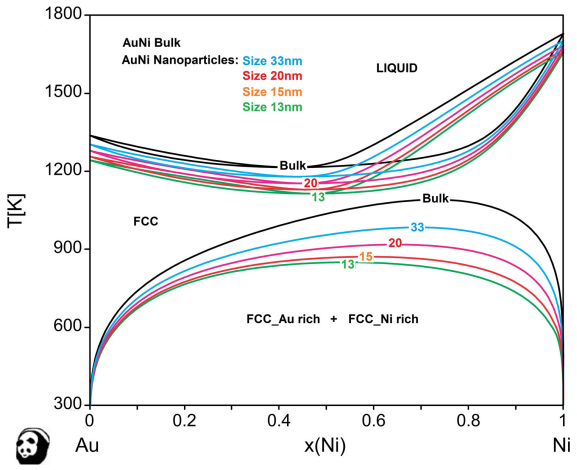

Figure 5.5: The predicted Au-Ni phase diagram for bulk material and different sizes of AuNi nanoparticles. The figure was taken from [8], with permission.

While the electronegativity is different, the Hume-Rothery substitutional solubility rules predict that Ni and Au can form an alloy, and the phase diagram given in figure 5.5 confirms it for bulk. However, on the nanoscale, we observed a hesitancy in forming an alloy, resulting in different structures like flower-like

and antenna-reactor. Conversely, Pt ($a = 0.3924\,\text{nm}$) and Ni have a smaller size difference, where a Ni atom is 11.79% smaller than a Pt atom, and the Ni lattice parameter is 10.19% smaller than the Pt lattice parameter. This suggests a better ability to form an alloy, and we observed a hedgehog structures forming in Paper I. It is important to note that the Hume-Rothery substitutional solubility rules do not predict whether a GRR is possible, but whether a bimetallic system is more likely to form a solid solution or an intermetallic compound [5].

Partial replacement and complete replacement of the less noble metal can be explained by the different degrees of electrochemical etching process introduced in section 2.3. The different degree of mixing is related to the Hume-Rothery substitutional solubility rules; however, the antenna-reactor particles with no touching Au and Ni seen in Paper I may also be the result of galvanic deposition. Analogous to the paper in appendix B, oxygen vacancies in the LSTO are created and may be present at the surface of the material, and the surrounding Ti could be present as Ti^{3+} with a neutral oxygen vacancy. It is interesting to note that this behavior has only been observed on LSTO, but not on A-site excess STO. It has previously been reported that La-doping promote the transformation of Ti^{4+} to Ti^{3+}, but it is yet unclear if a neutral $V_O^{\times}$ is present, and allow the adsorbtion of the Au on the surface and particle growth by oxidation of the surrounding LSTO surface, similar to appendix B. In that case, the STO without La has no stable site for the Au to adsorb and consequently does not show any of these deposited particles.

5.3 Copper, Ruthenium, or Silver Doped Thin Films and Iron Doped Powder

Additionally to the Cu-containing powder samples and all the samples presented in the publications, Cu-containing A-site excess STOCu ($Sr_{1.07}Ti_{0.93}Cu_{0.07}O_{3\pm\delta}$),

Ru-containing A-site excess STORu($Sr_{1.07}Ti_{0.93}Ru_{0.07}O_{3\pm\delta}$), Ag-containing A-site excess STOAg ($Sr_{1.07}Ti_{0.93}Ag_{0.07}O_{3\pm\delta}$), and Fe-containing A-site excess STOFe ($Sr_{1.07}Ti_{0.93}Fe_{0.07}O_{3\pm\delta}$) thin films were made. These thin films were deposited in oxygen atmosphere (5×10^{-2} mbar) with $3\,J\,cm^{-2}$ and a repetition rate of 10 Hz. 20'000 shots were applied at 9 cm substrate to target. The resulting thin films were exsolved in a ProboStat^{TM} (NorECs AS, Norway) in HArmix for 30 min at 800 °C. The ramp rate of $5\,°C\,min^{-1}$ was used to heat and cool. The surface MNPsS of the Cu, Ni, and Ru doped samples are likely oxidized after storage in ambient conditions.

The Cu and Ru thin films were subsequently used in photoelectrochemical (PEC) measurements. An Invium Vertex potentiostat/galvanostat was used with a standard three-electrode setup with 0.5 M Na_2SO_4 (pH = 7.5) as the electrolyte, a saturated calomel electrode (SCE) and platinum foil as the reference and counter electrodes, respectively. The working electrodes were prepared as in Paper II. The PEC measurements were carried out under 1 sun simulated solar light and are shown in figure 5.6. The potentials were corrected against the reversible hydrogen electrode (RHE), like in Paper II. The photocurrent of the sample taken at light on 0.795 V - light off 0.785 V is 3.66 nA for the STOCu sample, with the area and voltage the same as in Paper II. The photocurrent of the STOCu sample is higher than those of samples with exsolved Ni MNPs (STONi), and samples with 90s Au GRR (STONiAu90s). However, it is lower than the one of non-exsolved (STO(Ni)), 5s Au GRR (STONiAu5s), and 30 s Au GRR (STONiAu30s). The STORu sample is different from the other two, where no steady-state was achieved during the light on or off stated of the chopped light measurements, and no photocurrent recombination spikes visible. The current difference at the same voltages (0.795 V - 0.785 V) as the other samples is 26 nA. If the current difference is taken at the light switch points (light off to

on 0.778 V - light on to off 0.799 V) then the difference is 60 nA.

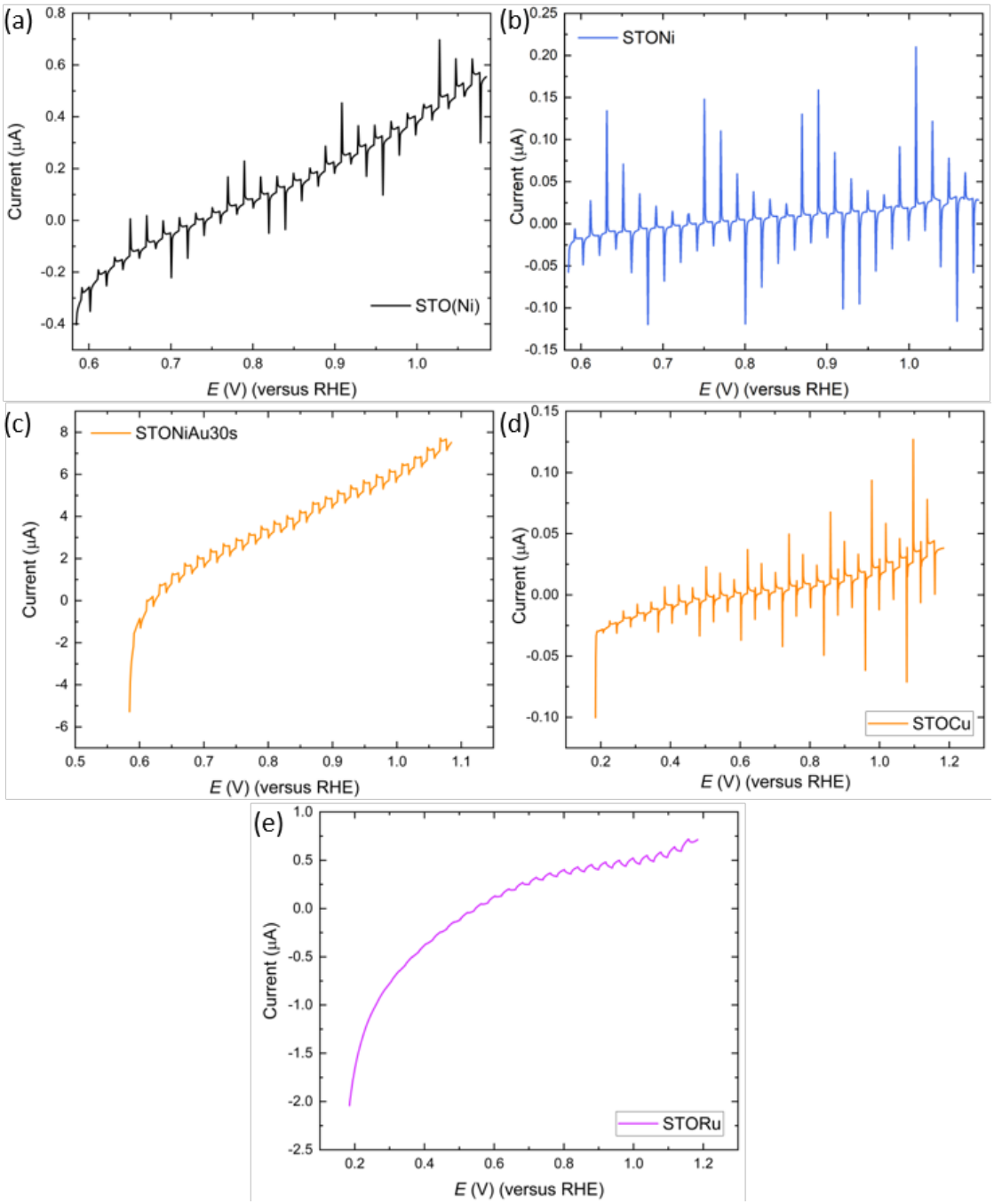

Figure 5.6: Linear sweep voltammetry performance of (a) the STO(Ni), (b) STONi, and (c)STONiAu30s samples of Paper II. (d) and (e) shows the LSV sweeps for the STOCu and STORu samples, respectively. All areas were normalized to be the same as the STONiAu30s sample.

Exsolving Ag MNPs within a thin film was challenging. As seen in figure 5.7,

after treating an A-site excess thin film doped with Ag in HArmix at 800 °C for 30 min, the film shows no columnar growth and no distinguishable MNPs. This is in contrast to thin films treated similarly but doped with Cu, Ni, Ru, or Fe. The thin films appeared as nanocrystalline/amorphous as the non-exsolved thin films reported in Paper II.

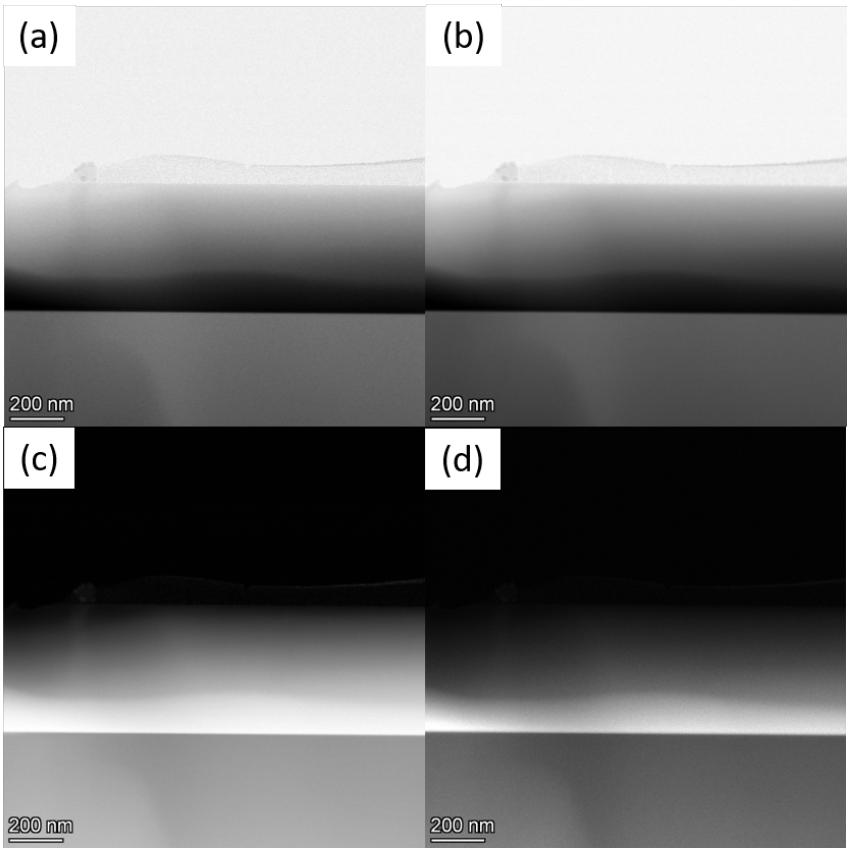

Figure 5.7: THe HAADF (a), DF4(b), DF(2), and (BF) (d) STEM image of an A-site excess STO thin film doped with Ag, after treating in HArmix at 800 °C for 30 min.

Ag MNPs were created by raising the time and temperature of the exsolution, i.e., to 850 °C for 2 h. The particles appear near or at grain boundaries, with fewer exsolved MNPs than in other samples. It is evident that exsolving Ag from A-site excess $Sr_{1.07}Ti_{0.93}Ag_{0.07}O_{3\pm\delta}$ is more difficult than exsolving Cu, Ni, Ru, or Fe. The reason could be a lower Goldschmidt tolerance factor than any the other factor of A-site excess STO synthesized in this work. Ag nanoparticles have

been exsolved in powders before, using hot ethylene glycol [9]. A reason for the difficulty to exsolve could also be a combination of the nanocrystalline/amorphous thin film on the Si wafer and the smaller Goldschmidt factor, leading to an initially larger barrier to overcome crystal formation and subsequent exsolution.

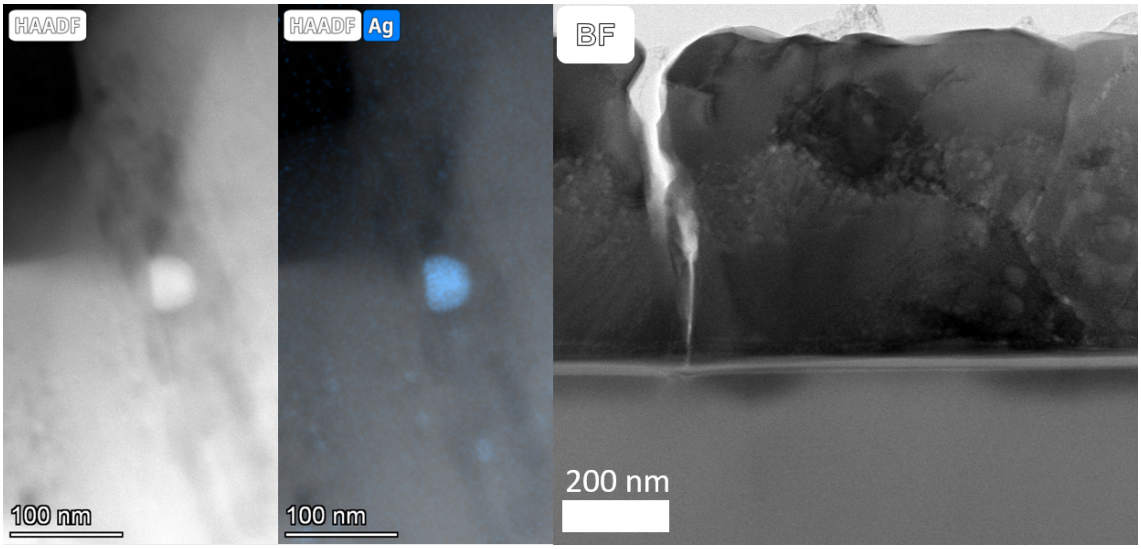

Figure 5.8: (Left) A HAADF image and HAADF image with the Ag EDX spectrum (Middle). The largest particle is about 50 nm in diameter, while there are several smaller particles. (Right) A BF STEM image of the thin film, showing no columnar structures like in Paper III.

Fe is the last dopant presented here and exsolved during this work. Iron substituting the Ti changed the oxygen stoichiometry slightly because Fe can exhibit two common oxidation states. Any presence of a Fe^{3+} ion reduces the number of oxygen vacancies. However, no efforts were made to identify the exact oxygen stoichiometry of the samples. The samples were exsolved in powder form at 850 °C under H_2 flow and studied by TEM, as seen in figure 5.9. The particles obtained were relatively large, about 50-100 nm in diameter.

All the STO powders and thin films in this work have a variety of stoichiometries and dopants. Consequently, their Goldschmidt tolerance factors, introduced in section 2.1, varied. An overview of the different Goldschmidt

tolerance factors is given in table 5.2. The A-site deficient powder has a lower tolerance factor, suggesting that the octahedra might tilt and not retain the perfect cubic lattice structure. In fact, as mentioned in Paper I, an extra shoulder at the (222) reflection ($\approx 86.4°$) has been identified. The extra shoulder disappears after exsolution. However, since the exact stoichiometry and oxidation state, and consequently the radii of the species involved are unknown, it is difficult to attribute a Goldschmidt tolerance factor to these structures. The A-site excess stoichiometries have tolerance factors close to 1, indicating they are closer to the cubic lattice. The samples with Ru might have a slightly disturbed structure with $\tau > 1$, indicating that the TiO_6 octahedra slightly stretched to accommodate Ru. However, as mentioned above, with the apparent nanocrystallinity/amorphousness of the films may create a situation where even a small deviation from the ideal structure leads to a larger barrier to overcome the crystal formation and subsequent exsolution.

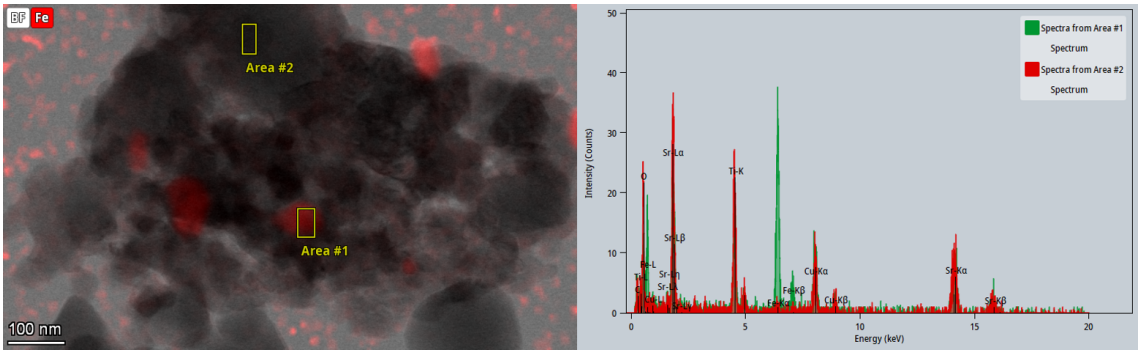

Figure 5.9: An A-site STO particle with Fe exsolution BF image overlayed with Fe EDX map, and two areas of interest are shown on the left. On the right, the corresponding graphs of the EDX measurements are shown where Area #1 shows a clear Fe peak not present in Area #2

The thin film samples in Paper II appeared nanocrystalline or amorphous, in contrast to the A-site deficient powders in Paper I. After exsolution, the dominant phase is the STO phase, while other phases were identified. This is

unintuitive when just observing the tolerance factor of the stoichiometries at hand. The lack of any XRD peak suggests that the interaction between the substrate and the material deposited does not force a particular orientation. However, the conditions during exsolution, specifically, the elevated temperature, are enough for crystal growth. The additional 200 °C during exsolution compared to the deposition temperature allows the formation of larger domains, appearing columnar shaped. The appearance of columns could indicate that the interaction between the substrate and the STO leads to a preferential crystallization direction. Columnar growth of thin films has been observed in other systems grown on Si wafers, like ZnO on Si wafers [10, 11]. It has additionally been shown that on different substrates, i.e., gallium arsenide (GaAs), the presence of SiO_2 is beneficial [10]. The crystal quality increases in these depositions while the c-axis is oriented perpendicular to the surface, like in samples where ZnO is deposited directly on Si wafer [11]. The STO thin films grown on Si wafers in this study, while present, appears less oriented, with XRD spectra showing a multitude of different phases. The presence of a Si−Sr−O phase identified as $3\,SrO\cdot SiO_2$ in Paper II in several thin films and the mismatch between the cell parameters suggest that the influence of the substrate on the crystallization orientation is minimal. It should further be noted that the RP phases can be identified by XRD but were not detected by TEM.

Independent of the form of the samples, exsolution occurred. The conditions were different, as described in chapter 3. The difference in requirement for a successful exsolution originates in the different sample geometry. The sample geometry during exsolution within the Probostat refers to the fact that the surface of a thin film is planar and directly exposed to the atmosphere. In contrast, the powders were typically piled up or, in the CaH_2 cases, pressed into a pellet. The surface area of loose powder is much higher than the surface area

of a planar thin film; however, densification either prior or during exsolution may change this. Previously, exsolution has been reported for powders by, i.e., Neagu et al. for $La_{0.4}Sr_{0.4}Ni_xTi_{1-x}O_{3-\delta}$ at 930 °C in dry 5% H_2/Ar for 20 h [12]. While exsolution occurred faster and at slightly lower temperatures in the case of our powders, the parameters are similar to the literature values.

Table 5.2: The Goldschmidt tolerance factors, τ, of the different stoichiometries considered in this work, the form (P for powder, TF for thin film) of the sample, and the part of the thesis the samples can be found are displayed. The A-site excess factors are calculated assuming the excess A-site excess exists as RP phase. It is assumed that all oxygen-sites are filled. The ionic radii are from Shannon [13].

Stoichiometry	τ	Form	Work
$La_{0.6}Sr_{0.2}Ti_{0.9}Ni_{0.1}O_{3-x}$	0.879	P	Paper I
$Sr_{1.07}Ti_{0.93}Ag_{0.07}O_{3\pm x}$	0.990	TF	chapter 5
$Sr_{1.07}Ti_{0.93}Cu_{0.07}O_{3\pm x}$	0.997	P, TF	chapter 5
$Sr_{1.07}Ti_{0.93}Fe_{0.07}O_{3\pm x}$	0.996	P	chapter 5
$Sr_{1.07}Ti_{0.93}Ni_{0.07}O_{3\pm x}$	0.999	TF	Paper II, Paper III,
$Sr_{1.07}Ti_{0.93}Ru_{0.07}O_{3\pm x}$	1.001	TF	chapter 5

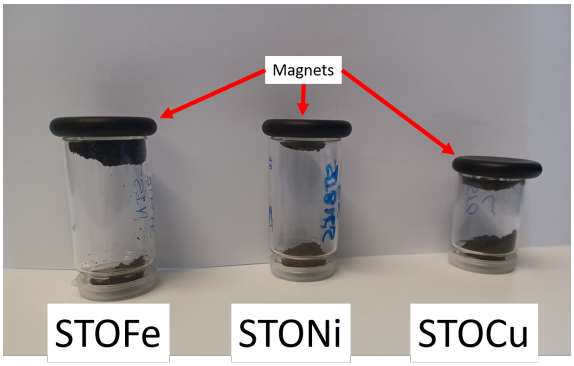

Figure 5.10: Three different powders are shown. They are (from left to right) A-site excess STO with Fe MNPs, A-site excess STO with Ni MNPs, and A-site excess STO with Cu MNPs.

Another property some powder samples exhibited are magnetic properties, as seen in figure 5.10. This effect was not only limited to the A-site excess STO with Fe MNPs, but also for similar powders with Ni MNPs or Cu MNPs.

Non-exsolved samples did not exhibit any attraction by magnets. It should be noted that STO powders appearing gray after exsolution, indicating a lesser degree of reduction, also showed no magnetic properties.

Their magnetic properties appeared to be proportional to the degree of reduction, i.e., black STO with Ni particles was magnetic, while gray STO with Ni particles was less magnetic. The magnetic properties are not surprising for the $Sr_{1.07}Ti_{0.93}Fe_{0.07}O_{3\pm x}$ and $Sr_{1.07}Ti_{0.93}Ni_{0.07}O_{3\pm x}$ stoichiometries because both Ni and Fe are ferromagnetic. However, exsolving $Sr_{1.07}Ti_{0.93}Cu_{0.07}O_{3\pm x}$ leads to Cu MNPs on STO, where Cu is diamagnetic. The question of where the magnetic properties come from for all samples is complicated. Certain MNPs can have magnetic properties, but also the matrix, e.g., Ti^{3+}, can have a magnetic moment. Consequently, the particle size, strain effects, and location of the particles (surface or bulk) influence the magnetic properties. The deconvolution of the different origins of magnetism is beyond the scope of this work but is potentially interesting for applications involving magnetic fields.

References

[1] Kang, X. *Novel nanostructured materials for energy applications*. eng. Vol. no. 2465. Series of dissertations submitted to the Faculty of Mathematics and Natural Sciences, University of Oslo (trykt utgave). Oslo: Department of Chemistry, Faculty of Mathematics and Natural Sciences, University of Oslo, 2021.

[2] Wu, N. “Plasmonic metal–semiconductor photocatalysts and photoelectrochemical cells: a review”. En. In: *Nanoscale* vol. 10, no. 6 (Feb. 2018). Publisher: The Royal Society of Chemistry, pp. 2679–2696.

[3] Kane, K. A. and Bertino, M. F. “Pulsed laser synthesis of highly active Ag–Rh and Ag–Pt antenna–reactor-type plasmonic catalysts”. In: *Beilstein journal of nanotechnology* vol. 10, no. 1 (2019), pp. 1958–1963.

[4] Zhou, L. et al. “Light-driven methane dry reforming with single atomic site antenna-reactor plasmonic photocatalysts”. In: *Nature Energy* vol. 5, no. 1 (2020), pp. 61–70.

[5] Scott, D. A. and Schwab, R. “The Structure of Metals and Alloys”. In: *Metallography in Archaeology and Art*. Springer, 2019, pp. 69–132.

[6] Greenwood, N. N. and Earnshaw, A. *Chemistry of the Elements*. Elsevier, 2012.

[7] Brown, I. and Skowron, A. "Electronegativity and Lewis acid strength". In: *Journal of the American Chemical Society* vol. 112, no. 9 (1990), pp. 3401–3403.

[8] Sopoušek, J. et al. "Au-Ni nanoparticles: Phase diagram prediction, synthesis, characterization, and thermal stability". In: *Calphad* vol. 58 (2017), pp. 25–33.

[9] Xu, X., Liu, G., and Azad, A. K. "Visible light photocatalysis by in situ growth of plasmonic Ag nanoparticles upon AgTaO3". In: *international journal of hydrogen energy* vol. 40, no. 9 (2015), pp. 3672–3678.

[10] Craciun, V. et al. "Growth of ZnO thin films on GaAs by pulsed laser deposition". In: *Thin solid films* vol. 259, no. 1 (1995), pp. 1–4.

[11] Van de Pol, F., Blom, F., and Popma, T. J. "Rf planar magnetron sputtered ZnO films I: Structural properties". In: *Thin Solid Films* vol. 204, no. 2 (1991), pp. 349–364.

[12] Neagu, D. et al. "In situ growth of nanoparticles through control of non-stoichiometry". In: *Nature Chemistry* vol. 5, no. 11 (Nov. 2013), pp. 916–923.

[13] Shannon, R. D. "Revised effective ionic radii and systematic studies of interatomic distances in halides and chalcogenides". In: *Acta crystallographica section A: crystal physics, diffraction, theoretical and general crystallography* vol. 32, no. 5 (1976), pp. 751–767.

Chapter 6

Conclusions

Increasing the efficiency of photocatalysts is a promising contribution to gaining independence from fossil fuels. In this work, well-known concepts such as galvanic replacement and exsolution have been combined and applied to create plasmonically active metal nanoparticles (MNPs) able to increase the photoelectrochemical response of strontium titanate (STO). Exsolution was achieved for Ni, Cu, Ag, Ru, and Fe. The crystallization of the thin films themselves assisted the exsolution process. If the STO thin films remained nanocrystalline/amorphous no exsolution occurred. Immediately after exsolution, galvanic replacement reaction (GRR) needs to follow to prevent the formation of an oxide layer on the exsolved MNPs while in air. GRR was employed to introduce noble metals, Au, Ag, and Pt, where the shape of the resulting particles is dependent on the replacement conditions, e.g., time or soluble polymers (PVP). The shape and geometry of the plasmonic active Au or Ag MNPs directly influence the localized surface plasmon resonance (LSPR) response and resulting enhancement of the photocatalyst.

The size dependency of the LSPR response of MNPs was exemplified by Au MNPs. All samples with Au MNPs and particle diameters below 50 nm outperformed the corresponding reduced STO, while larger particles appear to be detrimental for the photoelectrochemical (PEC) response. Reduced STO thin films with Cu MNPs have a larger PEC response than the equivalent Ni thin films or thin films with large Au particles. For A-site excess STO thin films, we also confirmed that too small or too large particles lead to a reduced

performance, indicating an ideal particle size. The response of Ag and Au particles differs significantly, where the LSPR of Au is at lower eV than Ag. Moreover, calculations suggest that spherical Au particles on STO have one peak, while a spherical particle of Ag has multiple peaks.

The geometry and composition of the MNP influence the LSPR band shape and peak position. Larger particles show multiple peaks, while smaller spherical ones tend to have only one. Partially burying the plasmonic MNPs increases not only their stability but also their LSPR response. The approach of exsolution and GRR allowed the incorporation of well-socketed Au and Ag MNPs on STO difficult to achieve by other means; particles, which, at least according to the computational models, have a larger absorption cross-section. While Ag and Au can be exsolved, it is more difficult and requires more noble metals than the introduction of Ag or Au MNPs by GRR. This work introduces a method offering the unique opportunity to optimize bulk and surface MNPs. The choice of dopant, pre-exsolution annealing, and exsolution parameters allow the design and synthesis of tunable, functional materials while the subsequent GRR introduces a further degree of tunability, resulting in a wealth of potential structures.

The minimal engineering of the approach described in this work makes it a versatile method, capable of performing in a plethora of applications, e.g., Pt MNPs, Au MNPs, or Ag MNPs. Simple changes, such as stoichiometry and form of the host, exsolution parameters, and GRR parameters lead to a variety of structures, including the ladybug, flower-like, antenna-reactor, or completely replaced MNPs, opening opportunities for new designs of materials and applications with tunable catalytic activities. Calculations can indicate potential candidate structures, and experiments can confirm them, while experimental data can be rationalized by computational methods.

Chapter 7

Outlook

A next step is to optimize the reaction parameters for the desired perovskite and metal nanoparticle (MNP) element and design the system for an economically competitive device. This includes stoichiometry of the perovskite, degree of reduction, electrolyte composition (e.g., surfactants, complexing agents, soluble polymers, etc.) of the galvanic replacement reaction (GRR), and geometry and composition of the plasmonic nanoparticle. More specifically, the choice of dopant to be exsolved is responsible partially for the bulk behavior of the powder or thin film. There are a variety of possible additional elements that can be used, i.e., Co [1], Rh [2], or Pd [3] would be of interest because of their catalytic applications. Co-exsolution, exsolving two elements simultaneously, would allow more complicated structures, potentially even tri-metallic structures, if GRR is utilized in addition. Structures previously synthesized by more complex synthesis methods, e.g., Pd-Co-Au trimetallics synthesized by micro-emulsion [4], could be achieved, that in addition can be made as supported multimetallic nanoparticles.

Utilizing exsolution in thin films leads to opportunities unavailable in powder exsolution because thin films have a defined direction from the surface to the interface with the substrate. As introduced in section 2.5, plasmonic MNPs can be designed based on their purpose, for example, to reflect light. A multilayered thin film, consisting of regions of different concentrations or regions of different dopants, allows the specific design of exsolved particles based on their location relative to the surface. GRR can also be included to modify the surface MNPs creating almost unlimited possibilities to design a thin film swarmed by a

multitude of different MNPs.

Control of the GRR, specifically to what extent the replacement takes place, would allow the selective design of surfaces where, for example, the ladybug-like structure is to be the dominant one. To unlock the ability to tailor the surface of a powder or thin film to an application, the role of the matrix and the GRR electrolyte composition should be studied. Antenna-reactor structures can be achieved by choosing these parameters correctly, leading the way to synthesize structures, i.e., like the Ag-Rh antenna-reactor MNPs previously achieved by pulsed laser synthesis [5], or Cu-Ni or Cu-Co antenna-reactor as shown in [6]. However, pressing questions remain. How can the ideal parameters for exsolution and GRR of multimetallic systems (two or three metals) be determined? Can a reliable synthesis of one particular multimetallic nanoparticle configuration achieved over a macroscopic sample? Can computational methods be employed to find the synthesis parameters for multimetallic systems?

New catalysts, more stable catalysts, utilizing lower amounts of precious metals, and the versatility to change the activity by simple adjustments can emerge from the work presented here. Moreover, plasmonically assisted photovoltaic devices can use similar MNPs to increase the conversion efficiency. Different geometries, such as the antenna-reactor geometry, may also have advantages for specific applications, e.g., H_2 generation, CO_2 reduction, or NH_2 fixation to NH_3, and investigating their reliable formation of them should be prioritized. Overall, pairing the simplicity of synthesis of the desired MNP system and the potential to reduce the quantity of noble metals needed per device together with the large-scale setup demonstrated by Domen et al. would not only make further investigations of these material systems attractive in a plethora of fields but also be potentially industrially highly relevant.

References

[1] Hou, W. et al. “Perovskite with in situ exsolved cobalt nanometal heterostructures for high rate and stable lithium-sulfur batteries”. In: *Chemical Engineering Journal* vol. 409 (2021), p. 128079.

[2] Kim, M. et al. “Direct Observation of Rhodium Ex-Solution from a Ceria Nanodomain and Its Use for Hydrogen Production via Propane Steam Reforming”. In: *ACS Applied Materials & Interfaces* vol. 13, no. 41 (2021), pp. 48508–48515.

[3] Li, J. et al. “A Highly Efficient and Robust Perovskite Anode with Iron–Palladium Co-exsolutions for Intermediate-Temperature Solid-Oxide Fuel Cells”. In: *ChemSusChem* vol. 11, no. 15 (2018), pp. 2593–2603.

[4] Sharma, G. et al. “Revolution from monometallic to trimetallic nanoparticle composites, various synthesis methods and their applications: A review”. In: *Materials Science and Engineering: C* vol. 71 (2017), pp. 1216–1230.

[5] Kane, K. A. and Bertino, M. F. “Pulsed laser synthesis of highly active Ag–Rh and Ag–Pt antenna–reactor-type plasmonic catalysts”. In: *Beilstein journal of nanotechnology* vol. 10, no. 1 (2019), pp. 1958–1963.

[6] Xu, Y. et al. “Boosting the on-demand hydrogen generation from aqueous ammonia borane by the visible-light-driven synergistic electron effect in antenna-reactor-type catalysts with plasmonic copper spheres and noble-metal-free nanoparticles”. In: *Chemical Engineering Journal* vol. 401 (2020), p. 126068.

Appendices

Appendix A

IV

Double Perovskite Cobaltites Integrated in a Monolithic and Noble Metal-Free Photoelectrochemical Device for Efficient Water Splitting

Junjie Zhu, Jónína B. Gudmundsdóttir, Ragnar Strandbakke, Kevin G. Both, Thomas Aarholt, Patricia A. Carvalho, Magnus H. Sørby, Ingvild J. T. Jensen, Matylda N. Guzik, Truls Norby, Halvard Haug, Athanasios Chatzitakis

Published in *ACS Applied Materials & Interfaces*, April 2021, volume 13, issue 17, pp. 20313–20325. DOI: 10.1021/acsami.1c01900.

The authors collectively acknowledge support from the Research Council of Norway for the following projects:PH2ON, Grant 288320; FunKey Cat, Grant 299736;Norwegian Center for Transmission Electron Microscopy, NORTEM, Grant 197405/F50. The assistance of the staff at Swiss-Norwegian Beamlines (SNBL, BM31; ESRF, Grenoble, France) is also acknowledged.

ACS APPLIED MATERIALS & INTERFACES

www.acsami.org

Research Article

Double Perovskite Cobaltites Integrated in a Monolithic and Noble Metal-Free Photoelectrochemical Device for Efficient Water Splitting

Junjie Zhu, Jónína B. Guðmundsdóttir, Ragnar Strandbakke, Kevin G. Both, Thomas Aarholt, Patricia A. Carvalho, Magnus H. Sørby, Ingvild J. T. Jensen, Matylda N. Guzik, Truls Norby, Halvard Haug, and Athanasios Chatzitakis*

Cite This: *ACS Appl. Mater. Interfaces* 2021, 13, 20313−20325

Read Online

ACCESS | Metrics & More | Article Recommendations | Supporting Information

ABSTRACT: Water photoelectrolysis has the potential to produce renewable hydrogen fuel, therefore addressing the intermittent nature of sunlight. Herein, a monolithic, photovoltaic (PV)-assisted water electrolysis device of minimal engineering and of low (in the μg range) noble-metal-free catalysts loading is presented for unassisted water splitting in alkaline media. An efficient double perovskite cobaltite catalyst, originally developed for high-temperature proton-conducting ceramic electrolyzers, possesses high activity for the oxygen evolution reaction in alkaline media at room temperatures too. $Ba_{1-x}Gd_{1-y}La_{x+y}Co_2O_{6-\delta}$ (BGLC) is combined with a NiMo cathode, and a solar-to-hydrogen efficiency of 6.6% in 1.0 M NaOH, under 1 sun simulated illumination for 71 h, is demonstrated. This work highlights how readily available earth-abundant materials and established PV methods can achieve high performance and stable and monolithic photoelectrolysis devices with potential for full-scale applications.

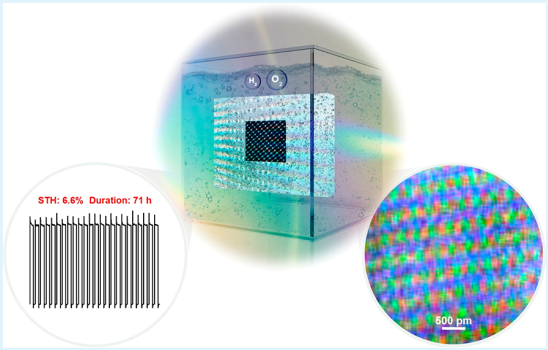

KEYWORDS: *photoelectrochemical water splitting, double perovskites, solar cells, earth abundant elements, bias-free water electrolysis, oxygen evolution reaction*

1. INTRODUCTION

Photoelectrochemical (PEC) water splitting is categorized among the six most promising pathways for the production of renewable hydrogen gas.[1] Solar-to-hydrogen (STH) energy conversion addresses the intermittent nature of sunlight, as well as the need for long-term energy storage and on-demand energy supply.[2] Moreover, hydrogen is an important feedstock for the reduction of CO_2 to hydrocarbons as well as in the fixation of N_2 to NH_3.[3−5]

PEC water splitting has roots back in 1972 with the pioneering work of Fujishima and Honda that spawned the modern field of artificial photosynthesis.[6] Some more recent major breakthroughs highlighting the importance of PEC water splitting were demonstrated by Turner and Khaselev, Nocera et al., as well as van de Krol et al.[7−9] In these works, the integration of "buried" photovoltaic junctions can provide the needed photovoltage and overpotentials for bias-free water photoelectrolysis. Immense efforts have since then been devoted to the electrolysis and photoelectrolysis of water with the key challenges still found for the complex four-electron oxygen evolution reaction (OER) and the stability of the (photoelectro)catalysts.[10−12] Additionally, the scarcity of certain highly efficient catalyst elements, such as Ir and Ru, renders photoelectrolysis of water nonviable so far. The amounts of Ir and Ru that are needed to achieve 1 TW of hydrogen through the state-of-the-art polymer electrolyte membrane (PEM) electrolyzer represent 180 and 12 years of the current annual productions of Ir and Ru, respectively.[13] Therefore, the development of efficient and robust catalysts based on earth-abundant elements is extremely important in order to increase the share of water electrolysis in the global hydrogen production. To that direction, oxide perovskites (ABO_3) have shown high efficiency and stability for the OER in alkaline water electrolysis.[14−17] The increasing interest in oxide perovskites stems from their chemical stability, as well as their structural, compositional, and electronic versatility.[18−20]

In this work, we investigate a family of double perovskite cobaltites as catalysts for the OER in alkaline media at room temperature. This work is inspired by recent advances in proton ceramic fuel cells and electrolyzers (PCFC and PCEs) that

Received: January 28, 2021
Accepted: April 14, 2021
Published: April 27, 2021

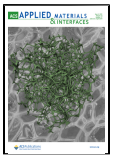

operate at elevated temperatures, i.e., 350−600 °C.[21] The double perovskite $Ba_{1-x}Gd_{1-y}La_{x+y}Co_2O_{6-\delta}$ (BGLC) has a p-type electronic conductivity, which is especially important for the OER, along with a minor partial proton conductivity. BGLC ($x = 0.5, y = 0.2$, BGLC587) demonstrated exceptional efficiency and chemical stability as the anode electrode in PCEs at high steam pressures.[21] Herein, we investigate the efficiency of BGLC587, BGLC82 ($x = 0$, $y = 0.2$) and BGLC37 ($x = 0$, $y = 0.7$) for the OER at room temperatures. Commercially available IrO_2 powder is used as a reference, and our results indicate that BGLCs exhibit high intrinsic catalytic activities approaching that of commercial IrO_2. In particular, BGLC587 shows exceptional operating stability, which is accompanied by surface amorphization. The reconstruction of the catalyst surface and formation of amorphous layers are attracting much attention as they are highly important to the overall performance of the material. It has been suggested that in the case of layered oxides and perovskites, vacant lattice oxygen sites at the surface are participating in the OER mechanism. Inequality in oxygen incorporation and evolution rates under current may be accompanied by uncoordinated cation sites, leading to cation loss and surface amorphization.[22−24] The participation of oxygen vacancies in the OER is commonly labeled the lattice oxygen oxidation mechanism (LOM). Although oxidation of lattice oxide ions is shown to lower the electrode overpotential with respect to the adsorbate evolution mechanism (AEM), the amorphization of the surface layers indicate that evolution of lattice oxygen is faster than incorporation. Hence, the LOM has a nonfaradaic component proportional to the oxygen loss in the amorphous layer. Enhancing oxygen conductivity in the electrode bulk is suggested as a mitigation for oxygen loss[24] but should theoretically only increase the nonfaradaic component and lead to further oxygen depletion from the electrode material. It may, however, appear as increased oxide ion conductivity is the *cause* of lowered overpotential. In reality, increasing oxygen vacancy concentration increases both oxide ion conductivity *and* OER by facilitating more surface reaction sites (vacancies). As surface amorphization is only initial and eventually comes to equilibrium with the crystalline bulk, exchange rates under current must be equal, AEM or equilibrated LOM is assumed to be dominant, and the current is all faradaic.

BGLC587 was integrated as the anode electrode in a photovoltaic (PV)-driven monolithic and "wireless" PEC cell of minimal engineering, crude handling, and minimal catalyst loadings. The PV−PEC cell based exclusively on earth abundant elements for both the OER and hydrogen evolution reaction (HER) delivered a 6.6% STH efficiency for 71 h under 1 sun simulated illumination. After the initial 71 h of laboratory operation, the PV−PEC was exposed to realistic, partially cloudy conditions with varying light intensities for 8 h. We demonstrated STH efficiencies ranging between 4.0% and 5.8% for light intensities between 0.2 and 1 sun in Oslo, Norway. Postoperation analyses highlighted the surface amorphization of BGC587 that was accompanied by Ba loss. Our work contributes to further understanding the perovskite-catalyzed OER, as well as to improving PEC water electrolysis cells for larger scale applications.

2. RESULTS

The phase composition and structure of BGLC587, BGLC82, and BGLC37 were examined by high resolution (HR) synchrotron radiation powder X-ray diffraction (SR-PXD) for the two former and laboratory PXD for the latter. On the basis of the sample phase analysis and Rietveld refinement results, it was found that BGLC587 contains multiple crystalline phases. The major Bragg peaks are consistent with rhombohedral $LaCoO_3$, a double perovskite phase, and an orthorhombic $Gd_{0.8}La_{0.2}CoO_3$. Additional minor peaks were assigned to $BaCO_3$ and Co_3O_4. Due to the substantial amount of $LaCoO_3$ in the sample, it was assumed that the double perovskite phase is La-poor, with a composition close to orthorhombic $BaGdCo_2O_{6-\delta}$ (space group (sg) *Pmmm*).[25] The refined phase fractions account for 50.2(4) wt % of rhombohedral $LaCoO_3$ (sg $R\bar{3}c$), 21.9(4) wt % of orthorhombic $BaGdCo_2O_{6-\delta}$ (sg *P4/mmm*), 21.3(3) wt % of orthorhombic $Gd_{0.8}La_{0.2}CoO_3$ perovskite (sg *Pnma*, $GdFeO_3$-type structure), 4.3(2) wt % of $BaCO_3$ (sg *Pmcn*), and 2.2(1) wt % of Co_3O_4 (sg $Fd\bar{3}m$) (Figure 1a). The refined unit cell volume of the double perovskite (229.3 Å^3) corresponds well with that reported for $BaGdCo_2O_{6-\delta}$ (228.6 Å^3), thus confirming the assumption of a La-poor double perovskite formation.

To further investigate the structural characteristics of the double perovskite, scanning transmission electron microscopy (STEM) was employed for a more detailed structural analysis on the nanoscale. Figure 1b and Figure 1c show the high-angle annular dark field (HAADF) STEM images of BGLC587 with increasing magnification, revealing the high crystallinity of the material. High resolution energy dispersive X-ray spectroscopy (HREDS) atomic mapping of the cations show a structure of alternating Ba and Co layers, with Co on the B-site and La weakly distributed over the A-site in both the Ba and Gd layers (Figure 1d, inset, and additional supplementary HREDS in Figure S1). These results confirmed the solubility of La in $BaGdCo_2O_{6-\delta}$. Such cation disorder may explain why the refined overall composition deviates somewhat from the material's nominal composition. Specifically, the refined composition is too rich in La and too poor in Gd and Ba. This may be due to substitution of La by Gd and Ba in some of the phases. The phase described as $Gd_{0.8}La_{0.2}CoO_3$ may for instance be more Gd-rich, with some Ba replacing La in $LaCoO_3$. However, due to the similar atomic numbers of these three elements, their X-ray (synchrotron radiation) scattering contrast is too weak to confirm such a substitution by the Rietveld refinements. BGLC82 contains the same phases as BGLC587, except for $Gd_{0.8}La_{0.2}CoO_3$, and has a higher content of the orthorhombic double perovskite phase, which accounts for 80.0(4) wt % of the sample. Its unit cell volume (229.4 Å^3) is similar to the one observed in BGL587. The remaining phases in the sample are rhombohedral $LaCoO_3$ (sg $R\bar{3}c$, 10.5(4) wt %), $BaCO_3$ (sg *Pmcn*, 7.5(2) wt %), and Co_3O_4 (sg $Fd\bar{3}m$, 2.0(2) wt %) (Figure S2). The overall refined composition is La-rich and Gd-poor compared to the nominal composition, which again may be due to substitution that is difficult to detect with synchrotron X-rays. The lab-PXD data of BGLC37 did not show any additional Bragg reflections and were fitted with a single phase (a tetragonal double perovskite unit cell, Figure S3).

All the major phases are related to the perovskite structure. $LaCoO_3$ and $Gd_{0.8}La_{0.2}CoO_3$ deviate from the ideal cubic perovskite symmetry due to tilting of the CoO_6 octahedra, which reduces the symmetries to rhombohedral and orthorhombic, respectively. The double perovskite phases have layered structures since the large size mismatch between the A-site cations induces ordering of Ba and Gd/La (see Figure 1e). The cation ordering doubles the *c*-axis, resulting in a tetragonal (*P4/mmm*) symmetry. This symmetry may be further lowered to orthorhombic (*Pmmm*) by oxygen vacancy ordering along the *b*-

https://doi.org/10.1021/acsami.1c01900
ACS Appl. Mater. Interfaces 2021, 13, 20313−20325

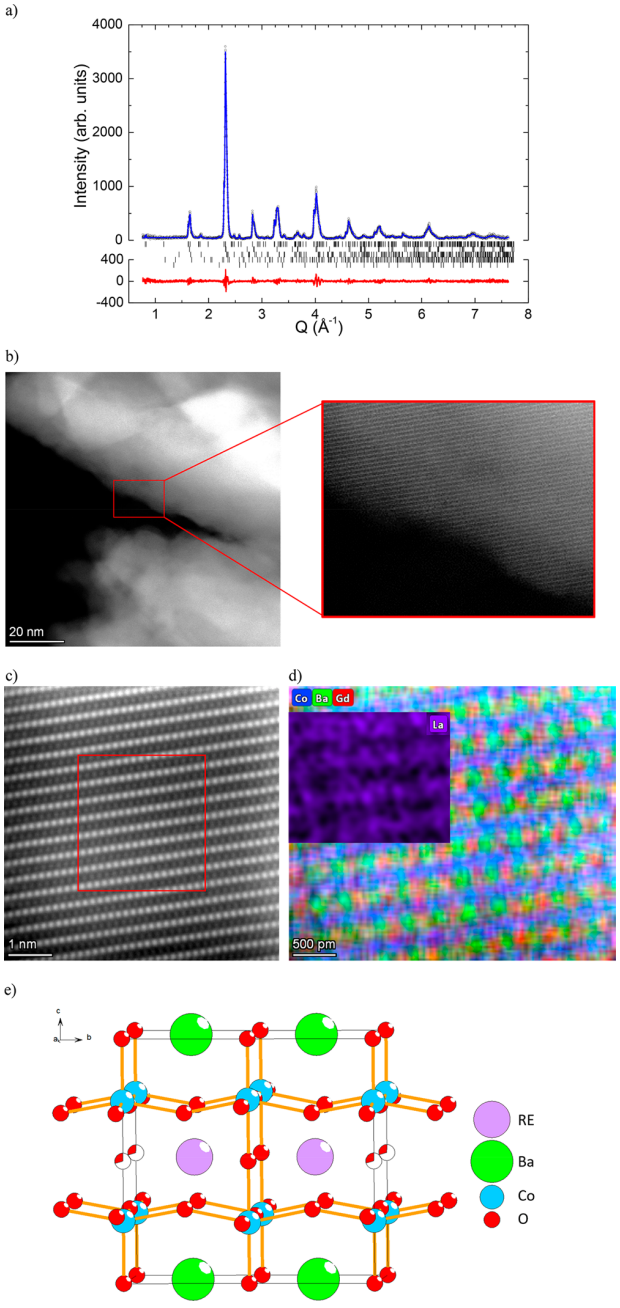

Figure 1. Structure and phase composition of BGLC587. (a) HR SR-PXD data with the Rietveld refinement results showing the rhombohedral $LaCoO_3$-related phase ($R\bar{3}c$, 50.2 wt %), orthorhombic double perovskite ($P4/mmm$, 21.9 wt %), $Gd_{0.8}La_{0.2}CoO_3$ ($Pnma$, 21.3 wt %), $BaCO_3$ ($Pmcn$, 4.3 wt %), and Co_2O_3 ($Fd\bar{3}m$, 2.2 wt %). (b) STEM HAADF image of the as-received double perovskite. (c) HRSTEM HAADF image of the as-received double perovskite and (d) HREDS atomic mapping of Ba, Gd, Co, and La (inset) for the selected area in the STEM image. (e) Crystal structure of orthorhombic double perovskite. Rare earth (RE): La and Gd. Additional STEM HAADF images and STEM nanobeam scanning diffraction data on the as prepared BGLC587 are given in Figures S5 and S6.

axis, resulting in an a2b2c double perovskite structure. This can be seen in the elemental mapping illustrated in Figure 1d and Figure S1 for BGLC587 and in Figure S2 for BGLC82. The larger La is more disordered between the two A-sites in the double perovskite structure. The overall morphology of the three BGLC powders and that of commercial IrO_2, used herein as reference OER catalyst, were observed by scanning electron microscopy (SEM). The double perovskites and commercial IrO_2 show crystal grain sizes ranging from a few hundreds of nanometers up to approximately 1 μm indicative of bulk materials (Figure S4). All powders appear with no distinct differences except that IrO_2 has a more conical rather than cubic appearance.

The composition of BGLC587 was further investigated by XPS. The XPS investigation did not show strong indications of more than one chemical state of La, Co, and Gd present in the BGLC587 sample (Figure S7). Unlike PXD, XPS is not very sensitive to variations in long-range periodicity, as long as the local chemical environment does not change substantially. Compared to the composition found by STEM elemental mapping (Table S1), XPS detects more La and less Co (Table S2). This may suggest an La-rich outermost surface, since the XPS technique only probes a few nm into the material. Interestingly, the relative composition of Ba and Co found by XPS is in excellent agreement with the STEM results (Table S3). In the Ba 4d spectrum (Figure S7), Ba is clearly seen to be present in two different chemical states, labeled I_{Ba} and II_{Ba}. The I_{Ba} component has been previously reported by Xu et al. for Ba being partially substituted by Pr in $Ba_{0.5}Sr_{0.5}Co_{0.8}Fe_{0.2}O_{3-\delta}$.[26] This suggests that the I_{Ba} component may be a result of the partial La substitution in $BaGdCo_2O_{6-\delta}$. Additional details can be found in Supplementary Note 1.

The OER behavior of the three BGLC compositions against commercially available IrO_2 in alkaline conditions is shown in the linear sweep voltammetry (LSV) of Figure 2a. The *iR* corrected curves are also given (Figure S8), but the electrolysis system is more accurately represented by the not-corrected ones.[27] All perovskite compositions seemingly outperform the commercial IrO_2 in both the onset overpotential (taken when $j \geq 0.3$ mA cm^{-2})[28] and the overpotential needed for 10 mA cm^{-2}. Table 1 summarizes the overpotentials, the interfacial kinetics of the OER, and the intrinsic catalytic activities of the electrocatalysts. The perovskites all show non-*iR*-corrected Tafel slopes (Figure 2b) of around 78 mV dec^{-1}, suggesting an OER mechanism with a two-electron transfer rate limiting step.[27,29] IrO_2 has a similar Tafel slope of 72 mV dec^{-1} in good accordance with slopes reported in the literature[30,31] but with significantly smaller exchange current density than the perovskites. We looked into the intrinsic catalytic activities (ICA) of the BGLCs at the operating overpotential for 10 mA cm^{-2} and revealed that they are indeed inferior but approaching that of IrO_2, especially BGLC587. The ICA of each catalyst was estimated by the $R_{ct}C_{dl}$ product, with units of Ω F that can be rearranged to (s) as the product reflects the time constant (t) of the studied reaction (see Table 1). We have already shown the validity of our approach,[14] which can be used complementarily with the traditionally estimated electrochemically active surface area (ECSA) that is extracted by the capacitance in a nonfaradaic region.[27,32] Electrochemical impedance spectroscopy (EIS) can separate capacitance and charge transfer resistance at any potential; therefore it can be applied in faradaic regions in contrast to the ECSA through cyclic voltammetry (CV). We have further validated our approach, which was applied in the nonfaradaic region, and the capacitances extracted by EIS are in good agreement with those from the ECSA (see Figures S9−S11, Tables S4−S7 and corresponding supplementary analysis). It is also noted that the capacitances get relatively lower when the

https://doi.org/10.1021/acsami.1c01900
ACS Appl. Mater. Interfaces 2021, 13, 20313−20325

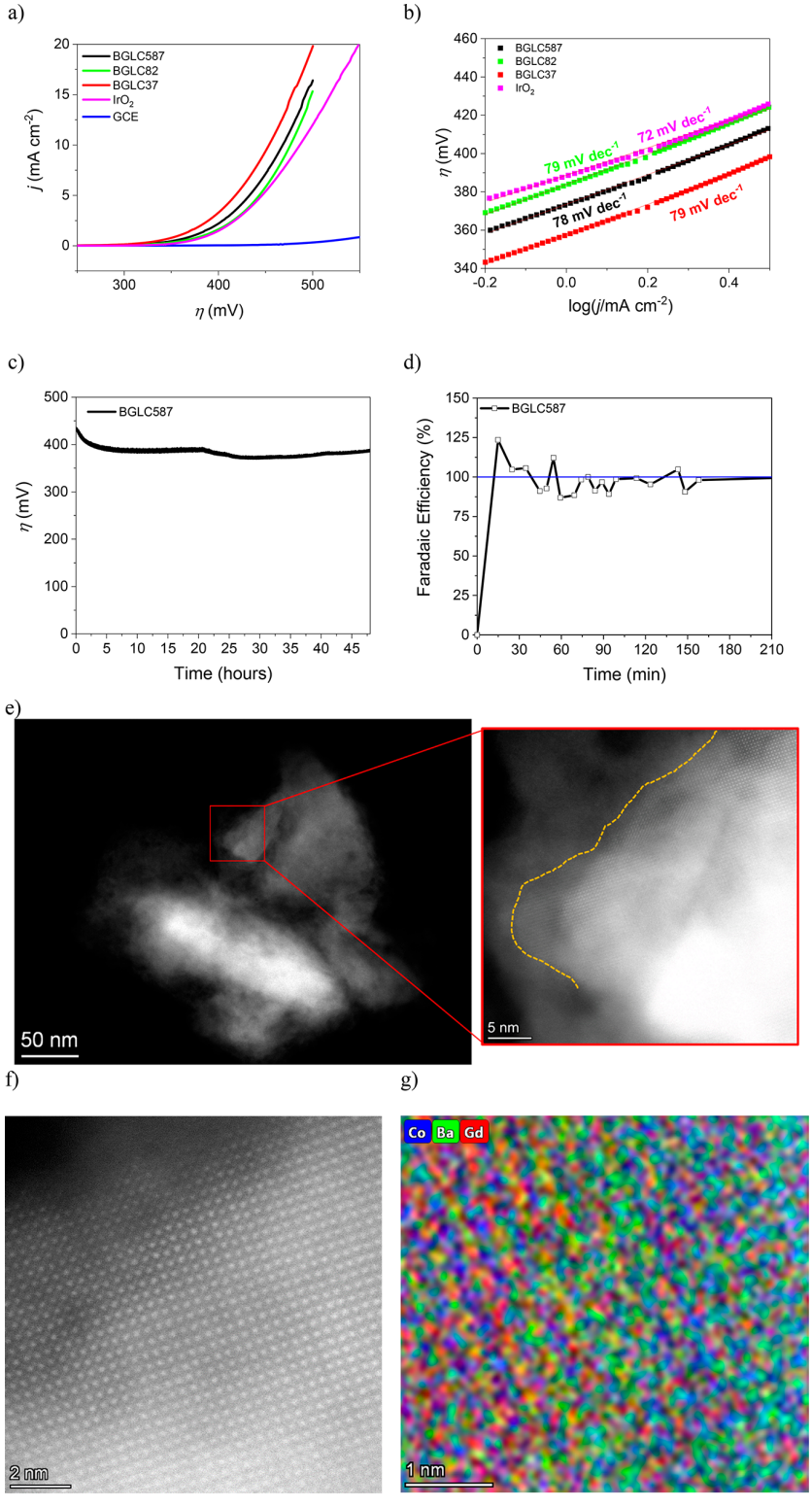

Figure 2. Electrochemical measurements of the double perovskite cobaltites and IrO_2 catalysts and stability performance of BGLC587. (a) LSV curves at a scanning rate of 10 mV s^{-1} in 1 M NaOH. (b) Tafel slopes. The non-*iR*-corrected curves were used. (c) Galvanostatic stability experiment at 10 mA cm^{-2} at 1000 rpm and 0.280 mg of catalyst. Hg/HgO (1 M NaOH) was used as the reference electrode. (d) Faradaic efficiency of the BGLC587 on carbon paper loaded with 2.1 mg cm^{-2}. (e) Postoperation STEM HAADF image of BGLC587. The yellow dashed line emphasizes the border of amorphous−crystalline layers. (f) HRSTEM image of the crystalline region and (g) HREDS mapping at a subsection of (f), showing postoperation A-site disorder between Gd and Ba.

https://doi.org/10.1021/acsami.1c01900
ACS Appl. Mater. Interfaces 2021, 13, 20313−20325

Table 1. Electrochemical Parameters As Estimated by the LSV and EIS Measurements of the Double Perovskites and IrO_2

catalyst	onset at 0.3 mA cm^{-2} (mV vs NHE)	η at 10 mA cm^{-2} (mV vs NHE)	Tafel slope (mV dec^{-1}), 1000 rpm	i_0 at $\eta = 0$ (mA cm^{-2})	$R_{ct}C_{dl} - \tau$ (s)
BGLC587	339	470	78	1.6×10^{-5}	5.5×10^{-4}
BGLC82	348	478	79	1.3×10^{-5}	7.0×10^{-4}
BGLC37	322	455	79	2.5×10^{-5}	11×10^{-4}
IrO_2	359	487	72	0.4×10^{-5}	5.1×10^{-4}

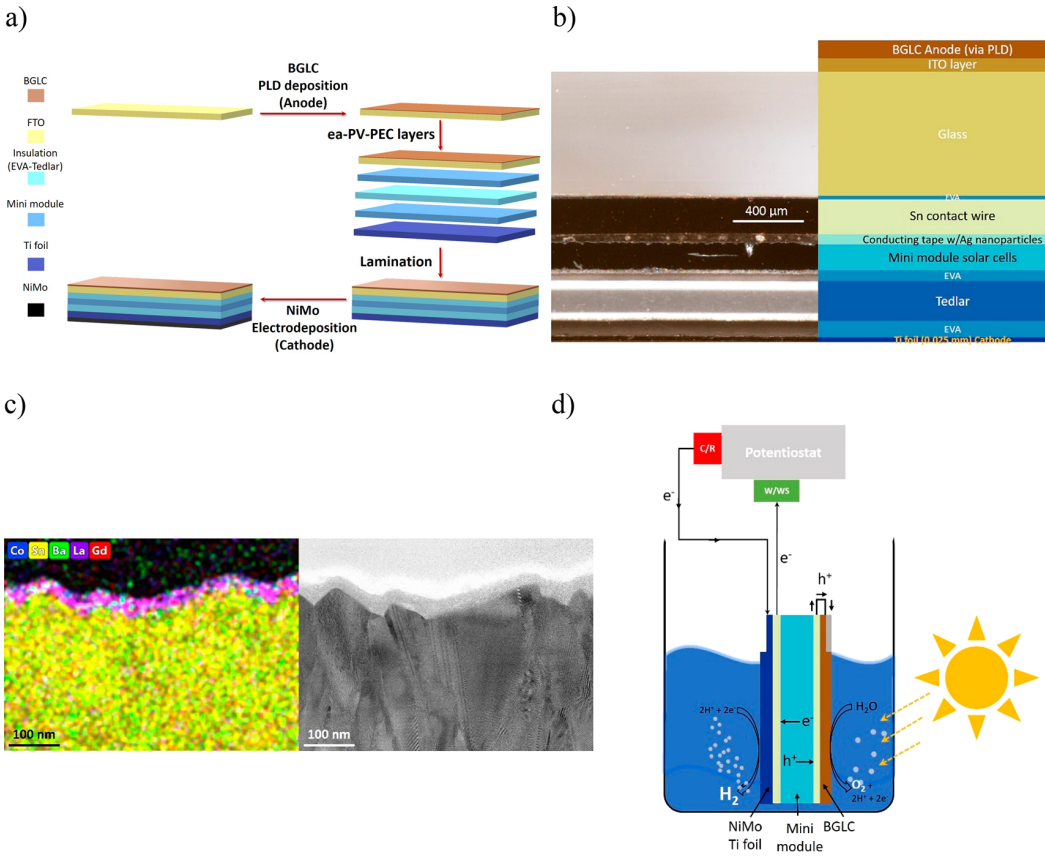

Figure 3. Assembly and visualization of the ea-PV−PEC device with BGLC587 as the OER catalyst and NiMo as the HER one. (a) Schematic presentation of the assembly of the ea-PV−PEC device. For simplicity, not all the layers are mentioned. The illuminated area matched the electrode area of 4 cm^2. (b) Tomography of the ea-PV−PEC device, where the different layers in the range of a few hundreds of micrometers can be seen. It is noted that the Tedlar layer comprises three layers that are primer (top white area)−PET (middle area)−Tedlar (bottom white area). (c) Cross section STEM image of the PLD-deposited BGLC layer on FTO-coated glass (right) and the corresponding EDS analysis (left). (d) ea-PV−PEC device configuration with in series connected potentiostat. The p-terminal of the minimodule is short-circuited by the Ag ink with the anode (BGLC on FTO) and isolated by epoxy (gray part on the BGLC layer). The n-terminal of the minimodule is connected with the working/working sense (W/WS) lead of the potentiostat, while the uncoated part of the Ti foil is connected to the counter/reference (C/R) lead of the potentiostat. The flow of the electrons and holes is also mentioned. In this way we avoided having the contacts in the electrolysis solution, but the evaporating electrolyte needed compensation. The rest of the monolithic device was isolated by EVA and Tedlar sheet, which are not shown for simplicity.

oxides are in the OER region of 10 mA cm^{-2}. This indicates that not all the surface area of the oxides is electrochemically active during the OER. From Table S7 it is also apparent that IrO_2 shows the highest relative decrease in ECSA. This finding correlates well with the higher ICA found for IrO_2 through the $R_{ct}C_{dl}$ product but also with the lowest exchange current density for the OER.

Stability measurements were conducted under galvanostatic conditions at 10 mA cm^{-2} with a rotating disk electrode (RDE) and with the same amount of powders of 0.28 mg cm^{-2} (Figure 2c). Except for BGLC587, the rest of the catalysts were detached from the surface of the glassy carbon (GC) tip after a few hours of operation. The experiments were conducted in triplicate, and representative curves for BGLC82, BGLC37, and IrO_2 are given in Figure S12. All overpotentials for galvanostatic operation at 10 mA cm^{-2} agree well with the ones expected by the LSV curves of Figure 2a. On the other hand, BGLC587 shows an exceptional operating stability over the course of the 48 h (Figure 2c), as well as after 300 cyclic voltammetry (CV) cycles, where 94% of the initial performance was maintained (Figure S13a). The performance of BGLC82 and BGLC37 was reduced by 24% and 17% after 300 CV cycles, respectively (Figure S13b,c). The faradaic efficiency (FE) of BGLC587 was measured under galvanostatic conditions at 10 mA cm^{-2}. Although fluctuations in the oxygen production are seen due to irregular bubble release and sampling from the headspace of the electrolysis cell, the FE remained around 100% (Figure 2d) in the studied 3 h window. Therefore, all of the current can be assigned to oxygen gas

https://doi.org/10.1021/acsami.1c01900
ACS Appl. Mater. Interfaces 2021, 13, 20313−20325

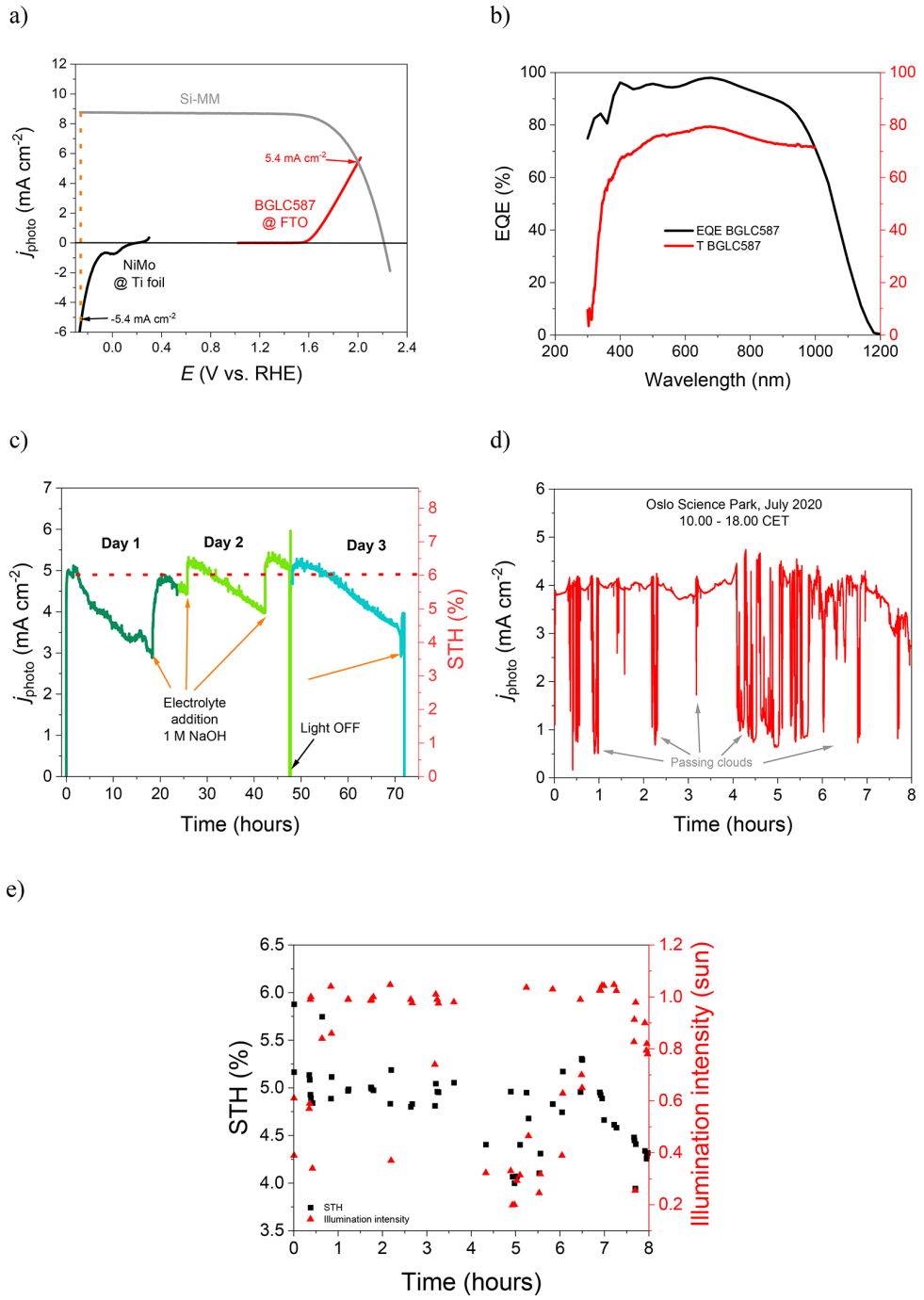

Figure 4. Indoor and outdoor performance of the all earth abundant PV−PEC device of 4 cm^2. (a) Current−voltage curve of the Si-MM and current−potential curves of the BGLC587 anode on FTO (0.023 mg cm^{-2}), NiMo cathode on Ti foil, and the expected photocurrent density of the ea-PV−PEC. (b) EQE and transmittance spectrum of the BGLC-coated FTO glass. (c) Indoor, bias free performance under 1 sun in 1 M NaOH. (d) Outdoor performance under varying light intensity conditions due to passing clouds. (e) Outdoor STH efficiency under varying light intensity conditions.

generation by BGLC587. Any eventual oxygen release from the initial amorphization of the BGLC surface layers is regarded as too small to have an impact on overall efficiency. The rest of the perovskites and IrO_2 showed a FE of around 100% for the studied 2 h window, as can be seen in Figure S12b.

After operation, BGLC587 loses the A-site ordering but maintains the crystalline perovskite structure, as can be seen in the HRSTEM image and HREDS elemental mapping for postoperation powder in Figure 2e−g. Postoperation analysis shows the expected formation of a thin (approximately 5−6 nm after 48 h of operation) amorphous layer (Figure 2e), which has been observed in several other perovskite materials operating in alkaline electrolytes.[16,33−38] The bulk of the BGLC587 grains is still crystalline, a fact that is supported by STEM images, atomic elemental mapping (Table S1), and the nanobeam diffraction line scan from the surface and toward the bulk of the grain

https://doi.org/10.1021/acsami.1c01900
ACS Appl. Mater. Interfaces 2021, 13, 20313−20325

(Figure S14). Quantification based on XPS measurements of BGLC587 pre- and postoperation also finds a decrease in Ba content postoperation (Table S3 and Supplementary Note 1), in excellent agreement with the STEM elemental mapping. The A-site order-to-disorder transition seen from pre- to postoperation (Figure 1d and Figure 2g), as well as Ba loss (Table S1), is not seen to affect the electrochemical performance. The amorphous surface layers may be beneficial for the catalytic activity toward the OER,[22,23,33,35,36] as before amorphization the BGLC surface is generally Co-depleted (in agreement with XPS data in Table S3) and deactivated by excess of Ba, La, and Gd. Moreover, Ba loss induces cation vacancies, to be charge-compensated by formation of oxygen vacancies or electron holes. It has previously been shown that the oxygen nonstoichiometry in BGLC587 varies little with pO_2 at lower temperatures, and it is therefore expected that Ba loss is compensated by formation of electron holes,[39] which further promote the OER. As mentioned previously, LOM is responsible for the surface restructuring of perovskite oxides employed as OER catalysts.[24] The faster rate of oxygen removal compared to oxygen vacancy refilling causes the formation of uncoordinated cation sites, leading to cation dissolution and surface amorphization.[24] Although we do not provide direct evidence, our findings corroborated well with the lattice oxygen oxidation mechanism and Ba loss, inducing electron holes, therefore facilitating the OER.

A collection of the state-of-the-art perovskites found in the literature are given in Table S8. It can be seen that BGLC587 shows high catalytic properties for the OER in alkaline media and shows promising kinetic properties (relatively low Tafel) and operating stability. Due to the higher La/Ba ratio in BGLC587 as compared to BGLC82 and BGLC37, the oxygen nonstoichiometry (and also lattice oxygen variation) is lower for the former. Still, the higher average A-site valence leaves the average Co valence lower for BGLC587 at room temperature. Co valence for BGLC587 and BGLC82 taken at 700 °C is 3.05 and 2.97, respectively,[39] calculated to be 3.14 and 3.37 at room temperature. These values are based on oxygen nonstoichiometry obtained by thermogravimetric analysis in dry air.[39] The inherent oxygen deficiency, mixed valence of Co, and good charge transfer characteristics between Co and oxygen supports the generally high electrocatalytic activity of BGLCs.

A PV−PEC device was constructed with BGLC587 deposited on F-doped SnO_2-coated glass (FTO) as the OER electrocatalyst, and a NiMo film deposited on Ti foil as the HER electrocatalyst. First, BGLC587 was deposited on the FTO by pulsed laser deposition (PLD). Then, a mini-PV module was prepared by four, series-connected solar cells (1×1.2 cm^2) cut from commercial p-type monocrystalline Si passivated emitter and rear cells (PERC) with conversion efficiency of 20.5% (see connection and cross section details in Figure S15). The mini-PV module was laminated with standard ethylene vinyl acetate (EVA) as the encapsulant, cathode substrate (Ti foil) at the backside, and the BGLC587-coated FTO as the front side. After lamination, the NiMo HER catalyst was electrodeposited on the Ti foil of the whole assembly (back side of the layered structure). The assembling procedure of the whole monolithic device is schematically given in Figure 3a. A more detailed description of the assembly of the earth abundant PV−PEC (ea-PV−PEC) can be found in the experimental part, but in Figure 3b we also present a cross section of a fully functional ea-PV−PEC, where all the different layers can be seen. A lower magnification cross section image taken by an optical microscope of the full assembly can be seen in Figure S16.

PLD is a deposition technique that achieves high stoichiometry between the target and the deposited material, leading to compact films of high quality.[40,41] Several PLD depositions under varying atmospheres were carried out in order to find the optimal conditions. The most promising results are presented in Figure S17, while deposition in O_2 rich atmosphere gave the best performing BGLC587 layer. This resulted in a 30 nm film of BGLC587 on the FTO as it can be seen by the cross-section TEM image of Figure 3c, where a cross-section cut is prepared by the focused ion beam (FIB) technique. On the basis of Rietveld refinement of the SR-PXD data and considering phase fractions as outlined in Suppporting Information, the theoretical density of BGLC587 is 7.33 g cm^{-3}, and a 30 nm layer equals to a mass of 0.023 mg cm^{-2}. A brief history of the cathode development in order to reach to the electrodeposited NiMo is discussed in the Supporting Information (see Figure S18, Figure S19, Table S9 and corresponding analysis).[42] The FE of NiMo on Ti foil was also 100% (Figure S20). In order to record the unassisted photocurrent density of the ea-PV−PEC, a potentiostat was connected in series, as described in Figure 3d. A fully standalone version can be constructed in the same way as the anode side by simply short circuiting the n-terminal with the cathode.

Before the bias-free, wireless photoelectrolysis of water, the j−V curves (the current−voltage notation of the solar cells is distinguished from the current−potential for the catalysts) of the mini-PV module (Si-MM), NiMo and BGLC587 are recorded and presented in Figure 4a. Since four crystalline Si solar cells are series connected, the V_{oc} of the Si-MM reaches approximately 2.3 V with a $j_{Si\text{-}MM}$ of 8.76 mA cm^{-2}. The expected photocurrent density is approximately 5.4 mA cm^{-2}; therefore an STH of approximately 6.6% is anticipated. Figure 4b shows the optical transmittance of the glass coated with the thin BGLC587 layer and the external quantum efficiency (EQE) of the Si-MM laminated with such a glass. The BGLC587-coated glass shows over 70% of the transmittance in the visible region, where the EQE has an excellent response.

The operation of the ea-PV−PEC device under solar simulated light for more than 70 h is shown in Figure 4c. The ea-PV−PEC device under bias-free, wireless operation exhibits photocurrent densities ranging from 5.0 to 5.4 mA cm^{-2} leading to a maximum STH of 6.6%, in agreement with the projected current densities of Figure 4a. Significant fluctuation is observed though, but it is purely related to electrolyte evaporation. The geometrical parameters of the ea-PV−PEC and the possibility to connect the potentiostat in series with the cell in order to record the photocurrent density had the disadvantage that the ea-PV−PEC is submerged just enough underneath the surface of the solution (Figure 3d). It is evident that when electrolyte is added after prolonged operation, all the active surface area of the ea-PV−PEC is then fully submerged again, and the photocurrent returns to its predicted value. Moreover, a constant evaporation rate is seen by the photocurrent slopes, while the fluctuations are due to irregular gas release from the anode and cathode surfaces (the device under operation can be seen in the supplementary video 1). An additional PV−PEC device was constructed showing great consistency and reproducibility to the above mention phenomena and STH efficiency (Figure S21). We also performed light on/off cycles in the beginning and at the end of the duplicate assembly to underline that the origin of the photocurrent is purely due to the incoming illumination. An actual activity loss can be seen a little after 71 h of operation, when the ea-PV−PEC does not retrieve the photocurrent

https://doi.org/10.1021/acsami.1c01900
ACS Appl. Mater. Interfaces 2021, 13, 20313−20325

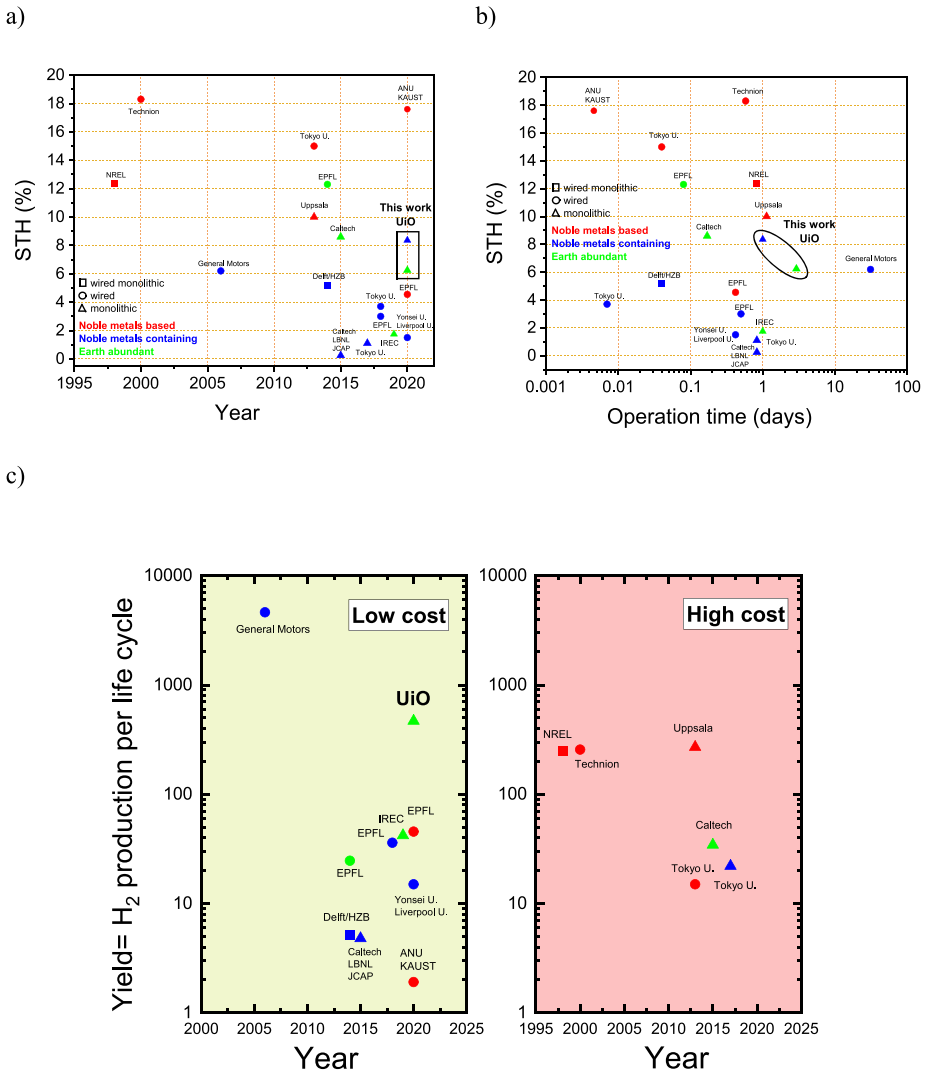

Figure 5. STH efficiency and stability benchmarks for a wide range of bias-free photoelectrolysers. (a) Some of the most important works since the pioneering work of Khaselev and Turner's. (b) Their operating durations. All works are summarized in Table S10. "Wired monolithic" refers to photoelectrolyzers where at least one electrode contains a "buried" PV junction and it is wired to the other electrode. "Wired" refers to purely PEC-based devices that are not assisted by "buried" PV junctions and PV-assisted electrolyzers. Finally, "monolithic" refers to purely tandem designs with no external wires. The majority of the devices used, either for the anode or cathode or for both electrodes, noble metal-based catalysts. The all-earth-abundant devices are denoted by green triangles. (c) Apparent H_2 production per life cycle of each solar water splitting system taking into account that in the reported operating times the systems did not degrade. The low-cost category includes systems that use Si-based solar cells, perovskites (although their market price is currently unknown, we regarded them as low-cost photoabsorbers), and photoelectrodes based on common semiconductors ($BiVO_4$, Cu_2O, etc.). The high-cost category includes III−V- and CIGS-based solar cells.

density of 5.4 mA cm^{-2} but reaches only 3.9 mA cm^{-2} after electrolyte addition (see detail in Figure S22). At this point, the whole setup was transferred outside for realistic operating conditions, and the results are given in Figure 4d and Figure 4e. First, under 1 sun intensity the STH is approximately 5%, as expected after the indoor performance loss at 71 h (Figure S22). Second, the photocurrent density fluctuates significantly due to the passing of clouds but the STH efficiency is kept constantly between 4% and 5%. This underlines the robustness of our bias-free, wireless, monolithic device under intense light/shade periods, which can be perceived as on/off cycles. The expected STH efficiencies according to the initial performance of the BGLC587 and NiMo catalysts are in a good agreement with the outdoor performance of the partially degraded ea-PV−PEC device (Figure S23). A video from the outdoor performance at 17.00 can be found in Supporting Information video 2.

The amorphization of the BGLC surface during operation in alkaline conditions is not seen to degrade the performance over time. This indicates that the surface reaction is well catalyzed by the AEM even when Co oxide is suspended in an amorphous matrix of Ba, Gd, and La oxides or hydroxides. But due to high partial oxide ion conductivity and since the total BGLC layer is only 30 nm thick, the complete amorphization after 71 h (Figure S24) leads to an irreversible performance degradation, emphasizing the significance of crystalline BGLC on cell performance. SEM observation of the NiMo film also indicates degradation of the HER catalyst. The EDS analysis shows an increase in the Ni:Mo ratio from 8.5 to 10.6, as well as an increase in the detection of the Ti substrate, indicating a partial

https://doi.org/10.1021/acsami.1c01900
ACS Appl. Mater. Interfaces 2021, 13, 20313−20325

loss of the NiMo film during the operation of the cell (Figure S19 and Table S9). The Si-MM was intact and the $j-V$ characteristics were not affected (data not shown).

3. DISCUSSION

Figure 5a and Figure 5b highlight the most important works in the field of unassisted water electrolysis in terms of both STH and stability of the presented devices since the ground-breaking work of Khaselev and Turner in 1998.[7] Our monolithic, wireless water splitting device has the second highest STH efficiency reported so far after the device by Verlage and co-workers in 2015.[43] They achieved an STH of 8.6% with a monolithic, "wireless" water splitting device of 1 cm^2. The device was based on earth-abundant elements exclusively, but it had limited stability reporting a 10% degradation after 4 h of laboratory conditions. Our STH of 6.6% is lower by 23%, but it showed no degradation in electrochemical performance for 71 h operation in laboratory conditions. Although our device needs 4 times more area to reach this high STH efficiency compared to Verlage et al., the cost of our Si solar cell used is negligible compared to a GaAs-based device (retail price of a triple-junction GaAs solar cell is ~$60 for 1 cm^2, while a piece of 6 in. Si based high efficiency solar cell (243 cm^2) costs less than $1). The advantages of series-connected solar cells in terms of complexity when compared with tandem solar cells are also highlighted by Jacobsson et al.[44] A chemical degradation could however be seen, as the amorphous surface layer gradually propagated throughout the thickness of the 30 nm electrode film. The loss of the crystalline backbone of the perovskite leads to additional charge transfer losses, a fact that poses important scientific challenges. Operando investigations of such degradation phenomena could also provide important insights on the role of each phase. Such in-depth studies should be further pursued.

Additionally, we have constructed a bias-free, wireless monolithic device with highly active IrO_2 nanoparticles electrodeposited as the anode electrode[45] instead of BGLC587. The electrodeposition of IrO_2 was carried out after the lamination of the 4 cell connected Si-MM and the electrodeposition of NiMo in the cathode. The device reached an STH of 8.4% that is almost as high as the monolithic device by Verlage et al., but the performance was reduced by 11% in the course of 24 h. The performance loss was attributed to the IrO_2 dissolution, as it could be re-electrodeposited and the performance be retrieved (Supplementary Note 2).

The high performance of our ea-PV−PEC is also underlined by the apparent H_2 yield given in Figure 5c. The yield of each system was calculated by multiplying the reported STH with the operating time in hours. The units could be regarded as yield of hydrogen in hours of operation showcasing the accumulation of fuel over the course of a stable cycle of each device. The two categories are roughly defined by the cost of the photoabsorbers only, not taking into account the cost of noble metals used as catalysts. Although the system developed by General Motors back in 2006 is the only one exceeding our ea-PV−PEC device,[46] it was partially based on noble metals and was not a monolithic one.

4. CONCLUSIONS

We have demonstrated a state-of-the-art monolithic solar water splitting device with minimum engineering and low loadings of novel and earth abundant catalysts. The anode of our ea-PV−PEC device was based on a new class of double perovskite cobaltites for the OER of the general formula $Ba_{1-x}Gd_{1-y}La_{x+y}Co_2O_{6-\delta}$ (BGLC) and showed high catalytic activity, reporting a 6.6% STH under 71 h of continuous illumination. HRSTEM HAADF imaging of BGLC587, which was the best performing among the presented double perovskites, revealed an A-site order-to-disorder transition from pre- to postoperation that did not affect the catalytic activity for the OER. On the contrary, the surface amorphization assisted in exposing the Co species, thus activating the AEM on BGLC, although a crystalline bulk backbone is necessary in retaining charge transfer (i.e., electron holes). The loss of Ba is predicted to lead to further Co oxidation by formation of electron holes to charge-compensate the cation vacancies. A partial amorphization of BGLC587 is most probably related to lower incorporation than evolution rates in the lattice oxygen oxidation mechanism under current. Due to fast oxygen transport in BGLC587, oxygen vacancies at the crystalline surface can be refilled and the LOM may dominate over AEM until a critical thickness of the amorphous layer is reached. Given the thin electrode layer of the ea-PV−PEC, full amorphization of the 30 nm thick BGLC film led to irreversible activity loss after 71 h of operation. On the other hand, the structure rearrangement and surface amorphization of OER catalysts are an open topic and a current knowledge gap that will assist in the development of catalyst materials of immense activity.[23]

Further improvements in lowering the overpotentials for the OER and HER will lead to even higher STH efficiencies and prolonged operating times by using commercially available and affordable Si-based solar cells. It is highlighted that the currently used lamination process shows potential for long-term operation of such PV−PEC devices in strongly alkaline media. The integration of high voltage, high current solar cells (e.g., affordable III−V semiconductors) can also be facile and can further boost the performance and also reduce land usage and costs. Our results are based on simple, scalable processes as well as on readily available materials that widen up research possibilities, bridging the gap toward commercially viable solar water electrolysis.

5. EXPERIMENTAL SECTION

5.1. BGLC Anode Electrode Preparation. BGLC powders (BGLC587, BGLC37, and BGLC82) were purchased from Marion Technologies (F) and were used as received. The synthesis can be performed by the sol−gel citrate method as described in Supplementary Note 3. BGLC587 was deposited on FTO coated glass by pulsed laser deposition (PLD, Surface-Tec system, laser Coherent COMPexPro 205F, KrF, wavelength of 248 nm). The films were deposited at 100 °C in an oxygen-rich environment (0.01 mbar) with 4.5 J cm^{-2}. The repetition rate was 5 Hz, and the distance between target and substrate was 9 cm.

5.2. NiMo Cathode Preparation. NiMo was electrodeposited on Ti foil (thickness 0.025 mm, Goodfellow, ≥99.6+%) in a two-electrode cell according to the procedure described by Fan et al.[47] with certain modifications. The molarities of $NiSO_4 \cdot 6H_2O$ (Sigma-Aldrich), $Na_2MoO_4 \cdot 2H_2O$ (Sigma-Aldrich), and $Na_3C_6H_5O_7 \cdot 2H_2O$ (Sigma-Aldrich) were kept the same, but the electrodeposition was carried out stepwise under potentiostatic control at 2.85 V. The Ti foil substrate served as the cathode electrode, and a Ni foam was used as sacrificial anode with the nominal area for both electrodes being 4 cm^2. Four electrodeposition steps are discerned with the main difference that in the two first steps the solution was not stirred, while in the following two steps the solution was stirred. Each step was applied successively and lasted for 60 s, and the current ranged between 33 and 40 mA cm^{-2}. This procedure gave visually the most homogeneous coatings, as well as optimized performance of the NiMo cathodes.

https://doi.org/10.1021/acsami.1c01900
ACS Appl. Mater. Interfaces 2021, 13, 20313−20325

5.3. IrO_2 on FTO Anode Preparation. Highly active IrO_2 on FTO glass (either stand alone or on the assembled mini-PV module) was deposited by electrodeposition adapted to the procedures described by Zhao et al.[45] The electrodeposition was carried out in a three-electrode configuration with the FTO glass, standard calomel electrode (SCE), and a Pt mesh as the working, reference, and counter electrodes, respectively. After a brief optimization of the deposition time (see Figure S17) it was found that 3.5 h at +1.45 V vs SCE produced the best performing IrO_2 film, which did not compromise the transparency of the FTO glass (see EQE and transmittance spectrum in Figure S29).

5.4. Materials Characterization. HR SR-PXD data for BGCL587 and BGLC82 were collected at BM31 of Swiss-Norwegian Beamlines, at ESRF in Grenoble (France). Powders were sealed in a boron glass capillary with an internal diameter d = 0.3 mm and measured over an angular range of 1−35° 2θ with a step size of 0.006° 2θ with 6 scintillation detectors, each fitted with a Si analyzer crystal in front. The wavelength (λ = 0.502 18 Å) was calibrated using Si as a standard material. Laboratory PXD data for BGLC37 were collected in a Bragg−Brentano geometry with a Bruker-AXS D8 Discovery diffractometer, equipped with a LynxEye 1D detector, and CuKα_1 radiation was selected by a Ge (111) monochromator. The angular range used was 10−90° 2θ, with the step size of 0.02° 2θ. Phase identifications from (SR-)PXD data were performed by search−match with the PDF4-2020 database embedded in the Bruker EVA software. Structure refinements and quantitative phase analysis were performed by the Rietveld method in the TOPAS Academic version 5.[48] The Bragg peak profiles were described by Thompson-Cox-Hastings pseudo-Voigt functions,[48] and the backgrounds were fitted with Chebychev polynomials.

STEM work was performed with a Titan G2 60-300 instrument, operated at 300 kV with 80 pA beam current and 0.08 nm of nominal spatial resolution. The samples were investigated using data collected by annular bright-field (ABF), low-angle annular dark-field (ADF), and high-angle annular dark-field (HAADF) detectors. Chemical information was obtained by X-ray energy dispersive spectroscopy (EDS) with a Bruker SuperX EDS system, comprising four silicon drift detectors. Convergence angle was set to 21 mrad for EDS and high-resolution and to 1.75 mrad for nanobeam scanning diffraction. STEM sample preparation was performed by focused ion beam (FIB) with Ga+ ions accelerated at 30 kV using a Thermofisher Helios multibeam system.

XPS was performed on a Kratos Axis Ultra DLD spectroscope with monochromated Al Kα X-rays ($h\nu$ = 1486.6 eV). Survey spectra were obtained using pass energy (PE) of 160 eV and step size of 1 eV, while PE of 20 eV and step size of 0.1 eV were used for high resolution spectra.

The SEM images were obtained with a Hitachi SU8200 ultrahigh resolution cold-field emission scanning electron microscope equipped with a secondary electron (SE) detector under an acceleration voltage of 2.0 kV.

An operating PV−PEC device was embedded in epoxy, and the cross section was observed by an optical microscope after standard metallographic preparation.

5.5. Rotating Disk Electrode Electrochemical Measurements. The electrochemical experiments were performed in 1 M NaOH solution in a three-electrode setup provided by Gamry. An RDE with a GC tip (RDE710 rotating electrode, Gamry Instruments) was used as the working electrode, and SCE was used as the reference and a graphite rod as the counter electrodes, respectively. The standard potential of the SCE was measured and calibrated against a reference SCE, as well as a reference Ag/AgCl (3 M KOH) after each experiment. The RDE tip was coated by the perovskite and IrO_2 (Sigma-Aldrich, CAS 12030-49-8) powders according to the procedure suggested by Zhu et al.[34] The catalyst ink was prepared by adding 10 mg of powder in 1 mL of ethanol and 100 μL of Nafion 5 wt % solution. The powder inks were sonicated for a few hours until a homogeneous suspension was obtained. The inks were drop-casted on the GC tip (0.196 cm^2) by applying 6 μL of ink and allowed to dry in air. This procedure resulted in a loading of approximately 0.280 mg cm^{-2} of the electrocatalyst. For long-term stability experiments, the same amount of powder was loaded by drop-casting on the RDE. In this case, Hg/HgO (1 M NaOH) was used as the reference electrode as SCE is not appropriate. The standard potential of the Hg/HgO (1 M NaOH) reference electrode was found according to our reference SCE. All the electrochemical measurements, such as cyclic voltammetry (CV), linear sweep voltammetry (LSV), electrochemical impedance spectroscopy (EIS), chronoamperometry (CA), and open circuit potential (OCP), were performed with a Gamry Reference 3000 potentiostat/galvanostat/ZRA. All overpotentials are given against the normal hydrogen electrode (NHE) taking into account that water electrolysis takes place thermodynamically at 1.23 V vs NHE. Potentials were corrected vs NHE according to the Nernst equation:

$$E_{NHE} = E_{meas} + 0.059\ pH + 0.242V_{SCE}$$

and

$$E_{NHE} = E_{meas} + 0.059\ pH + 0.123V_{Hg/HgO}$$

5.6. PV−PEC Device Assembling and Performance Testing Indoor and Outdoor. The mini-PV module contains four pieces of monocrystalline Si solar cells (1 × 1.2 cm^2 each) with shingled interconnection. The interconnection was realized by Ag nanoparticles containing double-sided conductive tape (3M, 220-9928). The interconnection overlap between the solar cells is 2 mm, resulting in an illumination area of 4 cm^2 indeed. The solar ribbon was attached to p- and n-terminal of the minimodule with the Ag-containing double-sided tape. The layered structure with the BGLC587-coated FTO, EVA, interconnected solar cells, EVA, Tedlar sheet, EVA, and Ti foil (0.025 mm) was laminated at 150 °C with standard lamination process. According to the manufacturer, the Tedlar DyMat CTE white sheet comprises a top primer layer, which is adhered to a PET (hydrolysis resistant, electrical grade) midlayer that is adhered to the Tedlar bottom layer.

After the lamination of the mini-PV module, the deposition of the HER catalyst took place. The electrodeposition of NiMo was performed on the Ti-foil as described previously and directly on the assembled layered structure. After the deposition of the cathode catalyst on the monolithic device, the ribbon from the n-terminal of the mini-PV module was connected to the cathode electrode, while the ribbon from the p-terminal was connected to the anode with Ag ink (Loctite). The ink was applied with brush, and it was cured in air after 2 h. Two layers of the Ag ink were necessary such that they were finally isolated by epoxy resin (Huntsman Araldite 2000). In the end, the circumference of the device was covered by epoxy in order to further protect the potential shunting due to the liquid.

The STH and PEC performance of the monolithic, wireless PV−PEC device was measured in 1 M NaOH under illumination of an AM 1.5G solar simulator (Newport Oriel LCS-100). The light intensity was regularly calibrated by a reference solar cell (Newport 91150V-KG5). The photocurrent density was recorded by a Gamry Reference 3000 potentiostat, which was connected in series with the monolithic device. For this purpose, an alternative connection was used in which the cathode of the monolithic device was connected to the reference/counter leads of the potentiostat, while the n-terminal was connected to the working/sense leads. The potentiostat was set to 0 V vs E_{ref}, and the connections are schematically given in Figure 3d. This series resistance was not compensated in our results.

For the indoor laboratory experiments, the monolithic, "wireless" device was inserted without any further modification in an approximately 300 mL solution of 1 M NaOH in a glass reactor of approximately 1 L that was equipped with a 5 cm × 5 cm flat quartz window. For the outdoor experiments under realistic conditions, the whole setup, including the monocrystalline Si PV reference cell, was placed side by side on a portable table and taken to the terrace on the fifth floor of the Oslo Science Park. The proper angle of approximately 45° was adjusted by measuring the light intensity inside the cell, in front of the quartz window before the experiment was initiated. The angle was kept constant throughout the experiment, and the sun was tracked manually. An 8 h long experiment from 10.00 to 18.00 CET was performed in July 2020 at the location WPR8+RG Oslo. The sunlight intensity and temperature of the monocrystalline Si PV reference cell were regularly recorded, while the photocurrent density was recorded by the Gamry potentiostat as in the indoor experiments.

https://doi.org/10.1021/acsami.1c01900
ACS Appl. Mater. Interfaces 2021, 13, 20313−20325

5.7. Gas Quantification. The O_2 and H_2 gases were measured with an Agilent 3000A Micro GC, and the gas samples were collected automatically every 5 min from an 80 mL headspace. N_2 gas was used to remove the dissolved O_2 gas from the solution, as well as the air in the headspace. The removal of O_2 from the electrolysis cell (total volume of 160 mL) was also monitored before the initiation of the faradaic efficiency (FE) experiments. The working electrodes for the FE measurements were carbon paper loaded with around 5 mg of each catalyst powder, while a Pt mesh was used as the counter electrode. The inks consisted of 160 mg of catalyst powder, 3.4 mL of water, 1 mL of isopropanol, and 40 μL of Nafion, 5 wt %.[49]

■ ASSOCIATED CONTENT

Supporting Information

The Supporting Information is available free of charge at https://pubs.acs.org/doi/10.1021/acsami.1c01900.

Additional figures and tables of results and Supplementary Notes 1−3 on XPS analysis, performance characteristics, and synthesis information (PDF)

Video 1 showing operation of the ea-PV-PEC device (MP4)

Video 2 showing outdoor performance of the ea-PV-PEC device (MP4)

■ AUTHOR INFORMATION

Corresponding Author

Athanasios Chatzitakis − *Centre for Materials Science and Nanotechnology, Department of Chemistry, University of Oslo, FERMiO, NO-0349 Oslo, Norway;* orcid.org/0000-0001-7193-3236; Email: a.e.chatzitakis@smn.uio.no

Authors

Junjie Zhu − *Institute for Energy Technology (IFE), NO-2007 Kjeller, Norway*

Jónína B. Guðmundsdóttir − *Centre for Materials Science and Nanotechnology, Department of Chemistry, University of Oslo, FERMiO, NO-0349 Oslo, Norway*

Ragnar Strandbakke − *Centre for Materials Science and Nanotechnology, Department of Chemistry, University of Oslo, FERMiO, NO-0349 Oslo, Norway*

Kevin G. Both − *Centre for Materials Science and Nanotechnology, Department of Chemistry, University of Oslo, FERMiO, NO-0349 Oslo, Norway*

Thomas Aarholt − *Department of Physics, University of Oslo, NO-0316 Oslo, Norway*

Patricia A. Carvalho − *SINTEF Materials Physics, NO-0373 Oslo, Norway*

Magnus H. Sørby − *Department for Neutron Materials Characterization, Institutt for Energiteknikk (IFE), NO-2027 Kjeller, Norway*

Ingvild J. T. Jensen − *SINTEF Materials Physics, NO-0373 Oslo, Norway;* orcid.org/0000-0002-8575-0171

Matylda N. Guzik − *Department of Technology Systems, University of Oslo, NO-2027 Kjeller, Norway;* orcid.org/0000-0001-6349-4659

Truls Norby − *Centre for Materials Science and Nanotechnology, Department of Chemistry, University of Oslo, FERMiO, NO-0349 Oslo, Norway*

Halvard Haug − *Institute for Energy Technology (IFE), NO-2007 Kjeller, Norway*

Complete contact information is available at: https://pubs.acs.org/10.1021/acsami.1c01900

Author Contributions

J.Z. performed work related to the PV and conceptualized the device design. J.B.G. performed the RDE experiments and SEM characterization. R.S. investigated originally all BGLCs and treated the structural and electrochemical analysis (FunKey Cat funding acquisition). K.G.B. performed the PLD work. T.A. and P.A.C. performed the TEM, additional SEM, and optical microscopy work. M.H.S. treated all the XRD refinements and provided the structural analysis. I.J.T.J. obtained the XPS data and performed the XPS data interpretation. M.N.G. obtained the HR SR-PXD data (beamline funding acquisition). T.N. did the supervision, provided facilities, and contributed scientific insights. H.H. contributed to the funding acquisition (PH2ON) and development of the ea-PV-PEC, and A.C. conceptualized, supervized, and obtained the main funding for the work (PH2ON), performed the full cell water splitting measurements, and wrote the original draft. All authors contributed to the preparation of the manuscript.

Notes

The authors declare no competing financial interest.

■ ACKNOWLEDGMENTS

The authors collectively acknowledge support from the Research Council of Norway for the following projects: PH2ON, Grant 288320; FunKey Cat, Grant 299736; Norwegian Center for Transmission Electron Microscopy, NORTEM, Grant 197405/F50. The assistance of the staff at Swiss-Norwegian Beamlines (SNBL, BM31; ESRF, Grenoble, France) is also acknowledged.

■ REFERENCES

(1) Albrecht, U.; Altmann, M.; Barth, F.; Bünger, U.; Fraile, D.; Lanoix, J.-C.; Schoberer, E. P.; Vanhoudt, W.; Weindorf, W.; Zerta, M.; Zittel, W. *Study on Hydrogen from Renewable Resources in the EU. Final Report*; European Union, 2015; p 17.

(2) Lewis, N. S. Developing a scalable artificial photosynthesis technology through nanomaterials by design. *Nat. Nanotechnol.* **2016**, *11* (12), 1010−1019.

(3) Graves, C.; Ebbesen, S. D.; Mogensen, M.; Lackner, K. S. Sustainable hydrocarbon fuels by recycling CO2 and H2O with renewable or nuclear energy. *Renewable Sustainable Energy Rev.* **2011**, *15* (1), 1−23.

(4) Xue, X.; Chen, R.; Yan, C.; Zhao, P.; Hu, Y.; Zhang, W.; Yang, S.; Jin, Z. Review on photocatalytic and electrocatalytic artificial nitrogen fixation for ammonia synthesis at mild conditions: Advances, challenges and perspectives. *Nano Res.* **2019**, *12* (6), 1229−1249.

(5) Medford, A. J.; Hatzell, M. C. Photon-Driven Nitrogen Fixation: Current Progress, Thermodynamic Considerations, and Future Outlook. *ACS Catal.* **2017**, *7* (4), 2624−2643.

(6) Fujishima, A.; Honda, K. Electrochemical Photolysis of Water at a Semiconductor Electrode. *Nature* **1972**, *238* (5358), 37−38.

(7) Khaselev, O.; Turner, J. A. A Monolithic Photovoltaic-Photoelectrochemical Device for Hydrogen Production via Water Splitting. *Science* **1998**, *280* (5362), 425−427.

(8) Reece, S. Y.; Hamel, J. A.; Sung, K.; Jarvi, T. D.; Esswein, A. J.; Pijpers, J. J. H.; Nocera, D. G. Wireless Solar Water Splitting Using Silicon-Based Semiconductors and Earth-Abundant Catalysts. *Science* **2011**, *334* (6056), 645−648.

(9) Abdi, F. F.; Han, L.; Smets, A. H. M.; Zeman, M.; Dam, B.; van de Krol, R. Efficient solar water splitting by enhanced charge separation in a bismuth vanadate-silicon tandem photoelectrode. *Nat. Commun.* **2013**, *4* (1), 2195.

(10) Kanan, M. W.; Nocera, D. G. In Situ Formation of an Oxygen-Evolving Catalyst in Neutral Water Containing Phosphate and Co^{2+}. *Science* **2008**, *321* (5892), 1072−1075.

(11) Koper, M. T. M. Thermodynamic theory of multi-electron transfer reactions: Implications for electrocatalysis. *J. Electroanal. Chem.* **2011**, *660* (2), 254−260.
(12) Rossmeisl, J.; Qu, Z. W.; Zhu, H.; Kroes, G. J.; Nørskov, J. K. Electrolysis of water on oxide surfaces. *J. Electroanal. Chem.* **2007**, *607* (1), 83−89.
(13) Sun, X.; Xu, K.; Fleischer, C.; Liu, X.; Grandcolas, M.; Strandbakke, R.; Bjørheim, T. S.; Norby, T.; Chatzitakis, A. Earth-Abundant Electrocatalysts in Proton Exchange Membrane Electrolyzers. *Catalysts* **2018**, *8* (12), 657.
(14) Andersen, H.; Xu, K.; Malyshkin, D.; Strandbakke, R.; Chatzitakis, A. A highly efficient electrocatalyst based on double perovskite cobaltites with immense intrinsic catalytic activity for water oxidation. *Chem. Commun.* **2020**, *56* (7), 1030−1033.
(15) Suntivich, J.; May, K. J.; Gasteiger, H. A.; Goodenough, J. B.; Shao-Horn, Y. A Perovskite Oxide Optimized for Oxygen Evolution Catalysis from Molecular Orbital Principles. *Science* **2011**, *334* (6061), 1383−1385.
(16) Grimaud, A.; May, K. J.; Carlton, C. E.; Lee, Y.-L.; Risch, M.; Hong, W. T.; Zhou, J.; Shao-Horn, Y. Double perovskites as a family of highly active catalysts for oxygen evolution in alkaline solution. *Nat. Commun.* **2013**, *4* (1), 2439.
(17) Li, X.; Zhao, H.; Liang, J.; Luo, Y.; Chen, G.; Shi, X.; Lu, S.; Gao, S.; Hu, J.; Liu, Q.; Sun, X. A-site perovskite oxides: an emerging functional material for electrocatalysis and photocatalysis. *J. Mater. Chem. A* **2021**, *9*, 6650−6670.
(18) Yin, W.-J.; Weng, B.; Ge, J.; Sun, Q.; Li, Z.; Yan, Y. Oxide perovskites, double perovskites and derivatives for electrocatalysis, photocatalysis, and photovoltaics. *Energy Environ. Sci.* **2019**, *12* (2), 442−462.
(19) Sun, H.; Hu, Z.; Xu, X.; He, J.; Dai, J.; Lin, H.-J.; Chan, T.-S.; Chen, C.-T.; Tjeng, L. H.; Zhou, W.; Shao, Z. Ternary Phase Diagram-Facilitated Rapid Screening of Double Perovskites As Electrocatalysts for the Oxygen Evolution Reaction. *Chem. Mater.* **2019**, *31* (15), 5919−5926.
(20) Weng, B.; Song, Z.; Zhu, R.; Yan, Q.; Sun, Q.; Grice, C. G.; Yan, Y.; Yin, W.-J. Simple descriptor derived from symbolic regression accelerating the discovery of new perovskite catalysts. *Nat. Commun.* **2020**, *11* (1), 3513.
(21) Vøllestad, E.; Strandbakke, R.; Tarach, M.; Catalán-Martínez, D.; Fontaine, M.-L.; Beeaff, D.; Clark, D. R.; Serra, J. M.; Norby, T. Mixed proton and electron conducting double perovskite anodes for stable and efficient tubular proton ceramic electrolysers. *Nat. Mater.* **2019**, *18* (7), 752−759.
(22) Wang, J.; Kim, S.-J.; Liu, J.; Gao, Y.; Choi, S.; Han, J.; Shin, H.; Jo, S.; Kim, J.; Ciucci, F.; Kim, H.; Li, Q.; Yang, W.; Long, X.; Yang, S.; Cho, S.-P.; Chae, K. H.; Kim, M. G.; Kim, H.; Lim, J. Redirecting dynamic surface restructuring of a layered transition metal oxide catalyst for superior water oxidation. *Nature Catalysis* **2021**, *4* (4), 212−222.
(23) Wan, G.; Freeland, J. W.; Kloppenburg, J.; Petretto, G.; Nelson, J. N.; Kuo, D.-Y.; Sun, C.-J.; Wen, J.; Diulus, J. T.; Herman, G. S.; Dong, Y.; Kou, R.; Sun, J.; Chen, S.; Shen, K. M.; Schlom, D. G.; Rignanese, G.-M.; Hautier, G.; Fong, D. D.; Feng, Z.; Zhou, H.; Suntivich, J. Amorphization mechanism of $SrIrO_3$ electrocatalyst: How oxygen redox initiates ionic diffusion and structural reorganization. *Science Advances* **2021**, *7* (2), No. eabc7323.
(24) Pan, Y.; Xu, X.; Zhong, Y.; Ge, L.; Chen, Y.; Veder, J.-P. M.; Guan, D.; O'Hayre, R.; Li, M.; Wang, G.; Wang, H.; Zhou, W.; Shao, Z. Direct evidence of boosted oxygen evolution over perovskite by enhanced lattice oxygen participation. *Nat. Commun.* **2020**, *11* (1), 2002.
(25) Wachowski, S. L.; Szpunar, I.; Sørby, M. H.; Mielewczyk-Gryń, A.; Balaguer, M.; Ghica, C.; Istrate, M. C.; Gazda, M.; Gunnæs, A. E.; Serra, J. M.; Norby, T.; Strandbakke, R. Structure and water uptake in BaLnCo2O6-δ (Ln = La, Pr, Nd, Sm, Gd, Tb and Dy). *Acta Mater.* **2020**, *199*, 297−310.
(26) Xu, X.; Chen, Y.; Zhou, W.; Zhu, Z.; Su, C.; Liu, M.; Shao, Z. A Perovskite Electrocatalyst for Efficient Hydrogen Evolution Reaction. *Adv. Mater.* **2016**, *28* (30), 6442−6448.
(27) Anantharaj, S.; Ede, S. R.; Karthick, K.; Sam Sankar, S.; Sangeetha, K.; Karthik, P. E.; Kundu, S. Precision and correctness in the evaluation of electrocatalytic water splitting: revisiting activity parameters with a critical assessment. *Energy Environ. Sci.* **2018**, *11* (4), 744−771.
(28) Suen, N.-T.; Hung, S.-F.; Quan, Q.; Zhang, N.; Xu, Y.-J.; Chen, H. M. Electrocatalysis for the oxygen evolution reaction: recent development and future perspectives. *Chem. Soc. Rev.* **2017**, *46* (2), 337−365.
(29) Fabbri, E.; Habereder, A.; Waltar, K.; Kötz, R.; Schmidt, T. J. Developments and perspectives of oxide-based catalysts for the oxygen evolution reaction. *Catal. Sci. Technol.* **2014**, *4* (11), 3800−3821.
(30) Ma, C.; Sun, W.; Qamar Zaman, W.; Zhou, Z.; Zhang, H.; Shen, Q.; Cao, L.; Yang, J. Lanthanides Regulated the Amorphization-Crystallization of IrO2 for Outstanding OER Performance. *ACS Appl. Mater. Interfaces* **2020**, *12* (31), 34980−34989.
(31) Shi, Q.; Zhu, C.; Du, D.; Wang, J.; Xia, H.; Engelhard, M. H.; Feng, S.; Lin, Y. Ultrathin dendritic IrTe nanotubes for an efficient oxygen evolution reaction in a wide pH range. *J. Mater. Chem. A* **2018**, *6* (19), 8855−8859.
(32) Wei, C.; Rao, R. R.; Peng, J.; Huang, B.; Stephens, I. E. L.; Risch, M.; Xu, Z. J.; Shao-Horn, Y. Recommended Practices and Benchmark Activity for Hydrogen and Oxygen Electrocatalysis in Water Splitting and Fuel Cells. *Adv. Mater.* **2019**, *31* (31), 1806296.
(33) Sun, H.; Hu, B.; Guan, D.; Hu, Z.; Fei, L.; Li, M.; Peterson, V. K.; Lin, H.-J.; Chen, C.-T.; Ran, R.; Zhou, W.; Shao, Z. Bulk and Surface Properties Regulation of Single/Double Perovskites to Realize Enhanced Oxygen Evolution Reactivity. *ChemSusChem* **2020**, *13* (11), 3045−3052.
(34) Zhu, Y.; Lin, Q.; Hu, Z.; Chen, Y.; Yin, Y.; Tahini, H. A.; Lin, H.-J.; Chen, C.-T.; Zhang, X.; Shao, Z.; Wang, H. Self-Assembled Ruddlesden-Popper/Perovskite Hybrid with Lattice-Oxygen Activation as a Superior Oxygen Evolution Electrocatalyst. *Small* **2020**, *16* (20), 2001204.
(35) May, K. J.; Carlton, C. E.; Stoerzinger, K. A.; Risch, M.; Suntivich, J.; Lee, Y.-L.; Grimaud, A.; Shao-Horn, Y. Influence of Oxygen Evolution during Water Oxidation on the Surface of Perovskite Oxide Catalysts. *J. Phys. Chem. Lett.* **2012**, *3* (22), 3264−3270.
(36) Yagi, S.; Yamada, I.; Tsukasaki, H.; Seno, A.; Murakami, M.; Fujii, H.; Chen, H.; Umezawa, N.; Abe, H.; Nishiyama, N.; Mori, S. Covalency-reinforced oxygen evolution reaction catalyst. *Nat. Commun.* **2015**, *6* (1), 8249.
(37) Jung, J.-I.; Jeong, H. Y.; Kim, M. G.; Nam, G.; Park, J.; Cho, J. Fabrication of Ba0.5Sr0.5Co0.8Fe0.2O3-δ Catalysts with Enhanced Electrochemical Performance by Removing an Inherent Heterogeneous Surface Film Layer. *Adv. Mater.* **2015**, *27* (2), 266−271.
(38) Zhao, B.; Zhang, L.; Zhen, D.; Yoo, S.; Ding, Y.; Chen, D.; Chen, Y.; Zhang, Q.; Doyle, B.; Xiong, X.; Liu, M. A tailored double perovskite nanofiber catalyst enables ultrafast oxygen evolution. *Nat. Commun.* **2017**, *8* (1), 14586.
(39) Vøllestad, E.; Schrade, M.; Segalini, J.; Strandbakke, R.; Norby, T. Relating defect chemistry and electronic transport in the double perovskite Ba1-xGd0.8La0.2+xCo2O6-δ (BGLC). *J. Mater. Chem. A* **2017**, *5* (30), 15743−15751.
(40) Kölbach, M.; Harbauer, K.; Ellmer, K.; van de Krol, R. Elucidating the Pulsed Laser Deposition Process of BiVO4 Photoelectrodes for Solar Water Splitting. *J. Phys. Chem. C* **2020**, *124* (8), 4438−4447.
(41) Lowndes, D. H.; Geohegan, D. B.; Puretzky, A. A.; Norton, D. P.; Rouleau, C. M. Synthesis of Novel Thin-Film Materials by Pulsed Laser Deposition. *Science* **1996**, *273* (5277), 898−903.
(42) Wang, Y.; Zhang, G.; Xu, W.; Wan, P.; Lu, Z.; Li, Y.; Sun, X. A 3D Nanoporous Ni-Mo Electrocatalyst with Negligible Overpotential for Alkaline Hydrogen Evolution. *ChemElectroChem* **2014**, *1* (7), 1138−1144.

(43) Verlage, E.; Hu, S.; Liu, R.; Jones, R. J. R.; Sun, K.; Xiang, C.; Lewis, N. S.; Atwater, H. A. A monolithically integrated, intrinsically safe, 10% efficient, solar-driven water-splitting system based on active, stable earth-abundant electrocatalysts in conjunction with tandem III-V light absorbers protected by amorphous TiO2 films. *Energy Environ. Sci.* **2015**, *8* (11), 3166−3172.
(44) Jacobsson, T. J.; Fjällström, V.; Sahlberg, M.; Edoff, M.; Edvinsson, T. A monolithic device for solar water splitting based on series interconnected thin film absorbers reaching over 10% solar-to-hydrogen efficiency. *Energy Environ. Sci.* **2013**, *6* (12), 3676−3683.
(45) Zhao, Y.; Hernandez-Pagan, E. A.; Vargas-Barbosa, N. M.; Dysart, J. L.; Mallouk, T. E. A High Yield Synthesis of Ligand-Free Iridium Oxide Nanoparticles with High Electrocatalytic Activity. *J. Phys. Chem. Lett.* **2011**, *2* (5), 402−406.
(46) Kelly, N. A.; Gibson, T. L. Design and characterization of a robust photoelectrochemical device to generate hydrogen using solar water splitting. *Int. J. Hydrogen Energy* **2006**, *31* (12), 1658−1673.
(47) Fan, C.; Piron, D. L.; Sleb, A.; Paradis, P. Study of Electrodeposited Nickel-Molybdenum, Nickel-Tungsten, Cobalt-Molybdenum, and Cobalt-Tungsten as Hydrogen Electrodes in Alkaline Water Electrolysis. *J. Electrochem. Soc.* **1994**, *141* (2), 382−387.
(48) Coelho, A. TOPAS and TOPAS-Academic: an optimization program integrating computer algebra and crystallographic objects written in C++. *J. Appl. Crystallogr.* **2018**, *51* (1), 210−218.
(49) Jung, S.; McCrory, C. C. L.; Ferrer, I. M.; Peters, J. C.; Jaramillo, T. F. Benchmarking nanoparticulate metal oxide electrocatalysts for the alkaline water oxidation reaction. *J. Mater. Chem. A* **2016**, *4* (8), 3068−3076.

https://doi.org/10.1021/acsami.1c01900
ACS Appl. Mater. Interfaces 2021, 13, 20313−20325

Appendix B

Galvanic Deposition of Pt Nanoparticles on Black TiO_2 Nanotubes for Hydrogen Evolving Cathodes

Aikaterini Touni, Dr. Xin Liu, Xiaolan Kang, Dr. Patricia A. Carvalho, Dr. Spyros Diplas, Kevin G. Both, Prof. Dr. Sotiris Sotiropoulos, Dr. Athanasios Chatzitakis

Published in *ChemSusChem*, October 2021, volume 14, issue 22, pp. 4893–5631. DOI: 10.1002/cssc.202101559.

V

This research has been co-financed by the European Regional Development Fund of the European Union and Greek national funds through the Operational Program Competitiveness, Entrepreneurship and Innovation, under the call RESEARCH – CREATE – INNOVATE (project code:T1EDK-00461). Funding from the Research Council of Norway is acknowledged (EnCaSE, project number 275058, PH2ON, project number 288320). The computer resources are supported by the National Infrastructure for High-Performance Computing and Data Storage in Norway (Project Number NN4604k). The authors wish to thank Assoc. Prof. Dimitra Lambropoulou for the ICP-MS measurements (A.U.Th., Greece).

Galvanic Deposition of Pt Nanoparticles on Black TiO_2 Nanotubes for Hydrogen Evolving Cathodes

Aikaterini Touni,[a] Xin Liu,[b] Xiaolan Kang,[b] Patricia A. Carvalho,[c] Spyros Diplas,[b, c] Kevin G. Both,[b] Sotirios Sotiropoulos,*[a] and Athanasios Chatzitakis*[b]

A galvanic deposition method for the in-situ formation of Pt nanoparticles (NPs) on top and inner surfaces of high-aspect-ratio black TiO_2-nanotube electrodes (bTNTs) for true utilization of their total surface area has been developed. Density functional theory calculations indicated that the deposition of Pt NPs was favored on bTNTs with a preferred [004] orientation and a deposition mechanism occurring via oxygen vacancies, where electrons were localized. High-resolution transmission electron microscopy images revealed a graded deposition of Pt NPs with an average diameter of around 2.5 nm along the complete nanotube axis (length/pore diameter of 130:1). Hydrogen evolution reaction (HER) studies in acidic electrolytes showed comparable results to bulk Pt (per geometric area) and Pt/C commercial catalysts (per mg of Pt). The presented novel HER cathodes of minimal engineering and low noble metal loadings (μg cm^{-2} range) achieved low Tafel slopes (30–34 mV dec^{-1}) and high stability in acidic conditions. This study provides important insights for the in-situ formation and deposition of NPs in high-aspect-ratio structures for energy applications.

Introduction

Recent studies, mainly carried out during the last ten years, reflect the unique properties of black titania. Titania is a semiconducting material with a large bandgap (3.2 eV for anatase), and its properties include earth abundance, non-toxicity, and chemical stability in different media.[1–3] In contrast to the pristine TiO_2, black titania shows metallic-like electronic conductivity,[2,4,5] which makes it an attractive oxide material for electrochemical investigations. Its dark color assists the adsorption of sunlight[6] in a wide wavelength range, from ultraviolet up to the near-infrared region,[7,8] due to the narrow bandgap and the mid-gap electronic states.[9] This material has gained great attention in the field of photocatalysis for the production of H_2 gas during water splitting[3,4,10–13] and decomposition of organic pollutants such as phenol,[14] toluene,[15] ethyl acetate,[15] and methyl orange[16] in wastewater treatment. Except for its importance in the field of photocatalysis, its use expands to a wide range of applications in the field of electrochemistry, such as lithium- and sodium-ion batteries,[3,4,17,18] supercapacitors,[19] and fuel cells.[20]

Various synthetic routes have been reported to synthesize nanostructured black titania,[2,4,21] such as hydrogenation (H_2, H_2/Ar, H_2/N_2 at high/ambient pressure, H_2 plasma),[18,22–27] chemical reduction (by Mg, Zn, Li, Al, $NaBH_4$, CaH_2),[5,11,13,15,28,29] laser ablation/pulsed laser ablation, and electrochemical reduction.[22] Also, microwave irradiation, ultrasonication,[30] and one-pot gel combustion have been reported in the literature[2,3,21] for the production of black titania.

In this work we utilized CaH_2 to chemically reduce TiO_2 nanotubes (TNT) in order to synthesize electronically conducting oxides of TNT (bTNT), which can then act as a support for Pt nanoparticles (Pt NPs) and the resulting electrode as an efficient cathode for the hydrogen evolution reaction (HER). Despite porous electrodes suffering from pore clogging when used in gas-evolving electrochemical reactions, they are often employed for such reactions since their large electroactive area offsets gas blanketing effects (see for example the use of porous/nanoporous Ni electrodes as hydrogen evolution cathodes in alkaline water electrolysis[31] or in electrochemical hydrogenation reactions[32]).

Although Pt/C powder catalysts adhered on the polymer electrolyte membrane is the common HER cathode choice in polymer electrolyte membrane (PEM) electrolyzers,[33] there are a number of other industrial applications whereby platinized Ti electrodes are used as HER cathodes; these include, for example, electrooxidation of organics[34] and photoelectrochemical water splitting.[35]

Our previous studies showed that highly oriented anatase bTNTs towards the [001] direction can be obtained when the CaH_2 is in contact with the material.[5] This is particularly important as the electronic conductivity of the material is significantly enhanced, a property that is highly desirable if it is

[a] A. Touni, Prof. Dr. S. Sotiropoulos
Department of Chemistry
Aristotle University of Thessaloniki
54124 Thessaloniki (Greece)
E-mail: eczss@chem.auth.gr
[b] Dr. X. Liu, X. Kang, Dr. S. Diplas, K. G. Both, Dr. A. Chatzitakis
Centre for Materials Science and Nanotechnology
Department of Chemistry
University of Oslo
Gaustadalléen 21, 0349 Oslo (Norway)
E-mail: athanasios.chatzitakis@smn.uio.no
[c] Dr. P. A. Carvalho, Dr. S. Diplas
SINTEF Industry
POB 124 Blindern, 0314 Oslo (Norway)

Supporting information for this article is available on the WWW under https://doi.org/10.1002/cssc.202101559

to be used as an electrode support. Pt is the state-of-the-art electrocatalyst for the HER in acidic media based on the relevant volcano plot.[36–38] In industrial electrolysis/photoelectrolysis and electrodialysis applications (where stable cathodes and anodes are needed, able to perform at high current densities), Pt particles are usually dispersed on a durable Ti-based support. The 1D orientation of bTNT exhibits orthogonality to light absorption[26] and provides high surface area,[11] which is desirable for the dispersion of electroactive nanoparticles, likely to lead to improved performances for the HER at low mass loadings. On the other hand, the high aspect ratio of these nanostructures confines the majority of the surface area and the deposition of NPs along the entire length of the nanotubes is not straightforward.

Pt deposition on various black titania nanomaterials have been reported in the literature. Zhang et al.[20] electrodeposited Pt on hydrogenated TNTs (H-TNTs) and used both as anode and cathode at polymer exchange membrane fuel cells (PEMFC). Wang et al.[39] prepared monodisperse Pt nanoparticles on N_{doped}-black TiO_{2-x} by a borohydride reduction method and tested them for the HER and oxygen reduction reaction (ORR). Li et al.[40] synthesized Pt/TiO_{2-x} microspheres and used them as photocatalysts. Recently, Wang et al[41] photo-deposited Pt on black TiO_2 powder for H_2 evolution, and Wei et al.[42] studied the HER on oxygen vacancy-rich (v_O-rich) and oxygen vacancy-deficient (v_O-deficient) TiO_2 support deposited with Pt nanoclusters. Last but not least, other precious metals that have been deposited on black titania include Rh for HER (by a sputtering method proposed by Szenti et al.[43]) and Pd for ORR (on Al reduced-TiO_{2-x} nanobelts via the borohydride method proposed by Yuan et al.[44]).

Herein and for the first time we take advantage of the metallic conductivity of oriented bTNTs and we propose the galvanic deposition/replacement method to deposit Pt particles on its surface. The galvanic deposition process takes place spontaneously by mere immersion of the bTNT in a Pt(IV) complex ion solution, which makes it an easy and simple way to prepare platinized bTNT. It should also be stressed that the galvanic deposition is expected to lead to low loading deposition of the precious metal on the surface of the substrate and may also allow the formation of Pt NPs in the interior of the nanotubes. This is because Pt ions are in the liquid solution, which can flood the pores of the nanotubes and form Pt deposits that are otherwise impossible for such high aspect ratio structures. Electrocatalysts prepared by the galvanic deposition method are reported by Papaderakis et al.[45] Lately, the galvanic deposition method has also been used by Schmuki and co-workers[46] to deposit metallic Ir on black titania for the HER, exhibiting high electrocatalytic performance.

The aim of this work has been the establishment of a simple galvanic deposition method to prepare metalized bTNT to be used as electrocatalytic materials. Its objectives have been: (i) preparation of Pt/bTNT by immersion of freshly CaH_2-reduced bTNT in a platinum chloro-complex solution; (ii) microscopic and spectroscopic characterization of the material with emphasis on Pt insertion into the pores and potential metal-substrate interactions; (iii) electrochemical characterization of the material via typical H adsorption/desorption and hydrogen evolution reactions; and (iv) elucidation of the deposition mechanism by density functional theory (DFT) calculations.

Results and Discussion

Structural characterization

The overall morphology of different types of samples as observed by scanning electron microscopy (SEM) can be seen in Figure 1a–c. Except for the bTNT0 sample, which appears with the expected hexagonal, honeycomb-like impressions left on the Ti foil from the bottom side of the peeled off nanotubes layer, the rest of the samples have the typical features of nanotubes grown in ethylene glycol-based electrolytes.[47,48] The top surface has the distinct honeycomb-like morphology, with increasing pore diameter as the anodization times increased, and is free of any "nanograss" or other irregular features.[49] Cross-sectional images revealed close-packed, vertically oriented, and relatively smooth nanotube surfaces of increasing lengths with increasing anodization times (Figure S1 in the Supporting Information). The geometrical parameters of the samples are summarized in Table S1 and are in good accordance with our previous studies.[47]

An estimate of the true projected area of the samples can be made by identifying the number of pores per unit area, calculating their area by means of the typical pore diameter and subtracting that from the nominal substrate area (see supplementary note 1 in the Supporting Information). Such an estimate gives a true geometric area that is 76 and 44% of the projected nominal area for samples Pt/bTNT5 and Pt/bTNT30, respectively.

After the galvanic deposition of Pt, the top-view images revealed that the platinized samples were evenly decorated with Pt particle aggregates as it can be seen in Figure 1d–f. More importantly though, the interior wall of the nanotubes was also partly decorated with some Pt NPs, as it can be seen in Figure 2. From the cross-sectional SEM images it appears that

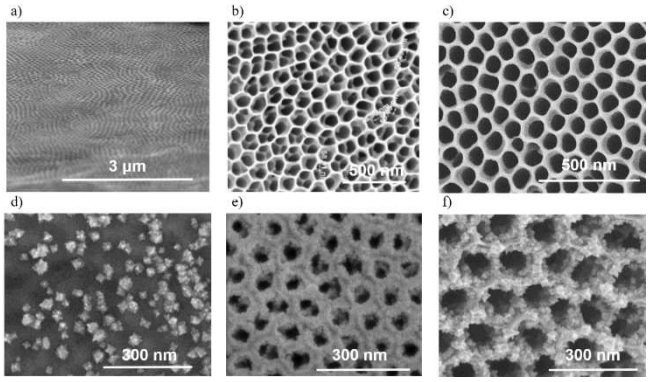

Figure 1. Top surface SEM images of (a) bTNT0, (b) bTNT5, and (c) bTNT30, before and after galvanic deposition of Pt in a solution containing 0.5 mM K_2PtCl_6 and 0.1 M $HClO_4$ to form (d) Pt/bTNT0, (e) Pt/bTNT5, and (f) Pt/bTNT30.

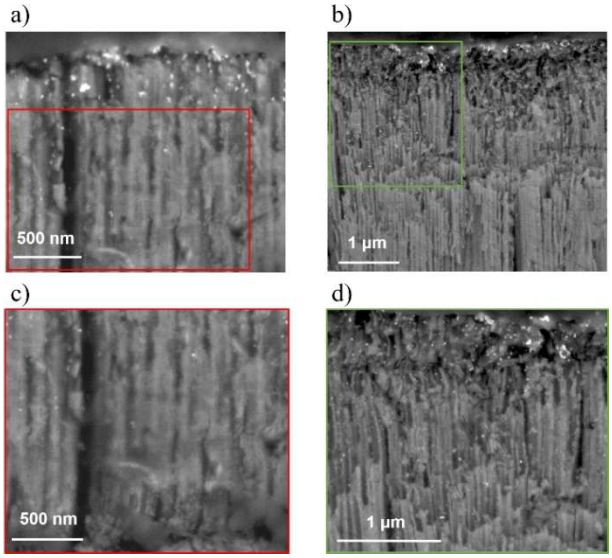

Figure 2. Cross-section SEM images of (a,c) Pt/bTNT5 and (b,d) Pt/bTNT30, and higher magnifications in the designated areas. The formation of Pt deposits well inside the nanotubular morphology is highlighted. Additional cross sections showing the whole length of the Pt/bTNT5 and Pt/bTNT30 are given in Figure S1c,d.

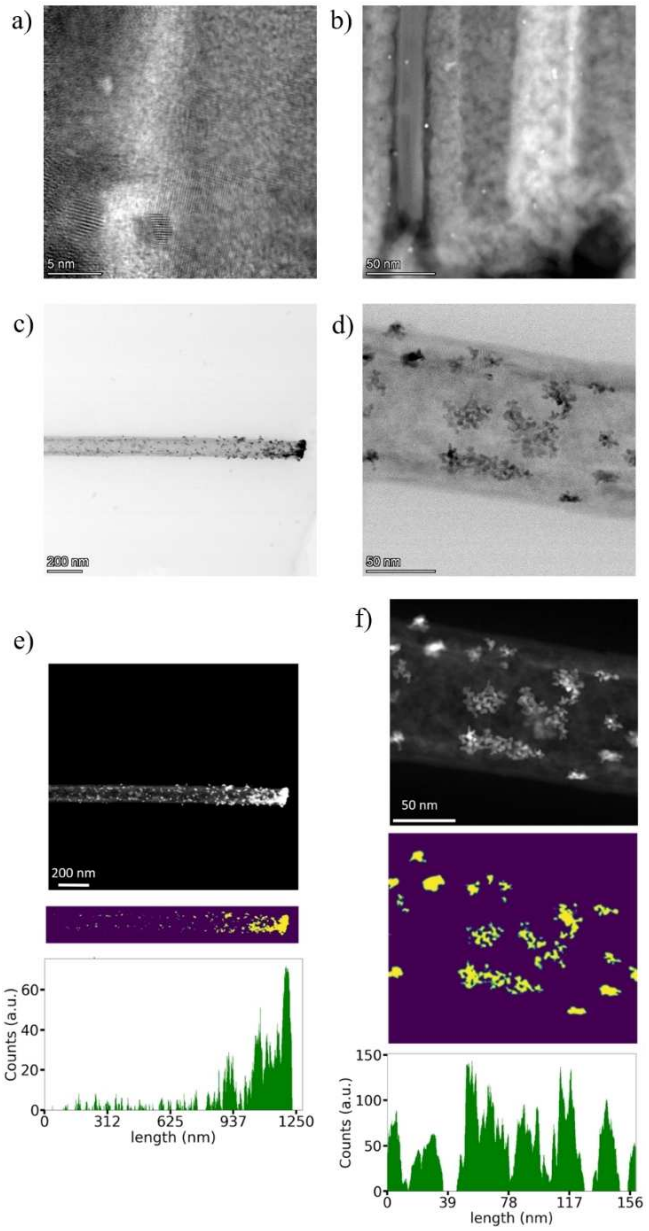

Figure 3. (a) High-resolution STEM high-angle annular dark-field (HAADF) image of the Pt/bTNT30 depicting a Pt nanoparticle of around 2 nm and its interface with bTNT. (b) STEM HAADF image of the Pt/bTNT30 sample close to the bottom of a single nanotube. (c,d) STEM images of different magnifications of a single TiO_2 nanotube from the Pt/bTNT30 sample, with a contour map of the bright pixels underneath. (e,f) The graphs show the number of bright pixels at each position in the *x* direction.

the Pt NPs have been deposited in a depth of approximately 0.8 and 4.2 µm from the opening of the nanotubes in the PtbTNT5 and PtbTNT30, respectively. The distribution of the galvanic deposits of Pt NPs on the walls of the nanotubes appeared graded, suggesting a diffusion-controlled deposition.

Scanning transmission electron microscopy (STEM) observations allowed to investigate at the nanoscale the electroless deposition of the Pt NPs on the interior wall of the nanotubes, as well as the depth range of the deposition. The Pt/bTNTs30 sample, which had the longest nanotubes, was observed, and Pt NPs with an average size of around 3.5 nm (Figure 3a) were detected all the way down to the bottom of the nanotubes (Figure 3b). The high crystallinity of the Pt NPs as well as its distinct interface with the crystalline TiO_2 surface is revealed in the STEM images of Figure 3a. These results (see also Figure S2) show an intimate interface between the Pt nanoparticle and the TiO_2 substrate. Lower magnification STEM images in Figure 3c,d underline the graded deposition of Pt along the nanotube axis. Close to the opening of the nanotube where the density of the particles is high, formation of Pt NPs aggregates is seen. It actually appears that these aggregates may be formed by a clustering of Pt NPs of around 2–3 nm (refer to Figure S3). This is interesting as these aggregates seem to provide a high catalytic surface area and moreover, the particle size matches the size of the Pt NPs deposited individually at the bottom of the nanotube. Furthermore, the interplanar distances match that of metallic Pt and the fast Fourier transform (FFT) suggests a cubic structure, as it can be seen in Figure S3c,d.

To better visualize the distribution of the Pt NPs a threshold was applied to the STEM images of Figure 3c,d, and the bright pixels of each column counted (Figure 3e,f). The result can be seen in the same figures. The maps below the STEM images show contour plots of the bright areas in the STEM image, with green marking the border and yellow the bright region. The graphs represent the number of bright pixels for each column. Figure 3e shows an entire nanotube, and a fluctuating, but ultimately decreasing number of bright pixels from right to left. Consequently, there is less Pt closer to the nanotube bottom than on the opening. Figure 3f shows a magnified region of Figure 3e and exemplifies that the distribution of brighter pixels across a short range varies significantly, while the mean

distribution remains roughly constant. We can see a graded galvanic deposition of Pt from the opening and across the nanotube axis following an exponential dependence. This finding suggests that either the reactivity of $bTiO_2$ decreases when approaching the bottom of the nanotube and/or the aqueous electrolyte displacement in the nanotube follows an exponential decay, assuming fast galvanic deposition kinetics. Another possibility could also be a depletion of the $PtCl_6^{-2}$ concentration along the nanotube axis strong capillary forces that can flood fast enough with solution these high aspect ratio structures. It is evident that nano-fluidic studies utilizing our suggested methodology of in-situ formation of nanoparticles in the interior wall of such high aspect ratio structures can be proven of significance, especially for applications in drug delivery, point-of-care testing, separation, sensors etc.[50,51] We also used such contour plots to get a better overview on the size distribution of the Pt NPs from a larger sample area (i.e. additional STEM images). Figure S4 shows histograms of four STEM images from the Pt/bTNT30 sample, as well as their sum. As we can see from the total histogram, most of the NPs have a diameter between 1 and 5 nm with the maximum being at 2 nm.

The X-ray diffraction (XRD) patterns of the different Pt/bTNT samples are presented in Figure 4a. The Pt/bTNT0 is not given for clarity of presentation, as both XRD diffractograms of the Pt/bTNT5 (short nanotubes of ≈2 μm) and Pt/bTNT0 (patterned Ti foil) samples were identical and contained mainly peaks from the Ti substrate and the Pt particles. In general, the main peaks were indexed according to the ICDD-JCPD files for anatase, hexagonal Ti, and cubic Pt, the latter in agreement with the STEM results above, as it can be seen in the reference curves included in Figure 4a. The increased intensity of the (004) peak in the Pt/bTNT30 sample indicates the preferential crystal orientation of TiO_2 along the tube growth direction. This is in agreement with our previous results, as we have shown that CaH_2 annealing favors the preferential orientation towards the [004] direction.[5,52] In general, the (101) surface of TiO_2 dominates the external surface of anatase (more than 94%),[53] therefore the increased intensity of the (004) surface compared to the (101) one in our Pt/bTNT30 further highlights the strongly oriented nanotube structure.

X-ray photoelectron spectroscopy (XPS) investigations were conducted in the Pt/bTNT0 and Pt/bTNT30 samples, as they represent the two limiting cases (patterned substrate and longest nanotubes, respectively). The superimposed and normalized XPS spectra of the Pt $4f_{5/2}$ and Pt $4f_{7/2}$ peaks (Figure 4b) at 74.5 ± 0.1 and 71.2 ± 0.1 eV show no essential differences in the line shape and the corresponding binding energies of the main peak, indicating no differences in the chemical state of Pt in these samples. Compared to the Pt $4f_{7/2}$ peak of a clean Pt standard (Figure 4c), both Pt/bTNT sample show slightly broader peak that may be attributed to chemisorbed O on Pt surface and/or PtO_x.[54] This is more clearly shown in the peak fitted spectra of Figure S5a, where the different oxidation states of Pt are also mentioned. The O 1 s peak at 530.7 ± 0.1 eV (Figure 4d) corresponds to the lattice oxygen in TiO_2, while the shoulder at the higher binding energy of 532.4 ± 0.1 eV is related to

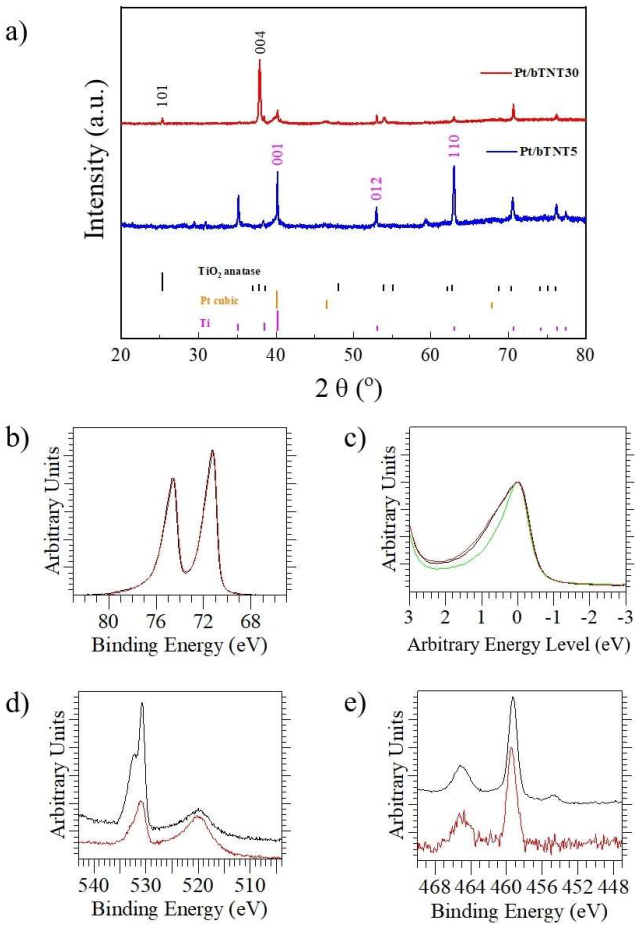

Figure 4. (a) XRD patterns of the Pt/bTNT5, and Pt/bTNT30 samples. The insets include high magnifications in the Miller indices of (101) and (004). The standard JCPDS cards of anatase TiO_2 (red), Ti foil (pink), and cubic Pt (blue) are also given for reference. (b) Superimposed and normalized XPS spectra of Pt $4f_{5/2}$ and Pt $4f_{7/2}$ of the Pt/bTNT30 (dark red curve) and Pt/bTNT0 samples (black curve). (c) Pt $4f_{7/2}$ peaks superimposed and normalized for same intensity of the Pt/bTNT30 and Pt/bTNT0 samples as compared to pure Pt (green curve)-peak maxima were placed arbitrarily at a 0 eV binding energy in order to compare the peak widths. (d) O 1 s peak and (e) Ti $2p_{1/2}$ and Ti $2p_{3/2}$ peaks.

oxygen-deficient sites and/or surface –OH groups.[55,56] As the difference in binding energies is approx. 1.7 eV this corresponds well with the presence of oxygen vacancies as molecular oxygen can be dissociatively adsorbed on the vacant sites (O_2^{2-}, O^-).[56] A deconvolution of the 1 s peak (Figure S5b) shows the presence of an intermediate peak in the case of Pt/bTNT30, which can be attributed to adsorbed species and the ex-situ type of the analysis. The peak at 519.9 ± 0.1 eV is assigned to the Pt $4p_{3/2}$.[57] Finally, the peaks at 465 ± 0.2 eV and 459.4 ± 0.2 eV correspond to Ti $2p_{1/2}$ and Ti $2p_{3/2}$ respectively of TiO_2. A low intensity peak at 454.7 ± 01 eV in the case of the Pt/bTNT0 sample can be assigned to metallic Ti (Ti^0) and most probably related to the Ti foil under a thin $bTiO_2$ film (Figure 4e). We have not identified any peak related to Ti^{3+} species in the Pt/bTNT30, but a slight possibility of such a presence is manifested by the Ti $2p_{3/2}$ peak broadening towards lower binding energies of the Pt/bTNT0 sample (see Figure S5c). However, as no

distinct peak is shown in the spectrum of Pt/bTNT30, the presence of Ti^{3+} is considered insignificant a fact that is in agreement with our previously results and electron paramagnetic resonance (EPR) measurements, where no Ti^{3+} signals were observed (see also Figure S6).[5,58]

Electrochemical results

The electrochemical behavior of three characteristic electrodes (Pt/bTNT0, Pt/bTNT5, and Pt/bTNT30 and their bTNT substrates) is depicted in the cyclic voltammetry (CV) profiles of Figure 5. As it can be seen in Figure 5a, bTNTs of the higher nanotube length and hence higher surface area have higher capacitive/pseudocapacitive currents, which is depicted as a higher capacitive (current) envelope of the voltammograms. The platinized bTNTs exhibit mixed surface electrochemistry of both Pt (see below H and O electrosorption/electrodesorption) and bTNT (large capacitive envelope), as it can be seen in Figure 5b that contains the CVs of all platinized bTNTs. This is more clear in Figure 5c, which presents the interfacial electrochemistry of Pt/bTNT5 and, for comparison, that of its respective substrate bTNT5.

Two sharp shaped and well distinguished reversible peaks attributed to strong and weak adsorption and desorption of underpotentially deposited hydrogen atoms (UPD–H) on the Pt particles appear at around $+0.20$ and $+0.10$ V_{RHE} (RHE: reversible hydrogen electrode). Pt oxide formation takes place at around $+0.95$ V_{RHE}, while its reduction is shown at the distinctive peak of $+0.73$ V_{RHE}. These typical Pt features are in accordance with the literature.[38] At the same time, the characteristic feature of bTNT during the anodic scan at around $+0.50$ V_{RHE} (see also Figure 5a) and the high capacitive currents due to their high surface area are also observed-superimposed in these CVs.

The electroactive area may be estimated from the UPD–H peaks of the CVs of the Pt/bTNT, as a monolayer of hydrogen atoms is adsorbed at Pt surface (corresponding to coverage of 210 $\mu C\,cm^{-2}$). However, in this case, the high capacitive currents of the bTNTs, especially in the case of Pt/bTNT30, are likely to limit the accuracy of such an estimate. Nevertheless, carrying out this calculation an electroactive surface area (ESA) of 26.463, 28.553, and 1.464 cm^2 per nominal cm^2 has been estimated for electrodes Pt/bTNT30, Pt/bTNT5, and Pt/bTNT0, respectively. The fact that the optimum value of mass-specific Pt electroactive area has been observed for the Pt/bTNT5 electrode could be explained by the fact that it contains much rougher deposits than the flat, patterned Pt/bTNT0 electrode (despite the latter having a larger true projected area and similar Pt loading). In contrast, isolated Pt nanoparticles within the long pores of the Pt/bTNT30 electrode may not be fully wetted or experience ohmic losses through the nanopores and/or bad electronic contact to the substrate.

Hydrogen evolution studies

Hydrogen evolution was studied by linear sweep voltammetry (LSV) at a slow scan rate of 5 $mV\,s^{-1}$ in 0.1 M $HClO_4$, recorded from $+0.30$ V_{RHE} (potential range prior to hydrogen adsorption) up to -0.15 V_{RHE}. Electrochemical impedance spectroscopy (EIS) spectra were recorded during HER to correct the potential for ohmic losses and, the solution ionic resistance was estimated at approximately 3.1–4.3 Ω. Figure 6a presents the hydrogen evolution performance of the Pt/bTNT and their respective substrates. The valuable contribution of Pt on the electrocatalytic performance of the platinized samples on HER is obvious when these are compared to their substrates, the latter requiring much higher overpotentials to achieve the same current. Note that in order to reach -10 $mA\,cm^{-2}$ bTNT require at least 590 mV, whereas Pt/bTNT 36 mV.

Pt/bTNT30 exhibits enhanced apparent electrocatalytic performance (i.e., per nominal substrate electrode area) towards the HER compared to the rest of Pt/bTNT samples. This should be attributed to the higher overall Pt loading that has been deposited on this electrode in contrast to Pt/bTNT5 and Pt/bTNT0, as it will be mentioned below. Their apparent electrocatalytic activity towards HER is comparable to bulk Pt as it can be seen in Figure 6a. However, the bulk Pt performance still appears superior at low overpotential values, but at -10 $mA\,cm^{-2}$ an overpotential of 31 mV for bulk Pt and 36 mV for Pt/bTNT30 is required. This may be due to the fact that

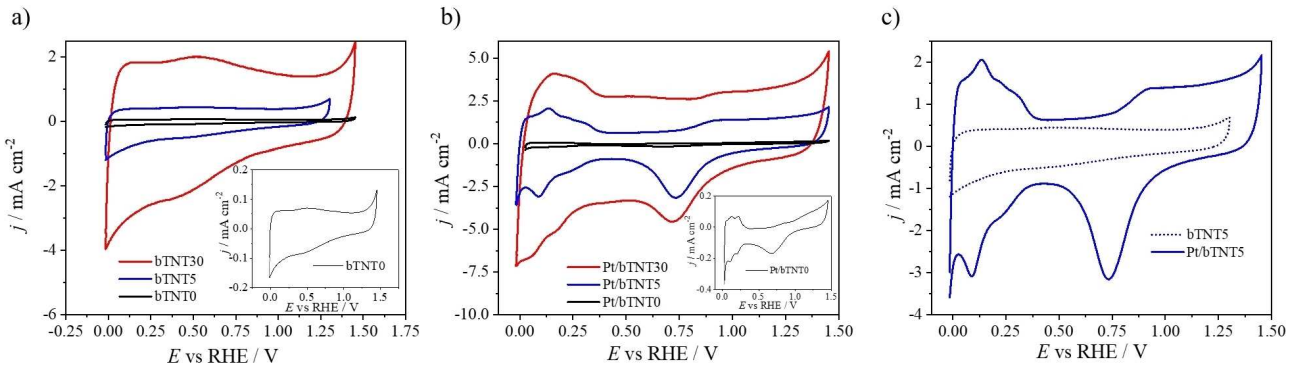

Figure 5. CV profiles of (a) bTNTs substrates, (b) Pt/bTNTs, and (c) Pt/bTNT5 and bTNT5 at 50 $mV\,s^{-1}$ in deaerated 0.1 M $HClO_4$.

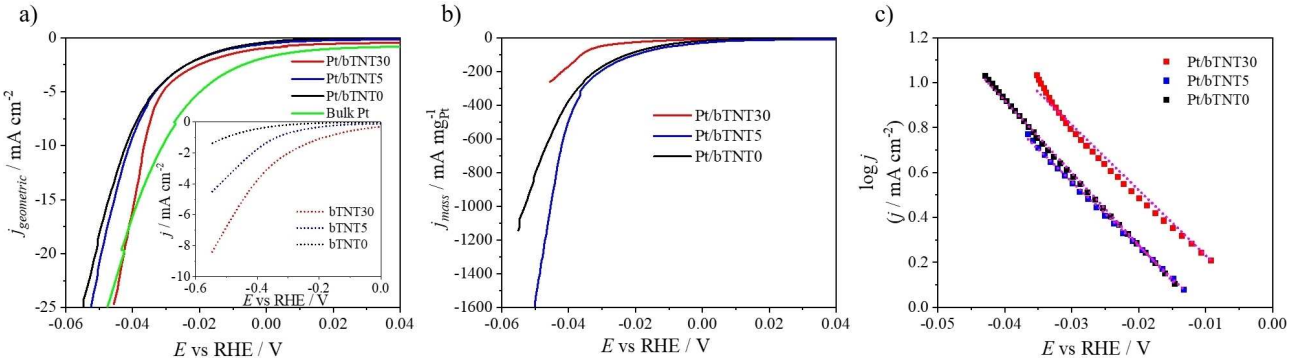

Figure 6. Polarization curves of *j* normalized (a) per Ti foil geometric area (inset shows the corresponding HER of the bTNT substrates) and (b) per Pt mass vs. *E* corrected for ohmic losses recorded by linear sweep voltammetry of Pt/bTNT and Pt bulk at 5 mV s^{-1} in deaerated 0.1 M $HClO_4$. (c) Tafel plots of the Pt/bTNT.

highly active and porous electrodes are more likely to be blanketed or clogged by evolving hydrogen than a smooth and flat foil electrode.

Pt mass can be estimated by the inductively coupled plasma mass spectrometry (ICP-MS) technique as described in the experimental section below. The results from the ICP-MS analysis gave 94.38, 18.56, and 22.58 μg cm^{-2} Pt for Pt/bTNT30, Pt/bTNT5, and Pt/bTNT0 respectively. We can observe that a significantly greater amount of Pt has been deposited via the galvanic deposition process at the Pt/bTNT with the higher nanotube length (Pt/bTNT30) than at those with a shorter nanotube length (Pt/bTNT5) or the patterned electrodes (Pt/bTNT0). The fact that the short nanotube length electrode (Pt/bTNT5) exhibits a similar Pt loading to the patterned flat sample (Pt/bTNT0) may be attributed to the lower (44% of its nominal value; see Experimental Section) true projected area of the former (where most deposition occurs), which is offset by a rougher deposit morphology and (limited) deposition into the pores. These loadings, together with the electroactive surface areas estimated by the hydrogen adsorption/desorption charge (see discussion of interfacial electrochemistry above) give Pt mass specific (electroactive) surface areas 28, 153, and 6.4 $m^2 g^{-1}$ for the Pt/bTNT30, Pt/bTNT5, and Pt/bTNT0 samples, respectively.

In Figure 6b Pt/bTNT electrodes are compared accounting for their Pt mass content. The Pt/bTNT5 electrode exhibits the highest per Pt mass performance. Similar Pt mass content has been deposited at Pt/bTNT0 and Pt/bTNT5, but Pt/bTNT5 gives slightly better results. This leads us to the conclusion that a length-optimized nanotube substrate assists appropriate Pt deposition and dispersion and as a result enhances HER performance in comparison to the patterned substrate. However, the superiority of the patterned or short nanotube samples, as far as Pt mass specific activity is concerned, when compared to the long nanotube sample Pt/bTNT30 (despite the latter bearing a higher Pt loading), means that it is only the outer Pt layers that are active, while particles down the nanotubes are likely to be inoperative due to pore clogging during hydrogen evolution. Notice that the cross-section SEM and the TEM images showed Pt particles deposition all the way down to the bottom of the nanotubes.

The HER is a two-step process; the first step is the Volmer step [Eq. (1)], based on which a proton (H^+) is reduced and adsorbed on the active site of catalyst surface as a H_{ads} atom and the subsequent second step involves the evolution of H_2 gas. The second step follows either the H^+ reduction on H_{ads} accompanied by an e^- transfer [Heyrovsky step; Eq. (2)] or the recombination of two H_{ads} [Tafel step; Eq. (3)] resulting at the formation of molecular $H_{2(g)}$.[37,59–61]

$$\text{Volmer reaction}: \quad H^+ + e^- \rightarrow H_{ads} \tag{1}$$

$$\text{Heyrovsky reaction}: \quad H_{ads} + H^+ + e^- \rightarrow H_{2(g)} \tag{2}$$

$$\text{Tafel reaction}: \quad 2H_{ads} \rightarrow H_{2(g)} \tag{3}$$

In our work, the Tafel slope is estimated to be 32, 34, and 30 mV dec^{-1} for Pt/bTNT30, Pt/bTNT5, and Pt/bTNT0 respectively (Figure 6c), corresponding to the same rate-determining step of 30 mV dec^{-1} of bulk polycrystalline Pt at low overpotential values.[37,59,62] This value indicates that the reaction follows the Volmer–Tafel pathway as the rate-determining step is the Tafel step. This means that the Pt-bTNTs interactions do not affect/modify the mechanism of HER on Pt at the prepared electrodes.

In Table 1 data for the hydrogen evolution performance of similar electrodes are summarized in order to compare results that are found in the literature with the results of this work for Pt/bTNT30 and Pt/bTNT5. As it can be seen, the platinized black TNT electrodes of the present work (prepared via the galvanic deposition method) exhibits comparable apparent (per substrate nominal geometric area) HER performance with most titania-based and carbon-based electrodes that appear in the literature. At overpotential values other than the 30 mV for which values are shown in Table 1, commercial Pt/C (20% Pt) electrocatalysts give 115 mA mg^{-1}_{Pt} at an overvoltage of 15 mV,[63] and 650 mA mg^{-1}_{Pt} at that of 40 mV,[64] while the catalysts of this work exhibit comparable mass performance of

Table 1. HER performance of platinized carbon and titania electrodes reported in the literature and this work.

Electrode	$\eta^{[a]}$ [mV]	$j^{[b]}$ [mA mg$^{-1}_{Pt}$]	HER conditions	Tafel slope [mV dec^{-1}]	Ref.
Pt bulk	26	–	potential pulses, $HClO_4$	31	[65]
Pt/C (20 %wt Pt) commercial	27	112.75	5 mV s^{-1}, H_2SO_4	35	[66]
Pt/C (5 %wt Pt) commercial	50	137.25	5 mV s^{-1}, H_2SO_4	40	[66]
Pt/graphite tubes; electrochemical deposition	18	–	2 mV s^{-1}, H_2SO_4	24	[67]
Pt/graphite tubes; electrochemical deposition	66	–	2 mV s^{-1}, $HClO_4$	24	[67]
Pt/C	81	19.64	2 mV s^{-1}, $HClO_4$	30.4	[67]
Pt/C commercial	44.17	224.7	20 mV s^{-1}, H_2SO_4	–	[68]
Pt/N_x:TiO_{2-x}; borohydride reduction	40	157	10 mV s^{-1}, H_2SO_4	33	[39]
(v_O-rich Pt/TiO_2)/GC	60	1250	5 mV s^{-1}, H_2SO_4	33	[42]
(v_O-deficient Pt/TiO_2)/GC	160	–	5 mV s^{-1}, H_2SO_4	102	[42]
Pt/bTNT30; galvanic deposition	36	49	5 mV s^{-1}, $HClO_4$	32	this work
Pt/bTNT5; galvanic deposition	41	206	5 mV s^{-1}, $HClO_4$	34	this work

[a] Overpotential values required to reach current density of −10 mA cm^{-2}. [b] Current density per Pt mass at an overvoltage of 30 mV.

20–76 mA mg$^{-1}_{Pt}$ at 15 mV and 172–500 mA mg$^{-1}_{Pt}$ at 40 mV, respectively.

Stability testing of the Pt/bTNT30 sample was performed under galvanostatic conditions at −10 mA cm^{-2} for 48 h at the same experimental acidic conditions of 0.1 M $HClO_4$. Figure S7 shows that after 48 h of operation the potential showed a minimal increase, clearly indicating the high stability of the platinized bTNT. Post-operation energy-dispersive X-ray spectroscopy (EDS) analysis of the electrode showed no change at the Pt content, which further indicates the good stability during HER performance. The stability tests were also carried out in a Nafion-membrane separated two-compartment cell with no detectable change observed during the course of the experiment (not presented).

Galvanic deposition mechanism

The initial assumption behind the deposition mechanism included the oxidation of reduced surface species of bTiO_2 by Pt(IV) cations. The kinetic force behind the galvanic/electroless deposition was considered to lie in the positive difference between the standard reduction potentials of TiO_2 and Pt(IV). In our case the reduced surface species on TiO_2 are neutral oxygen vacancies as Ti^{3+} is apparently not present according to our XPS and EPR measurements. In order to further elucidate the deposition mechanism, first-principles calculations were considered using DFT.

The optimized TiO_2 surface structures with three different facets [001], [100], and [101] are displayed in Figure 7. There are two types of oxides ion sites for all three facets (marked as O_2c and O_3c), yielding two types of oxygen vacancies correspondingly. For both types of neutral oxygen vacancies ($v_O^\times$), they are found to exist as defect complexes composed of the effective positively charged defect ($v_O^{\bullet\bullet}$) and two electron polarons at the adjacent Ti atoms ($Ti_{Ti}^{/}$). These electronic defects ($Ti_{Ti}^{/}$) create in-gap states and thereby extend the light adsorption in the near-infrared region, rationalizing the black color of the anatase TiO_2.

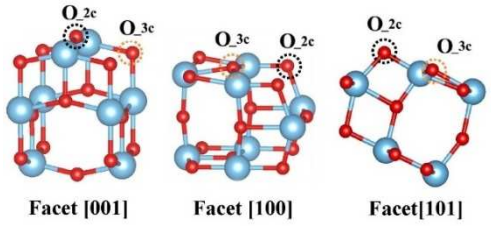

Figure 7. Surface structures of anatase TiO_2 with different facets [001], [100], and [101].

The defect formation energies of $v_O^\times$ are summarized in Table 2. For each crystal facet, the formation energy of $v_O^\times$_2c is significantly lower than that of $v_O^\times$_3c, showing the strong site preference of $v_O^\times$ formation. Meanwhile, the formation energy of $v_O^\times$_2c also exhibits facet dependency, that is, the formation energy on facet [001] is significantly lower than those on [100] and [101] facets. These computational results indicate that the [001]-oriented TiO_2 promotes the formation of oxygen vacancies under the imposed reducing conditions. Thus, our facile method for the preparation of black TiO_2 with tunable crystal structure is advantageous and matches perfectly with the simple galvanic deposition method for the deposition of high-performance catalyst of low loadings (μg cm^{-2} range).

To explore the formation process of Pt particles on TiO_2, we calculated the adsorption energy of single Pt atom on the different facets. It is also assumed that the adsorbed Pt atom can act as the nuclei for the Pt particles growth. The Pt adsorption energies are summarized in Table 3.

It is found that the Pt adsorption energies on oxygen-deficient surface are significantly lower compared to that on

Table 2. Formation energies of neutral oxygen vacancy under dry H_2 (H_2 = 10 bar and $H_2O = 10^{-5}$ bar) at 500 C.

Oxide ion site	Formation energy [eV] Facet [001]	Facet [100]	Facet [101]
$v_O^\times$_2c	−1.55	−0.63	0.40
$v_O^\times$_3c	0.70	0.28	1.09

Table 3. Adsorption energies of Pt atom at different TiO_2 surfaces.

Surface type	Pt adsorption energy [eV] Facet [001]	Facet [100]	Facet [101]
pristine surface	−1.75	−2.02	−1.02
surface with $v_O^{\times}$-2c	−3.39	−3.04	−1.22

the pristine surface, showing that the defective surface favors the Pt adsorption on the surface. Among the three crystal facets studied and considered herein, the Pt adsorption energy on oxygen-deficient [001] facet was the lowest compared to that of other two facets with a value of −3.39 eV. Furthermore, an analysis of the charge distribution clearly indicated that the electrons transfer from $v_O^{\times}$ towards the Pt atom during the adsorption process (Figure 8). The excess of electrons on Pt may additionally promote the reduction of the next adsorbed Pt ions, promoting the growth of Pt particles. Pt deposition on bTNT can be described with the following half-reaction [Eq. (4)], based on which Pt(IV) is reduced as metallic Pt:

$$PtCl_6^{2-} + 2\ (2e^- + v_O^{\bullet\bullet}) \rightarrow Pt + 2v_O^{\bullet\bullet} + 6\ Cl^- \quad (4)$$

where the positively charged oxygen vacancy $v_O^{\bullet\bullet}$ and e- stand for the neutrally charged oxygen vacancy $(v_O^{\times})$. Finally, it is worth adding that the galvanic replacement process involves a partial surface oxidation of bTNT at locations nearby to those of Pt deposition. However, the rest of the material is expected to be unaffected because the oxide ion mobility at room temperature is very low, therefore the bulk of TiO_2 can still maintain the high oxygen deficiency. Moreover, the loss of electrons during Pt deposition is compensated during operation as cathode. These assumptions are macroscopically confirmed by the clear, not distorted by ohmic losses electrochemistry.

Conclusion

In this work and for the first time, we showed the deposition of Pt nanoparticles (NPs) across the whole length of high aspect ratio black TiO_2 nanotubes. This was achieved by an in-situ formation and deposition of the Pt NPs, facilitated by the galvanic deposition method. Our density functional theory studies elucidated the synergy between the preferential [004] orientation and the in-situ formation of Pt NPs. Our results suggested that localized electrons at the oxygen vacancy sites can reduce Pt(IV) ions from an aqueous electrolyte solution and deposit Pt NPs of approximately 2.5 nm. This mechanism and formation of Pt NPs are favored in the [004] oriented nanotubes and an exponential deposition profile of Pt NPs along the black TiO_2-nanotubes (bTNTs) has been observed by high-resolution scanning transmission electron microscopy analysis. Meanwhile, inductively coupled plasma mass spectrometry measurements found that the mass loadings of Pt was in the range of a few tens of $\mu g\,cm^{-2}$. The prepared platinized bTNT samples were tested as hydrogen evolution cathodes exhibiting high hydrogen evolution reaction (HER) performances, comparable to state-of-the-art Pt-based cathodes. Their performance could be tuned by varying the nanotube length, and the best results per substrate nominal geometric area were obtained for platinized nanotubes of a length of 10 μm, whereas those per mg of Pt were obtained for 2 μm long nanotubes. Finally, the good stability of the platinized bTNT has been witnessed by the minimal potential change in a 48 h long galvanostatic experiment. This work contributes to the preparation of highly active HER cathodes based on noble metal catalysts of low mass loadings by minimal engineering. Moreover, this facile method of in-situ NPs formation can assist in nano-fluidic studies in high-aspect-ratio nanostructured materials with applications in drug delivery, sensors, membranes, and others. Finally, we provided important insights on the underlying deposition mechanism, correlated to tunable structural and electronic properties.

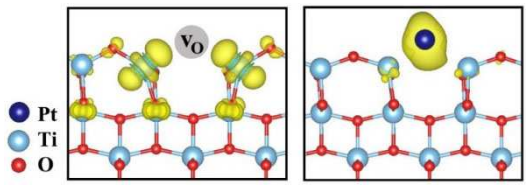

Figure 8. Isosurface of neutral oxygen vacancies ($v_O^{\times}$) and a single Pt atom adsorption on $v_O^{\times}$.

Experimental Section

Chemicals and apparatus

Ti sheet (0.25 mm thick, 99.7% purity), ethylene glycol (analytical grade), and ammonium fluoride (analytical grade) were purchased from Sigma-Aldrich. The DC power supply used to prepare titania nanotubes was by Keithley Instruments (Model 2200–72-1DC). Calcium hydride (CaH_2, ≥97.0% powder) and potassium hexachloroplatinate (K_2PtCl_6, ≥99.9% trace metals basis) were supplied from Sigma Aldrich, perchloric acid ($HClO_4$, 70%) from Merck, and hydrochloric acid (HCl, 37% for laboratory use) and nitric acid (HNO_3, 65%) from ChemLab.

Preparation of the Pt/bTNT electrocatalysts

The synthesis of the Pt/bTNT electrocatalysts included the preparation of the bTNT and the Pt deposition on them via the spontaneous galvanic deposition method. Self-ordered TNT was synthesized by the well-established two-step anodization process of Ti foils. Before anodization, the Ti foils (1 cm × 1 cm) were ultasonicated in isopropanol, acetone, and then water for 15 min in each solution and left to dry vertically in air. Ti foils were anodized applying a voltage of 60 V by a DC power supply, in an organic ethylene glycol solution containing 0.25 wt% NH_4F and 2 wt% H_2O, in a two-electrode system. Each Ti foil was placed at a constant distance of 2 cm from a Pt foil, used as the counter electrode. Ti foils were anodized in two anodization steps. The first anodization step lasted 90 min and the oxide layer was removed, revealing a TNT pattern on the Ti surface. During the second step the patterned Ti substrate was subjected to the anodization process in a fresh solution for a further period of time to create stable, self-ordered,

and well-structured titania nanotubes. The growth of the titania nanotubes was assisted by the already formed TNT pattern on the Ti substrate. Varying the duration of the second anodization step resulted in different TNT lengths, with 30, 5, and 0 min corresponding to 10, 2, and 0 μm length of the titania nanotubes, as reported in a previous work.[47] Note that samples of 0 μm length correspond to the patterned Ti substrates. The TNT/Ti foils were left in the same solution for at least 1 h to improve nanotube adhesion. The thus prepared TNT/Ti foils were placed in a quartz tube in direct contact with CaH_2 and the tube was sealed under vacuum and then placed in a furnace to anneal the samples at 500 C for 2 h (with heating and cooling rates of 1.6 C min^{-1}). The TNTs obtained anatase structure at 500 C and metallic-like conductivity at the reducing atmosphere resulted in conductive bTNT (refer to our electrochemical impedance data in our previous works[5,52]). In this work these bTNT samples are referred as bTNT30, bTNT5, and bTNT0, respectively, based on the second step anodization time.

The deposition of metallic Pt was achieved by the galvanic deposition method. The sealed quartz tube was opened and the freshly reduced and completely dry specimens were immersed immediately in a Pt(IV) ion complex solution. This step ensures that the complex solution fills the TNT pores and the Pt deposition can happen all the way to the bottom of the nanotube. The N_2-deaerated Pt(IV) solution contained 0.5 mM K_2PtCl_6 and 0.1 M $HClO_4$. The galvanic deposition took place at 65 C for 10 min under a continuous N_2 flow above the solution. The chloroplatinate solution was deoxygenated with N_2 gas to avoid O_2 reduction instead of Pt(IV) reduction, as O_2 reduction is a thermodynamically competitive reaction.

Microscopic and spectroscopic analyses

SEM (Hitachi SU8230, an acceleration voltage of 3 kV) equipped with EDS was used to analyze the overall morphology and composition of the prepared electrodes. The cross-sectional SEM images were obtained after polishing of epoxy resin-embedded samples in order to obtain true images of the interior of the nanotubes. STEM was performed with a Titan G2 60–300 instrument, operated at 300 kV with 80 pA beam current and 0.08 nm of nominal spatial resolution, to obtain the morphology of single nanotubes and Pt nanoparticles. The samples were investigated using data collected by annular bright-field (ABF), low-angle annular dark field (ADF), and high-angle annular dark field (HAADF) detectors. The crystalline phase of the samples was identified by XRD (Bruker D8 Discover, Cu $K_{\alpha 1}$-filters radiation, $\lambda = 1.5406$ Å, Bragg–Brentano) with a 0.02 (2θ) step, and dwell time of 10 s $step^{-1}$. For the identification of the chemical state of the sample surfaces, XPS was performed on a KRATOS Axis Ultra^{DLD} using monochromatic Al K_α radiation (1486.6 eV). Survey and high-resolution scans were acquired at the pass energies of 160 and 20 eV, respectively. All spectra were acquired at a 0 angle of emission (vertical emission). The casaXPS software was used for data processing. The Pt mass loading was determined by ICP-MS, at a Thermoscientific iCAP Q ICP-MS controlled by Q Tegra Software. Each sample was subjected to chemical digestion in 4 mL aqua regia ($HCl + HNO_3$) for 30 min. The leachates were diluted in 2% HNO_3 before measurement.

Electrochemical setup

The electrochemical experiments were conducted in a three-electrode system to study the platinized bTNTs and their corresponding substrates. A Pt foil was used as the counter electrode and a saturated calomel electrode (SCE sat. KCl) as the reference electrode. All the referred potentials in the plots of this work are quoted versus RHE (reversible hydrogen electrode) based on the following Equation (5) (applied for 0.1 M $HClO_4$ and pH = 1):

$$E_{RHE} = E_{SCE} + E^0{}_{SCE} + 0.059\ \text{pH} = E_{SCE} + 0.244 + 0.059\,\text{V} = E_{SCE} + 0.303\,\text{V} \quad (5)$$

Note that the equilibrium potential for the hydrogen evolution reaction in 0.1 M $HClO_4$ at room temperature is shifted at −0.303 V vs. SCE and is 0 V vs. RHE. Hence, the applied potential referring to RHE and the overpotential coincide in the case of HER.

The electrochemical behavior was studied by CV between the onset of hydrogen and oxygen evolution reactions at a potential scan rate of 50 $mV\,s^{-1}$ in 0.1 M $HClO_4$. HER was studied by near-steady-state linear sweep voltammetry (LSV) carried out at a low scan rate of 5 $mV\,s^{-1}$ up to −0.45 V_{SCE} in 0.1 M $HClO_4$. After the HER study, impedance curves were recorded to determine the resistance of the solution at high frequencies in order to correct the potential for ohmic losses. EIS experiments were performed in the frequency range between 100 kHz and 100 mHz in the DC potential range of −0.3 to −0.36 V_{SCE} in 20 mV intervals, recording alternate current response at an AC voltage amplitude of 10 mV, in order to correct the uncompensated resistance during the HER. The electrochemical experiments were conducted with an Ivium Vertex potentiostat/galvanostat (Ivium Technologies) controlled by Ivium Software. Also, evaluation of the electrocatalyst stability was carried out at $-10\,mA\,cm^{-2}$ in 0.1 M $HClO_4$, recording the potential response during 48 h. All electrochemical studies were carried out at room temperature (≃20 C). Finally, in order to compare the platinized bTNTs with the state-of-the-art HER electrocatalyst, a bulk Pt was scanned at the same conditions using a Pt rotating disk electrode at 1500 rpm in order to avoid H_2 gas blocking of its horizontally placed surface.

Computational methods

First-principles calculations were performed using DFT as implemented in the VASP code.[69,70] The revised Perdew-Burke-Ernzerhof (RPBE) exchange-correlation functional[71] was used throughout to describe exchange and correlation with a Hubbard-U correction (GGA + U) of 3 eV to Ti 3d orbitals. This U value was determined by using the piece-wise linearity methodology[72] for a single localized electron in bulk anatase TiO_2. The electronic wave functions were described using a plane-wave basis set with an energy cutoff of 500 eV. The anatase TiO_2 with different facet [001], [100], and [101] were represented as p(3×3), p(3×1), and p(2×3) slabs, respectively. The neighboring slabs were separated in the direction perpendicular to the surface with a vacuum layer of 16 Å and a 2×2×1 Γ-centered k-mesh was used for all calculations.

The formation energies of neutral oxygen vacancies ($v_O^\times$) were calculated according to Equation (6):[73]

$$\Delta E^f_{v_o} = E^{tot}_{v_o} - E^{tot}_{Perfect} + \mu_o \quad (6)$$

where $E^{tot}_{v_o}$ is the total energy of a supercell with neutral oxygen vacancy, while $E^{tot}_{Perfect}$ represents the total energy of the host supercell. As the experiments were performed by reducing TiO_2 with the CaH_2 powder, the chemical potential ofμ_o was calculated through $\mu_O = \mu_{H_2O} - \mu_{H_2}$ under a dry reducing condition (H_2 = 10 bar, $H_2O = 10^{-5}$ bar.) The chemical potentials of μ_{H_2} and μ_{H_2O} are calculated as following [Eq. (7)]:

$$\mu(p,T) = E_0 + H^\theta(T) - TS^\theta(T) + RT\ln\frac{p}{p^\theta} \quad (7)$$

$H^{\theta}(T)$ and $S^{\theta}(T)$ of the gas phases are taken from tabulated data.[74]

The adsorption energies (ΔE_{ad}) for a Pt atom adsorbed on the different TiO_2 surfaces were calculated by Equation (8):

$$\Delta E_{ad} = E_{Pt/TiO_2} - (E_{TiO_2} + E_{Pt}) \quad (8)$$

where E_{Pt}, E_{TiO_2}, and E_{Pt/TiO_2} are the total energies of the individual Pt atom, TiO_2 substrate, and Pt/TiO_2 cluster, respectively.

Finally, the gradient in amount of Pt on a single nanotube was graphically represented by applying a threshold to a dark field image. The intensity of Pt is much higher than the intensity of the TiO_2 tube in a dark field TEM image. By determining the number of high intensity pixels for each column of the dark field image, the distribution of Pt on the TiO_2 nanotube can be determined. To perform this, a python code utilizing hyperspy was used.[75]

Author Contributions

A. Touni investigation, formal analysis, methodology, writing – original draft; X. Liu data curation, formal analysis, investigation, methodology; X. Kang investigation; P. A. Carvalho investigation, funding acquisition, S. Diplas investigation, K. Both, investigation, data curation, formal analysis; S. Sotiropoulos conceptualization, supervision, validation, funding acquisition, writing review and editing; A. Chatzitakis formal analysis, investigation, methodology, project administration, resources, supervision, validation, funding acquisition, writing-review and editing.

Acknowledgements

This research has been co-financed by the European Regional Development Fund of the European Union and Greek national funds through the Operational Program Competitiveness, Entrepreneurship and Innovation, under the call RESEARCH – CREATE – INNOVATE (project code:T1EDK-00461). Funding from the Research Council of Norway is acknowledged (EnCaSE, project number 275058, PH2ON, project number 288320). The computer resources are supported by the National Infrastructure for High-Performance Computing and Data Storage in Norway (Project Number NN4604k). The authors wish to thank Assoc. Prof. Dimitra Lambropoulou for the ICP-MS measurements (A.U.Th., Greece).

Conflict of Interest

The authors declare no conflict of interest.

Keywords: electrocatalysis · electrode materials · hydrogen evolution · Pt electrocatalyst · TiO_2 nanotubes

[1] F. Fresno, R. Portela, S. Suárez, J. M. Coronado, *J. Mater. Chem. A* **2014**, *2*, 2863–2884.
[2] A. Chatzitakis, S. Sartori, *ChemPhysChem* **2019**, *20*, 1272–1281.
[3] T. S. Rajaraman, S. P. Parikh, V. G. Gandhi, *Chem. Eng. J.* **2020**, *389*, 123918.
[4] Y. Liu, L. Tian, X. Tan, X. Li, X. Chen, *Sci. Bull.* **2017**, *62*, 431–441.
[5] X. Liu, P. Carvalho, M. N. Getz, T. Norby, A. Chatzitakis, *J. Phys. Chem. C* **2019**, *123*, 21931–21940.
[6] M. Zimbone, G. Cacciato, M. Boutinguiza, V. Privitera, M. G. Grimaldi, *Beilstein J. Nanotechnol.* **2017**, *8*, 196–202.
[7] Z. Li, H. Bian, X. Xiao, J. Shen, C. Zhao, J. Lu, Y. Y. Li, *ACS Appl. Nano Mater.* **2019**, *2*, 7372–7378.
[8] B. Wang, S. Shen, S. S. Mao, *J. Mater.* **2017**, *3*, 96–111.
[9] X. Chen, L. Liu, P. Y. Yu, S. S. Mao, *Science* **2011**, *331*, 746–750.
[10] S. E. Heo, H. W. Lim, D. K. Cho, I. J. Park, H. Kim, C. W. Lee, S. H. Ahn, J. Y. Kim, *J. Catal.* **2020**, *381*, 462–467.
[11] H. Cui, W. Zhao, C. Yang, H. Yin, T. Lin, Y. Shan, Y. Xie, H. Gu, F. Huang, *J. Mater. Chem. A* **2014**, *2*, 8612–8616.
[12] H. Lu, B. Zhao, R. Pan, J. Yao, J. Qiu, L. Luo, Y. Liu, *RSC Adv.* **2014**, *4*, 1128–1132.
[13] J. Xu, Z. Tian, G. Yin, T. Lin, F. Huang, *Dalton Trans.* **2017**, *46*, 1047–1051.
[14] K. M. Fuentes, D. Venuti, P. Betancourt, *React. Kinet. Mech. Catal.* **2020**, *131*, 423–435.
[15] Q. Bi, X. Huang, Y. Dong, F. Huang, *Catal. Lett.* **2020**, *150*, 1346–1354.
[16] W. H. Saputera, G. Mul, M. S. Hamdy, *Catal. Today* **2015**, *246*, 60–66.
[17] J. Chen, Z. Ding, C. Wang, H. Hou, Y. Zhang, C. Wang, G. Zou, X. Ji, *ACS Appl. Mater. Interfaces* **2016**, *8*, 9142–9151.
[18] S. T. Myung, M. Kikuchi, C. S. Yoon, H. Yashiro, S. J. Kim, Y. K. Sun, B. Scrosati, *Energy Environ. Sci.* **2013**, *6*, 2609–2614.
[19] J. Zhi, C. Yang, T. Lin, H. Cui, Z. Wang, H. Zhang, F. Huang, *Nanoscale* **2016**, *8*, 4054–4062.
[20] C. Zhang, H. Yu, Y. Li, Y. Gao, Y. Zhao, W. Song, Z. Shao, B. Yi, *ChemSusChem* **2013**, *6*, 659–666.
[21] X. Yan, Y. Li, T. Xia, *Int. J. Photoenergy* **2017**, *2017*, 8529851.
[22] N. Liu, C. Schneider, D. Freitag, E. M. Zolnhofer, K. Meyer, P. Schmuki, *Chem. A Eur. J.* **2016**, *22*, 13810–13814.
[23] X. Chen, L. Liu, Z. Liu, M. A. Marcus, W. C. Wang, N. A. Oyler, M. E. Grass, B. Mao, P. A. Glans, P. Y. Yu, J. Guo, S. S. Mao, *Sci. Rep.* **2013**, *3*, 1510.
[24] N. Denisov, S. Qin, G. Cha, J. E. Yoo, P. Schmuki, *J. Electroanal. Chem.* **2020**, *872*, 114098.
[25] L. Li, L. Song, L. Zhu, Z. Yan, X. Cao, *Catal. Sci. Technol.* **2018**, *8*, 1277–1287.
[26] N. Liu, C. Schneider, D. Freitag, M. Hartmann, U. Venkatesan, J. Mueller, E. Spiecker, P. Schmuki, *Nano Energy* **2014**, *14*, 3309–3313.
[27] J. Liu, J. Yan, Q. Shi, H. Dong, J. Zhang, Z. Wang, W. Huang, B. Chen, H. Zhang, *J. Phys. Chem. C* **2019**, *123*, 4094–4102.
[28] G. Zhu, H. Yin, C. Yang, H. Cui, Z. Wang, J. Xu, T. Lin, F. Huang, *ChemCatChem* **2015**, *7*, 2614–2619.
[29] J. Gao, Q. Shen, R. Guan, J. Xue, X. Liu, H. Jia, Q. Li, Y. Wu, *J. CO2 Util.* **2020**, *35*, 205–215.
[30] C. Fan, C. Chen, J. Wang, X. Fu, Z. Ren, G. Qian, Z. Wang, *Sci. Rep.* **2015**, *5*, 11712.
[31] A. N. Colli, H. H. Girault, A. Battistel, *Materials* **2019**, *12*, 1336.
[32] Z. He, Y. Tong, S. Ni, X. Ye, C. P. Makwarimba, X. Huang, S. Zhang, S. Song, *Electrochim. Acta* **2018**, *292*, 685–696.
[33] M. Carmo, D. L. Fritz, J. Mergel, D. Stolten, *Int. J. Hydrogen Energy* **2013**, *38*, 4901–4934.
[34] K. Bensadok, N. El Hanafi, F. Lapicque, *Desalination* **2011**, *280*, 244–251.
[35] A. Landman, R. Halabi, P. Dias, H. Dotan, A. Mehlmann, G. E. Shter, M. Halabi, O. Naseraldeen, A. Mendes, G. S. Grader, A. Rothschild, *Joule* **2020**, *4*, 448–471.
[36] S. Trasatti, *J. Electroanal. Chem.* **1972**, *39*, 163–184.
[37] N. Dubouis, A. Grimaud, *Chem. Sci.* **2019**, *10*, 9165–9181.
[38] D. Pletcher, *A First Course in Electrode Processes*, Royal Society of Chemistry, **2009**.
[39] X. Wang, X. Yuan, X. Liu, W. Dong, C. Dong, M. Lou, J. Li, T. Lin, F. Huang, *J. Alloys Compd.* **2017**, *701*, 669–675.
[40] Z. Li, Y. Wang, A. A. Elzatahry, X. Yang, S. Pu, W. Luo, X. Cheng, Y. Deng, *Chin. Chem. Lett.* **2020**, *31*, 1598–1602.
[41] T. Wang, Y. Zhu, Z. Luo, Y. Li, J. Niu, C. Wang, *Environ. Chem. Lett.* **2021**, *19*, 1815–1821.
[42] Z. W. Wei, H. J. Wang, C. Zhang, K. Xu, X. L. Lu, T. B. Lu, *Angew. Chem. Int. Ed.* **2021**, *60*, 16622–16627.
[43] I. Szenti, L. Bugyi, Z. Kónya, *Top. Catal.* **2018**, *61*, 1362–1374.
[44] X. Yuan, X. Wang, X. Liu, H. Ge, G. Yin, C. Dong, F. Huang, *ACS Appl. Mater. Interfaces* **2016**, *8*, 27654–27660.
[45] A. Papaderakis, I. Mintsouli, J. Georgieva, S. Sotiropoulos, *Catalysts* **2017**, *7*, 80.

[46] U. Lačnjevac, R. Vasilić, A. Dobrota, S. Đurđić, O. Tomanec, R. Zbořil, S. Mohajernia, N. T. Nguyen, N. Skorodumova, D. Manojlović, N. Elezović, I. Pašti, P. Schmuki, *J. Mater. Chem. A* **2020**, *8*, 22773–22790.
[47] A. Chatzitakis, M. Grandcolas, K. Xu, S. Mei, J. Yang, I. J. T. Jensen, C. Simon, T. Norby, *Catal. Today* **2017**, *287*, 161–168.
[48] J. Gong, Y. Lai, C. Lin, *Electrochim. Acta* **2010**, *55*, 4776–4782.
[49] S. Ozkan, A. Mazare, P. Schmuki, *Electrochim. Acta* **2015**, *176*, 819–826.
[50] S. Hassan, A. Tariq, Z. Noreen, A. Donia, S. Z. J. Zaidi, H. Bokhari, X. Zhang, *Diagnostics* **2020**, *10*, 509.
[51] Y. Zhu, K. Petkovic-Duran, *Microfluid. Nanofluidics* **2010**, *8*, 275–282.
[52] M. N. Getz, A. Chatzitakis, X. Liu, P. A. Carvalho, T. S. Bjørheim, T. Norby, *Mater. Chem. Phys.* **2020**, *239*, 4–9.
[53] C. Z. Wen, H. B. Jiang, S. Z. Qiao, H. G. Yang, G. Q. (Max) Lu, *J. Mater. Chem.* **2011**, *21*, 7052–7061.
[54] Y. S. Kim, A. Bostwick, E. Rotenberg, P. N. Ross, S. C. Hong, B. S. Mun, *J. Chem. Phys.* **2010**, *133*, 034501.
[55] X. Zhang, W. Hu, K. Zhang, J. Wang, B. Sun, H. Li, P. Qiao, L. Wang, W. Zhou, *ACS Sustainable Chem. Eng.* **2017**, *5*, 6894–6901.
[56] J. Lim, Y. Yang, M. R. Hoffmann, *Environ. Sci. Technol.* **2019**, *53*, 6972–6980.
[57] A. Naumkin, A. Kraut-Vass, S. W. Gaarenstroom, C. J. Powell, "NIST X-ray Photoelectron Spectroscopy Database," **n.d**.
[58] X. Kang, C. Berberidou, A. Galeckas, C. Bazioti, E. Sagstuen, T. Norby, I. Poulios, A. Chatzitakis, *Catalysts* **2021**, *11*, 228.
[59] M. Zeng, L. Yanguang, *J. Mater. Chem. A* **2019**, 3971–3978.
[60] E. Kemppainen, A. Bodin, B. Sebok, T. Pedersen, B. Seger, B. Mei, D. Bae, P. C. K. Vesborg, J. Halme, O. Hansen, P. D. Lunda, I. Chorkendorff, *Energy Environ. Sci.* **2015**, *8*, 2991–2999.
[61] T. Shinagawa, A. T. Garcia-Esparza, K. Takanabe, *Sci. Rep.* **2015**, *5*, 13801.
[62] G. Zhao, K. Rui, S. X. Dou, W. Sun, *Adv. Funct. Mater.* **2018**, *28*, 1803291.
[63] W. Luo, J. Gan, Z. Huang, W. Chen, G. Qian, X. Zhou, X. Duan, *Front. Mater.* **2019**, *6*, 251.
[64] Q. Wang, C. Q. Xu, W. Liu, S. F. Hung, H. Bin Yang, J. Gao, W. Cai, H. M. Chen, J. Li, B. Liu, *Nat. Commun.* **2020**, *11*, 4246.
[65] A. Papaderakis, N. Pliatsikas, P. Patsalas, D. Tsiplakides, S. Balomenou, A. Touni, S. Sotiropoulos, *J. Electroanal. Chem.* **2018**, *808*, 21–27.
[66] D. Liu, X. Li, S. Chen, H. Yan, C. Wang, C. Wu, Y. A. Haleem, S. Duan, J. Lu, B. Ge, P. M. Ajayan, Y. Luo, J. Jiang, L. Song, *Nat. Energy* **2019**, *4*, 512–518.
[67] J. N. Tiwari, S. Sultan, C. W. Myung, T. Yoon, N. Li, M. Ha, A. M. Harzandi, H. J. Park, D. Y. Kim, S. S. Chandrasekaran, W. G. Lee, V. Vij, H. Kang, T. J. Shin, H. S. Shin, G. Lee, Z. Lee, K. S. Kim, *Nat. Energy* **2018**, *3*, 773–782.
[68] Y. Shi, Z. R. Ma, Y. Y. Xiao, Y. C. Yin, W. M. Huang, Z. C. Huang, Y. Z. Zheng, F. Y. Mu, R. Huang, G. Y. Shi, Y.-Y. Sun, X.-H. Xia, W. Chen, *Nat. Commun.* **2021**, *12*, 3021.
[69] G. Kresse, D. Joubert, *Phys. Rev. B: Condens. Matter Mater. Phys.* **1999**, *59*, 1758–1775.
[70] G. Kresse, J. Furtmueller, *Phys. Rev. B* **1996**, *54*, 11 169.
[71] B. Hammer, L. B. Hansen, J. K. Nørskov, *Phys. Rev. B: Condens. Matter Mater. Phys.* **1999**, *59*, 7413–7421.
[72] B. Sadigh, P. Erhart, D. Åberg, *Phys. Rev. B: Condens. Matter Mater. Phys.* **2015**, *92*, 075202.
[73] S. B. Zhang, J. E. Nortrup, *Phys. Rev. Lett.* **1991**, *67*, 2339–2342.
[74] M. W. Chase, *NIST-JANAF Thermochemical Tables, The American Institute of Physics for The National Institute of Standards and Technology*, American Institute Of Physics, **1998**.
[75] F. de la Pena, E. Prestat, V. T. Fauske, P. Burdet, T. Furnival, P. Jokubauskas, M. Nord, T. Ostasevicious, J. Lahnemann, K. E. MacArthur, et al., **n.d.**, DOI 10.5281/zenodo.4923970.

Manuscript received: July 23, 2021
Revised manuscript received: August 23, 2021
Accepted manuscript online: September 3, 2021
Version of record online: October 6, 2021